

2

WL-TR-93-4059

RAPIDLY SOLIDIFIED OXIDATION  
RESISTANT NIOBIUM BASE ALLOYS

AD-A273 211



C.M.AUSTIN, J.R.DOBBS, H.L.FRASER,  
D.G.KONITZER, D.J.MILLER, M.J.PARKS,  
J.C.SCHAEFFER, AND J.W.SEARS

GENERAL ELECTRIC AIRCRAFT ENGINES  
ONE NEUMANN WAY  
CINCINNATI OH 45215-6301

MARCH 1992

FINAL REPORT FOR 06/01/87-03/01/92

APPROVED FOR PUBLIC RELEASE; DISTRIBUTION IS UNLIMITED.

DTIC  
DATE  
1993  
E D

MATERIALS DIRECTORATE  
WRIGHT LABORATORY  
AIR FORCE SYSTEMS COMMAND  
WRIGHT PATTERSON AFB OH 45433-7734

21715  
93-28510

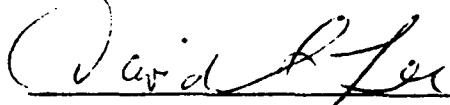
93 11 22 126


NOTICE

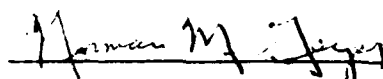
When Government drawings, specifications, or other data are used for any purpose other than in connection with a definitely Government-related procurement, the United States Government incurs no responsibility or any obligation whatsoever. The fact that the government may have formulated or in any way supplied the said drawings, specifications, or other data, is not to be regarded by implication, or otherwise in any manner construed, as licensing the holder, or any other person or corporation; or as conveying any rights or permission to manufacture, use, or sell any patented invention that may in any way be related thereto.

This report is releasable to the National Technical Information Service (NTIS). At NTIS, it will be available to the general public, including foreign nations.

This technical report has been reviewed and is approved for publication.

  
\_\_\_\_\_  
CAPT DAVID S. LEE  
Project Engineer  
Metals and Ceramics Division

  
\_\_\_\_\_  
WALTER H. REIMANN, Chief  
Materials Development Branch

  
\_\_\_\_\_  
NORMAN M. GEYER, Actg Asst Chief  
Metals and Ceramics Division

If your address has changed, if you wish to be removed from our mailing list, or if the addressee is no longer employed by your organization please notify WL/MLLM, WPAFB, OH 45433-7734 to help us maintain a current mailing list.

Copies of this report should not be returned unless return is required by security considerations, contractual obligations, or notice on a specific document.

REPORT DOCUMENTATION PAGE			Form Approved OMB No. 0704-0188
<small>Public reporting burden for this collection of information is estimated to average 1 hour per response, including the time for reviewing instructions, searching existing data sources, gathering and maintaining the data needed, and completing and reviewing the collection of information. Send comments regarding this burden estimate or any other aspect of the collection of information, including suggestions for reducing this burden, to Washington Headquarters Service, Directorate for Information Operations and Reports, 1215 Jefferson Davis Highway, Suite 1204, Arlington, VA 22202-4302, and to the Office of Management and Budget, Paperwork Reduction Project (0704-0188), Washington, DC 20503.</small>			
1. AGENCY USE ONLY (Leave blank)	2. REPORT DATE MARCH 1992	3. REPORT TYPE AND DATES COVERED FINAL, JUNE 1987-MARCH 1992	
4. TITLE AND SUBTITLE RAPIDLY SOLIDIFIED OXIDATION RESISTANT NIOBIUM BASE ALLOYS		5. FUNDING NUMBERS C F33615-87-C-5298 PE 61101F PR ILIR TA 02 WU 02	
6. AUTHOR(S) C.M. AUSTIN, J.R. DOBBS, H.L. FRASER, D.G. KONITZER, D.J. MILLER, M.J. PARKS, J.C. SCHAEFFER, J.W. SEARS		8. PERFORMING ORGANIZATION REPORT NUMBER	
7. PERFORMING ORGANIZATION NAME(S) AND ADDRESS(ES) GENERAL ELECTRIC AIRCRAFT ENGINES ONE NEUMANN WAY CINCINNATI, OHIO 45215-6301		10. SPONSORING / MONITORING AGENCY REPORT NUMBER  WL-TR-93-4059	
9. SPONSORING / MONITORING AGENCY NAME(S) AND ADDRESS(ES) MATERIALS DIRECTORATE WRIGHT LABORATORY, AIR FORCE MATERIEL COMMAND WRIGHT-PATTERSON AIR FORCE BASE, OH 45433-7734		11. SUPPLEMENTARY NOTES THIS RESEARCH WAS PARTIALLY FUNDED BY THE INHOUSE INDEPENDENT RESEARCH FUND	
12a. DISTRIBUTION / AVAILABILITY STATEMENT APPROVED FOR PUBLIC RELEASE; DISTRIBUTION IS UNLIMITED.		12b. DISTRIBUTION CODE	
13. ABSTRACT (Maximum 200 words) The initial effort concentrated on using melt spinning as the rapid solidification method for binary, ternary, quaternary and complex alloys. Ribbons were produced and given heat treatments to determine the effect on the microstructure. The ductility of the ribbons was tested in both the as-melt spun and heat treated conditions by bend testing. Four alloys were chosen for scaleup. The scaleup rapid solidification method was atomization. However, sufficient quantities and quality of powder could not be obtained for the high melting point alloys to be studied. Therefore, the decision was made to pursue ingot approaches to producing the alloys. The decision to pursue the ingot approach was made based on the difficulty of producing powder and on promising results which had been obtained on Nb-Ti alloys at GE-CRD. The Nb-Ti base alloys had been shown to have improved oxidation resistance over conventional Nb alloys, although, with a reduction in the high temperature creep strength. However, because the actual needs of the expected application were for a lower temperature, this loss in temperature capability was not considered a significant problem. Twenty alloys were chosen for screening, and produced as vacuum arc remelted (VAR) pins, forged into pancakes, and given one of three heat treatments to determine the effect on microstructure.			
14. SUBJECT TERMS Niobium Base Alloys, Columbium Base Alloys, Rapid Solidification, Melt Spun Ribbons, Vacuum Arc Remelted Ingots.		15. NUMBER OF PAGES 218	
17. SECURITY CLASSIFICATION OF REPORT Unclassified		16. PRICE CODE	
18. SECURITY CLASSIFICATION OF THIS PAGE Unclassified		19. SECURITY CLASSIFICATION OF ABSTRACT Unclassified	
20. LIMITATION OF ABSTRACT Unlimited			





## List Of Figures

Figure 2.1	Arc-Melt Spinner used for production of Nb Alloy Ribbons.....	7
Figure 2.2	Arc Melting Apparatus used in Melt Spinner.....	7
Figure 3.1	a) Bright field TEM micrograph of as-melt spun Nb-12Al, b) bright field TEM micrograph of as-melt spun Nb-15Al.....	23
Figure 3.2	Bright field TEM of melt spun and heat treated Nb-12Al. The heat treatment was for 1 hour at 1000°C.....	24
Figure 3.3	Bright field TEM of as-melt spun Nb-20Cr showing the cellular microstructure observed in most of the ribbons.....	24
Figure 3.4	Bright field TEM of as-melt spun Nb-20Cr showing a discontinuous array of particles in an $\alpha$ -Nb matrix in the thinnest areas of the ribbon.....	25
Figure 3.5	Bright field TEM of melt-spun and heat treated Nb-20Cr. The heat treatment was for 1 hour at 1000°C.....	25
Figure 3.6	Bright field TEM of as-melt spun Nb-15Fe showing a cellular microstructure.....	26
Figure 3.7	Bright field TEM of as-melt spun Nb-15Fe showing a discontinuous array of particles in an $\alpha$ -Nb matrix in the thinnest areas of the ribbon. Some NbFe phase also decorates the cell boundaries.....	26
Figure 3.8	Bright field TEM of melt-spun and heat treated Nb-15Fe. The heat treatment was for 1 hour at 1000°C.....	27
Figure 3.9	Graph of estimated strain versus Cr content for two levels of Al additions for as-melt spun ribbon. ....	27
Figure 3.10	Estimated strain versus Cr content for two levels of Al additions for ribbon which has been melt-spun and subsequently heat treated at 600°C for 1 hour .....	28

Figure 3.11	Estimated strain versus Cr content for two levels of Al additions for ribbon heat treated at 600°C for 1 hour followed by 1200°C for 1 hour. ....	28
Figure 3.12	Bright field TEM micrograph of as-melt spun Nb-10Al-5Cr (alloy H1).....	29
Figure 3.13	Bright field TEM micrograph of as-melt spun Nb-10Al-10Cr (alloy H2).....	29
Figure 3.14	Bright field TEM micrograph of as-melt spun Nb-10Al-20Cr (alloy H3).....	30
Figure 3.15	Bright field TEM micrograph of as-melt spun Nb-15Al-5Cr (alloy H4).....	30
Figure 3.16	Bright field TEM micrograph of as-melt spun Nb-15Al-10Cr (alloy H5).....	31
Figure 3.17	Bright field TEM micrograph of as-melt spun Nb-15Al-20Cr (alloy H6).....	31
Figure 3.18	Bright field TEM micrograph of as-melt spun Nb-10Al-20Cr (alloy H3) showing the segregated microstructure frequently observed in alloys containing additions of both Al and Cr.....	32
Figure 3.19	Bright field TEM micrograph of Nb-10Al-5Cr (alloy H1) melt-spun ribbon after heat treatment at 600°C for 1 hour.....	32
Figure 3.20	Bright field TEM micrograph of Nb-10Al-10Cr (alloy H2) melt-spun ribbon after heat treatment at 600°C for 1 hour.....	33
Figure 3.21	Bright field TEM micrograph of Nb-10Al-20Cr (alloy H3) melt-spun ribbon after heat treatment at 600°C for 1 hour.....	33
Figure 3.22	Bright field TEM micrograph of Nb-15Al-5Cr (alloy H4) melt-spun ribbon after heat treatment at 600°C for 1 hour.....	34
Figure 3.23	Bright field TEM micrograph of Nb-15Al-10Cr (alloy H5) melt-spun ribbon after heat treatment at 600°C for 1 hour.....	34
Figure 3.24	Bright field TEM micrograph of Nb-15Al-20Cr (alloy H6) melt-spun ribbon after heat treatment at 600°C for 1 hour.....	35

Figure 3.25	Estimated strain versus Ti alloy content for two base compositions of as-melt spun ribbon; Alloy 1 is Nb-10Al-10Cr-Ti and Alloy 2 is Nb-15Al-20Cr-Ti.....	35
Figure 3.26	Estimated strain versus Ti alloy content for two base compositions of as-melt spun ribbon heat treated at 600°C/ 1 hour; Alloy 1 is Nb-10Al-10Cr-xTi and Alloy 2 is Nb-15Al-20Cr-xTi.....	36
Figure 3.27	Estimated strain versus Ti alloy content for two base compositions of as-melt spun ribbon heat treated at 600°C/ 1 hour followed by 1200°C/one hour; Alloy 1 is Nb-10Al-10Cr-xTi and Alloy 2 is Nb-15Al-20Cr-xTi.....	36
Figure 3.28	Chart of estimated strains in ribbons subjected to bending for the various alloys shown. The conditions noted correspond to as-melt spun, heat treated at 600°C for 1 hour, and heat treated at 600°C for 1 hour followed by 1200°C for 1 hour.....	37
Figure 3.29	Bright field TEM micrograph of as-melt spun Nb-10Al-10Cr-10Ti (alloy H7).....	37
Figure 3.30	Bright field TEM micrograph of as-melt spun Nb-15Al-20Cr-10Ti (alloy H8).....	38
Figure 3.31	Bright field TEM micrograph of as-melt spun Nb-10Al-10Cr-20Ti (alloy H9).....	38
Figure 3.32	Bright field TEM micrograph of as-melt spun Nb-15Al-20Cr-20Ti (alloy H10).....	39
Figure 3.33	Bright field TEM micrograph of Nb-10Al-10Cr-10Ti (alloy H7) melt-spun ribbon after heat treatment at 600°C for 1 hour.....	39
Figure 3.34	Bright field TEM micrograph of Nb-15Al-20Cr-10Ti (alloy H8) melt-spun ribbon after heat treatment at 600°C for 1 hour.....	40
Figure 3.35	Bright field TEM micrograph of as-melt spun Nb-10Al-10Cr-5V (alloy H11).....	40
Figure 3.36	Bright field TEM micrograph of as-melt spun Nb-10Al-10Cr-5Hf (alloy H12).....	41
Figure 3.37	Bright field TEM micrograph of as-melt spun Nb-10Al-10Cr-5Zr (alloy H13).....	41
Figure 3.38	Bright field TEM micrograph of as-melt spun Nb-10Al-10Cr-5Ta (alloy H14).....	42

Figure 3.39	Bright field TEM micrograph of Nb-10Al-10Cr-5Zr (alloy H11) melt-spun ribbon after heat treatment at 600°C for 1 hour.....	42
Figure 3.40	Bright field TEM micrograph of as-melt spun Nb-10Al-10Cr-10Ti-15W (alloy S1).....	43
Figure 3.41	Bright field TEM micrograph of as-melt spun and heat treated Nb-10Al-10Cr-10Ti-15W (alloy S1). Heat treatment was at 600°C for 1 hour.....	43
Figure 3.42	Bright field TEM micrograph of as-melt spun Nb-13Al-35Cr-2.5Ni (alloy S3).....	44
Figure 3.43	Bright field TEM micrograph of as-melt spun and heat treated Nb-13Al-35Cr-2.5Ni (alloy S3). Heat treatment was at 600°C for 1 hour.....	44
Figure 3.44	Bright field TEM micrograph of as-melt spun Nb-10Al-10Cr-10Ti-10W-1Zr (alloy S4).....	45
Figure 3.45	Bright field TEM micrograph of as-melt spun Nb-10Al-10Cr-10Ti-10W-1Er (alloy S5).....	45
Figure 3.46	Bright field TEM micrograph of as-melt spun and heat treated Nb-10Al-10Cr-10Ti-10W-1Er (alloy S5). Heat treatment was at 600°C for 1 hour.....	46
Figure 3.47	Bright field TEM micrograph of as-melt spun Nb-10Al-10Cr-10Ti-10W-1Y (alloy S6).....	46
Figure 3.48	Bright field TEM micrograph of as-melt spun and heat treated Nb-10Al-10Cr-10Ti-10W-1Y (alloy S6). Heat treatment was 600°C for 1 hour.....	47
Figure 3.49	Bright field TEM micrograph of as-melt spun Nb-15Ti-15W-3Mo-1Zr-1Er (alloy S7).....	47
Figure 3.50	Bright field TEM micrograph of as-melt spun and heat treated Nb-15Ti-15W-3Mo-1Zr-1Er (alloy S7). Heat treatment was 600°C for 1 hour.....	48

Figure 3.51	Bright field TEM micrograph of as-melt spun Nb-5Al-5Cr-15Ti-15W-3Mo-1Zr-1Er (alloy S8).....	48
Figure 3.52	Bright field TEM micrograph of as-melt spun and heat treated Nb-5Al-5Cr-15Ti-15W-3Mo-1Zr-1Er (alloy S8). Heat treatment was 600°C for 1 hour.....	49
Figure 3.53	Bright field TEM micrograph of as-melt spun Nb-10Al-10Cr-15Ti-10W-3Mo-1Zr-1Er (alloy S9).....	49
Figure 3.54	Bright field TEM micrograph of as-melt spun and heat treated Nb-10Al-10Cr-15Ti-10W-3Mo-1Zr-1Er (alloy S9). Heat treatment was 600°C for 1 hour.....	50
Figure 3.55	Bright field TEM micrograph of as-melt spun Nb-10Al-10Cr-15Ti-15W-1Zr-1Er (alloy S10).....	50
Figure 3.56	Bright field TEM micrograph of as-melt spun Nb-10Al-10Cr-15Ti-15W-1Zr-1Er (alloy S10).....	51
Figure 3.57	Bright field TEM micrograph of as-melt spun and heat treated Nb-10Al-10Cr-15Ti-10W-1Zr-1Er (alloy S11). Heat treatment was at 600°C for 1 hour.....	51
Figure 3.58	Bright-field transmission electron micrographs recorded from typical areas taken from thin foils of powders of alloy P5. Note the dendritic and interdendritic regions, marked A and B, respectively. Also note the presence of small particles, which have been identified as $Er_2O_3$ .....	52
Figure 3.59	Bright-field transmission electron micrograph of sample of powders of alloy P5 following heat-treatment for 4 hours at 1200°C.....	52
Figure 3.60	EDS spectra recorded from a thin foil of a powder of alloy P5 following heat-treatment for 4 hours at 1200°C with the electron beam incident on (a) the $\alpha$ -Nb matrix, (b) a particle of $Nb_3Al$ and (c) a particle of TiC.....	53-54
Figure 3.61	Bright-field transmission electron micrographs recorded from areas of thinned powders of alloy P6.....	54

Figure 3.62	EDS spectrum recorded from $\alpha$ -Nb in powders of alloy P6.....	55
Figure 3.63	EDS spectrum recorded from NbCr <sub>2</sub> in powders of alloy P6.....	55
Figure 3.64	Transmission electron micrograph of a typical area observed in powders of alloy P6 following heat-treatment for 4 hours at 1200°C.....	56
Figure 3.65	Transmission electron micrograph of the $\alpha$ -Nb matrix phase in a sample from alloy P6 following heat-treatment for 4 hours at 1200°C revealing tweed-like contrast.....	56
Figure 3.66	Typical bright field transmission electron micrograph recorded from a thin foil of powder of alloy P7 in the as-atomized condition.....	57
Figure 3.67	EDS x-ray spectra recorded from a thinned powder of alloy P7 in the as-atomized condition. a) from the matrix; b) from a second phase particle, identified as NbCr <sub>2</sub> .....	58
Figure 3.68	Typical bright-field transmission electron micrograph recorded from a thin foil of powder of alloy P7 following heat-treatment (see text).....	59
Figure 3.69	Typical bright-field transmission electron micrograph recorded from a thin foil of powder of alloy P8 in the as-atomized condition.....	59
Figure 3.70	EDS spectra recorded from two different regions (a and b) of the matrix of thinned powders of P8 (as-atomized), shown in Fig. 3.69, revealing the inhomogeneous composition of the matrix.....	60
Figure 3.71	Typical bright-field transmission electron micrograph recorded from a thin foil of powder of alloy P8 following heat treatment (see text).....	61
Figure 4.1	Optical micrographs of the microstructure of Alloy 2 in the a) as- forged, b) solution treated, c) solution treated and aged, and d) direct aged conditions.....	85
Figure 4.2	Optical micrographs of the microstructure of Alloy 3 in the a) as- forged, b) solution treated, c) solution treated and aged, and d) direct aged conditions.....	86

Figure 4.3	Optical micrographs of the microstructure of Alloy 4 in the a) as-forged, b) solution treated, c) solution treated and aged, and d) direct aged conditions.....	87
Figure 4.4	Optical micrographs of the microstructure of Alloy 5 in the a) as-forged, b) solution treated, c) solution treated and aged, and d) direct aged conditions.....	88
Figure 4.5	Optical micrographs of the microstructure of Alloy 6 in the a) as-forged, b) solution treated, c) solution treated and aged, and d) direct aged conditions.....	89
Figure 4.6	Optical micrographs of the microstructure of Alloy 7 in the a) as-forged, b) solution treated, c) solution treated and aged, and d) direct aged conditions.....	90
Figure 4.7	Optical micrographs of the microstructure of Alloy 8 in the a) as-forged, b) solution treated, c) solution treated and aged, and d) direct aged conditions.....	91
Figure 4.8	Optical micrographs of the microstructure of Alloy 9 in the a) as-forged, b) solution treated, c) solution treated and aged, and d) direct aged conditions.....	92
Figure 4.9	Optical micrographs of the microstructure of Alloy 10 in the a) as-forged, b) solution treated, c) solution treated and aged, and d) direct aged conditions.....	93
Figure 4.10	Optical micrographs of the microstructure of Alloy 11 in the a) as-forged, b) solution treated, c) solution treated and aged, and d) direct aged conditions.....	94
Figure 4.11	Optical micrographs of the microstructure of Alloy 12 in the a) as-forged, b) solution treated, c) solution treated and aged, and d) direct aged conditions.....	95

Figure 4.12	Optical micrographs of the microstructure of Alloy 13 in the a) as-forged, b) solution treated, c) solution treated and aged, and d) direct aged conditions.....	96
Figure 4.13	Optical micrographs of the microstructure of Alloy 14 in the a) solution treated, b) solution treated and aged, and c) direct aged conditions.....	97
Figure 4.14	Actual microstructure of Alloy 11 as observed in the room temperature tensile test. Specimen was solution heat treated at 1050°C / 4h and aged at 700°C / 24h.....	98
Figure 4.15	Actual microstructure of Alloy 12 as observed in the room temperature tensile test. Specimen was solution heat treated at 1050°C / 4h and aged at 800°C / 24h.....	99
Figure 4.16	Optical micrographs of the microstructure of Alloy 15 in the a) as-forged, b) solution treated, c) solution treated and aged, and d) direct aged conditions.....	100
Figure 4.17	Optical micrographs of the microstructure of Alloy 17 in the a) as-forged, b) solution treated, c) solution treated and aged, and d) direct aged conditions.....	101
Figure 4.18	Optical micrographs of the microstructure of Alloy 19 in the a) as-forged, b) solution treated, c) solution treated and aged, and d) direct aged conditions.....	102
Figure 4.19	Optical micrographs of the microstructure of Alloy 20 in the a) as-forged, b) solution treated, c) solution treated and aged, and d) direct aged conditions.....	103
Figure 4.20	Comparison of the elevated temperature yield strengths for Alloys 3-6.....	104
Figure 4.21	Comparison of ultimate tensile strength of contract alloys with the conventional niobium alloy Cb752.....	104



<b>Figure 4.22</b>	<b>Comparison of the ultimate tensile strength of the C and Si modified alloys based on Alloy 4 with the unmodified Alloy 4.....</b>	<b>105</b>
<b>Figure 4.23</b>	<b>Backscattered electron images of Alloy 10 following tensile testing at room temperature showing fracture of the large primary phase, either Laves or Silicide, away from the fracture surface.....</b>	<b>106</b>
<b>Figure 4.24</b>	<b>Comparison of the ultimate tensile strength of the C and Si modified alloys based on Alloy 4 with the conventional niobium alloy Cb752.....</b>	<b>107</b>
<b>Figure 4.25</b>	<b>Graph showing the weight change / area versus time for Nb-Ti alloys, commercial Nb alloys and Rene'41 during the 800°C cyclic oxidation test. The test was performed in a low velocity oxidation rig that burnt natural gas / air mixtures and rapidly cycled the samples three times an hour to room temperature.....</b>	<b>107</b>
<b>Figure 4.26</b>	<b>Bar chart summarizing microstructural and kinetic observations for downselected Nb-Ti alloys and commercial Nb alloys. Systems that lost weight rapidly had little evidence of a layer enriched with interstitials, while alloys with moderate weight change had the layer present.....</b>	<b>108</b>
<b>Figure 4.27</b>	<b>Cyclic oxidation weight change curves as a function of time for the alloys examined in Figure 4.26.....</b>	<b>108</b>
<b>Figure 4.28</b>	<b>Bar chart comparing the cyclic oxidation resistance of various high temperature materials. The Nb-Ti alloys represent a compromise in properties with better oxidation resistance than Nb alloys.....</b>	<b>109</b>
<b>Figure 4.29</b>	<b>Cross sectional optical micrographs of Rene'41 after cyclic oxidation at 800°C for 140h, a thin continuous chromia scale is observed on the surface.....</b>	<b>109</b>
<b>Figure 4.30</b>	<b>Cross sectional optical micrographs of Cb752 after cyclic oxidation at 800°C for 20h. An unadherent, flaky white scale was observed on a heavily cold worked substrate.....</b>	<b>110</b>

Figure 4.31	Cross sectional optical micrographs of WC3009 after cyclic oxidation at 800°C for 115h. Spallation was observed on the sample in the form of chips.....	110
Figure 4.32	Cross sectional optical micrographs of 3899-3 ( Nb-37.5Ti-5Hf-5V-5Cr-5Al-0.5Zr-0.3C ) after cyclic oxidation at 800°C for 140h. The oxide was adherent and a layer enriched in interstitials is apparent.....	111
Figure 4.33	Cross sectional optical micrographs of Alloy 2 ( Nb-29Ti-25Cr-15Mo ) after cyclic oxidation at 800°C for 140h. The alloy had good oxidation resistance but was difficult to fabricate.....	112
Figure 4.34	Cross sectional optical micrographs of Alloy 3 ( Nb-20Ti-30Cr ) after cyclic oxidation at 800°C for 90h. Brown, layered porous scales were relatively non-protective. A thick case developed underneath the external oxide scale.....	113
Figure 4.35	Cross sectional optical micrographs of Alloy 4 ( Nb-30Ti-15Cr ) after cyclic oxidation at 800°C for 140h. Brown, layered porous scales were relatively non-protective. A thick case developed underneath the external oxide scale.....	113
Figure 4.36	Cross sectional optical micrographs of Alloy 5 ( Nb-20Ti-15Cr ) after cyclic oxidation at 800°C for 140h. Brown, layered porous scales were relatively non-protective. A thick case developed underneath the external oxide scale.....	114
Figure 4.37	Cross sectional optical micrographs of Alloy 6 ( Nb-30Ti-30Cr ) after cyclic oxidation at 800°C for 140h. Brown, layered porous scales were relatively non-protective. A thick case developed underneath the external oxide scale. The high Cr resulted in massive spallation.....	114
Figure 4.38	Cross sectional optical micrographs of Alloy 7 (Nb-29Ti-15Cr-1.5C) after cyclic oxidation at 800°C for 140h. Brown, layered porous scales were relatively non-protective. A thick case developed underneath the external oxide scale.....	115

Figure 4.39	Cross sectional optical micrographs of Alloy 8 (Nb-29Ti-15Cr-3C) after cyclic oxidation at 800°C for 140h. Brown, layered porous scales were relatively non-protective. A thick case developed underneath the external oxide scale.....	115
Figure 4.40	Cross sectional optical micrographs of Alloy 9 (Nb-28Ti-15Cr-3Si) after cyclic oxidation at 800°C for 140h. The alloy had good oxidation resistance with a large volume fraction of a second phase.....	116
Figure 4.41	Cross sectional optical micrographs of Alloy 10 (Nb-28Ti-15Cr-5Si) after cyclic oxidation at 800°C for 140h. The alloy had good oxidation resistance with a large volume fraction of a second phase.....	116
Figure 4.42	Cross sectional optical micrographs of Alloy 11 (Nb-40Ti-10Al) after cyclic oxidation at 800°C for 140h. The alloy had good oxidation resistance but segregation affected oxidation kinetics.....	117
Figure 4.43	Cross sectional optical micrographs of Alloy 12 (Nb-40Ti-15Al) after cyclic oxidation at 800°C for 140h. The alloy had good oxidation resistance but segregation resulted in a hole being oxidized through the pin.....	117
Figure 4.44	Cross sectional optical micrographs of Alloy 13 (Nb-35Ti-20Al) after cyclic oxidation at 800°C for 140h. The alloy had good oxidation resistance but segregation affected oxidation kinetics.....	118
Figure 4.45	Cross sectional optical micrographs of Alloy 14 (Nb-39Ti-20Al) after cyclic oxidation at 800°C for 140h. The alloy had good oxidation resistance and segregation was not as apparent as in Alloys 11-13.....	118
Figure 4.46	Cross sectional optical micrographs of Alloy 17 (Nb-20Ta-15Cr) after cyclic oxidation at 800°C for 140h. The lack of Ti in the alloy harms oxidation resistance and resulted in massive spallation.....	119
Figure 4.47	Cross sectional optical micrographs of Alloy 19 (Nb-30Ti-15Cr-15Al-3Si) after cyclic oxidation at 800°C for 140h. Visually the pin looked good for the first 100h and then turned brown and spalled.....	119

Figure 4.48	Cross sectional optical micrographs of Alloy 20 (Nb-30Ti-15W-15Al-3Si) after cyclic oxidation at 800°C for 140h. The pin had a heterogeneous surface with some areas displaying a thin oxide and others a thick oxide. The pin broke during the test which affected kinetic measurements.....	120
Figure 5.1	Backscattered electron images of the as-extruded microstructure of scaled up Alloy 1.....	147
Figure 5.2	EDS spectra taken from the a) light and b) dark bands seen in Figure 5.1.....	148
Figure 5.3	Backscattered electron images of Alloy 1 following heat treatment at a) 1100°C / 1h, b) 1100°C / 4h, c) 1150°C / 1h, and d) 1150°C / 4h.....	149
Figure 5.4	Optical micrographs of Alloy 1 following heat treatment at a) 1100°C / 1h, b) 1100°C / 4h, c) 1150°C / 1h, and d) 1150°C / 4h.....	150
Figure 5.5	Optical micrograph of Alloy 1 taken from the room temperature tensile specimen indicating that the desired structure was achieved.....	151
Figure 5.6	Fracture surface from the room temperature tensile test taken at a) low magnification and b) high magnification showing intergranular failure with a small amount of dimple failure.....	151
Figure 5.7	Micrographs taken from the 370°C tensile test specimen showing a) secondary electron image of dimples present on the fracture surface and b) microstructure of the material below the fracture surface.....	152
Figure 5.8	Micrographs taken from the 870°C tensile test specimen showing three magnifications of the fracture surface showing the presence of surface cracks a), cleavage initiation and intergranular fracture b), and beachmarkings c) and d) the microstructure of the specimen below the fracture surface.....	153
Figure 5.9	Micrographs taken from the tensile specimen which was tested in inert environment at 870°C showing a) ductile fracture surface, b) lack of surface cracking and large amount of reduction of area, and c) microstructure below the fracture surface exhibiting the grain boundary failures.....	154

<b>Figure 5.10</b>	<b>Micrographs taken from tensile specimens which had undergone thermal exposure prior to the test, a) exposed then tested at room temperature, b) exposed then tested at 870°C, and c) microstructure of the specimen below the fracture surface showing the presence of an aligned precipitate.....</b>	<b>155</b>
<b>Figure 5.11</b>	<b>Micrographs taken from the notch tensile specimens tested at a) room temperature, b) 870°C, and c) high magnification of the 870°C test showing the beachmarkings and cleavage fracture.....</b>	<b>156</b>
<b>Figure 5.12</b>	<b>Low magnification secondary electron images of specimens which were creep tested at a) 870°C / 275MPa, and b) 870°C / 205 MPa.....</b>	<b>157</b>
<b>Figure 5.13</b>	<b>Micrographs taken from the fracture surface of specimens which were creep tested at a) 870°C / 275MPa, and b) 870°C / 205 MPa.....</b>	<b>157</b>
<b>Figure 5.14</b>	<b>Secondary electron images of the fracture surface of specimens which were creep tested at a) 870°C / 275MPa, and b) 870°C / 205 MPa.....</b>	<b>158</b>
<b>Figure 5.15</b>	<b>Optical micrographs of the microstructure below the fracture surface of specimens which were creep tested at a) 870°C / 275MPa, and b) 870°C / 205 MPa.....</b>	<b>158</b>
<b>Figure 5.16</b>	<b>Secondary electron images of the fracture surface from LCF specimens showing cleavage fracture at initiation and intergranular final fracture, a) strained to 1.2% strain and b) strained to 1.0% strain.....</b>	<b>159</b>
<b>Figure 5.17</b>	<b>Optical micrographs of the structure present in the ingot of Alloy 2 during the forging attempts. The structure consists of a grain boundary phase, a precipitate within the grains and porosity.....</b>	<b>160</b>
<b>Figure 5.18</b>	<b>Optical micrographs of a) crack near the bottom of the ingot showing the cracking mechanism to be linking of the porosity, and b) crack near the top of the ingot showing the crack progressing along the grain boundaries.....</b>	<b>161</b>
<b>Figure 5.19</b>	<b>Picture of the as-received billet of Alloy 3.....</b>	<b>161</b>

Figure 5.20	Optical micrographs of specimens from Alloy 11 which had been heat treated at a) 800°C / 4h, b) 800°C / 4h plus 500°C / 24h, c) 800°C / 4h plus 600°C / 24h, and d) 800°C / 4h plus 700°C / 24h.....	162
Figure 5.21	Optical micrographs of specimens from Alloy 12 which had been heat treated at a) 900°C / 4h, and b) 950°C / 4h.....	163
Figure 5.22	Optical micrographs of specimens from Alloy 12 which had been heat treated at a) 1000°C / 24h, b) 1000°C / 4h plus 500°C / 24h, c) 1000°C / 4h plus 600°C / 24h, and d) 1000°C / 4h plus 700°C / 24h.....	164
Figure 5.23	Optical micrograph of the as-forged structure present in the billet of Alloy 3.....	165
Figure 5.24	Optical micrograph of material from Alloy 3 which had been heat treated at 950°C/1h.....	165
Figure 5.25	Optical micrograph of material which had been aged at 650°C / 20h following either an a) 950°C / 1h or b) 1100°C / 4h solution treatment showing the presence of both recrystallized and unrecrystallized regions in the microstructure.....	166
Figure 5.26	Optical micrographs of material which had been aged for either a) 700°C / 20h or b) 750°C / 20h following a solution treatment of 950°C / 1h.....	166
Figure 5.27	Optical micrographs of material which had been aged at 800°C / 20h following a solution treatment of 950°C / 1h.....	167
Figure 5.28	Optical micrographs of material which had been forged and then aged at a) 650°C / 20h, b) 700°C / 20h, c) 750°C / 20h, and d) 800°C / 20h.....	168
Figure 5.29	Optical micrograph of material which had been solution treated at 1100°C / 8 h followed by an age treatment of a) 750°C / 50h, and b) 750°C / 100h.....	169
Figure 5.30	Secondary electron images taken at a) low and b) high magnification of room temperature tensile specimen.....	169

Figure 5.31	Comparison of the dimple size in a) room temperature and b) 260°C tensile tests.....	170
Figure 5.32	Low magnification secondary electron images of a) specimen surface and b) fracture surface from a specimen which was tensile tested at 650°C.....	170
Figure 5.33	Optical micrographs taken at two magnifications showing a) necking to a point and oxidation, and b) grain structure in the specimen following the test.....	171
Figure 5.34	Secondary electron micrographs of a tensile specimen which was tested in inert environment at 650°C showing a) reduction of area and lack of surface cracks, and b) dimples present on the fracture surface following inert test for comparison with c) dimples on the fracture surface for a specimen which was tested in air.....	172
Figure 5.35	Comparison of backscattered electron images of material which had been tensile tested a) as-heat treated and b) following a thermal exposure at 650°C / 100h.....	173
Figure 5.36	Secondary electron micrograph showing the dimple size in a specimen which had been tensile tested following thermal exposure at 650°C / 100h.....	173
Figure 5.37	Secondary electron micrographs taken at three magnifications from a specimen which had been creep tested to failure in 3.1h at 540°C / 560MPa.....	174
Figure 5.38	Optical micrographs of specimens following creep for 100 hr at a) 650°C and b) 760°C.....	175
Figure 5.39	Secondary electron images of specimens which were tensile tested following creep for 100 hr at 650°C a) specimen surface, and b) fracture surface and for 100 hr at 760°C c) specimen surface, and d) fracture surface.....	176
Figure 5.40	Backscattered electron images of the microstructure of specimens which were creep tested for 100h at a) 650°C and b) 760°C.....	177

Figure 5.41	Secondary electron images of the fracture surface from LCF specimens showing a) dimples and b) striations.....	177
Figure 5.42	Secondary electron image taken from the fracture surface of an HCF specimen.....	178
Figure 5.43	Optical micrographs of the microstructure below the fracture surface for a specimen from heat treatment 2 in Alloy 3 which was tensile tested at room temperature a) low, and b) high magnification.....	178
Figure 5.44	Micrographs taken of a specimen from heat treatment 2 in Alloy 3, a) optical micrograph showing the presence of grain boundary failures away from the fracture surface, and b) secondary electron images of the surface of the tensile specimen.....	179
Figure 5.45	Optical micrograph of the microstructure of the specimen which was tested at 980°C.....	179
Figure 5.46	Optical micrographs of specimens for heat treatment 2 following creep for 100 h at a) 650°C and b) 760°C.....	180
Figure 5.47	Secondary electron images of the fracture surface of specimens which were tensile tested at room temperature following a creep exposure at a) 650°C / 100h, and b) 760°C / 114h.....	181
Figure 5.48	Secondary electron image of the fracture surface of a specimen which was tensile tested at room temperature following creep exposure at 650°C / 100h indicating the presence of tear ridges associated with the microstructural laths.....	181
Figure 5.49	Weight change/area versus hot time data for various alloy systems during a 760°C cyclic oxidation test in air. The thermal cycle was 1h at temperature followed by a forced air cool down to room temperature for 10 minutes.....	182
Figure 5.50	Weight change/area versus hot time data for various alloy systems during a 760°C cyclic oxidation test in air. The expanded y-axis shows the gap between Nb-Ti alloys and other alternative systems. The gap can be closed with further alloy development or the use of an environmental coating.....	182



<b>Figure 5.51</b>	<b>Low magnification surface micrograph of René 41 after 61hr of cyclic oxidation at 760°C in air. The surface shows no spalling and a continuous chromia scale.....</b>	<b>183</b>
<b>Figure 5.52</b>	<b>Low magnification surface micrograph of Ti-48Al-2Cr-2Nb (top) and Ti-24.5Al-12.5Nb-1.5Mo after 61h of cyclic oxidation at 760°C in air. The 48-2-2 gamma alloy shows a thick oxide with little spallation, while the 12.5-1.5 alpha-2 alloy shows patchy spallation.....</b>	<b>183</b>
<b>Figure 5.53</b>	<b>Low magnification surface micrograph of a) Beta 21S, b) Ti-20Al-23Nb and c) Ti-22Al-27Nb after 61h of cyclic oxidation at 760°C in air. These alloys all showed signs of spallation. The beta 21S had a heterogeneous oxide scale, while the Ti-Nb alloys had a more homogeneous white scale.....</b>	<b>184</b>
<b>Figure 5.54</b>	<b>Low magnification surface micrograph of a) Alloy 1 (Nb-32Ti-10Cr-6Al) and b) Alloy 2 (Nb-28Ti-15Cr-1.5Si ) after 61h of cyclic oxidation at 760°C in air. These alloys showed spallation and a dark orange brown scale.....</b>	<b>185</b>
<b>Figure 5.55</b>	<b>Low magnification surface micrograph of a) Alloy 3 ( Nb-41Ti-12.5Al-1.5Mo and b) 3899-3 (Nb-37.5Ti-5Hf-5V-5Cr-5Al-0.5Zr-0.3C) after 61h of cyclic oxidation at 760°C in air. Alloy 3 showed white spalling scales, while the 3899-3 was brown grey with less spallation.....</b>	<b>185</b>
<b>Figure 5.56</b>	<b>Low magnification surface micrograph of Cb752 after 21h of cyclic oxidation at 760°C. The 0.9mm thick sheet was totally oxidized into Nb<sub>2</sub>O<sub>5</sub>.....</b>	<b>186</b>
<b>Figure 5.57</b>	<b>Hardness profiles of the various alloy systems after 760°C cyclic oxidation in air. The Nb-Ti alloys show a distinct case.....</b>	<b>186</b>
<b>Figure 5.58</b>	<b>Optical cross sectional micrographs of etched Rene'41 after 760°C cyclic oxidation and hardness testing. A denuded layer that is softer than the base alloy is observed under the Cr-rich scale.....</b>	<b>187</b>
<b>Figure 5.59</b>	<b>Optical cross sectional micrographs of etched Ti-48Al-2Cr-2Nb after 760°C cyclic oxidation and hardness testing. No hardening was observed near the surface after test although a sublayer was not tested.....</b>	<b>187</b>

Figure 5.60	Optical cross sectional micrographs of etched Ti-24.5Al-12.5Nb-1.5Mo after 760°C cyclic oxidation and hardness testing. A dark etching layer was noted near the surface but hardness readings were not much different than the base alloy.....	188
Figure 5.61	Optical cross sectional micrographs of etched Beta 21S after 760°C cyclic oxidation and hardness testing. A visible scale is noted as well as extensive grain boundary precipitates. A white imaging alpha case may be developed under the external scale.....	188
Figure 5.62	Optical cross sectional micrographs of etched Ti-20Al-23Nb after 760°C cyclic oxidation and hardness testing. A thick external scale and a dark etching hard layer are evident.....	189
Figure 5.63	Optical cross sectional micrographs of etched Ti-22Al-27Nb after 760°C cyclic oxidation and hardness testing. Little external scale was observed due to spallation or mounting procedures.....	189
Figure 5.64	Optical cross sectional micrographs of etched 3899-3 after 760°C cyclic oxidation and hardness testing. A thick external scale and interstitial layer are observed.....	190
Figure 5.65	Optical cross sectional micrographs of etched Nb-32Ti-10Cr-6Al after 760°C cyclic oxidation and hardness testing. A thick external scale and interstitial layer are observed.....	190
Figure 5.66	Optical cross sectional micrographs of etched Nb-28.5Ti-15Cr-1.5Si after 760°C cyclic oxidation and hardness testing. A thick external scale and interstitial layer are observed.....	191
Figure 5.67	Optical cross sectional micrographs of etched Nb-41Ti-12.5Al-1.5Mo after 760°C cyclic oxidation and hardness testing. A thick external scale and interstitial layer are observed.....	191

## List Of Tables

Table 2.1	Summary Of Nominal Alloy Compositions (At.%) Studied.....	5
Table 2.2	Summary Of Bend Test Results; All Heat Treatments Were For 1 Hour. As-MS Is As-Melt Spun.....	6
Table 3.1	Compositions (In At.%) Of Alloys For Atomization Studies.....	22
Table 4.1	Screening Alloy Forging Conditions.....	76
Table 4.2	Screening Heat Treatment Conditions .....	77
Table 4.3	Final Heat Treatment Conditions.....	78
Table 4.4a	Results Of Creep Testing.....	79
Table 4.4b	Results Of Tensile Testing at 20°C.....	80
Table 4.4c	Results Of Tensile Testing at 870°C.....	81
Table 4.4d	Results Of Tensile Testing at 1095°C.....	82
Table 4.5	Compositions For Alloys 11 - 14 .....	83
Table 4.6	Summary Of Weight Gains For The Screening Alloys.....	84
Table 5.1	Compositions (Atm.%) Of Alloys Selected For Scale-Up.....	138
Table 5.2	Mechanical Property Results For Alloy 1.....	139-140
Table 5.3	Aging Studies.....	141
Table 5.4	Heat Treatment Matrix For Alloy 3.....	142
Table 5.5	Mechanical Property Results For Alloy 3.....	143-144
Table 5.6	Mechanical Properties For Alternate Heat Treatment Of Alloy 3.....	145
Table 5.7	Knoop Hardness of Interstitial Layer .....	146

## 1.0 Introduction

This Air Force contract was intended to study the possibility of improving the combination of oxidation resistance and mechanical properties for Nb base alloys. The method to be used to achieve this improvement in the alloys was to be rapid solidification. These alloys contained relatively high levels of Al and Cr which have been shown in previous efforts to have a beneficial effect on the oxidation resistance but a detrimental effect on the ductility, making the alloys brittle. The rationale was that by producing a refined dispersion of the brittle second phase through rapid solidification, the ductility would not be seriously degraded and the strength may be increased.

The initial effort concentrated on using melt spinning as the rapid solidification method for binary, ternary, quaternary and complex alloys. Ribbons were produced and given selected heat treatments to determine the effect on the microstructure. The ductility of the ribbons was tested in both the as-melt spun and heat treated conditions. The method used for determining the effect of the rapid solidification and heat treatment on mechanical properties was bend testing of ribbon materials. Based on the results of the rapid solidification studies on ribbons, four alloys were chosen for scaleup. The scaleup rapid solidification method was to produce powder through atomization. The equipment for making powder had been under development at the University of Illinois concurrent with the melt spinning studies. However, sufficient quantities and quality of powder could not be obtained for the high melting point alloys to be studied. Therefore, the decision was made to pursue ingot approaches to producing the alloys.

The decision to pursue the ingot approach was made based on the difficulty of producing powder and on promising results which had been obtained on Nb-Ti alloys at GE-CRD. The Nb-Ti base alloys had been shown to have improved oxidation resistance over conventional Nb alloys, although, with a reduction in the high temperature creep strength. However, because the actual needs of the expected application were for a lower temperature, this loss in temperature capability was not considered a significant problem. The first part of the ingot approach was to choose 20 alloys for screening. These alloys were chosen based on past work on alloy additions which improve the oxidation resistance of Nb alloys. The 20 alloys were produced as vacuum arc remelted (VAR) pins, forged into pancakes, and given one of three selected heat treatments to determine the effect of heat treatment on microstructure. These alloys were evaluated using tensile and creep testing prior to downselect to three scaleup alloys. The three selected scaleup alloys were produced as VAR ingots and reduced to billet using standard metalworking practices. One of the scaleup alloys cracked during the initial billet reduction step and was therefore removed from the contract. The final two alloys were subjected to an expanded mechanical test matrix which included, strength, toughness, creep, stability, and fatigue testing. This report covers all of the effort performed under this contract, both the rapid solidification and the ingot approaches.

## 2.0 Rapid Solidification Studies

### 2.1 Alloy Selection and Rationale

The alloy designations, and compositions (in atomic %), are shown in Table 2.1. All compositions referred to in this report are given as atomic percent. Rapid solidification of the alloys was carried out by melt spinning. Characterization of the microstructures and assessment of the ductility of these alloys was performed in both the as-melt spun and heat treated conditions. Such examination has been performed on ribbons heat treated at 1000°C in an argon atmosphere and on ribbons heat treated at 850°C in air. In the final series of alloys, W and Mo were added, since these elements were expected to be required for strengthening purposes and also to maintain, or elevate, the melting point. Finally, the role of internal gettering by the addition of Zr, Er and Y was investigated.

### 2.2 Production of Rapidly Solidified Material

The first task in the initial stages of this program was the efficient production of rapidly solidified material in order to enable alloy screening. An essential element necessary to accomplish this task is the arc-melt spinning apparatus (AMS) used to produce rapidly solidified melt-spun ribbons. Processing of Nb-base alloys is generally a difficult task due to their high melting point, reactivity, and contamination problems. Thus, the design and assembly of an AMS device that is capable of producing clean ribbons of high melting point refractory alloys in spite of these difficulties must be considered a major accomplishment.

The AMS device used in this study is shown schematically in Figure 2.1. Much of the device features melt spinning technology suitable for processing a wide variety of materials. The device consists of a melting chamber, spinning chamber, and collection chamber. During operation, molten material is directed onto a rapidly rotating copper disk. Solidification of the melt begins upon contact with the disk, which serves as the quenching substrate. Due to the rotation of the disk, the solidified filament is flung from the wheel as new melt material makes contact with the wheel. In this manner, the process generally produces continuous filaments or ribbons of rapidly solidified material.

The processing of refractory materials such as niobium requires specialized melting equipment. An arc melting apparatus is utilized for melting of these materials in this device and is shown schematically in Figure 2.2. This apparatus consists of a chamber which can be independently pressurized, a non-consumable tungsten electrode, and a copper hearth with a central hole over which a tungsten insert is seated. The chamber walls, electrode, and hearth are water cooled. The tungsten insert has a central hole which serves as the ejection nozzle. One difficulty encountered

involves preventing the nozzle material from melting while simultaneously avoiding solidification of the melt in the ejection nozzle. The insert size, material, and nozzle diameter have been adjusted appropriately to compensate for these competing processes. In view of the high melting point and complete solubility in niobium, tungsten proves to be an ideal insert material.

Prior to processing, the entire device is evacuated to  $\approx 10^{-6}$  torr. During operation, an inert He atmosphere is maintained in the spinning and collection chambers. An exhaust port fitted with a relief valve allows a continuous flow of clean gas to be supplied to the unit. Melting of the alloy is achieved by directing the arc towards the alloy button. At the onset of melting, the melting chamber is independently pressurized with argon, ejecting the molten material through the ejection nozzle onto the rotating copper wheel. The surface velocity of the wheel is maintained at  $\approx 55$  m/s. As the last of the melt is ejected through the nozzle, the arc is extinguished to prevent melting of tungsten. Analysis of ribbons using these techniques has shown no tungsten contamination.

The processing of the final set of alloys in this manner proved to be extremely difficult and time consuming. The main difference between these alloy compositions and those of the previous sets is the addition of tungsten to many of the alloys, one effect of which is to increase the melting temperature of the given alloy. It appears that in each of the tungsten containing alloys, inhomogeneities in the liquid existed which resulted in poor quality ribbons upon casting. The origin of these inhomogeneities is not well understood, but it may be that either sufficient heat cannot be generated (noting that the melting is performed on a water-cooled copper hearth) causing the solid to be only partially melted, or that the liquid charge consists of two immiscible liquids. In any case, the ribbons produced were of a poor quality and rather inhomogeneous. Thus, it is expected that any estimate of strain to failure using bend tests on ribbons will be low because the ribbons will contain many defects. Also, the presence of inhomogeneities will mean that observations made using electron microscopy will tend to be biased toward those areas of the ribbon which are mechanically more stable, that is, those areas that are relatively homogeneous and free of segregation. For these reasons, close correlation between the microstructures and estimates of ductility cannot be made for these particular samples.

### 2.3 Ductility of Rapidly Solidified Material

In light of the objectives of this program, the ductility of as-rapidly solidified material was determined to be the best physical measure of the response of these alloys to RSP. In this regard, the production of rapidly solidified material by melt spinning is particularly advantageous since material is produced in ribbon form on which a simple bend test can give a reliable indication of ductility.

Initially, it was thought that a simple  $180^\circ$  bend test would be a sufficient measure of ductility. In this simple test, the ribbon is bent back upon itself and creased under moderate pressure. If the

ribbon can sustain this bending, the ribbon is considered ductile. A major drawback of this technique is the difficulty in quantifying the ductility to enable comparisons between different alloys. For example, in the case of the as-rapidly solidified binary alloys, the two Nb-Al alloys could be creased while none of the Nb-Fe or Nb-Cr alloys could withstand such bending. However, some ribbons which could not be creased could nonetheless be bent around a fairly sharp radius. Thus, a gauge was devised to allow a comparable measure of ductility.

The strain capability of the ribbon is estimated to correspond to the smallest diameter around which the ribbon can be bent without breaking. The strain that corresponds to a particular radius of bending is then determined.

The results of the ductility measurements are summarized in Table 2.2. Some of the binary alloys could not be tested due to a lack of segments suitable for bending around the test gauge and could not be creased either; these are designated "low" in the table. An estimated strain  $>5\%$  indicates that the ribbon could be creased.

#### 2.4 Specimen Preparation for Microstructure Studies

Transmission electron microscopy (TEM) has been performed on specimens prepared by several techniques. Both electron transparent regions of as-rapidly solidified ribbons and thin foils prepared by electropolishing or ion milling were examined. The former regions are generally associated with the thinnest regions of the foil and consequently are regions which have experienced the highest undercoolings; the latter regions are more representative of the bulk. Electropolishing was performed in a jet polisher using a solution consisting of 10%  $H_2SO_4$  and 90% methanol. Acceptably polished foils could be prepared only within a rather narrow range of polishing conditions. Generally, using a freshly mixed polishing solution yielded the best results. For the Nb-Al and Nb-Cr binary alloys, a temperature of  $-25^\circ$  to  $-30^\circ$  C and a current of  $\approx 85$  mA yielded the best results, although considerable difficulty was encountered with the latter alloys. For the Nb-Fe binary, a somewhat higher current,  $>100$  mA was used. For the ternary alloys, a temperature of  $-30^\circ$  to  $-35^\circ$  C and a current of  $\approx 60$  to 80 mA produced the best foils. As in the case of the binary alloys, the Cr-containing materials proved exceptionally challenging to polish. The difficulty in polishing some of these materials is presumed to be related to a certain extent to the microstructure of these materials as well as the formation of a resistant oxide film. For the cases in which electropolishing was not effective, ion milling was used to prepare thin foil specimens.

Table 2.1: SUMMARY OF NOMINAL ALLOY COMPOSITIONS (AT.%) STUDIED

Alloy Designation	Alloy Composition
<b>Binary Alloys</b>	
B1	Nb-12Al
B2	Nb-15Al
B3	Nb-20Cr
B4	Nb-35Cr
B5	Nb-10Fe
B6	Nb-15Fe
<b>Ternary Alloys</b>	
H1	Nb-10Al-5Cr
H2	Nb-10Al-10Cr
H3	Nb-10Al-20Cr
H4	Nb-15Al-5Cr
H5	Nb-15Al-10Cr
H6	Nb-15Al-20Cr
<b>Quaternary Alloys</b>	
H7	Nb-10Al-10Cr-10Ti
H8	Nb-15Al-20Cr-10Ti
H9	Nb-10Al-10Cr-20Ti
H10	Nb-15Al-20Cr-20Ti
H11	Nb-10Al-10Cr-5V
H12	Nb-10Al-10Cr-5Hf
H13	Nb-10Al-10Cr-5Zr
H14	Nb-10Al-10Cr-5Ta
<b>Complex Alloys</b>	
S1	Nb-10Al-10Cr-10Ti-15W
S2	Nb-15Al-15Cr-10Ti-15W
S3	Nb-13Al-35Cr-2.5Ni
S4	Nb-10Al-10Cr-10Ti-10W-1Zr
S5	Nb-10Al-10Cr-10Ti-10W-1Er
S6	Nb-10Al-10Cr-10Ti-10W-1Y
S7	Nb-15Ti-15W-3Mo-1Zr-1Er
S8	Nb-5Al-5Cr-15Ti-15W-3Mo-1Zr-1Er
S9	Nb-10Al-10Cr-15Ti-10W-3Mo-1Er-1Zr
S10	Nb-10Al-10Cr-15Ti-15W-1Er-1Zr
S11	Nb-10Al-10Cr-15Ti-10W-1Er-1Zr



Table 2.2: SUMMARY OF BEND TEST RESULTS; ALL HEAT TREATMENTS WERE FOR 1 HOUR. AS-MS IS AS-MELT SPUN

Alloy		Estimated Strain (%) or Bend Test Results			
		as-MS	600°C	1000°C	1200°C
<b>Binary Alloys</b>					
B1	Nb-12Al	>5.0		0.2	
B2	Nb-15Al	>5.0		0.6	
B3	Nb-20Cr	low		0.8	
B4	Nb-35Cr	low		0.4	
B5	Nb-10Fe	low		>5.0	
B6	Nb-15Fe	low		1.0	
<b>Ternary Alloys</b>					
H1	Nb-10Al-5Cr	>5.0	1.0		1.0
H2	Nb-10Al-10Cr	1.0	0.8		1.0
H3	Nb-10Al-20Cr	0.8	0.8		1.0
H4	Nb-15Al-5Cr	>5.0	1.0		0.5
H5	Nb-15Al-10Cr	>5.0	1.0		0.5
H6	Nb-15Al-20Cr	1.0	0.4		=0
<b>Quaternary Alloys</b>					
H7	Nb-10Al-10Cr-10Ti	>5.0	1.0		1.0
H8	Nb-15Al-20Cr-10Ti	1.0	0.5		=0
H9	Nb-10Al-10Cr-20Ti	>5.0	1.0		0.4
H10	Nb-15Al-20Cr-20Ti	0.8	0.4		=0
H11	Nb-10Al-10Cr-5V	>5.0	1.0		0.6
H12	Nb-10Al-10Cr-5Hf	1.0	0.6		0.6
H13	Nb-10Al-10Cr-5Zr	0.8	0.6		0.5
H14	Nb-10Al-10Cr-5Ta	5.0	1.0		1.0
<b>Complex Alloys</b>					
S1	Nb-10Al-10Cr-10Ti-15W	0.6			
S2	Nb-15Al-15Cr-10Ti-15W	0.4			
S3	Nb-13Al-35Cr-2.5Ni	0.3	=0		
S4	Nb-10Al-10Cr-10Ti-10W-1Zr	0.8	0.4		
S5	Nb-10Al-10Cr-10Ti-10W-1Er	1.0	0.5		
S6	Nb-10Al-10Cr-10Ti-10W-1Y	0.4	0.3		
S7	Nb-15Ti-15W-3Mo-1Zr-1Er	1.0	0.8		
S8	Nb-5Al-5Cr-15Ti-15W-3Mo-1Zr-1Er	1.0	0.4		
S9	Nb-10Al-10Cr-15Ti-10W-3Mo-1Er-1Zr	0.8	0.6		
S10	Nb-10Al-10Cr-15Ti-15W-1Er-1Zr	0.6			
S11	Nb-10Al-10Cr-15Ti-10W-1Er-1Zr	0.5	0.3		

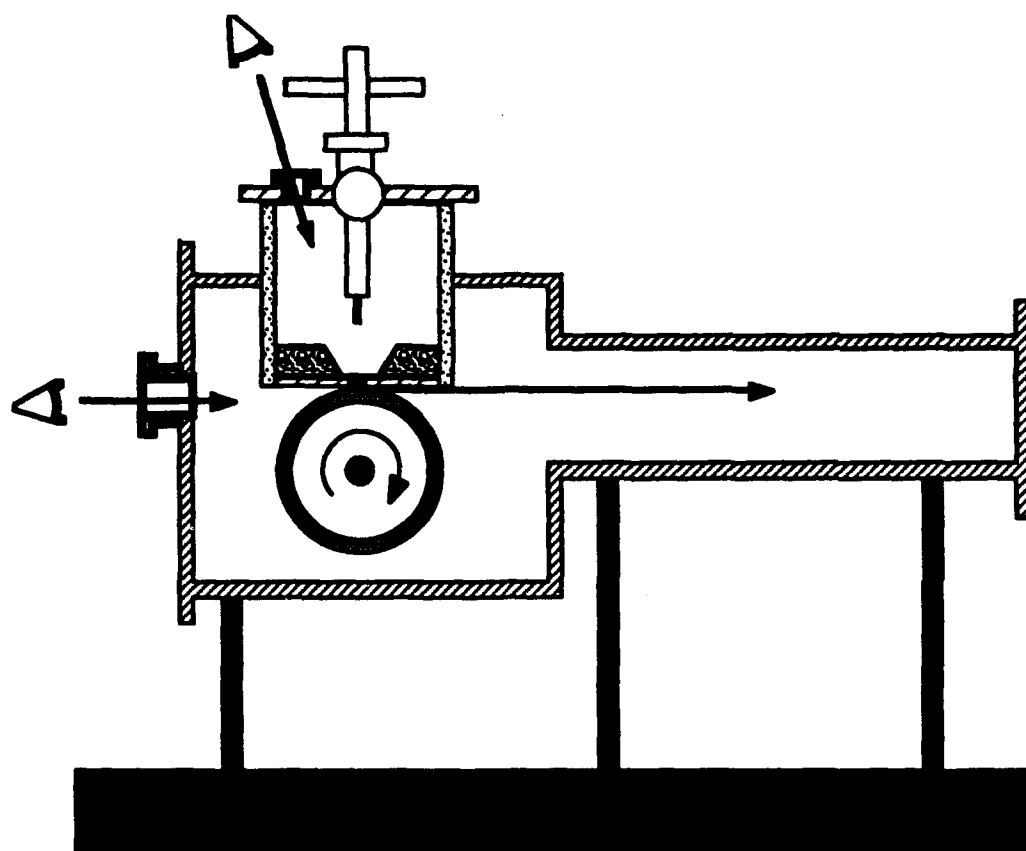


Figure 2.1 Arc-Melt Spinner used for production of Nb Alloy Ribbons.

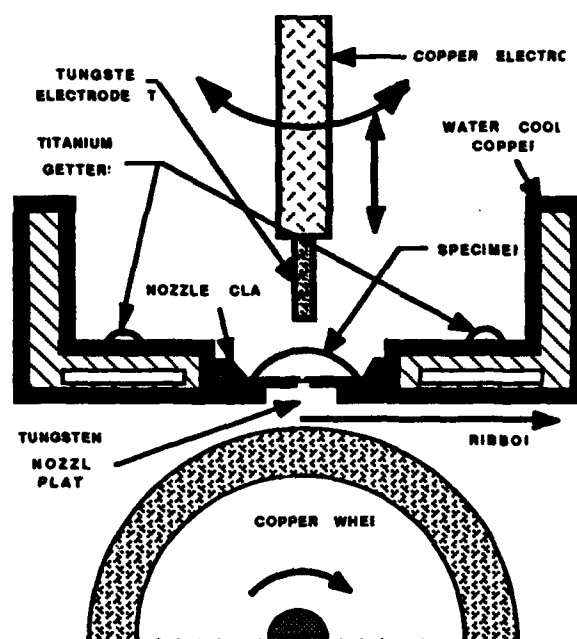


Figure 2.2 Arc Melting Apparatus used in Melt Spinner.

### 3.0 Results of Rapid Solidification on Specific Alloys

#### 3.1 Binary Alloys

##### 3.1.1 Binary Alloys Bend Test Results

The as-rapidly solidified ribbons of Nb-12Al and the Nb-15Al alloys exhibited good ductility in bend tests. None of the ribbons of Nb-Cr or Nb-Fe could be creased. However, qualitative observations revealed that the Nb-Cr ribbons were extremely brittle whereas the Nb-Fe ribbons could withstand some bending and were apparently much more ductile than the Cr-containing alloys.

After heat treatment at 1000°C for 1 hour, some ductility loss was observed in the Al-containing alloys. The loss of ductility results from growth of large grains of Nb<sub>3</sub>Al. Since the gauge could not be used to assess the ductility of the Nb-Cr and Nb-Fe melt spun ribbons, direct comparison with heat treated ductility was not possible. In general, the ductility appeared to remain approximately the same after heat treatment. However, some heat treated ribbons of Nb-10Fe which were fairly thin could be creased whereas the as-melt spun counterpart could not. Although the reason for this is not well understood, it is presumed to be related to coarsening of the continuous intercellular phase observed in the as-melt spun ribbon. This coarsening frequently results in a somewhat discontinuous second phase.

##### 3.1.2 Binary Alloys Microstructure Results

Microstructural characterization and phase identification in the binary alloys was performed for both as-melt spun and heat treated conditions. The results of each alloy system is discussed in turn.

**Nb-Al Alloys:** The microstructures of both as-rapidly solidified Nb-Al alloys (12Al and 15Al) were essentially single phase  $\alpha$ -Nb grains with a few small Al-rich particles. An example of this microstructure in Nb-12Al and Nb-15Al is shown in Figure 3.1. Diffraction data from these particles were consistent with the Nb<sub>3</sub>Al phase. After heat-treatment at 1000°C for 1 hour, the microstructure of these alloys consisted of rather large particles of Nb<sub>3</sub>Al, which presumably account for the lack of ductility. The microstructure of the heat-treated Nb-12Al is shown in Figure 3.2. It was believed that the temperature of heat-treatment (1000°C) may have been high enough to allow only a few crystals of Nb<sub>3</sub>Al to form and grow rapidly, resulting in the rather large particles. Thus, the heat-treatment was repeated at a lower temperature (600°C) to promote the fine scale precipitation of Nb<sub>3</sub>Al. The results are not clearly understood, but TEM observations do reveal small particles in some instances. However, regions which exhibit larger grains of Nb<sub>3</sub>Al have also been observed.

**Nb-Cr Alloys:** The melt-spun ribbons of both Nb-Cr alloys (i.e. 20 and 35%) exhibited little ductility. The predominant microstructure of the binary Nb-Cr alloys consisted of a cellular microstructure based on  $\alpha$ -Nb cells surrounded by an intermetallic phase identified by electron diffraction to be the NbCr<sub>2</sub> phase. An example of this cellular microstructure in Nb-20Cr is shown in Figure 3.3. However, in the thinnest areas of the ribbon, where more solute trapping had occurred, the microstructure consisted of grains with a discontinuous array of NbCr<sub>2</sub> particles. An example of this type of region in Nb-20Cr is shown in Figure 3.4. Heat-treatment resulted in coarsening of the intercellular phase, resulting in an arrangement of particles along the cell boundaries and reducing somewhat the continuous nature of the intercellular region. An example of this type of microstructure is seen in Figure 3.5 of the Nb-20Cr alloy.

**Nb-Fe Alloys:** The Nb-Fe alloy ribbons (10Fe and 15Fe) exhibited limited ductility. The predominant microstructure of the Nb-Fe binary alloys consisted of a cellular microstructure based on  $\alpha$ -Nb cells surrounded by an intermetallic phase, similar to that observed in the Nb-Cr alloys. Examples of this cellular microstructure are shown in Figure 3.6 for the Nb-15Fe alloy. *Diffraction data from the intercellular phase was consistent with the NbFe phase.* As in the case of the Nb-Cr alloys, more complete solute trapping had occurred in the thinnest areas of the ribbon and the microstructure of these regions consisted of  $\alpha$ -Nb grains with an array of NbFe particles, as seen in Figure 3.7. Compositional analysis indicated that  $\approx 8\%$  Fe was present in the Nb solid solution. Heat-treatment (1000°C for 1 hour) resulted in coarsening of the intercellular phase, resulting in an arrangement of coarse particles along the cell boundaries. An example of this type of microstructure is seen in Figure 3.8 of the Nb-15Fe alloy.

## 3.2 Ternary Alloys

### 3.2.1 Ternary Alloys Bend Test Results

The effect of additions of both Al and Cr on the ductility of Nb-base melt-spun ribbons is somewhat different from that observed in the binary alloys containing single additions of those elements. It has been observed that additions of Al improve the ductility of Cr-containing ribbon in the as-melt spun condition. Furthermore, increasing the Al content increases the level of Cr-content above which ductility decreases. A comparison of the microstructure of alloys H3 (10Al-20Cr) and H6 (20Al-20Cr) reveals that the effect of Al is a lower density of second phase particles in the more ductile alloy, namely H6. After heat treatment, however, this beneficial effect is less apparent, and large additions of Al (15%) may in fact result in a decrease in ductility.

As can be seen in the graph of Figure 3.9, which shows the estimated strain versus Cr content for the as-melt spun ribbons, additions of Al promote ductility in ribbons which contain Cr. In

binary alloys which contain Cr, the ductility decreases rapidly with increasing Cr content. In Figure 3.9 it can be observed that this decrease in ductility is shifted to higher Cr levels as the level of Al is increased. The most notable difference corresponds to a level of 10% Cr at which the alloy containing a higher Al content (15%) exhibits improved ductility compared to that of the material with a somewhat reduced Al content (10%). When the concentration of Cr is too high, as in the case of 20% Cr, even large additions of Al are insufficient to preserve good ductility. Figures 3.10 and 3.11 show similar plots for melt-spun ribbon which has been heat treated at 600°C for 1 hour, to stabilize the alloy, Figure 3.10, and for ribbon which has been heat treated at 600°C for 1 hour followed by 1200°C for 1 hour, to test the thermal stability, Figure 3.11. As seen in Figure 3.10, the higher Al content (15%) results in a slight decrease in ductility in the high Cr-content ribbon following heat treatment. A similar trend can be observed in Figure 3.11 in which a detrimental effect of high Al content on ductility is apparent. Thus, in the case of either element, excessive additions resulted in a decrease in ductility. From these results, a composition based on Nb-10Al-10Cr was deemed to benefit most from rapid solidification and the apparent synergistic relationship between Al and Cr in these alloys.

### 3.2.2 Ternary Alloys Microstructure Results

The alloys H1 to H3 were composed of Nb-10% Al, with Cr content varying up to 20%. The microstructures of the ribbons showed a strong correlation with Cr content. Alloy H1 (Nb-10Al-5Cr) was essentially single phase as is evident in Figure 3.12, which shows the as-melt spun microstructure of this alloy. Virtually all of the solute was retained, and the microstructure thus consisted of large grains of BCC  $\alpha$ -Nb. A few small particles were observed within grain interiors. The microstructure of alloy H2 (Nb-10Al-10Cr) was essentially the same as that of alloy H1 and consisted of large grains of  $\alpha$ -Nb, as seen in Figure 3.13. Again, only a few small particles were observed. Diffraction data from these particles were consistent with the hexagonal form of NbCr<sub>2</sub>. The microstructure of alloy H3 (Nb-10Al-20Cr), with 20% Cr, was markedly different from that observed in alloys H1 and H2, containing a high density of second phase particles, Figure 3.14. The particles are presumed to be NbCr<sub>2</sub> and were typically between 100 and 150 nm in diameter.

The alloys H4 to H6 were composed of Nb-15% Al, with Cr content varying up to 20%. Again, the microstructures of these ribbons showed a strong correlation with Cr content, following the same trend as the alloys with 10% Al. Alloy H4 (Nb-15Al-5Cr) possessed a single phase microstructure consisting of large  $\alpha$ -Nb grains, Figure 3.15. As in the microstructure of alloy H1, a few small particles were observed occasionally. Alloy H5 (Nb-15Al-10Cr) also possessed an essentially single phase microstructure consisting of large  $\alpha$ -Nb grains with a few small particles. The microstructure of this material, Figure 3.16, was essentially the same as that of alloy H4. The microstructure of alloy H6 (Nb-15Al-20Cr) was markedly different from that of alloys H4 or H5, containing many second phase particles, Figure 3.17. Diffraction data from

these particles was consistent with the hexagonal form of  $\text{NbCr}_2$ . The heavily faulted appearance of these particles is similar to that observed in  $\text{NbCr}_2$  particles identified in the Cr-containing binary. These particles were approximately in the same size range as those observed in alloy H3; however, the number density of particles appeared to be much lower. While the apparent density of particles observed in TEM samples can be affected by several factors such as foil thickness, this observed difference appeared to be genuine and was reflected in the ductility of the ribbons.

An additional feature which was commonly observed in all of the ternary alloy samples (in fact, in all samples containing both Al and Cr) was the presence of regions which displayed some short range segregation. One example of a region such as this, of alloy H3, is shown in Figure 3.18. In such areas, there are regions which appear "thick" or "thin," thin regions appearing somewhat lighter than thick regions. There is some difference in thickness between such regions, and these differences in thickness are attributed to different polishing rates of these regions as a result of variations in composition. The thick regions, which polish more slowly, are enriched in both Al and Cr compared to thin regions. Using energy dispersive spectroscopy (EDS) on thin foil samples in the TEM, a significant variation was found in the concentration of these elements in thick and thin regions. For example, EDS measurements indicated 5.3% Al and 4.7% Cr in thin regions of matrix in alloy H1, for which the nominal compositions of those elements are 5% each. In thick regions, the measured concentration of those elements was more than double, corresponding to 11.7 and 11.2%, respectively. Similar variations, with concentrations in thick regions being about twice those of thin regions, have been measured in a number of the ternary and quaternary alloys.

**Heat Treated:** The microstructure of alloy H1 in the heat treated condition consisted of large  $\alpha$ -Nb grains with a few small particles, as seen in Figure 3.19. Compositional analysis showed these particles to be rich in Al. In contrast, the microstructure of alloy H2 in the heat treated condition contained a relatively fine dispersion of Cr-rich particles in grain interiors, Figure 3.20. Some particles rich in Al also were observed. In some of the smaller grains, no particles were observed in the grain interiors; instead, somewhat larger particles decorated the grain boundaries. The microstructure of alloy H3, with 20% Cr, contained large particles rich in Cr, Figure 3.21. Occasionally, small Al-rich particles were also observed.

The alloys H4 to H6 contained 15% Al, with Cr content varying up to 20%. The microstructures of these ribbons in the heat treated condition showed a less pronounced correlation with Cr content compared to the alloys with 10% Al. As shown in Figure 3.22, after heat treatment alloy H4 possessed a single phase microstructure consisting of large Nb grains. As in the microstructure of alloy H1, a few small particles were observed occasionally, and these particles were found to be rich in Al. The microstructure of alloy H5, shown in Figure 3.23, also consisted of large Nb grains with a few small particles, similar to that of alloy H4. The microstructure of alloy H6 was somewhat different from that of alloys H4 or H5. The most

frequently observed microstructure of alloy H6 consists of a Nb matrix with second phase particles rich in Cr decorating the grain boundaries, Figure 3.24. Additionally, some smaller Al-rich particles were observed in grain interiors. In some regions, the Cr-rich particles, which normally appeared only along grain boundaries, were also observed to form a network within the grain interiors.

### 3.3 Quaternary Alloys

#### 3.3.1 Quaternary Alloys Bend Test Results

The first set of quaternary alloys, H7-H10, was designed to examine the effect of Ti on two base compositions to which varying amounts of Ti were alloyed. The first base alloy was Nb-10Al-10Cr, which possesses a relatively small amount of second phase and responds favorably to RSP as described above. The second base composition, Nb-15Al-20Cr, was selected as a representative alloy which contains a larger amount of second phase. These base compositions were alloyed with Ti at levels of 10 and 20%. In general, additions of Ti have little or no effect on the ductility in as-melt spun ribbons, but large additions of Ti (20%) result in a slight decrease in ductility in heat treated ribbons.

Figure 3.25 shows a plot of estimated strain in each of the two base alloys as a function of Ti content for as-melt spun ribbons. For the alloys with a small amount of second phase (H7 and H9), increasing the Ti content to 10 or 20% improves ductility somewhat. For the alloys with a larger amount of second phase (H8 and H10), additions of Ti have little influence on ductility. Figure 3.26 shows a similar plot for ribbons heat treated at 600°C for 1 hour, showing little correlation between ductility and Ti content. At all levels of Ti additions, the alloy with a smaller amount of second phase is more ductile than the alloy with a large amount of second phase. Finally, in Figure 3.27, it can be seen that there is a somewhat detrimental effect of a high Ti content (20%) in ribbons which have been heat treated at 600°C for 1 hour followed by 1200°C for 1 hour. In this condition, the alloy with a larger amount of second phase shows nil ductility at all alloying levels, whereas the alloy with a smaller amount of second phase shows moderate ductility with 0 and 10% Ti and a decrease in ductility at 20% Ti.

The relationship between ductility and composition in these alloys appears to be primarily a function of the amount of second phase, as observed in the case of the ternary alloys, and is basically unaffected by additions of Ti which in general remain in solid solution.

The second set of quaternary alloys is based on the composition Nb-10Al-10Cr with additions of V, Hf, Zr, and Ta. These quaternary additions are expected to be beneficial in terms of oxidation resistance or gettering. After heat treatment, ribbons of these quaternary compositions show no significant variation in ductility compared to the base composition. The estimated strain for each

alloy in each condition is plotted in Figure 3.28. Two of the quaternary compositions, one containing V and one containing Ta, displayed ductility superior to that of the other quaternary compositions or to that of the base composition in the as-melt spun condition. After heat treatment at 600°C for 1 hour, the ductility of each of the quaternary alloy ribbons was approximately the same as that of ribbons of the base composition. Additional heat treatment at 1200°C for 1 hour resulted in little change in ductility in these ribbons.

### 3.3.2 Quaternary Alloys Microstructure Results

**Alloys H7-H10 As-Melt Spun:** The microstructure of H7-H10 is very similar to those observed previously in the ternary alloys. In the as-melt spun condition, all of the alloys showed essentially single phase  $\alpha$ -Nb microstructures, with second phase Cr-rich particles observed in some cases. Figure 3.29 shows the microstructure of alloy H7 in the as-melt spun condition. In this material, few second phase particles were observed. In alloy H8, which contains higher concentrations of Al and Cr, Cr-rich particles were observed in grain interiors and to a lesser extent along grain boundaries. As seen in Figure 3.30, such particles were typically observed in bands corresponding to solute segregation. The microstructure of alloy H9 in the as-melt spun condition, Figure 3.31, was similar to that of alloy H7, consisting of large grains of Nb with little evidence of second phase particles. Figure 3.32 shows the microstructure of alloy H10, which consists of large Nb grains with NbCr<sub>2</sub> particles along the grain boundaries. The segregated microstructure mentioned previously was frequently observed in both the as-melt spun and heat treated ribbons.

**Heat Treated:** After heat treatment at 600°C for 1 hour, few microstructural changes were noted in the low intermetallic containing ribbons, whereas the high intermetallic containing ribbons showed more significant changes. For example, the microstructure of alloy H7 remained essentially unchanged except for the presence of a few scattered Cr-rich particles in grain interiors and along grain boundaries, as seen in Figure 3.33. In contrast, the particles which were already present in alloy H8 as-melt spun appeared to have coarsened somewhat as a result of heat treatment, and additional precipitates formed a nearly continuous network along grain boundaries. An example of this microstructure is shown in Figure 3.34. The microstructures of alloys H9 and H10 are similar to those observed in alloys H7 and H8, respectively. For the case of alloy H9, the microstructure was primarily single phase whereas in alloy H10, NbCr<sub>2</sub> particles decorated grain boundaries.

**Alloys H11-H14 As-Melt Spun:** In the as-melt spun condition, alloy H11 (Nb-10Al-10Cr-5V) possessed a microstructure consisting of relatively large grains of  $\alpha$ -Nb with a fairly small number of spherical particles distributed throughout these grains, Figure 3.35. EDS measurements showed these particles to be rich in Al, with a negligible amount of either Cr or V. The microstructure of alloy H12 (Nb-10Al-10Cr-5Hf), Figure 3.36, is generally similar to that



of H11, consisting of large  $\alpha$ -Nb grains with a somewhat higher density of small, spherical particles. In this case, however, EDX measurements showed the particles to be rich in Hf. In some instances, larger particles were observed along grain boundaries in this material. The grain size in alloy H13 (Nb-10Al-10Cr-5Zr) appeared to be somewhat smaller than that in the other alloys, and a larger number of spherical particles was observed in this material, Figure 3.37. In the case of this alloy, EDX measurements showed the particles to be rich in Zr. Figure 3.38 shows the microstructure of alloy H14 (Nb-10Al-10Cr-5Ta) in the as-melt spun condition. This microstructure consisted of large grains of  $\alpha$ -Nb and a very few particles rich in Al. In each of these materials, a somewhat segregated microstructure is apparent, with certain regions within individual grains showing higher concentrations of alloying elements. As mentioned previously, this type of segregation has been observed in all of the alloys containing Al and Cr.

**Heat Treated:** For most of these alloys, subsequent heat treatment at 600°C for 1 hour produced relatively small changes in microstructure. Heat treatment of alloy H11 had little or no effect on the as-melt spun microstructure. The microstructure of alloy H12 in the heat-treated condition is also very similar to that of the as-melt spun material, showing small particles in an  $\alpha$ -Nb matrix. The microstructure of alloy H13 showed the most striking changes as a result of heat treatment. As seen in Figure 3.39, heat treatment resulted in the precipitation of relatively large particles of NbCr<sub>2</sub> along grain boundaries. The spherical Zr-rich particles seemed to be unaffected by the heat treatment. The effect of heat treatment on the microstructure of alloy H14 was minimal, and no additional precipitates were observed.

### 3.4 Complex Alloy Microstructure Results

As stated previously, the ribbons produced from these alloys are rather inhomogeneous, and so studies of their microstructures using transmission electron microscopy may be of limited overall value since observations will tend to be made of those regions which will be stable in the thinned state. Those areas that are generally less segregated and mechanically more sound than the thicker regions. Therefore, the micrographs presented below generally represent microstructures of these types of areas. Where possible, comments will be given concerning the thicker regions of foils.

#### I. Alloy S1

The microstructure of this alloy is presented in Figures 3.40 and 3.41. The microstructure shown in Figure 3.40 is typical of thinned samples of as-melt spun ribbon. A cellular dendritic morphology was observed, with evidence of some segregation. Presentable images could not be obtained in thicker regions, where there was evidence of a large degree of segregation. The nature of the segregation could not be determined. However, this microstructural inhomogeneity is consistent with the limited ductility exhibited by the ribbons. In the heat-treated condition,

similar observations were made from Figure 3.41 with the exception of the precipitation of particles of NbCr<sub>2</sub> within the regions defined by the original cellular dendrites.

## II. Alloy S2

It was not possible to make thin foils of ribbons of this alloy for TEM examination, either in the as-melt spun or heat-treated conditions.

## III. Alloy S3

The microstructures of thinned samples of ribbons of this alloy in the as-melt-spun and also heat-treated conditions are shown in Figures 3.42 and 3.43. Even in the rapidly solidified condition, the microstructure consists of a fairly coarse distribution of two phases, which appear to have formed by a eutectic reaction. The identity of the two phases has not been determined.

## IV. Alloys S4, S5 and S6

These alloys share the same base (10Al-10Cr-10Ti-10W) with additions of 1 atomic % of Zr, Er or Y. The microstructures of thinned ribbons of these alloys in the as-melt spun and heat-treated conditions are shown in Figures 3.44 through 3.48. In general the micrographs display the result of cellular dendritic solidification with some evidence of segregation. These microstructures show no evidence to explain the measurements of ductility, which would be expected to be fairly good based on the microstructures presented in the figures. However, the inhomogeneous nature of the ribbons is more likely responsible for the mechanical response of the ribbons.

## V. Alloys S7, S8 and S9

These three alloys are based on the addition of W and Mo, together with 15 atomic % Ti and 1 atomic % of Zr and Er. The microstructures of thinned ribbons of these alloys in the as-melt spun and heat-treated conditions are shown in Figures 3.49 through 3.54. Again, these alloys exhibit promising microstructures in thin areas, with evidence of a small degree of segregation. Observations of thicker regions show that the segregation is more pronounced, however, presumably due to the presence of W and the problems associated with melting these alloys. Alloys S8 and S9 contain Al and Cr, which do not appear to contribute to a segregation problem.

## VI. Alloys S10 and S11

These last two alloys are similar to alloys S1 and S2, but with increased Ti contents as well as additions of the elements thought to act as internal getters, Zr and Er. The microstructures of thinned ribbons of these alloys in the as-melt spun (alloy S10) and heat-treated (alloy S11) conditions are shown in Figures 3.55 through 3.57, and resemble those shown in Figures 3.40 and 3.41 for the case of alloy S1. There are a few particles present associated with the elements Er and Zr, but the identity of these has not been established. The microstructures of these ribbons appears to be fairly consistent, but again the significant concentration of W has caused the

ribbons to be very inhomogeneous. In the present processing apparatus, a concentration of 15 atomic % W is too high.

It is to be noted that none of these ribbons exhibited large strains to failure, as in the case of melt-spun ribbons of some of the simpler alloys, where strains of >5% have been estimated. In view of the comments made above (concerning the inhomogeneous nature of the ribbon), this is not a surprising result. Encouraging results were obtained for alloys S4 and S5, and S7, S8, and S9, which have some degree of ductility despite the inhomogeneity of the melt spun ribbons. The interesting observation concerning these five alloys is that they contain the elements Zr and/or Er; although the presence of these elements does not guarantee ductility (see disappointing results for alloys S10 and S11), it is tempting to speculate that they offer a beneficial role concerning scavenging of interstitial impurity elements. Alloys S4 and S5 contain 10at.% each of Al, Cr and Ti; in reviewing the results from earlier work in this program, it seems that these concentrations show the greatest promise. The alloy S7 contains Ti, W and Mo, these elements exhibit continuous solid solutions with Nb and are not expected to be affected strongly by rapid solidification. The addition of the elements Zr and Er, which do respond to rapid solidification (note that in the case of Zr, the RS effect is to distribute Zr homogeneously throughout the alloy before heat-treatment) may well act as internal getters and permit this alloy to deform plastically. The alloys S8 and S9 contain varying amounts of Al and Cr together with 15 atomic % Ti, as well as W and Mo, plus Zr and Er. There appears to be a useful combination of all of these elements.

### 3.5 Results of Powder Processing of Alloys

#### 3.5.1 Rationale for Composition of Powder Alloys

It is of interest to compare these results with some of those from previous work. As can be seen for alloys H7, H9, H11, H12, H13 and H14, reasonable ductilities are observed; each of these alloys contains 10 at.% of both Al and Cr. Three of the most promising alloys which show reasonable ductilities, in view of the inhomogeneities referred to above, also contain these elements at approximately these concentrations. It seemed reasonable to conclude then that reasonable ductilities may be realized in P/M bulk samples of alloys which contain the following elements:

- 10Al, 10Cr and 10Ti: for oxidation resistance,
- 1Er and/or 1Zr to act as an internal getter, and
- 10W and/or 3-5Mo to strengthen the material and raise the melting point.

On this basis, but also bearing in mind the difficulties with reducing to powder (using the arc-melt/centrifugal atomizer) alloys whose melting points are much greater than 2000°C, the alloys in Table 3.1 were fabricated.

P5 is most similar to alloys that were shown to be ductile in ribbon form; Er has been added to getter interstitials. P6 is an alloy that was shown to be highly oxidation resistant during the prior era of Nb development. P7 is an Er-containing version of P6. P8 is based on both the previous work of this program and on independent GE work on Nb-Ti-based alloys.

### 3.5.2 Processing of Powder Alloys

A great deal of effort was expended in the development of the atomization devices available to the subcontractor for the production of powders of alloys. Two approaches were at first adopted. The first of these was to make use of an arc-melt/centrifugal atomizer, which incorporates a heated graphite tundish and a graphite atomization disk. The second approach was to develop a clean atomization system in which the melt stream would not come into contact with any ceramic materials. This was to be based on a plasma melting furnace.

In the case of the arc-melt/centrifugal atomizer, it is necessary to raise the tundish temperature above  $\approx 2200^{\circ}\text{C}$  in order to produce powders of the alloys given in Table 3-1. This proved to be a difficult task, and much work was required. Utilizing zirconia based ceramic insulation, but without the use of heat-shields, tundish temperatures in the range of  $1900 - 1950^{\circ}\text{C}$  were reached while drawing full power from the generator. Attempts were made to place a heat shield between the coil and the tundish, but this alone did not result in the desired temperatures being realized. The shield was fabricated from a thin foil of a refractory material. Several different configurations of insulation packages, heat-shields and induction lead design were employed. The centrifugal atomizer required rebuilding following melting of several components associated with the tundish. Using a combination of zirconia cement and flexible graphite felt, the temperature of the tundish was raised to the point where atomization studies were feasible. Studies involving the atomization of alloy P5 commenced. A few minor problems were then encountered with the melting of the alloy. This resulted from the fact that about 300 gms of alloy were to be melted at one time, in order to produce  $\approx 100$  gms of powder. This relatively large amount of alloy required a rather large heat input to cause the alloy to be essentially completely molten while on a water-cooled Cu hearth. The principal problem involved erosion of the arc-melting tip, and subsequent contamination of the melt. However, preliminary powder runs were performed and small batches of powders were produced.

Modifications began on the plasma unit for atomization of relatively large quantities of Nb prealloyed powders under very clean conditions, i.e. the atomization of powders without the liquid metal impinging on a graphite tundish or a ceramic atomization disk. The design involves continuous feed of material into the melt hearth, followed by overflow of the liquid into a water-cooled Cu nozzle which provides a controlled stream of liquid metal suitable for gas atomization. Preliminary experiments were conducted to verify the production of a controlled stream of liquid through the water-cooled Cu nozzle. Regarding the problems associated with melt-overflow from the water-cooled Cu hearth, it appears that two factors were important: First, the surface

tension of the melt appears to influence in a detrimental manner the controlled flow of metal over the lip of the water-cooled hearth. Second, the positions of the plasma torches are also important, especially the lip torch as this tends to drive the liquid metal away from the lip itself, and back towards the melt-pool. This also tends to destabilize the stream of overflowing liquid metal. Various nozzle designs were examined, including an open nozzle; however, our first attempt involving a rather simple, spherically symmetric, geometry appeared to be optimum.

The successful operation of the plasma unit for clean powder production requires that a material feeder be available to permit continuous replenishing of the melt-hearth with molten alloy. For this reason, a feeder was designed and produced, and fitted into the plasma system. The feeder worked successfully in that it was possible to melt a rod of Ti-6Al-4V of diameter 2.5cm in a continuous fashion. However, preliminary experiments involving the continuous replenishment of molten alloy while overflow was occurring were not successful; thus, it appeared that it was not possible to feed liquid material at a sufficiently rapid rate to deliver a continuous stream of molten liquid to the water-cooled nozzle. The cause of this was attributed to the level of power available for these experiments which could not exceed 64kW. It is estimated that  $\approx 100\text{kW}$  is required, a power level that was thought at the outset of these experiments to be available. Because of this lack of power, this processing technique was not pursued further.

Rapidly solidified powders of alloys P5 - P8 were produced using the arc-melt/centrifugal atomizer. About 100gm lots of powder with diameters approximately less than  $350\mu\text{m}$  were collected. The microstructures of these powders in the as-atomized and also heat-treated conditions have been characterized and this is described below.

### 3.5.3 Characterization of Powders

Powders of alloys P5 - P8 were characterized by means of scanning electron microscopy (SEM) and analytical transmission electron microscopy. Preparation of these powders, in both the as-atomized and also heat-treated conditions, for examination in the transmission electron microscope was performed by use of special techniques developed at the University of Illinois. Essentially, a sandwich of the powders in a Ni binder is produced using electroplating. This composite sample is then thinned in the normal way using electrochemical techniques. The main problems encountered involved the preferential thinning of the Ni binder in preference to the Nb alloy powders. This was overcome by a considerable iterative effort, and reasonable foils were eventually obtained.

#### **Alloy P5**

*As-atomized:* In the case of powders of alloy P5, micrographs of the thin foils, presented in Figure 3.58, reveal that the as-atomized microstructure is for the most part single phase, although some second phase, with diameters of approximately  $0.2\text{-}0.3\mu\text{m}$ , are also present. Selected area and micro-diffraction techniques have been used to reveal that, as expected, the matrix phase is

$\alpha$ -Nb. By comparing simulated and experimental diffraction patterns it can be shown that the second phase corresponds to  $\text{Er}_2\text{O}_3$ . It was also noted from the micrographs that the dendritic regions polished in a different manner to the interdendritic regions, and this difference may be attributed to a difference in composition. Thus, using energy dispersive x-ray spectroscopy (EDS), the dendritic region was shown to have a lower concentration of the alloying elements Al, Cr and Ti. Also, there are dislocation networks associated with the interdendritic phase, Figure 3.58. These may be present as a result of solidification, or may in fact be present to account for a difference in lattice parameters between the two regions (dendritic and interdendritic) of  $\alpha$ -Nb.

These results are somewhat similar (with the exception of information concerning Er) to the results obtained for alloy H7 in the melt-spun condition. However, in that study, occasional particles of  $\text{NbCr}_2$  were observed, which have not been observed here in the case of as-atomized powders. This difference is most probably due to the greater degrees of undercooling achievable in powders compared to melt-spinning of Nb alloys.

*Heat-treated for 4 hours at 1200°C* Rapidly solidified powders of alloy P5 were heat-treated for 4 hours at 1200°C. This heat-treatment was designed to assess the thermal stability of these microstructures. Some very interesting observations have been made in these samples, examples of which are presented in Figure 3.59. In addition to the small rare earth oxide particles of  $\text{Er}_2\text{O}_3$ , the dendritic and interdendritic regions have decomposed into a number of (somewhat unexpected) phases. Thus, selected area and micro-diffraction techniques have been used to establish the identity of these phases. It is found that the matrix is  $\alpha$ -Nb. In addition, as indicated in Figure 3.59 there are particles of  $\text{Nb}_3\text{Al}$  and  $\text{TiC}$  present. These determinations are supported by energy dispersive x-ray spectroscopy (EDS), where it has been demonstrated that the  $\alpha$ -Nb matrix contains smaller amounts of Al and Ti than in the case of the as-atomized powders, Figure 3.60. EDS spectra have also been recorded from the  $\text{Nb}_3\text{Al}$ , Figure 3.60b, and  $\text{TiC}$ , Figure 3.60c, particles and these are again consistent with the phase identification. This behavior was not anticipated at the outset of these experiments; the formation of  $\text{Nb}_3\text{Al}$  in preference to  $\text{NbCr}_2$  is of interest, and the presence of  $\text{TiC}$  is caused by contamination of the samples during processing, i.e., by interaction of the molten liquid with the graphite tundish.

### Alloy P6

*As-atomized:* The microstructure of thinned powders was found to be a rather coarse distribution of two phases, one being  $\alpha$ -Nb, the other being  $\text{NbCr}_2$  as shown in Figure 3.61. This identification was effected by means of both selected area and micro-diffraction techniques, and verified by means of computer simulation of the diffraction patterns. Energy dispersive X-ray spectroscopy (EDS) has also been employed to establish the alloy content of both phases; the  $\alpha$ -Nb contains appreciable amounts of Cr Figure 3.62, and the  $\text{NbCr}_2$  particles Figure 3.63 exhibit the expected chemistry. These results may be compared to the observations made of alloy S3,

which in the melt-spun condition was also found to be two phase ( $\alpha$ -Nb and NbCr<sub>2</sub>) and of a similar morphology.

*Heat-treated for 4 hours at 1200°C:* Heat-treatment of these alloy powders produced very little change in morphology or phase distribution. Thus, a coarse distribution of  $\alpha$ -Nb and NbCr<sub>2</sub> has been observed as shown in Figure 3.64. This identification has been confirmed by use of energy dispersive X-ray spectroscopy. The contrast exhibited by the  $\alpha$ -Nb is of interest, showing a tweed-like structure Figure 3.65. This is not unexpected in view of the substantial alloy content of this phase even after heat-treatment.

### **Alloy P7**

*As-atomized:* The microstructure of alloy P7 in the as-atomized condition, consists of two phases, one being  $\alpha$ -Nb and the other NbCr<sub>2</sub>. A typical electron micrograph of this material is shown in Figure 3.66. Using energy dispersive X-ray spectroscopy (EDS), x-ray spectra recorded with the electron probe positioned on the matrix and a second phase particle, are shown in Figure 3.67 (a and b), respectively. This latter X-ray spectrum is consistent with an approximate composition of NbCr<sub>2</sub>, but the height of the Al peak (implying a significant concentration of this element) is surprisingly large. The fact that this material is single phase is consistent with its composition.

*Heat treated for 4 hours at 1200°C:* Rapidly solidified powders of alloy P7 were heat-treated for 4 hours at 1200°C. The result of the heat treatment was to cause precipitation of relatively coarse particles of Er<sub>2</sub>O<sub>3</sub>; these may be seen in the electron micrograph recorded from a thinned, heat treated powder in Figure 3.68.

### **Alloy P8**

*As-atomized:* The microstructure of thinned powders of this material was found to be single phase  $\alpha$ -Nb, shown in Figure 3.69. An interesting feature of this microstructure is that the composition of the matrix was found to vary spatially. EDS spectra recorded from regions of a thinned powder of similar foil thicknesses (to avoid differences in absorption) are shown in Figure 3.70 (a and b), and it can be seen that the alloying content in the  $\alpha$ -Nb varies significantly. This effect is most probably due to inhomogeneities resulting from processing, although this is not easy to understand since the regions from which the spectra were recorded were spatially rather close (within 5-10  $\mu$ m).

*Heat treated for 4 hours at 1200°C:* Heat treatment of these powders was found to result in precipitation of particles of a Ti rich phase. The microstructure typical of thinned powders is shown in Figure 3.71. The nature of the second phase has not been determined unambiguously,

but the diffraction maxima observed from this phase taken together with the EDS spectrum are consistent with a compound based on TiC. The presence of TiC is caused presumably by contamination of the samples during processing, i.e., by interaction of the molten liquid with the graphite tundish.

#### 3.5.4 Consolidated Samples

Small quantities of powders of all four compositions (P5-P8) were produced. The powders were canned and consolidated by HIP'ing. The HIP'd compacts were approximately 1cm in diameter and 7.5cm long. The microstructure of the compacts showed several types of defects, such as porosity, and foreign matter. Because of the poor quality of these specimens and the problems with making large quantities of powder it was decided not to do any testing on the compacts.

As was discussed in the introduction, several problems surfaced with the rapid solidification approach. One of the most difficult problems was the inability to make sufficient quantities of powder to support the test matrix which was planned for the scaleup. Therefore, the decision was made to use an ingot approach.



Table 3.1. Compositions (in at.%) of alloys for atomization studies.

Alloy Designation	Al	Cr	Ti	Ni	Er
P5	10.0	10.0	10.0		1.0
P6	13.0	35.0		2.5	
P7	13.0	35.0		2.5	1.0
P8	12.0	6.0	41.0		

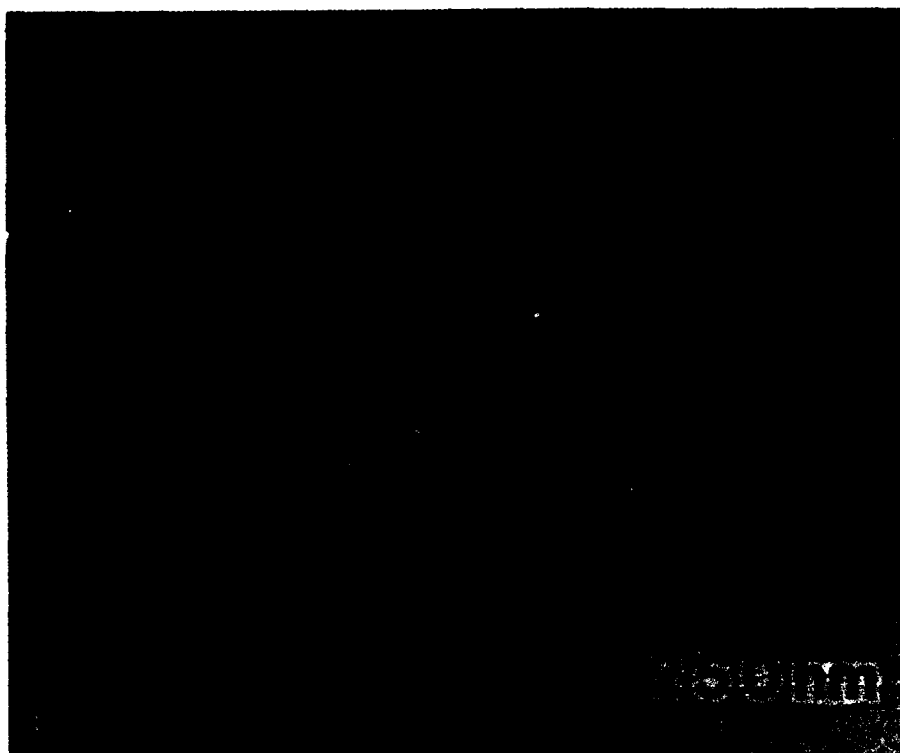
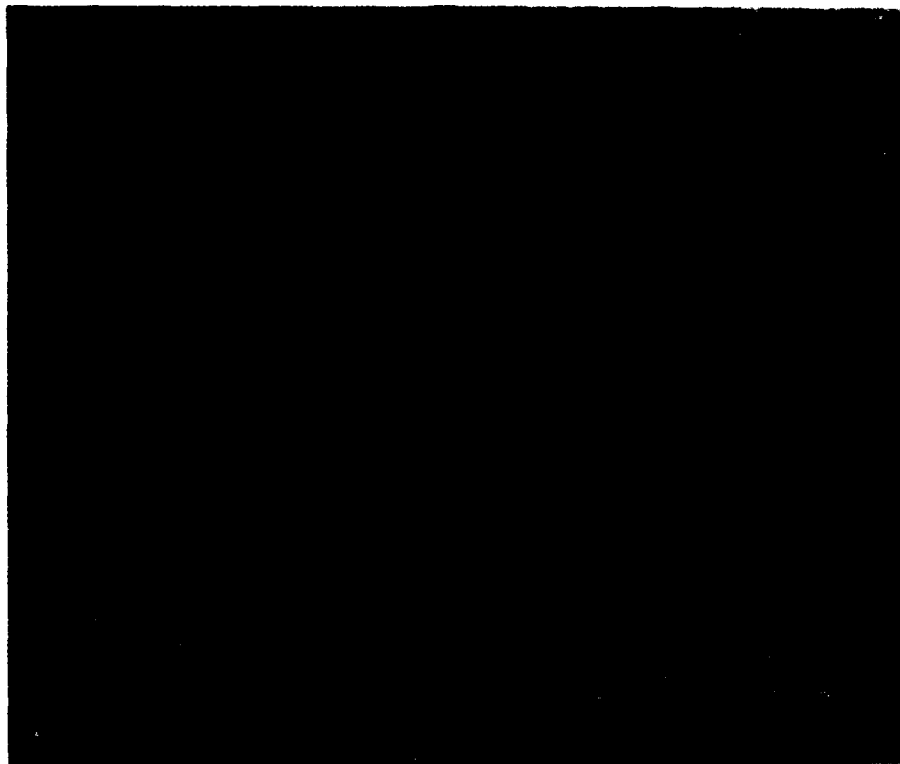


Figure 3.1 a) Bright field TEM micrograph of as-melt spun Nb-12Al, b) bright field TEM micrograph of as-melt spun Nb-15Al.

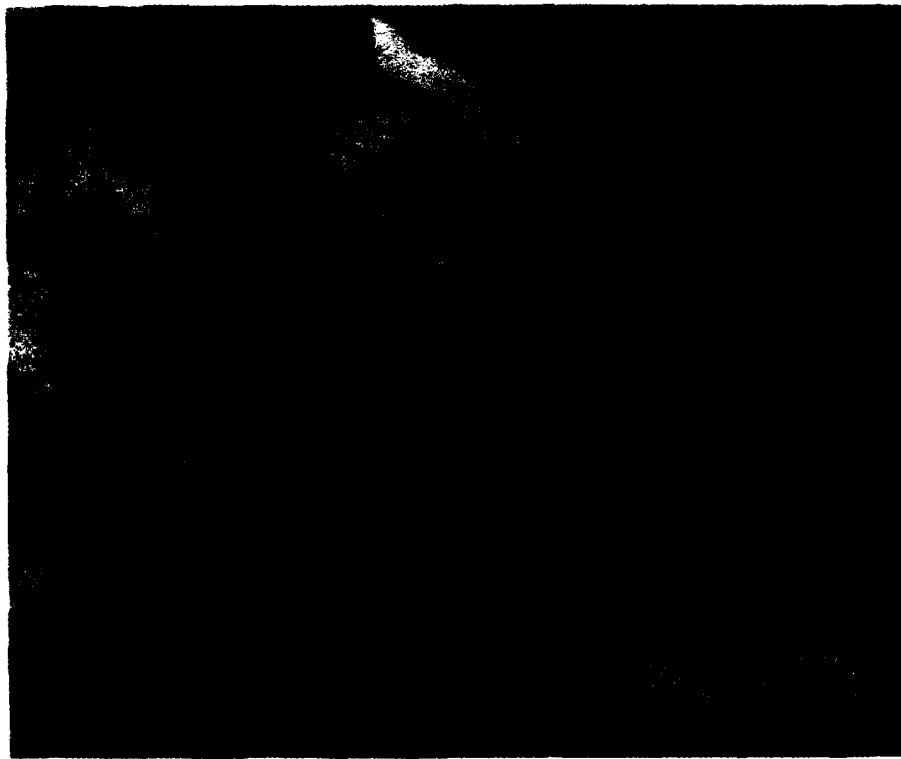


Figure 3.2 Bright field TEM of melt spun and heat treated Nb-12Al. The heat treatment was for 1 hour at 1000°C.

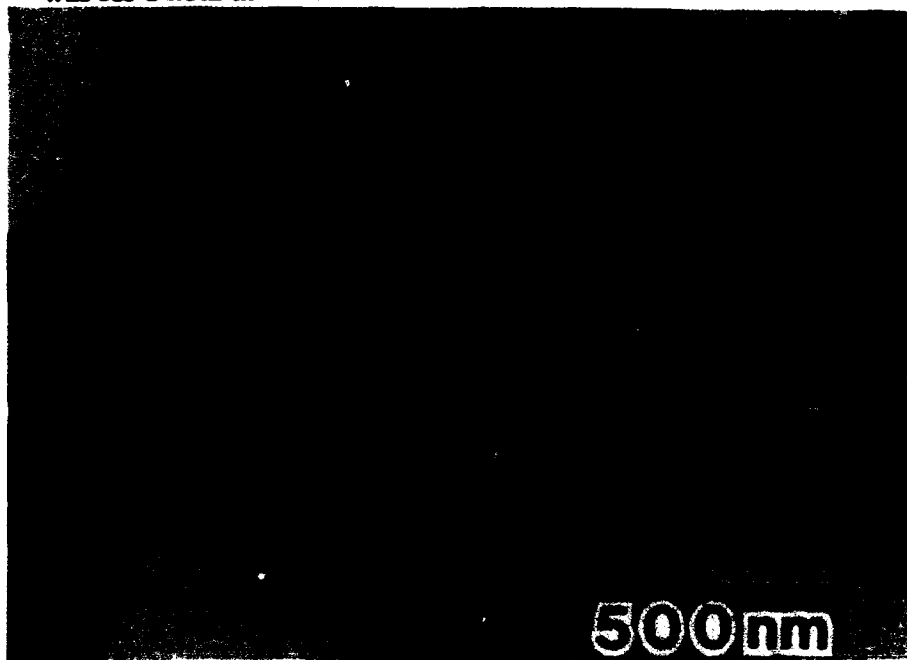


Figure 3.3 Bright field TEM of as-melt spun Nb-20Cr showing the cellular microstructure observed in most of the ribbons.

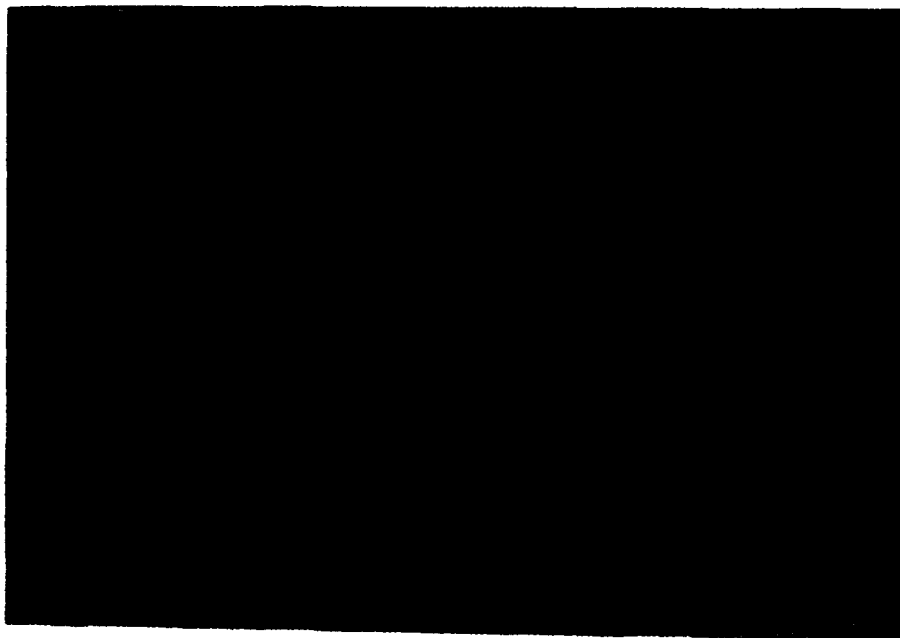


Figure 3.4 Bright field TEM of as-melt spun Nb-20Cr showing a discontinuous array of particles in an  $\alpha$ -Nb matrix in the thinnest areas of the ribbon.

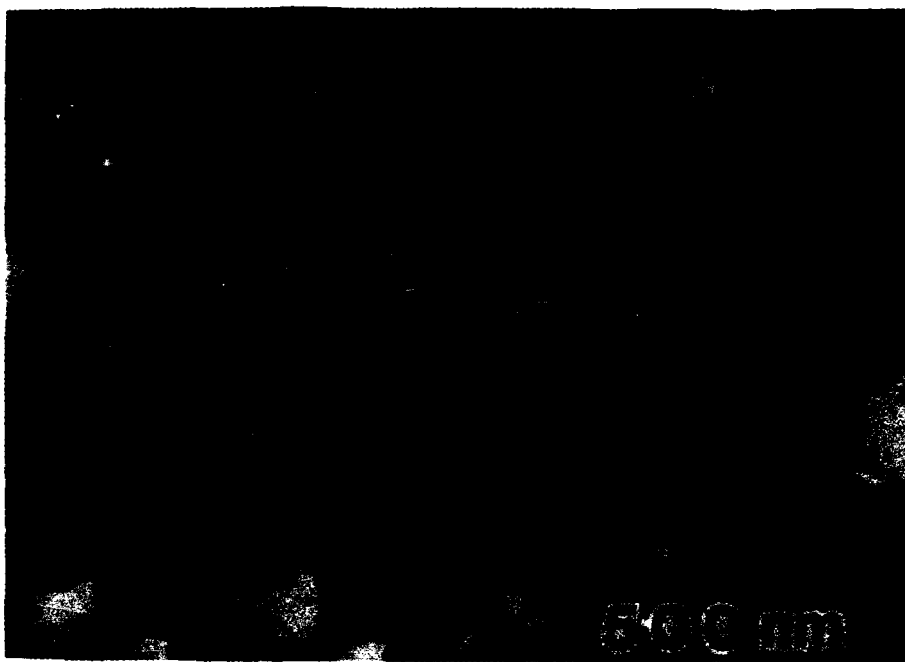


Figure 3.5 Bright field TEM of melt-spun and heat treated Nb-20Cr. The heat treatment was for 1 hour at 1000°C.

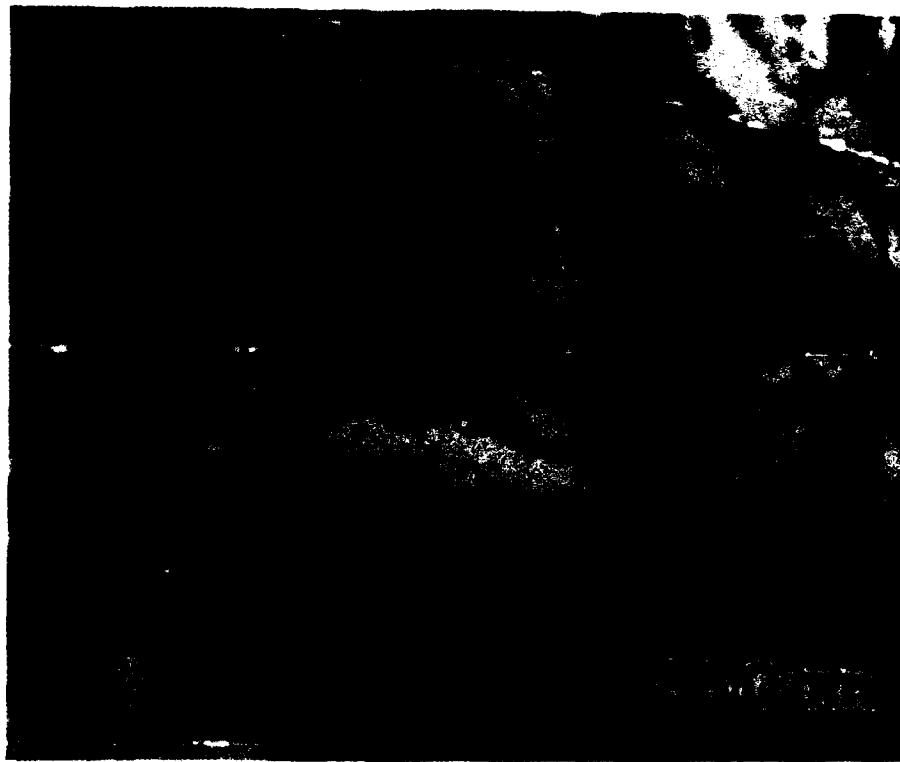


Figure 3.6 Bright field TEM of as-melt spun Nb-15Fe showing a cellular microstructure.

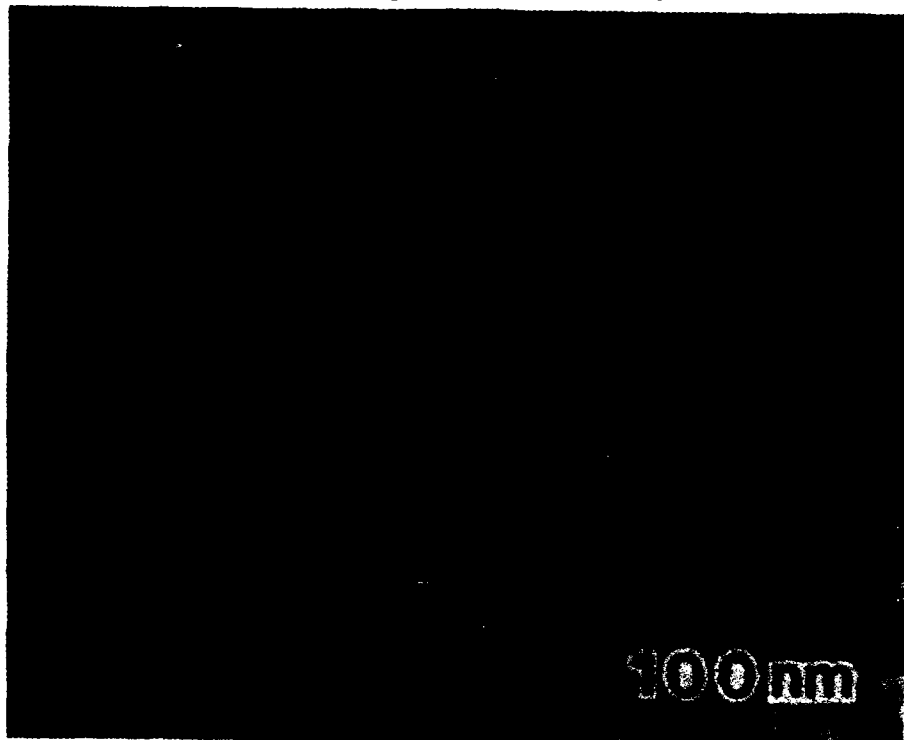


Figure 3.7 Bright field TEM of as-melt spun Nb-15Fe showing a discontinuous array of particles in an  $\alpha$ -Nb matrix in the thinnest areas of the ribbon. Some NbFe phase also decorates the cell boundaries.

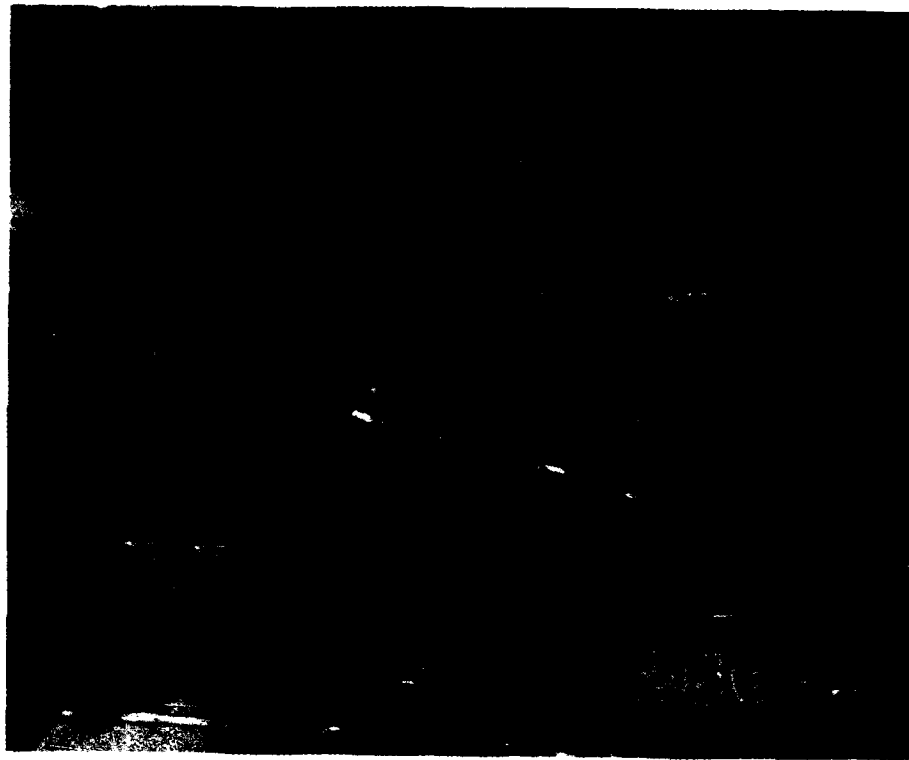


Figure 3.8 Bright field TEM of melt-spun and heat treated Nb-15Fe. The heat treatment was for 1 hour at 1000°C.

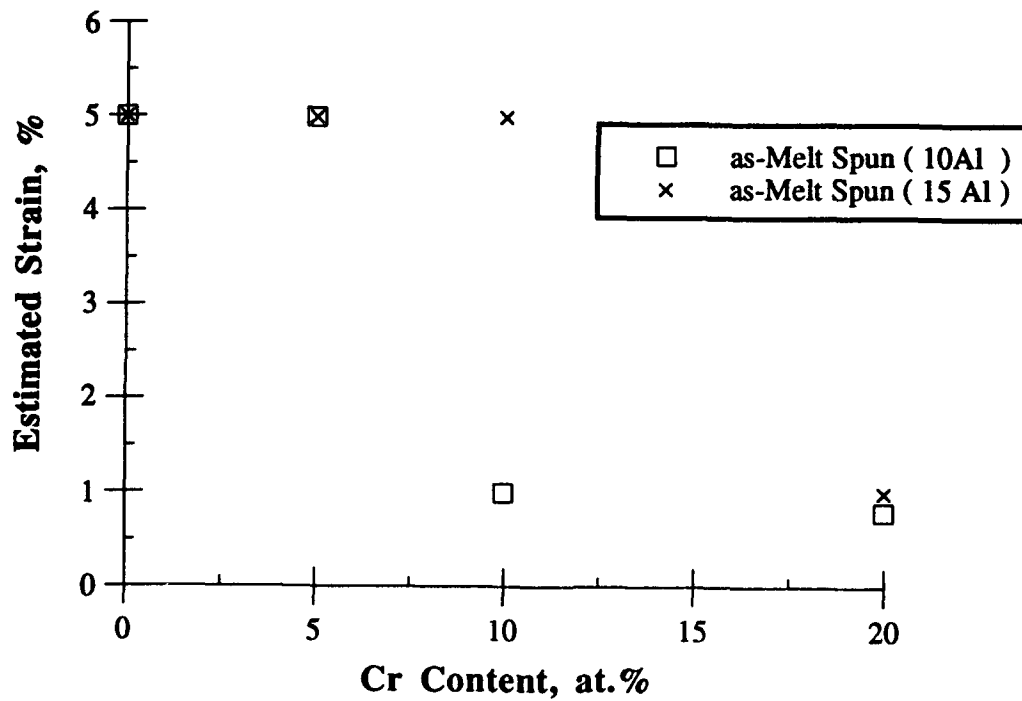


Figure 3.9 Graph of estimated strain versus Cr content for two levels of Al additions for as-melt spun ribbon.

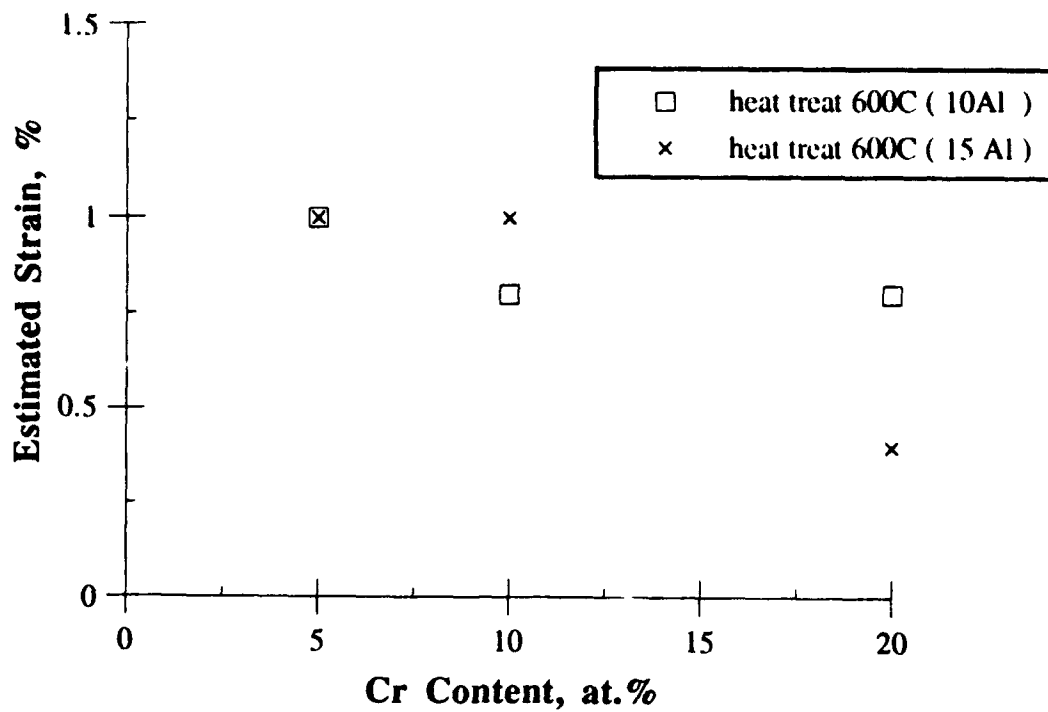


Figure 3.10 Estimated strain versus Cr content for two levels of Al additions for ribbon which has been melt-spun and subsequently heat treated at 600°C for one hour

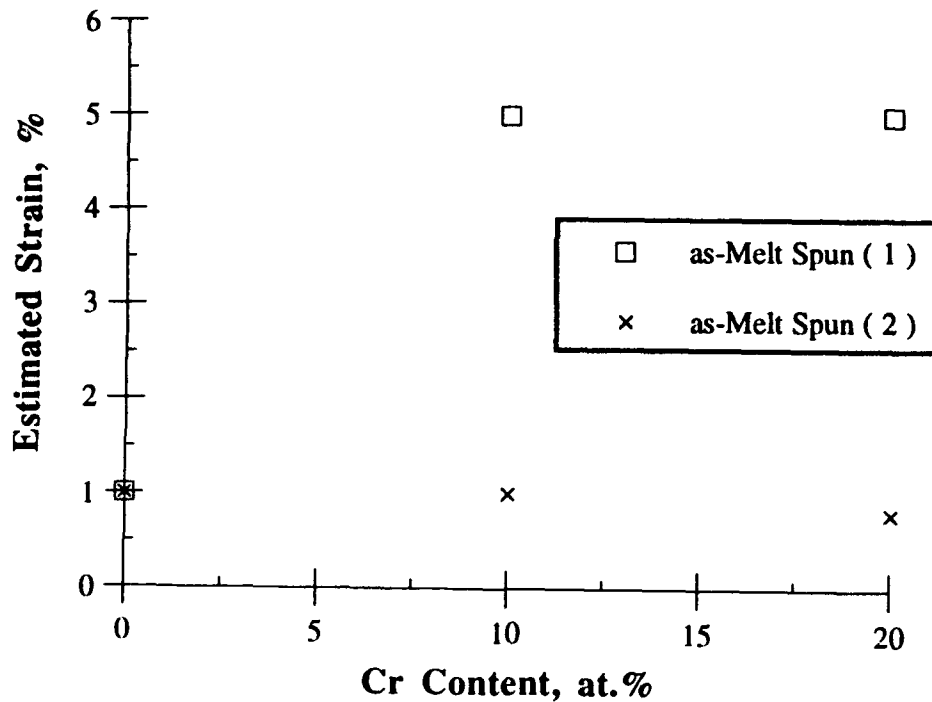


Figure 3.11 Estimated strain versus Cr content for two levels of Al additions for ribbon heat treated at 600°C for 1 hour followed by 1200°C for 1 hour.

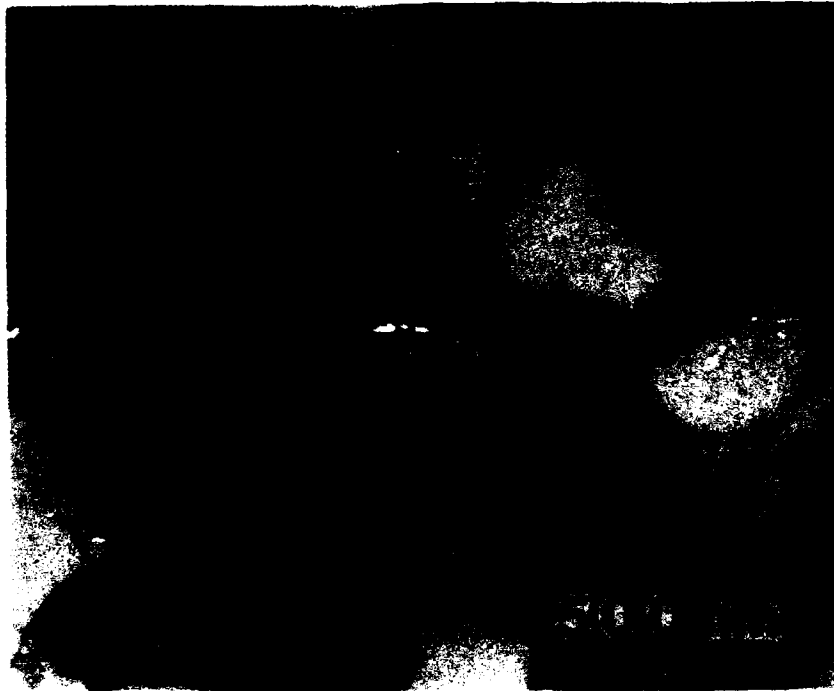


Figure 3.12 Bright field TEM micrograph of as-melt spun Nb-10Al-5Cr (alloy H1).



Figure 3.13 Bright field TEM micrograph of as-melt spun Nb-10Al-10Cr (alloy H2).





Figure 3.14 Bright field TEM micrograph of as-melt spun Nb-10Al-20Cr (alloy H3).



Figure 3.15 Bright field TEM micrograph of as-melt spun Nb-15Al-5Cr (alloy H4).



Figure 3.16 Bright field TEM micrograph of as-melt spun Nb-15Al-10Cr (alloy H5).

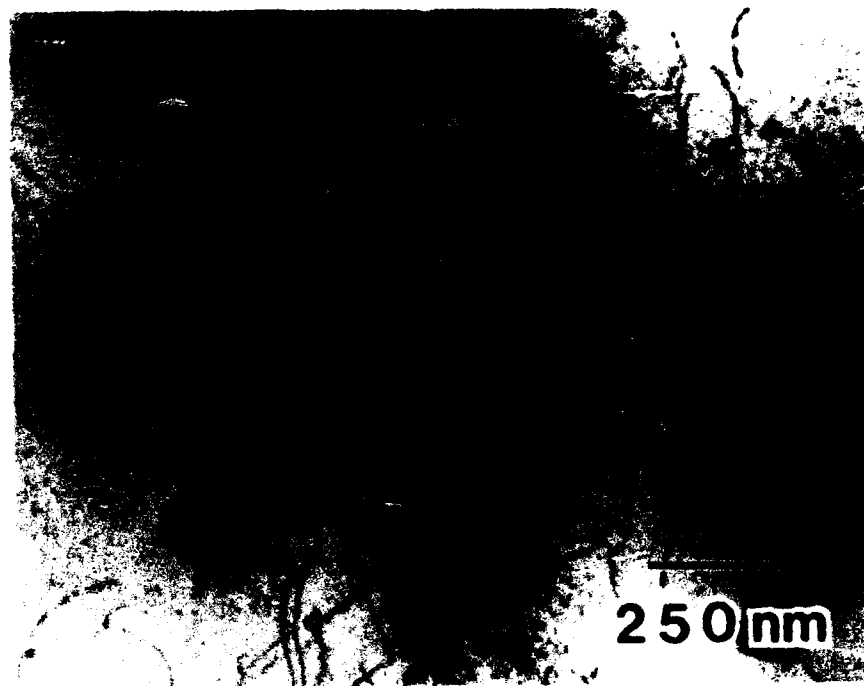


Figure 3.17 Bright field TEM micrograph of as-melt spun Nb-15Al-20Cr (alloy H6).

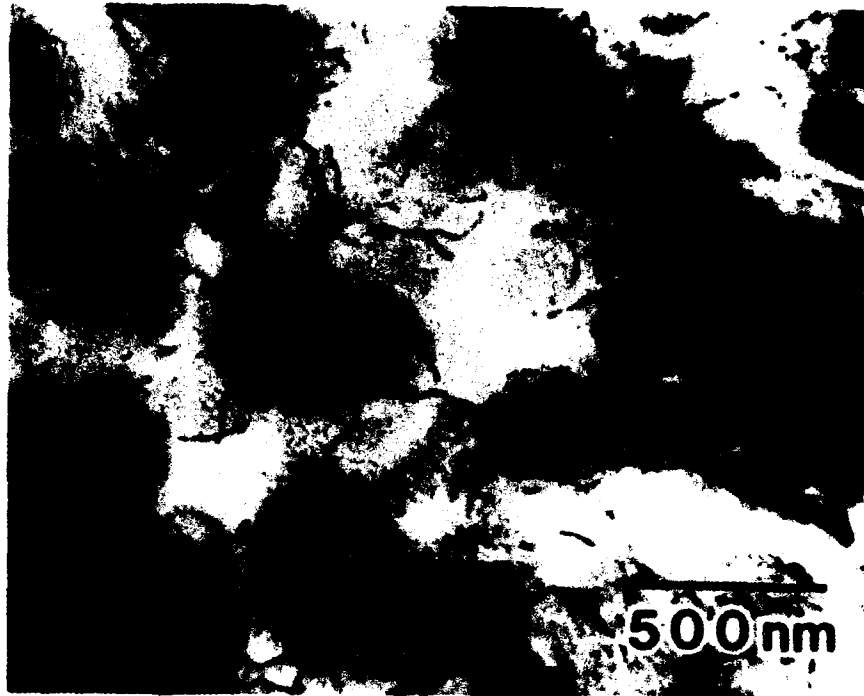


Figure 3.18 Bright field TEM micrograph of as-melt spun Nb-10Al-20Cr (alloy H3) showing the segregated microstructure frequently observed in alloys containing additions of both Al and Cr.

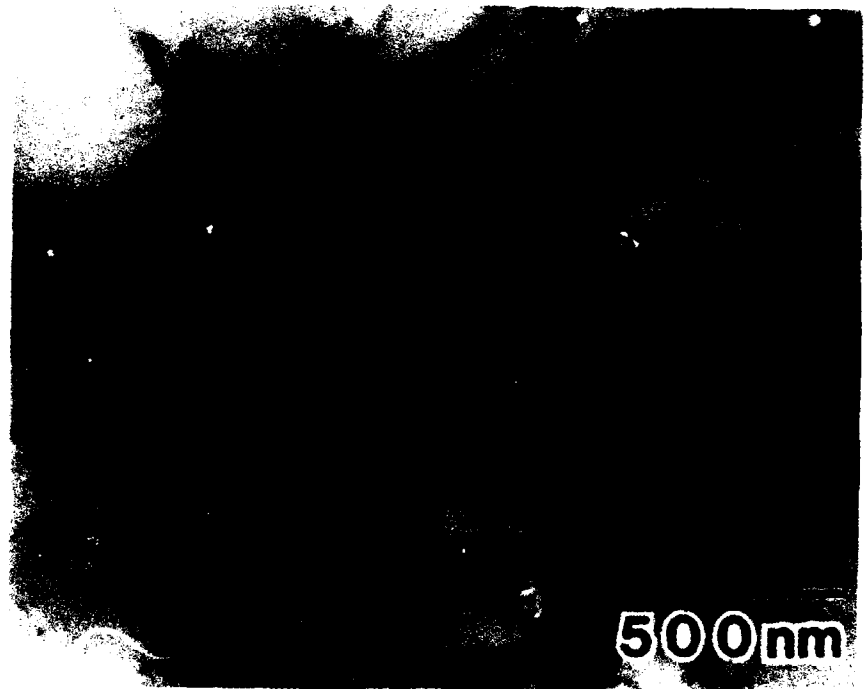
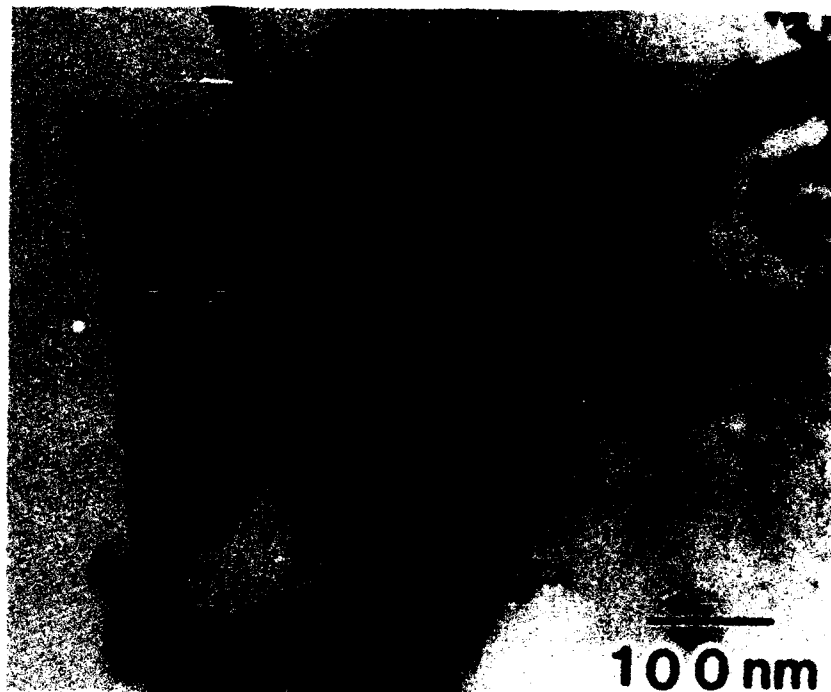


Figure 3.19 Bright field TEM micrograph of Nb-10Al-5Cr (alloy H1) melt-spun ribbon after heat treatment at 600°C for 1 hour.



**Figure 3.20** Bright field TEM micrograph of Nb-10Al-10Cr (alloy H2) melt-spun ribbon after heat treatment at 600°C for 1 hour.



**Figure 3.21** Bright field TEM micrograph of Nb-10Al-20Cr (alloy H3) melt-spun ribbon after heat treatment at 600°C for 1 hour.

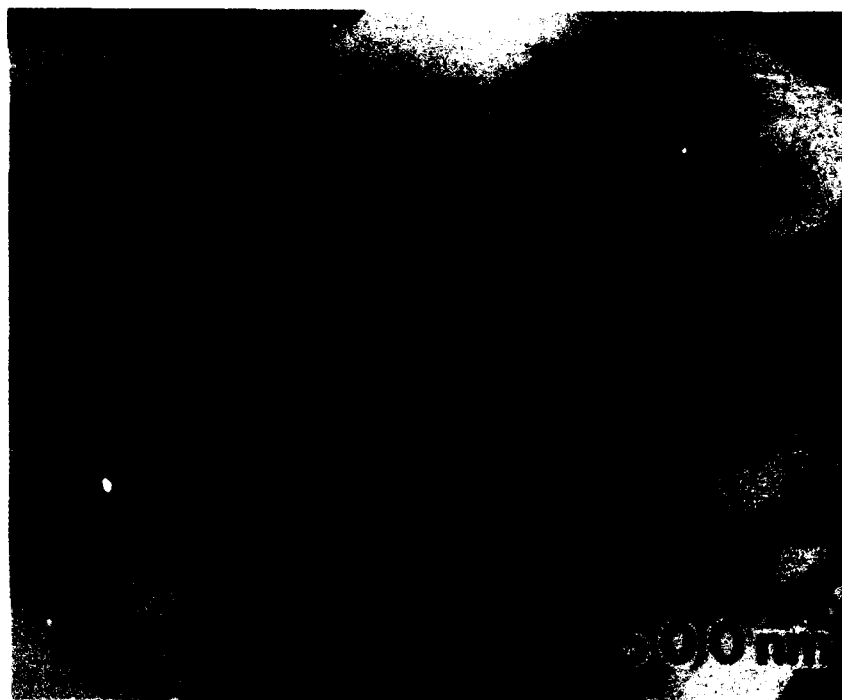


Figure 3.22 Bright field TEM micrograph of Nb-15Al-5Cr (alloy H4) melt-spun ribbon after heat treatment at 600°C for 1 hour.



Figure 3.23 Bright field TEM micrograph of Nb-15Al-10Cr (alloy H5) melt-spun ribbon after heat treatment at 600°C for 1 hour.



Figure 3.24 Bright field TEM micrograph of Nb-15Al-20Cr (alloy H6) melt-spun ribbon after heat treatment at 600°C for 1 hour.

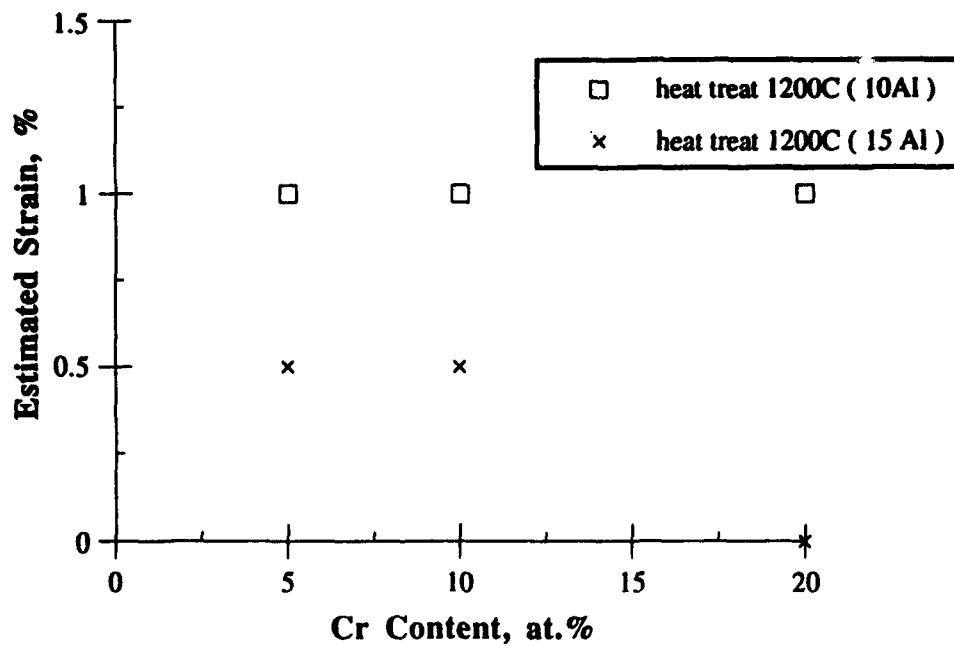


Figure 3.25 Estimated strain versus Ti alloy content for two base compositions of as-melt spun ribbon; alloy 1 is Nb-10Al-10Cr-Ti and alloy 2 is Nb-15Al-20Cr-Ti.

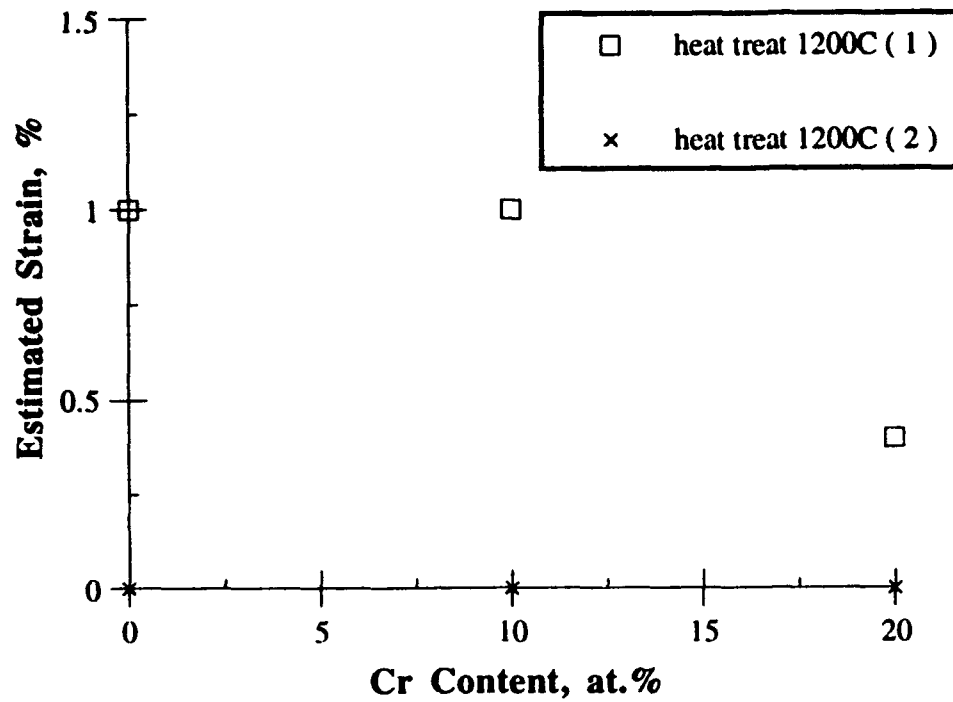


Figure 3.26 Estimated strain versus Ti alloy content for two base compositions of as-melt spun ribbon heat treated at 600°C/ 1 hour; Alloy 1 is Nb-10Al-10Cr-xTi and Alloy 2 is Nb-15Al-20Cr-xTi.

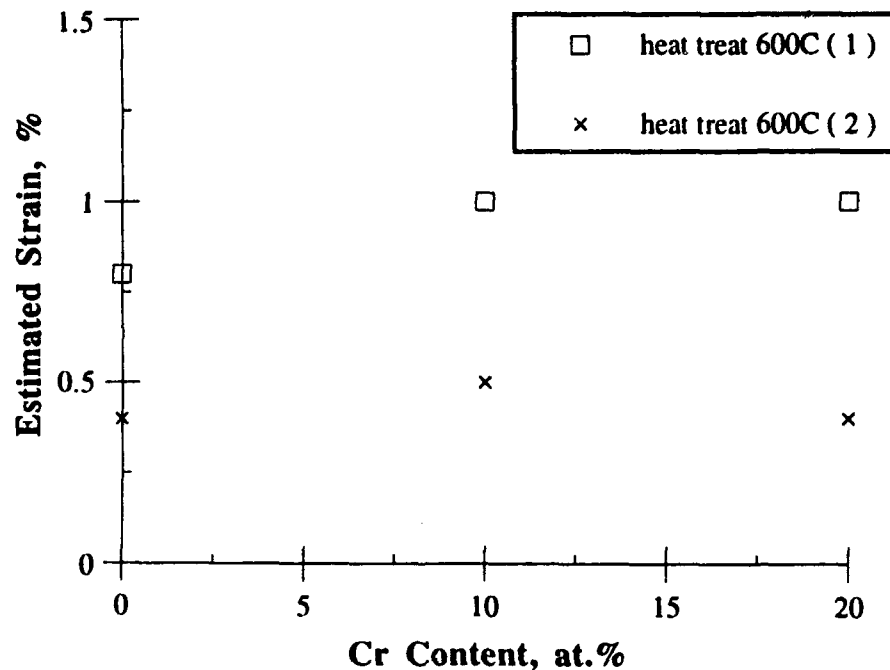


Figure 3.27 Estimated strain versus Ti alloy content for two base compositions of as-melt spun ribbon heat treated at 600°C/ 1 hour followed by 1200°C/one hour; Alloy 1 is Nb-10Al-10Cr-xTi and Alloy 2 is Nb-15Al-20Cr-xTi.

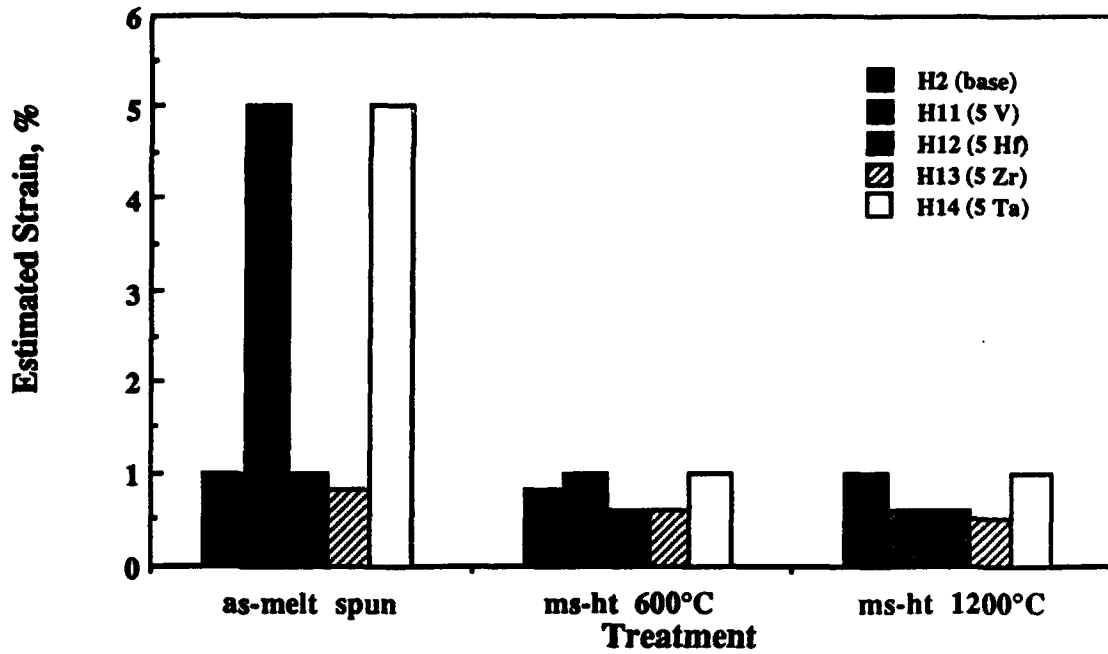


Figure 3.28 Chart of estimated strains in ribbons subjected to bending for the various alloys shown. The conditions noted correspond to as-melt spun, heat treated at 600°C for 1 hour, and heat treated at 600°C for 1 hour followed by 1200°C for 1 hour.

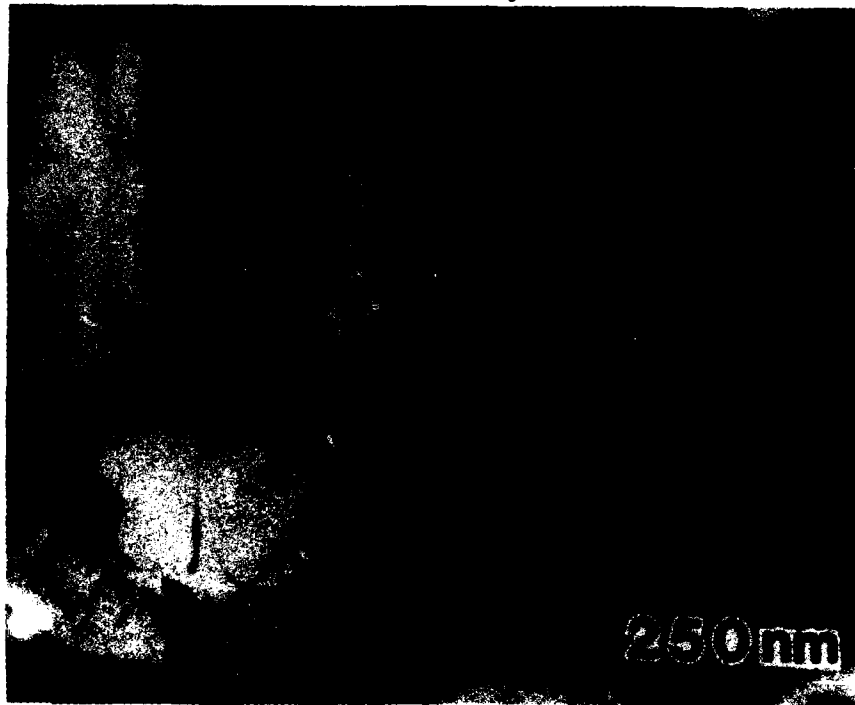


Figure 3.29 Bright field TEM micrograph of as-melt spun Nb-10Al-10Cr-10Ti (alloy H7).



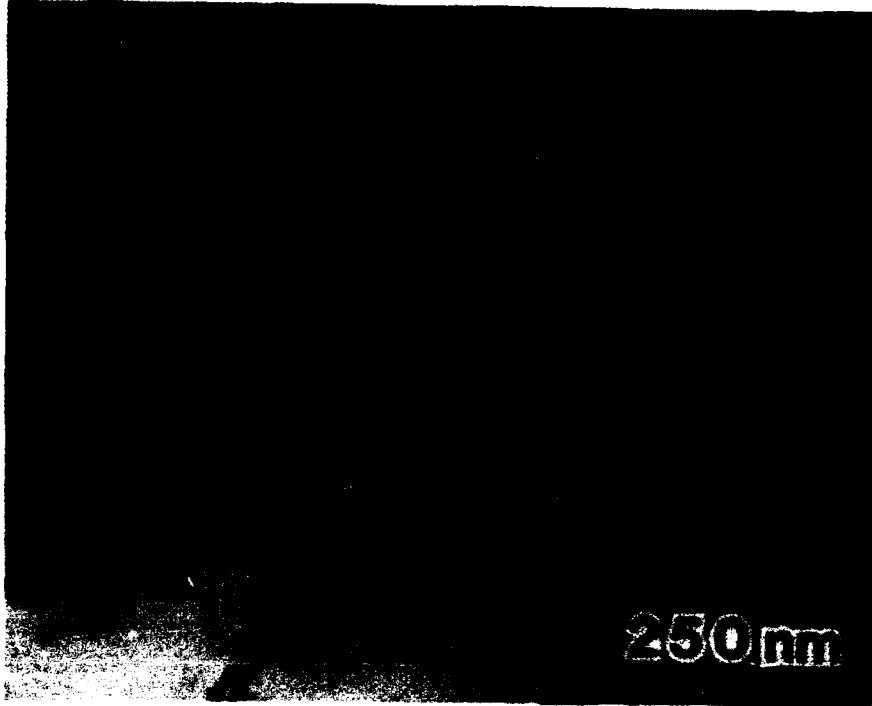


Figure 3.30 Bright field TEM micrograph of as-melt spun Nb-15Al-20Cr-10Ti (alloy H8).



Figure 3.31 Bright field TEM micrograph of as-melt spun Nb-10Al-10Cr-20Ti (alloy H9).

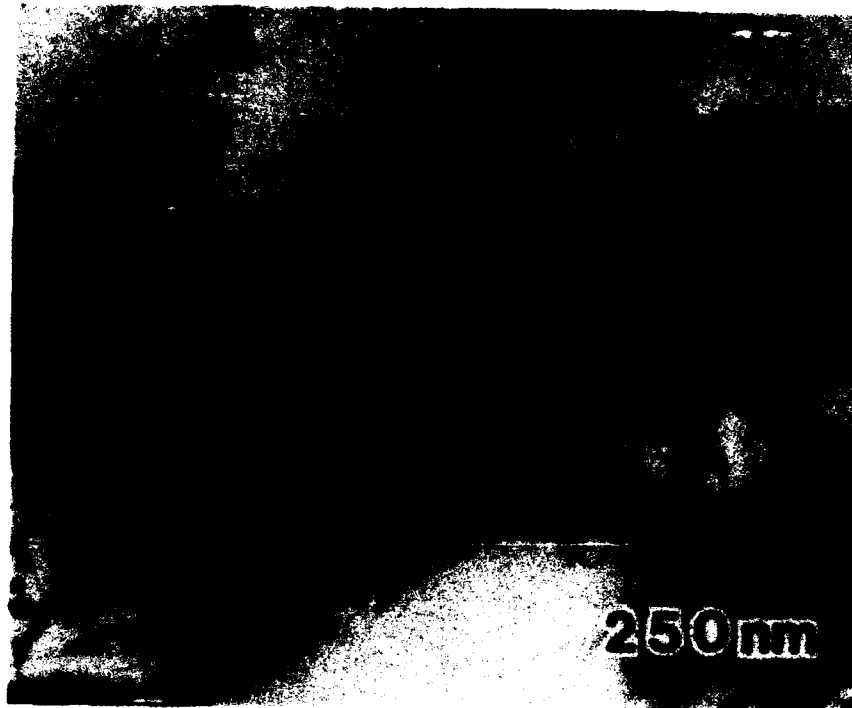
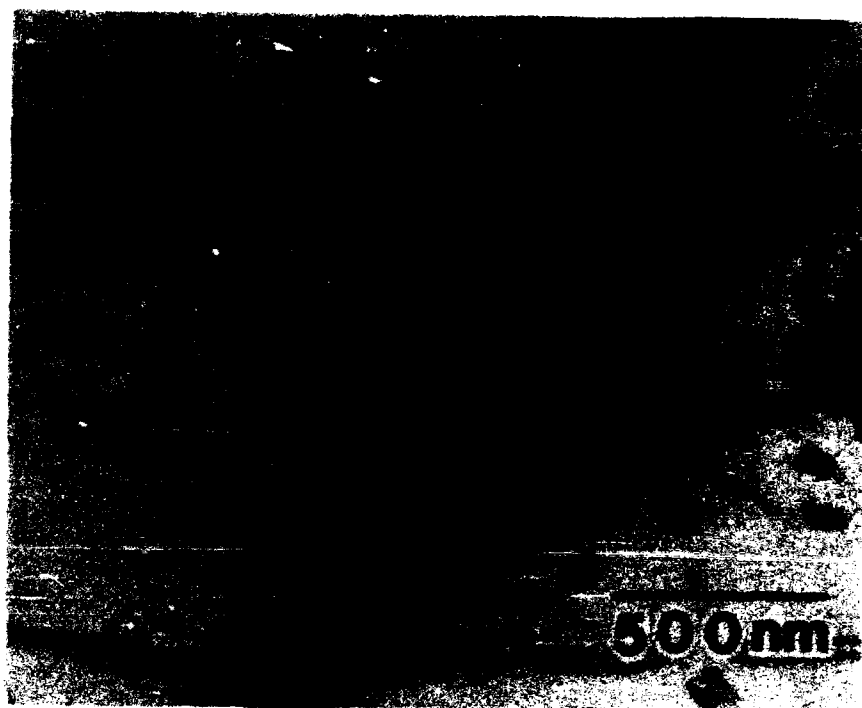


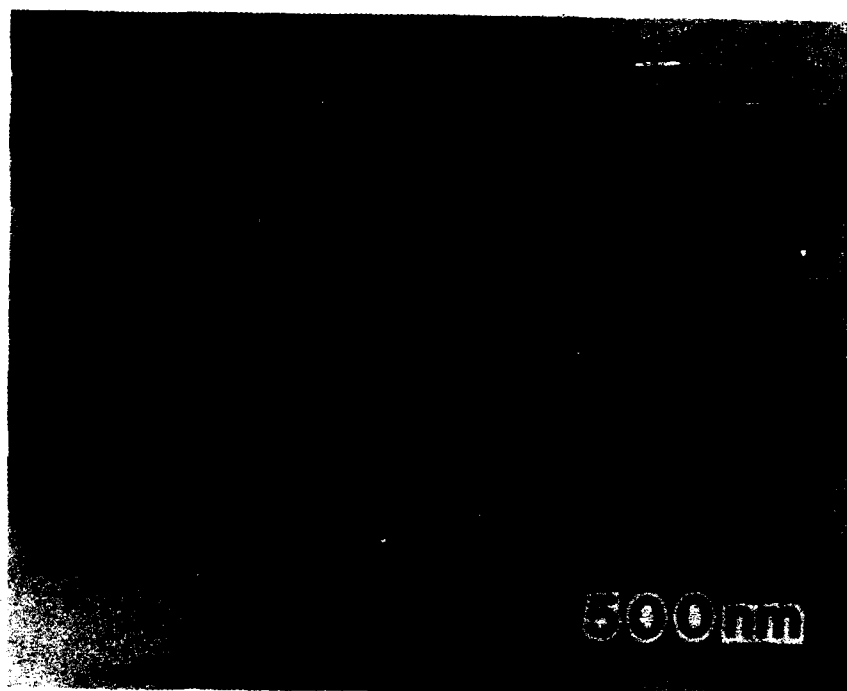
Figure 3.32 Bright field TEM micrograph of as-melt spun Nb-15Al-20Cr-20Ti (alloy H10).



Figure 3.33 Bright field TEM micrograph of Nb-10Al-10Cr-10Ti (alloy H7) melt-spun ribbon after heat treatment at 600°C for 1 hour.



**Figure 3.34** Bright field TEM micrograph of Nb-15Al-20Cr-10Ti (alloy H8) melt-spun ribbon after heat treatment at 600°C for 1 hour.



**Figure 3.35** Bright field TEM micrograph of as-melt spun Nb-10Al-10Cr-5V (alloy H11).

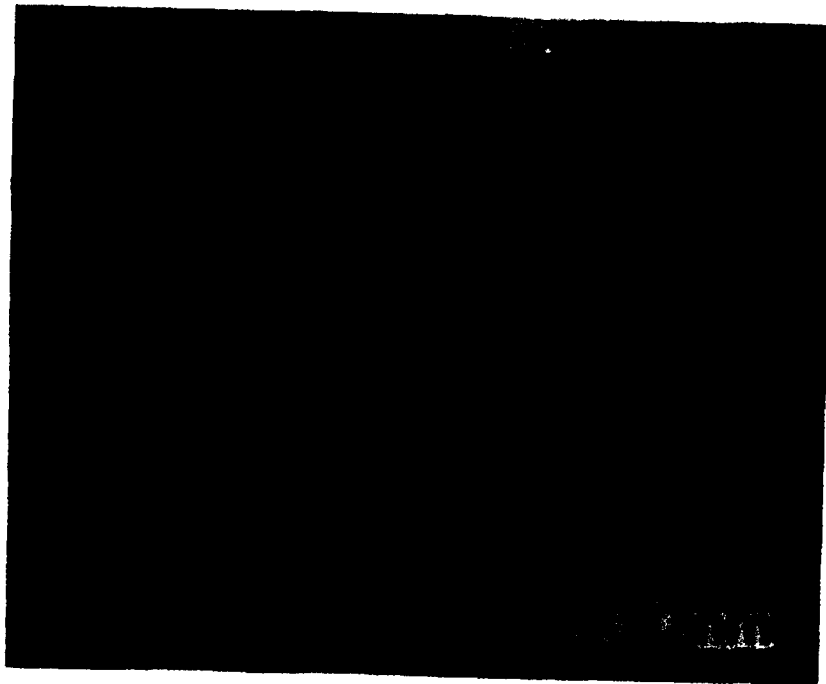


Figure 3.36 Bright field TEM micrograph of as-melt spun Nb-10Al-10Cr-5Hf (alloy H12).

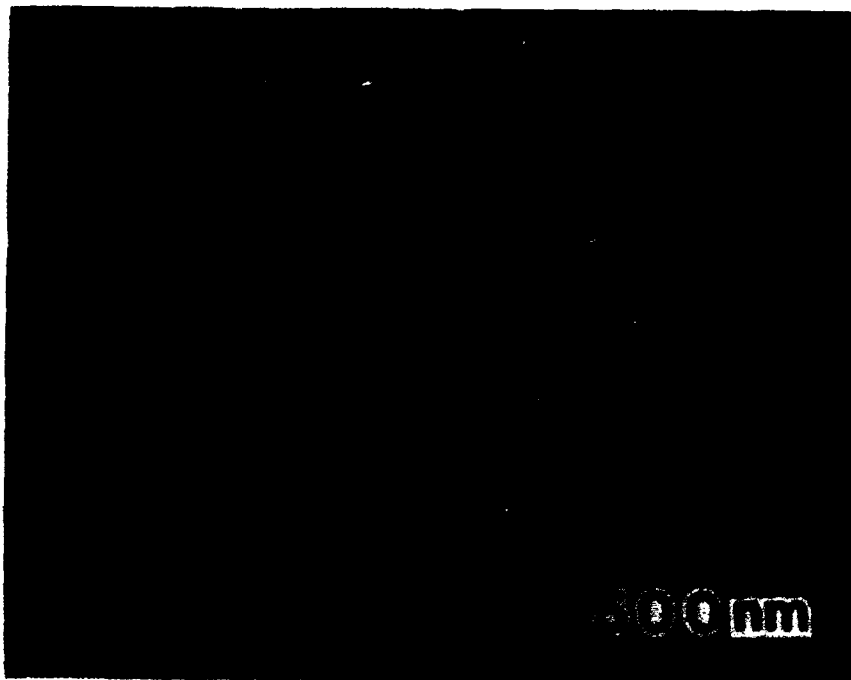


Figure 3.37 Bright field TEM micrograph of as-melt spun Nb-10Al-10Cr-5Zr (alloy H13).

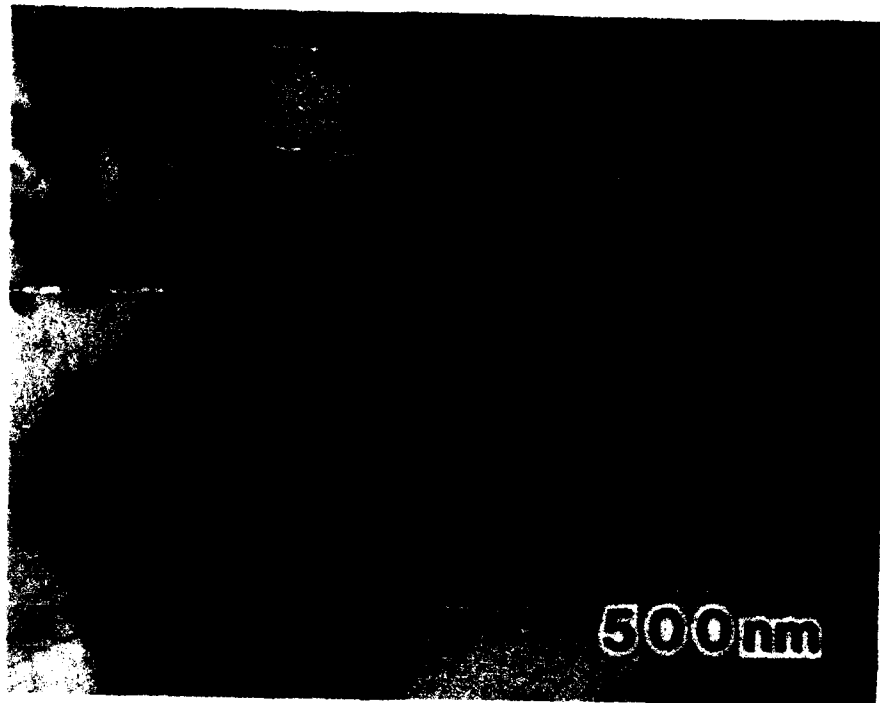


Figure 3.38 Bright field TEM micrograph of as-melt spun Nb-10Al-10Cr-5Ta (alloy H14).

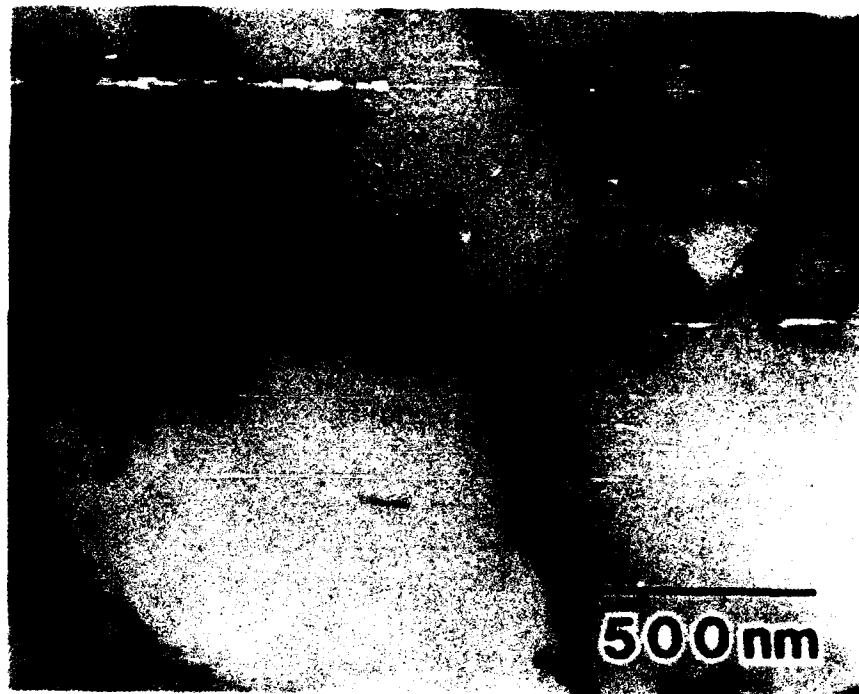


Figure 3.39 Bright field TEM micrograph of Nb-10Al-10Cr-5Zr (alloy H11) melt-spun ribbon after heat treatment at 600°C for 1 hour.

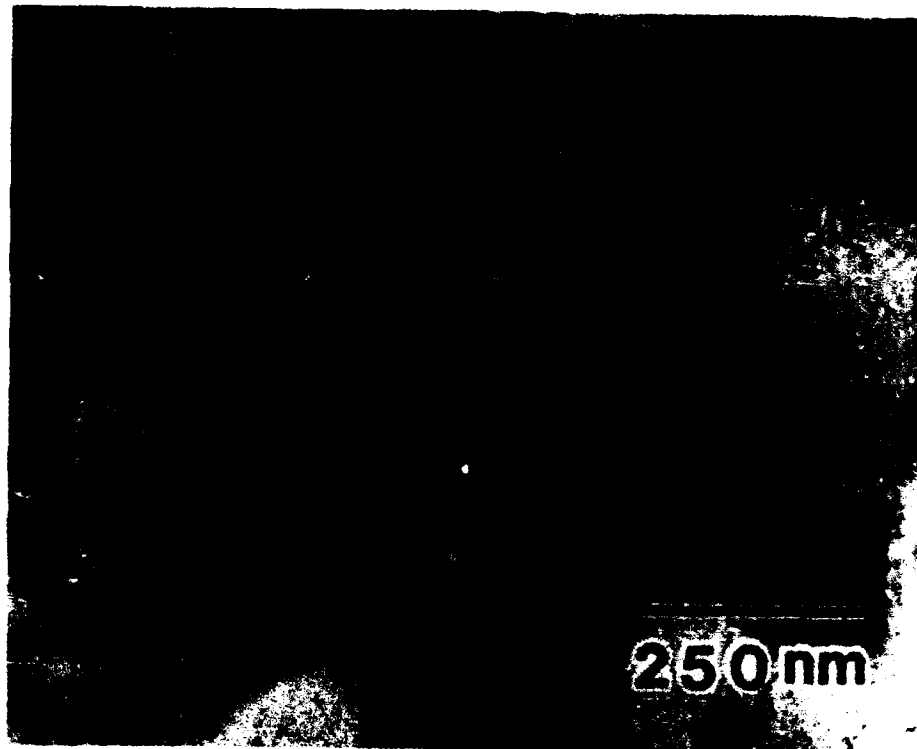
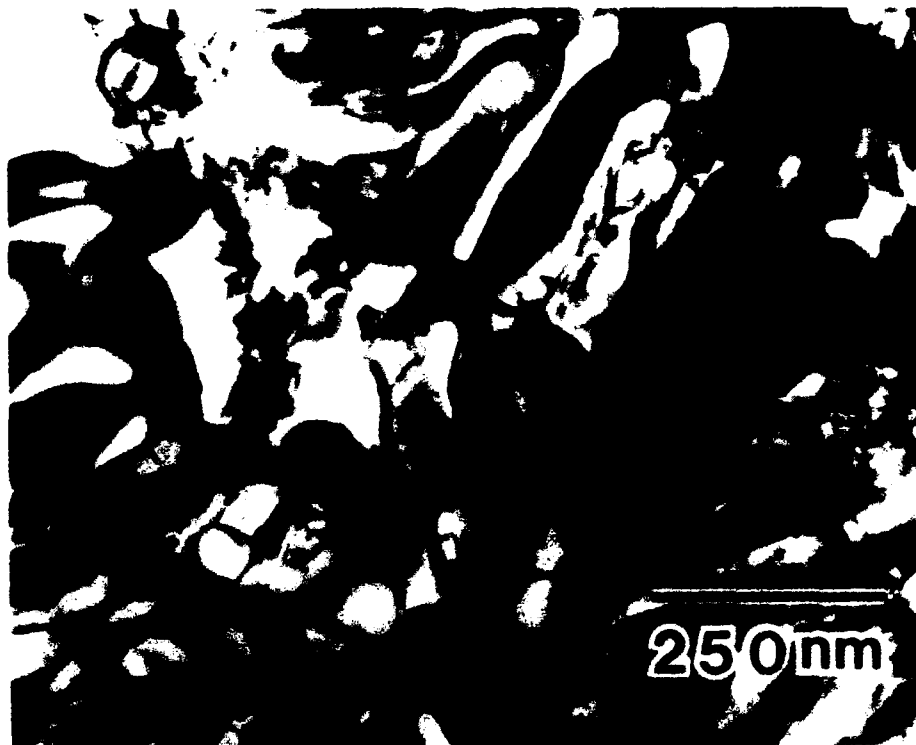


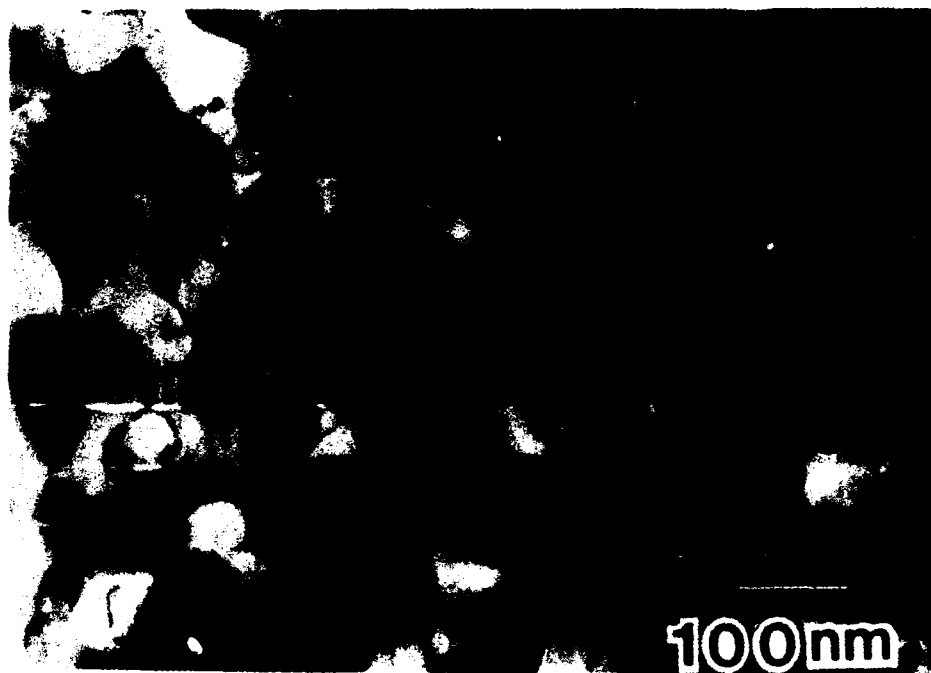
Figure 3.40 Bright field TEM micrograph of as-melt spun Nb-10Al-10Cr-10Ti-15W (alloy S1).



Figure 3.41 Bright field TEM micrograph of as-melt spun and heat treated Nb-10Al-10Cr-10Ti-15W (alloy S1). Heat treatment was at 600°C for 1 hour.



**Figure 3.42** Bright field TEM micrograph of as-melt spun Nb-13Al-35Cr-2.5Ni (alloy S3).



**Figure 3.43** Bright field TEM micrograph of as-melt spun and heat treated Nb-13Al-35Cr-2.5Ni (alloy S3). Heat treatment was at 600°C for 1 hour.



Figure 3.44 Bright field TEM micrograph of as-melt spun Nb-10Al-10Cr-10Ti-10W-1Zr (alloy S4).



Figure 3.45 Bright field TEM micrograph of as-melt spun Nb-10Al-10Cr-10Ti-10W-1Er (alloy S5)





Figure 3.46 Bright field TEM micrograph of as-melt spun and heat treated Nb-10Al-10Cr-10Ti-10W-1Er (alloy S5). Heat treatment was at 600°C for 1 hour.

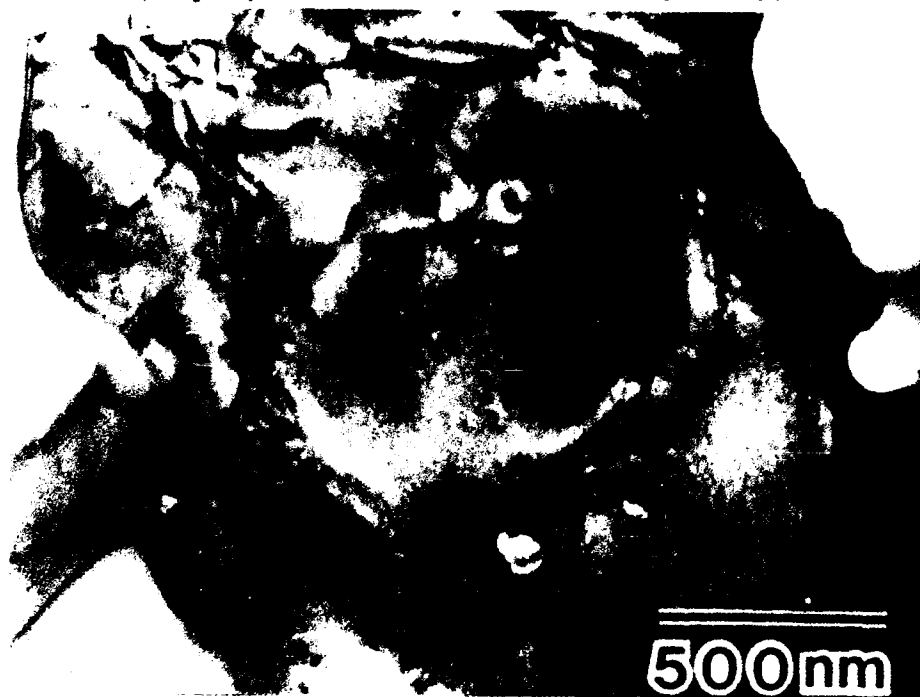


Figure 3.47 Bright field TEM micrograph of as-melt spun Nb-10Al-10Cr-10Ti-10W-1Y (alloy S6)



Figure 3.48 Bright field TEM micrograph of as-melt spun and heat treated Nb-10Al-10Cr-10Ti-10W-1Y (alloy S6). Heat treatment was 600°C for 1 hour.

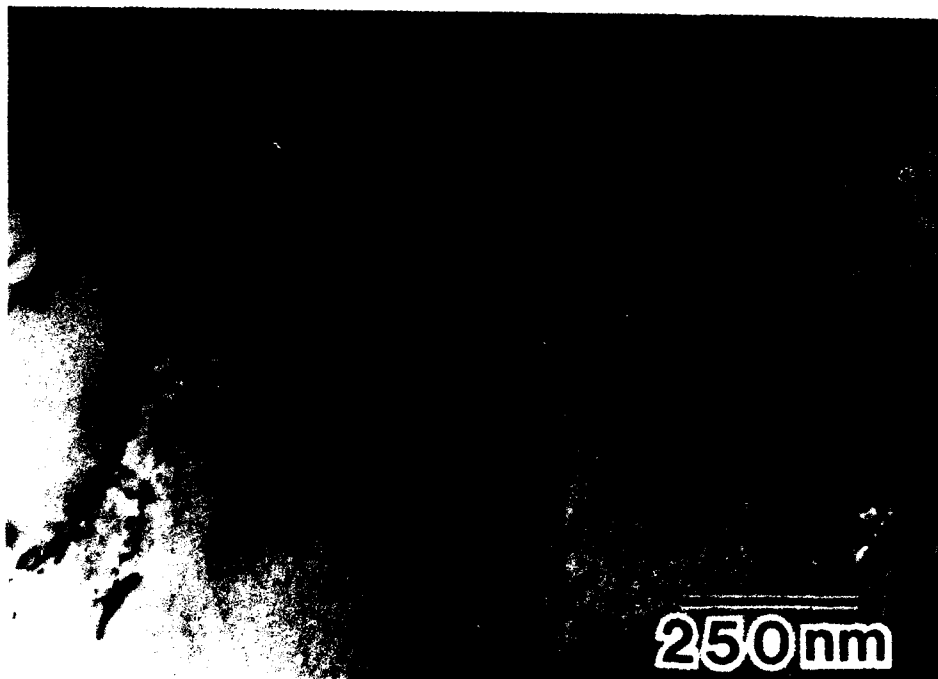


Figure 3.49 Bright field TEM micrograph of as-melt spun Nb-15Ti-15W-3Mo-1Zr-1Er (alloy S7)



Figure 3.50 Bright field TEM micrograph of as-melt spun and heat treated Nb-15Ti-15W-3Mo-1Zr-1Er (alloy S7). Heat treatment was 600°C for 1 hour.



Figure 3.51 Bright field TEM micrograph of as-melt spun Nb-5Al-5Cr-15Ti-15W-3Mo-1Zr-1Er (alloy S8).

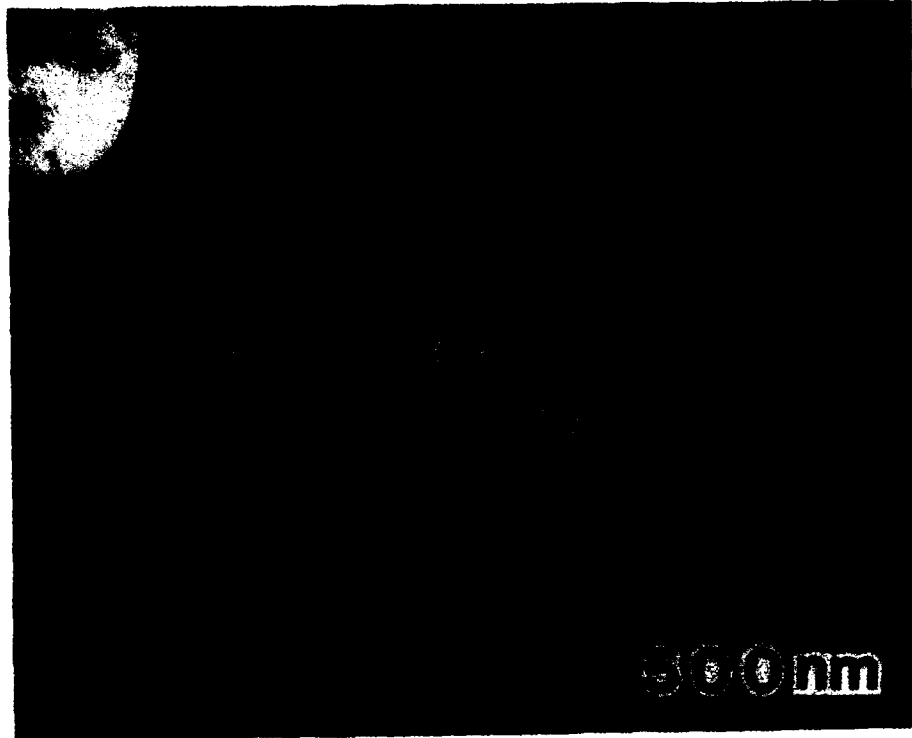


Figure 3.52 Bright field TEM micrograph of as-melt spun and heat treated Nb-5Al-5Cr-15Ti-15W-3Mo-1Zr-1Er (alloy S8). Heat treatment was 600°C for 1 hour.

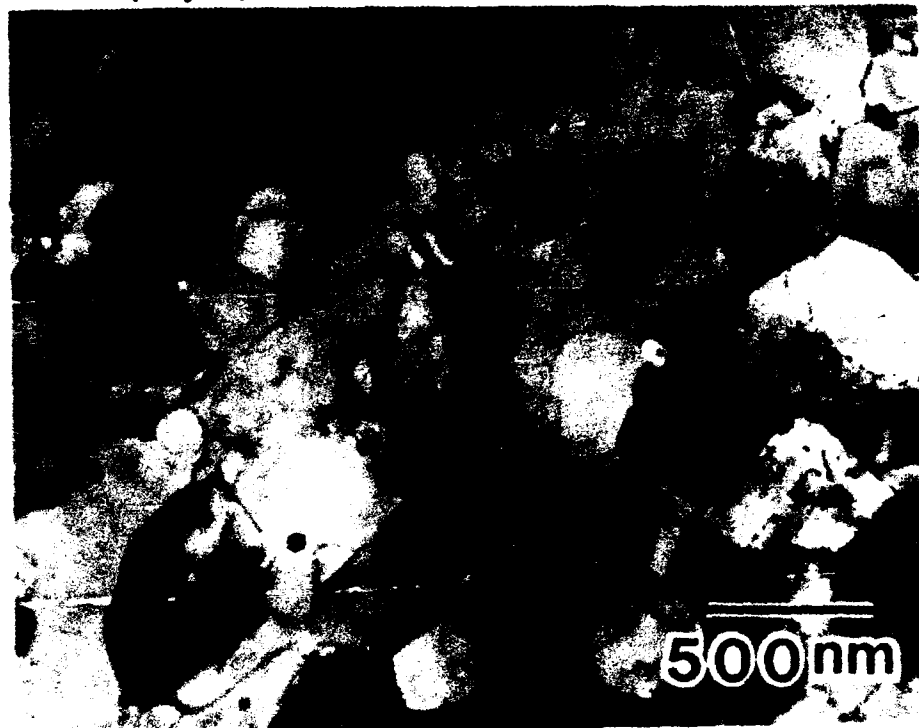


Figure 3.53 Bright field TEM micrograph of as-melt spun Nb-10Al-10Cr-15Ti-10W-3Mo-1Zr-1Er (alloy S9).

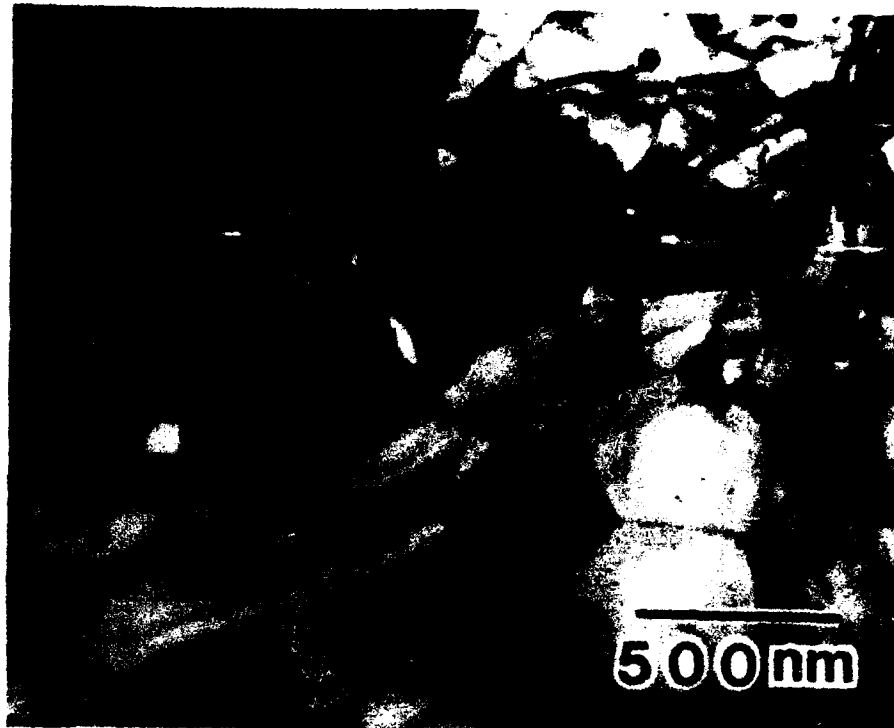


Figure 3.54 Bright field TEM micrograph of as-melt spun and heat treated Nb-10Al-10Cr-15Ti-10W-3Mo-1Zr-1Er (alloy S9). Heat treatment was 600°C for 1 hour.



Figure 3.55 Bright field TEM micrograph of as-melt spun Nb-10Al-10Cr-15Ti-15W-1Zr-1Er (alloy S10).



Figure 3.56 Bright field TEM micrograph of as-melt spun Nb-10Al-10Cr-15Ti-15W-1Zr-1Er (alloy S10).



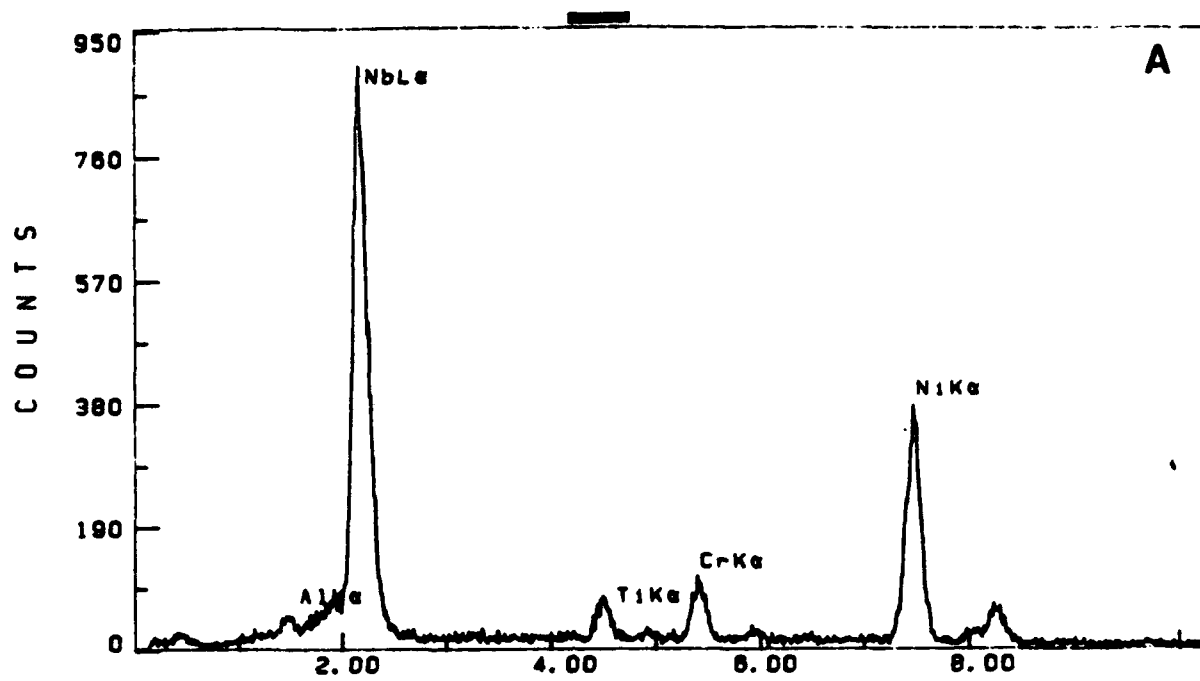
Figure 3.57 Bright field TEM micrograph of as-melt spun and heat treated Nb-10Al-10Cr-15Ti-10W-1Zr-1Er (alloy S11). Heat treatment was at 600°C for 1 hour.



Figure 3.58. Bright-field transmission electron micrographs recorded from typical areas taken from thin foils of powders of alloy P5. Note the dendritic and interdendritic regions, marked A and B, respectively. Also note the presence of small particles, which have been identified as  $\text{Er}_2\text{O}_3$ .



Figure 3.59. Bright-field transmission electron micrograph of sample of powders of alloy P5 following heat-treatment for 4 hours at  $1200^\circ\text{C}$ .



(a)

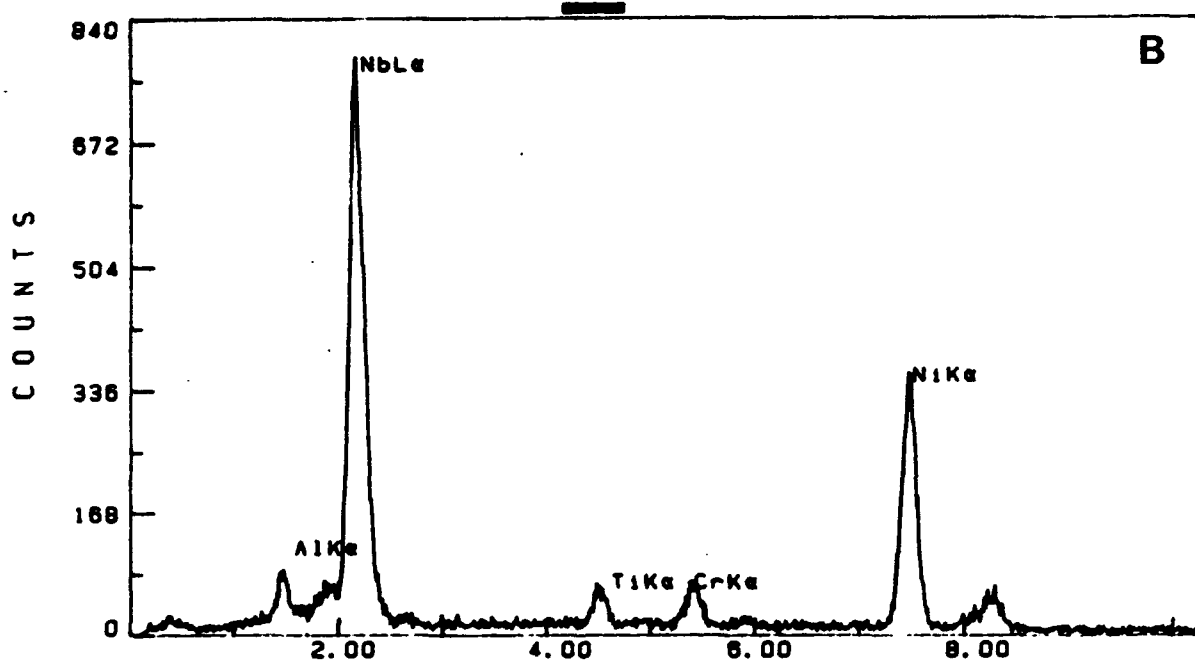


Figure 3.60. EDS spectra recorded from a thin foil of a powder of alloy P5 following heat-treatment for 4 hours at 1200°C with the electron beam incident on (a) the  $\alpha$ -Nb matrix, (b) a particle of Nb<sub>3</sub>Al and (c) a particle of TiC.



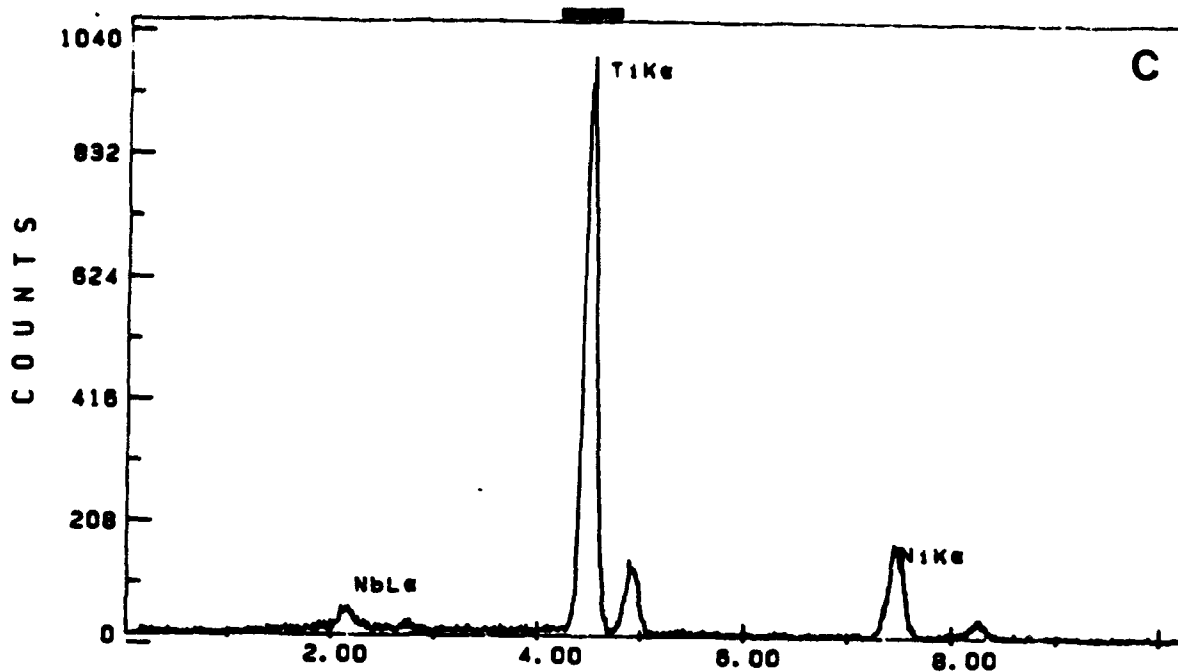


Figure 3.60c



Figure 3.61. Bright-field transmission electron micrographs recorded from areas of thinned powders of alloy P6.

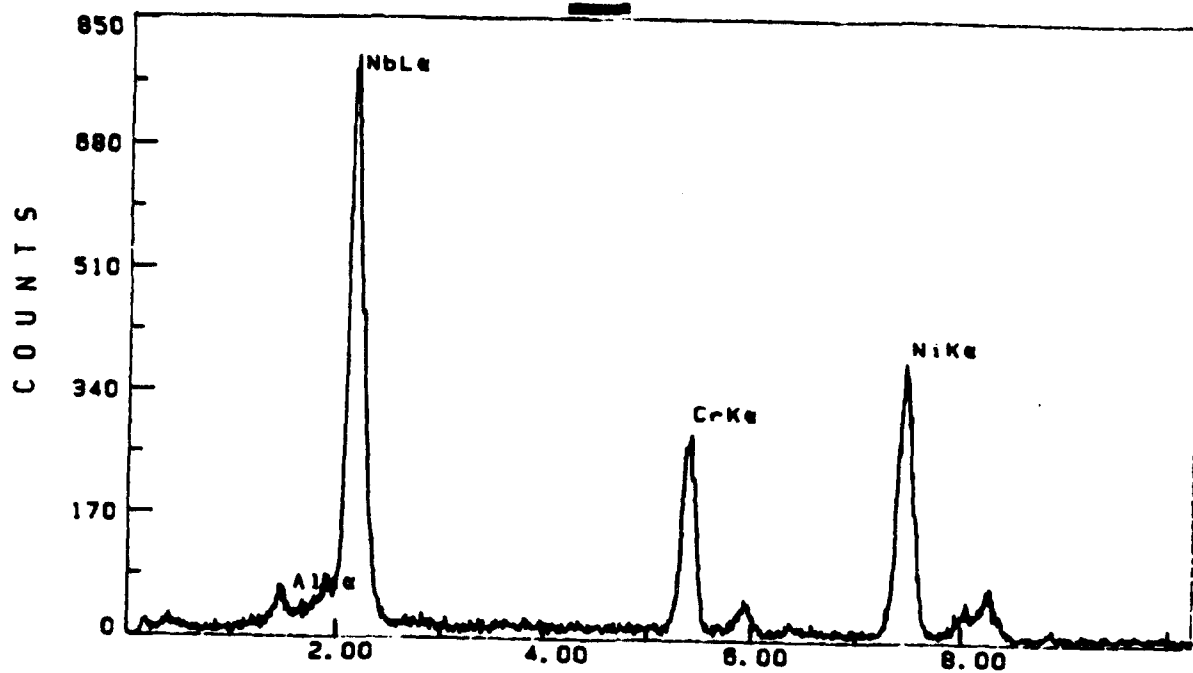


Figure 3.62. EDS spectrum recorded from  $\alpha$ -Nb in powders of alloy P6.

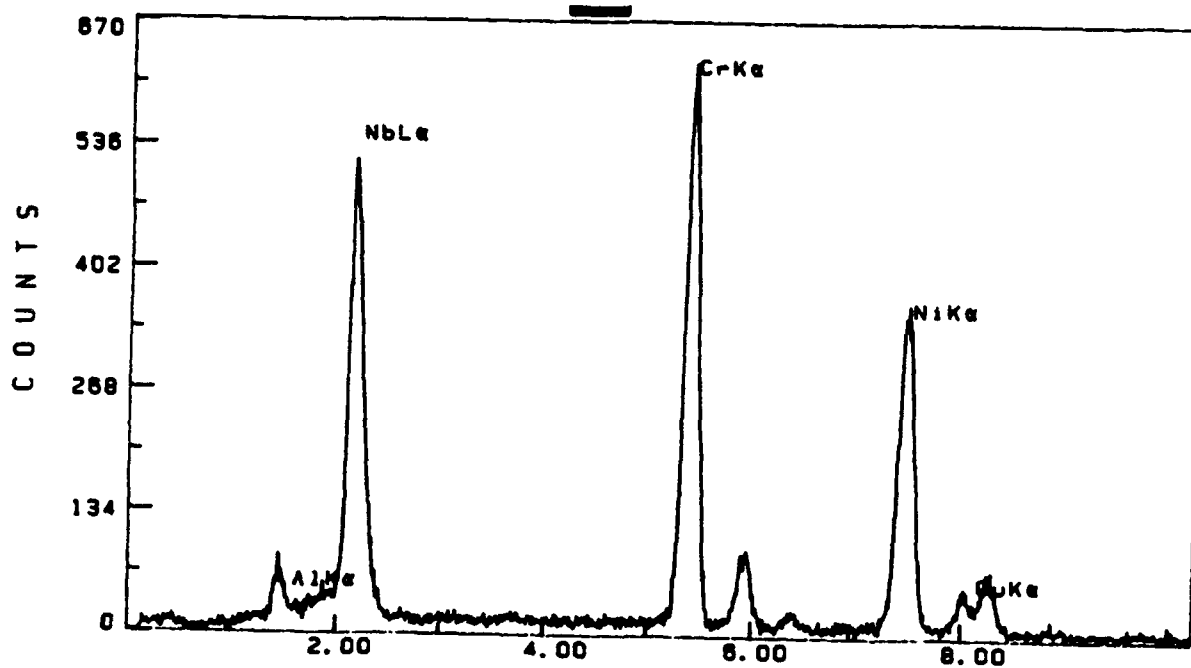


Figure 3.63. EDS spectrum recorded from NbCr<sub>2</sub> in powders of alloy P6.



Figure 3.64. Transmission electron micrograph of a typical area observed in powders of alloy P6 following heat-treatment for 4 hours at 1200°C.



Figure 3.65. Transmission electron micrograph of the  $\alpha$ -Nb matrix phase in a sample from alloy P6 following heat-treatment for 4 hours at 1200°C revealing twinned-like contrast.



Figure 3.66. Typical bright field transmission electron micrograph recorded from a thin foil of powder of alloy P7 in the as-atomized condition.

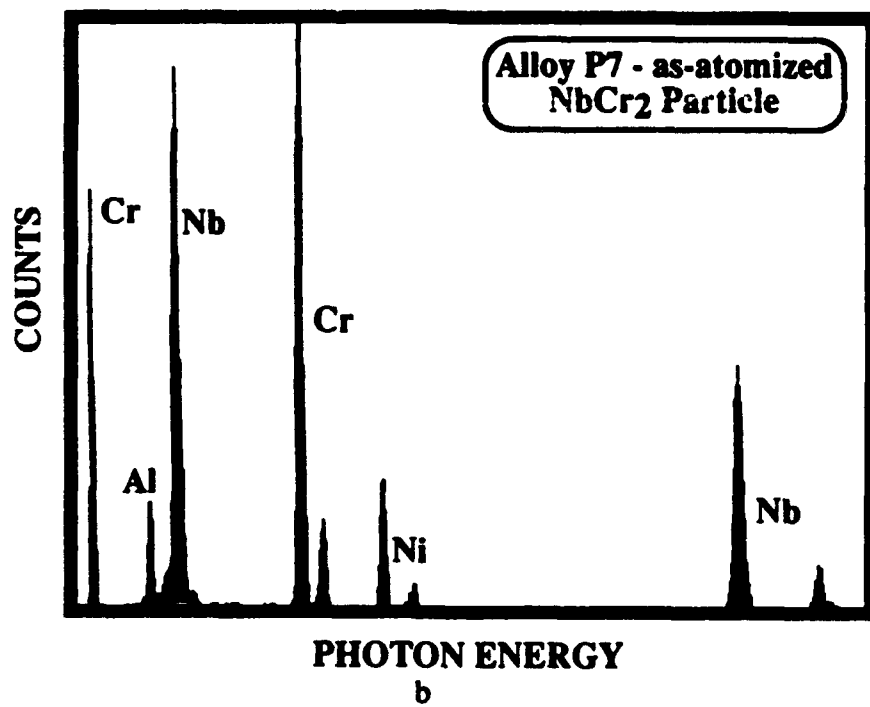
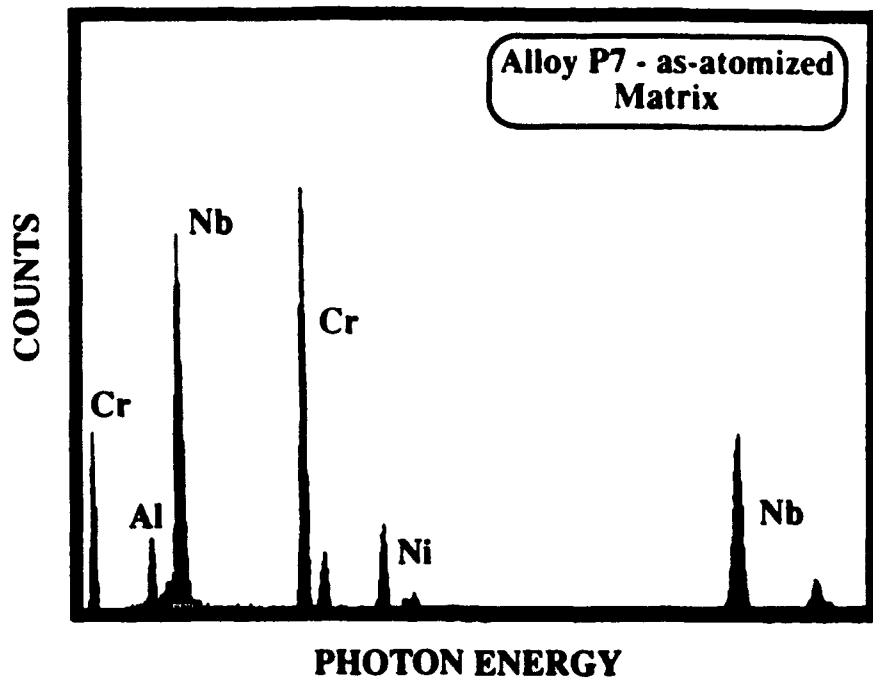


Figure 3.67. EDS x-ray spectra recorded from a thinned powder of alloy P7 in the as-atomized condition. a) from the matrix; b) from a second phase particle, identified as NbCr<sub>2</sub>.



Figure 3.68. Typical bright-field transmission electron micrograph recorded from a thin foil of powder of alloy P7 following heat-treatment (see text).



Figure 3.69. Typical bright-field transmission electron micrograph recorded from a thin foil of powder of alloy P8 in the as-atomized condition.

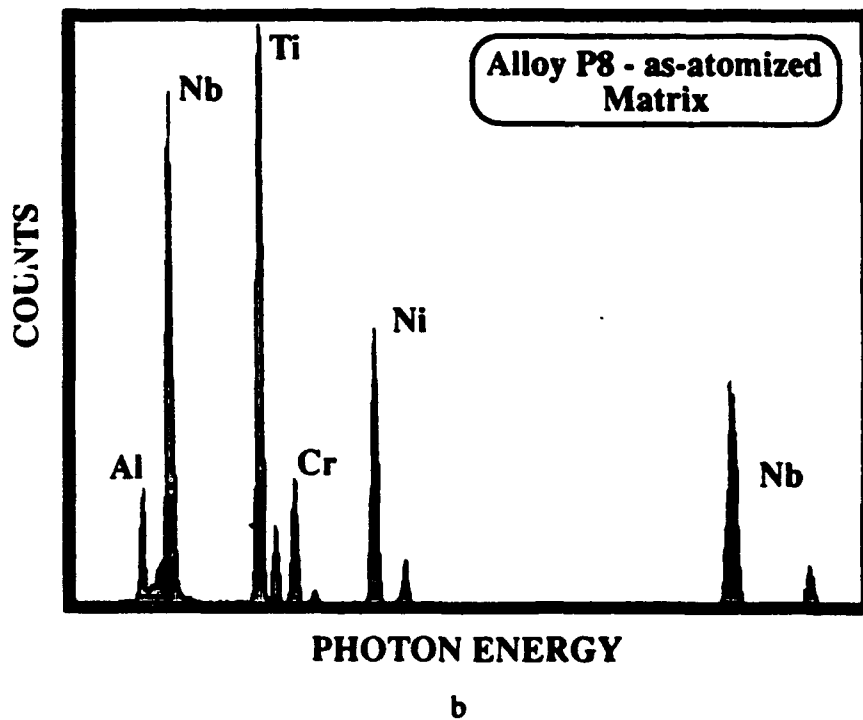
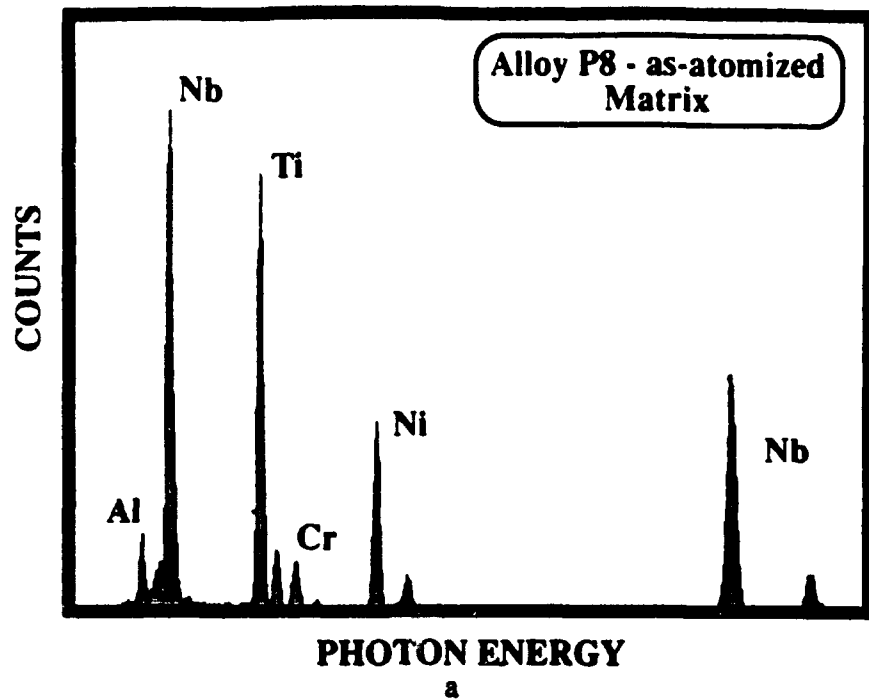


Figure 3.70. EDS spectra recorded from two different regions (a and b) of the matrix of thinned powders of P8 (as-atomized), shown in Fig. 3.69, revealing the inhomogeneous composition of the matrix.



Figure 3.71. Typical bright-field transmission electron micrograph recorded from a thin foil of powder of alloy P8 following heat treatment (see text).



## 4.0 Ingot Alloy Screening

### 4.1 Ingot Alloy Selection Rationale

The alloys which had been developed in the early part of the program were based on the use of rapid solidification to obtain a fine second phase dispersion size. However, the same compositions were not expected to be ductile without the refinement which could be achieved with rapid solidification. Therefore, another screening step was added to screen alloys for the ingot approach. Small (2.5cm x 10cm) ingots were produced at Iowa State University by VAR. The additions chosen were based on an expected benefit of both environmental resistance and mechanical properties. A list of the 20 alloys chosen for the preliminary screening phase of the program is given in Table 4.1. In the preliminary screening, there are six distinct families of alloys. Alloys 1 and 2 contain Mo and Cr, and were designed for high specific modulus by addition of elements which have high specific moduli. Alloys 3, 4, 5 and 6 contain two levels of Cr & Ti with varying Nb/Ti ratios. These alloys were designed to determine the effect of the Laves phase and Nb/Ti ratio on strengthening. Alloys 7, 8, 9 and 10 have the same base composition as Alloy 4 and were used to evaluate the addition of C, Alloys 7 and 8, or Si, Alloy 9 and 10, to a known base alloy. Alloys 11, 12, 13 and 14 contain various Al additions and were designed to determine the effect of various phases in the Nb-Ti-Al system on strengthening combined with the expected improved oxidation resistance of the Al addition. Alloys 15, 16, 17 and 18 were all based on either ternary or quaternary additions which have been shown in past reports to improve the oxidation resistance of Nb. The level of Ta addition in Alloys 17 and 18 was chosen to be similar to the level of Ti added in Alloys 4 and 5. The rationale for this similarity is based on the similarity of the Ti-Cr with the Ta-Cr binary phase diagrams. This comparison was to determine the effect of the addition of the higher melting point element, Ta, on the properties compared with the lower melting point element Ti. From these four alloys, 16 and 18 had melting temperatures that prohibited them from being produced as ingot material. Alloys 15 and 17 were successfully melted and forged into specimens. Alloys 19 and 20 were designed to combine alloying additions which had been shown in previous reports (1) to improve the oxidation resistance of Nb. GE-CRD studies, performed on IRD funding, have shown that Al and Cr added together improve oxidation resistance and the inclusion of Si may result in further enhancement. The substitution of W for Cr in Alloy 20 was to try to increase the melting point of the alloy.

### 4.2 Deformation Processing / Heat Treatment

All of the 18 alloys which could be melted were prepared for deformation processing, which was by isothermal forging. Of the ingots produced, only Alloy 1 did not result in a useful pancake being produced. The deformation processing conditions for each of the alloys are given in Table 4.1.

Following deformation processing, the resulting pancake was cut into specimens to study the effects of heat treatment on structure and for tensile and creep testing. Pieces of the 17 alloys which were forged were given three heat treatments following the deformation; a) solution treatment only, b) solution treatment and age, and c) age only. The microstructures for these four conditions will be presented for each alloy. The heat treatment conditions for each alloy are given in Table 4.2.

#### 4.3 Results of Processing / Heat Treatment on Microstructure

The response of the alloys to heat treatment will be discussed in the following sections for each alloy class.

##### Alloys 1 and 2

The composition of Alloy 1 is 31Nb-29Ti-25Mo-15Cr. This alloy was castable into ingot form, but it was not able to be forged at 1300°C. Two attempts at producing a forging from this alloy were unsuccessful. The initial trial was performed using 1200°C and 0.9mm/s and the second trial was performed at 1300°C and 0.09mm/s. There was some improvement in going to the higher temperature and slower strain rate on the second attempt, but a useful forging was still not obtained.

The composition of Alloy 2 is 31Nb-29Ti-15Mo-25Cr. This alloy was forgeable at 1300°C, although there were cracks near the edge of the forging. The microstructures of Alloy 2 are shown in Figure 4.1 for the four conditions. The forging parameters for Alloy 2 were 1300°C and a crosshead speed of 0.09mm/sec, and were chosen based on the results of the forging trials on Alloy 1. The presence of fractures at the grain boundary triple points can be seen in all process conditions. A large volume fraction of second phase, probably the Cr<sub>2</sub>(Nb,Ti) Laves phase, is present after exposure at 1300°C, which was the solution treatment temperature. There is little change in the structure following aging at 1000°C. The direct age exhibits a similar microstructure to the solution and age materials.

##### Alloys 3, 4, 5 and 6

Alloys 3, 4, 5 and 6 are Cr containing alloys with varying Nb to Ti ratios and two levels of Ti and Cr, 15 at % Cr in Alloys 4 and 5 and 30 at % Cr in Alloys 3 and 6. These levels of Cr should produce a low and high volume fraction of the Laves phase, respectively.

The microstructures for Alloy 3, 50Nb-20Ti-30Cr, are shown in Figure 4.2. There is little difference between the three heat treatment conditions which appear only to have spherodized the second phase.

Alloy 4, 55Nb-30Ti-15Cr, microstructures are shown in Figure 4.3. The 1300°C solution temperature was sufficient to produce a single phase at temperature. The grains grew in size during the solution treatment and were more uniformly equiaxed than either the forged or direct aged material. The aging treatment of 1000°C / 24h produced a fine dispersion of second phase in the bcc matrix, although the volume fraction is small. Direct aging of the forged structure at 1000°C / 24h resulted in an elongated grain structure with precipitation similar to the solution and aged material. Alloy 4 is the baseline for Alloys 7, 8, 9 and 10.

The microstructures for Alloy 5, 65Nb-20Ti-15Cr, are shown in Figure 4.4. Solution treating of Alloy 5 at 1300°C, like Alloy 4, resulted in a single phase structure with large equiaxed grains. Aging at 1000°C produced a platelike dispersion of the second phase in both the solution treated and aged and direct aged conditions with a higher volume fraction of precipitate than that seen in Alloy 4. The higher volume fraction results from the change in the Nb-Ti ratio which pushes the alloy further into the two phase Laves plus BCC phase field of the Nb-Ti-Cr ternary diagram.(2)

Alloy 6, 40Nb-30Ti-30Cr, is microstructurally similar to Alloy 3, as shown in Figure 4.5, although it appears to have a lower volume fraction of second phase. The solution heat treatment had little effect on the second phase, and neither of the aging treatments had any detectable effect on the scale of the microstructure.

#### **Alloys 7, 8, 9 and 10**

These alloys are all based on Alloy 4, but Alloys 7 and 8 contain 1.5 and 3 at % C, respectively, and Alloys 9 and 10 contain 3 and 5 at % Si, respectively.

Alloy 7, 55Nb-28.5Ti-15Cr-1.5C, and Alloy 8, 55Nb-27Ti-15Cr-3C, have similar microstructures for all conditions studied, Figures 4.6 and 4.7. Solution treating of the forged structure at 1300°C / 4h results in an equiaxed grain structure with a second phase present both in the grains and at the grain boundaries. This second phase appears to be a carbide although the exact stoichiometry has not been determined. The grain boundary carbides appear to have pinned the grain boundaries during solution treatment, since the grains are finer for these two alloys than they were for Alloy 4 following similar heat treatments. In addition to the carbide dispersion a fine precipitate has formed in the grains. Aging of the material at 1000°C / 24h, either following solution treatment or forging, results in precipitation of a higher volume fraction of the fine phase with no effect on either the grain structure or the carbide dispersion. There does appear to be a larger volume fraction of the precipitate in Alloy 8 than that seen in Alloy 7 and in the direct age versus the solution heat treat and age for each alloy.

Alloy 9, 54Nb-28Ti-15Cr-3Si, and Alloy 10, 53Nb-27Ti-15Cr-5Si, respond similarly to each of the process conditions, Figure 4.8 and 4.9. The grains retain the elongated structure which was present following the deformation through the solution treatment at 1300°C / 4h. There appear to be three phases present in the solution treated structure, the matrix and two primary phases. These two primary phases are presumably a silicide and laves phase, although the compositions and stoichiometries have not been determined. The solution plus age ( 1000°C / 24h ) treated material, for both Alloys 9 and 10, shows a higher volume fraction of the fine precipitates in the matrix than in Alloys 7 and 8. This suggests that the Si addition decreases the solubility of Cr compared to the ternary alloy. The precipitation in the matrix of Alloys 7-10 is of a higher volume fraction and much finer than that seen in Alloy 4.

In order to determine whether it was possible to achieve a finer grain size, an alternate treatment consisting of a solution treatment at 1300°C for 1 hour was studied. These microstructures exhibited the same grain size as the 4-hour heat treatment and therefore for consistency the 4-hour treatment was used.

#### **Alloys 11, 12, 13 and 14**

The microstructure for these alloys are shown in Figures 4.10 - 4.13. Forging of the alloys resulted in a grain structure which was elongated in the direction of material flow. Solution treated material exhibited large equiaxed grains. Aging of the solution treated structure did not cause precipitation in Alloys 11 and 12 but did in Alloys 13 & 14. It should be realized that because of the various Al levels it is not expected that the precipitating phase is the same in each of the four alloys. Alloys 12 and 13 exhibited segregation in some of the heat treatments. This segregation is believed to be a remnant of the original ingot structure.

The final heat treatment condition for Alloy 11 was 1050°C solution treatment, and 700°C age. These conditions are different from the conditions shown in the photos in Figure 4.10. The final conditions were chosen to try to reduce the grain growth which was present following the 1150°C solution. The actual microstructure for Alloy 11 was determined on the room temperature tensile specimen and is shown in Figure 4.14. The microstructure consisted of both recrystallized, regions which did not contain precipitates, and unrecrystallized regions which contained a fine dispersion of precipitates. For Alloy 12 the final heat treatment consisted of a solution at 1050°C followed by an age at 800°C. This heat treatment was chosen for the same reasons as those described for Alloy 11. The actual structure for Alloy 12 is shown in Figure 4.15. The microstructure of this alloy is similar to that of Alloy 11 except with smaller amounts of recrystallized material. The unrecrystallized material consists of a uniform dispersion of fine precipitates while the recrystallized material consists of a lower volume fraction of coarser precipitates. The heat treatments for Alloys 13 and 14 were 1150°C solution treatment followed by a 950°C age.

### **Alloys 15, 16, 17 and 18**

Alloy 15, 86Nb-12Cr-2Ni, was designed to have Cr in solution for improved strengthening, and the addition of Ni to improve the oxidation resistance. The beneficial effect of Ni was also observed in the RS material. The microstructure of this alloy following the various processing routes is shown in Figure 4.16. The grains grew during the 1300°C solution treatment. In addition, a primary phase and a fine ppt were present following the solution treatment. Aging this structure at 1000°C following solution heat treatment (SHT) did not seem to result in further precipitation. The direct aged structure had a similar grain structure to the forged specimen but with a larger amount of fine precipitates compared to the solution treat and age (STA) structure.

Alloy 17, 65Nb-20Ta-15Cr, is the same composition as Alloy 4 but with Ta substituted for Ti. There appears to be some segregation present in the microstructure shown in the as-forged condition. The microstructures for Alloy 17 and Alloy 4 look similar after solution treatment, although Alloy 17, shown in Figure 4.17, was solutioned at 1600°C compared with 1300°C for Alloy 4 and the grains are, therefore, larger for this alloy. The alloy showed no precipitation on aging at 1000°C, following the solution treatment, however there appears to be some precipitation in the direct aged structure. The material for mechanical testing will be solution treated at 1300°C to reduce grain growth and aged at 1000°C.

### **Alloys 19 and 20**

Alloys 19 and 20 were designed to include all of the elements which have been shown in past studies (1) to improve the oxidation resistance of Nb base alloys.

The microstructures for Alloy 19, 37Nb-30Ti-15Cr-15Al-3Si, are shown in Figure 4.18. The grain size in the solution treated condition was relatively fine and appears to result from the presence of the primary phases present in the alloy during the solution treatment. Aging of the solution treated material at 1000°C / 24h results in the transformation of the matrix to a fine plate structure. Direct aging of the alloy, also at 1000°C / 24h, following the forging gives a similar matrix and primary phase structures to these seen in the solution and age conditions.

Alloy 20, 37Nb-30Ti-15W-15Al-3Si, is the same composition as Alloy 19, but has W substituted for Cr. The microstructure, shown in Figure 4.19, consists of the finest grain size seen in any of the alloys following the solution treatment. The primary phases appear to be responsible for the fine grain size although the presence of the W may act to slow grain growth by reducing the overall diffusion rate in the alloy. Aging the alloy at 1000°C / 24h resulted in the formation of a dispersion of fine precipitates, however the entire matrix was not transformed, as was seen in Alloy 19. Direct aging of the as-forged structure results in more precipitation than in

the solution and age condition, presumably because of the higher level of retained deformation. The grain structure in the direct age alloy was elongated, similar to the as-forged specimen.

Based on the results of these evaluations of the response of the material to processing and heat treatment, a final heat treatment was chosen for each alloy and is given in Table 4.3. For each alloy the direct aged structure resulted in either an elongated grain structure or a bimodal distribution of grain sizes. Therefore, the solution and age condition was chosen for each alloy.

#### 4.4 Results of Microstructure on Mechanical Properties

The results of mechanical testing are shown in Table 4.4. Because of the small size of the pancake forgings, only one test was performed for each alloy/processing/test condition combination.

The tests which were attempted were three tensiles, at 21°C, 870°C, and 1095°C, and two creeps at 870°C / 140MPa, and 1095°C / 25MPa. These creep conditions were reduced for some of the materials, as shown in Table 4.4, based on the results of the tensile tests. Some tests were not performed either because of problems with the specimens or it was not possible to obtain sufficient specimens from the pancake.

#### Alloy 2

Yield strength data could not be determined at any temperature since the alloy never reached 0.2% offset. The elongations shown in Table 4.4 were determined by placing the specimen pieces together and measuring an elongation, and therefore are not as accurate as the elongations determined with the extensometer.

#### Alloys 3, 4, 5, and 6

None of these alloys were ductile enough at room temperature to achieve 0.2% elongation and therefore, only yield strength data at elevated temperatures is shown in Figure 4.20. The only yield strength data obtained for Alloy 4 was at 1095°C. As illustrated in the figure, Alloy 6, which has the highest level of Cr addition and the lowest Nb to Ti ratio, has the lowest yield strength at both elevated temperatures, while Alloy 5, which has the highest Nb to Ti ratio and the lowest level of Cr addition, has the highest yield strength at both temperatures. Comparing Alloy 3 with Alloy 6 and Alloy 4 with 5, such that similar Cr levels are being compared, indicates that for the same amount of Cr in an alloy the higher Nb/Ti alloys have higher strength at elevated temperatures. It should be remembered however that the grain size for each of these alloys was different and that the strength would be affected by grain size. Since the finer grain

size, Alloys 3 and 6, should give a higher strength, the difference in mechanical properties may have been larger if similar grain sizes had been compared. The determination of the effect of the variables grain size, Nb/Ti ratio and Cr level would have to be performed to further understand these alloys.

In order to compare these alloys to present Nb base alloys, the conventional Nb alloy Cb752 was chosen. Cb752 contains 10W and 2.5Zr in weight percent and is a solid solution strengthened alloy. To compare the present alloys to Cb752, the ultimate tensile strength for alloy Cb752 is included with the ultimate tensile strength data in the plot in Figure 4.21. From this plot it can be seen that all of the alloys developed in this study have strengths which are greater than Cb752 at temperatures below 900°C and that it is not until temperatures of 1050°C are reached that Cb752 is superior to all alloys. This curve is not density corrected.

The 870°C / 140MPa time to rupture ranged from 4.6 to 56.2 hours while the 1095°C / 25MPa time to rupture ranged from 19.7 to 35.7 hours. Alloy 5 had the best creep resistance at 870°C, while the alloys were roughly similar at 1095°C. The fine grain size, low Nb / Ti ratio and lack of a precipitate in Alloys 3,4, and 6 may have resulted in the lower creep resistance compared to Alloy 5 which had a coarse grain size, high Nb / Ti ratio and an acicular precipitate, all of which would be expected to improve the creep resistance.

#### **Alloys 7, 8, 9, and 10**

The yield strength versus temperature of these four alloys should be compared to that of the baseline Alloy 4. These alloys exhibit yield behavior at room temperature and 870°C, whereas Alloy 4 did not exhibit yield at either temperature. The finer grain size exhibited by Alloys 7-10 may be responsible for the improved ductility compared to Alloy 4. The ultimate tensile strength of Alloys 7-10, Figure 4.22, was similar to Alloy 4 at both elevated temperatures.

A comparison of Alloys 8 and 9, which compare similar base alloys, except with a 3% C addition in Alloy 8 and a 3% Si addition in Alloy 9, indicates that on a per atom basis the C addition provides more strengthening than does the Si addition at elevated temperature while the Si provides higher strength at room temperature. However, at all temperatures the Si containing alloy had a higher elongation to fracture than did the C containing alloy. Again, it is difficult to separate out the effects of grain structure from composition since the Si containing alloys also had a finer grain size than the C containing alloys. This finer grain size may have resulted in higher strength and ductility for the Si containing alloy. It should be pointed out that these differences in strength are very small and may have been within the statistical distribution of strengths from these alloys.

A study was undertaken to determine the failure mechanism in Alloy 10. The study was to determine whether the primary phase had a role in the ductility. Longitudinal cross section specimens were prepared which showed the fracture surface and the microstructure through the gauge section. Using this method it is possible to look for fractures which have occurred in the material away from the fracture surface prior to final fracture. A backscattered SEM micrograph of the microstructure in the gauge section is shown in Figure 4.23. It can be seen that the primary phase cracked prior to the final fracture. EDS analysis indicated that the primary phase was rich in Si. The cracks in the primary phase are arrested by the matrix, indicating the ductility of the matrix. Therefore, it appears that the primary phase is reducing the ductility of the alloy. It is expected that this correlation would be the same for all of the Alloys 7-10. Based on this study the composition of the B alloy was altered for scaleup alloys by reducing the amount of Si in the alloy. The reduction in Si should result in a reduction in primary phase which may result in a coarser-grain size, but may also reduce the number of fracture initiation sites.

Similar to the Cr containing alloys it was desirable to compare the data obtained in this effort with other Nb base alloys. Thus, the ultimate strengths for each of the alloys was compared to Cb752 in Figure 4.24. From these plots it again appears that the alloys developed in this effort have higher strengths than Cb752 up to temperatures of around 1000°C.

The 870°C/140MPa time to rupture was slightly higher for all of these tests than it was for the base, Alloy 4. The time to rupture was roughly the same for all four of these alloys. The similarity in time to rupture was to be expected based on the similarity between the tensile properties and microstructures.

#### **Alloys 11, 12, 13, and 14**

The aim and actual compositions for these four alloys are given in Table 4.5 from which it can be seen that the alloys are very close to their aim compositions. As shown in table 4.4, Alloy 12 was stronger than Alloy 11 at room temperature. All of these alloys were very weak at 1095°C and would not be considered for the very highest temperatures. Alloys 11 and 12 exhibited good ductilities at room temperature while 13 and 14 were brittle at both 20°C and 870°C. The brittleness observed in Alloys 13 and 14 is presumably associated with the large volume fraction of coarse primary phase which is presumably brittle. The ductility observed in these alloys suggests that the maximum amount of Al which can be added to a Nb-Ti alloy with a Nb/Ti ratio of about 1, while retaining ductility is between 15 and 20 atomic percent.

The creep conditions originally selected for these alloys were 650°C / 175MPa. These conditions were selected based on the low tensile properties of the alloys at higher temperatures and to provide a comparison with conditions which have been used on titanium aluminide materials. The alpha-2 and orthorhombic materials have times to 0.2% creep of approximately 10-40 hours



for these conditions. The results for Alloys 11 and 12 showed times to 0.2% creep of approximately 80-100 hours. The stress was increased to 200 and 240 MPa before the test was stopped at 900 hours. This creep resistance was much better than expected from these alloys. Alloys 13 and 14 did not show as good creep resistance at 650°C but may have had problems because of their poor ductility. At 870°C all alloys showed long times to failure for the stress used.

#### **Alloys 15, 17, 19 and 20**

Alloy 15 exhibited good strength at all temperatures tested, and had a strength similar to that of Cb752 at 1095°C. The ductility of the alloy was low at room temperature and 870°C. Alloy 15 had creep resistance similar to other alloys at 870°C but had the longest life for the 1095°C test. This alloy appears to be the closest to the conventional Nb alloys in tensile strength but it still lags those alloys in creep strength.

Alloy 17 had both ductility and oxidation problems at the elevated temperatures. This alloy was based on Alloy 5 but with a substitution of 20% Ta for the 20% Ti in Alloy 5. However, because of the lack of specimens and failure to reach 0.2% yield the actual yield comparison could not be made. A comparison of the UTS for the alloys does show an improvement in strength for Alloy 17 over Alloy 5.

Good tensile tests on Alloy 19 were only achieved at 1095°C. The alloy had low strength at that temperature. Because of the similarity in the tensile properties of Alloy 19 to Alloys 11 and 12 the creep testing was done using the lower set of conditions used for those alloys. The only valid creep data was obtained for the 870°C test which exhibited data very similar to the Al containing Alloys 11-14.

Two out of three tensile specimens for Alloy 20 broke during mounting. The tensile test at 20°C failed before reaching yield, therefore, Alloy 20 did not have a valid tensile test. The problems with tensile testing indicate that the alloy has low ductility, at least at room temperature. The one creep specimen at 870°C had the longest life of any of the alloys.

#### **4.5 Results of Oxidation Testing**

##### **Background**

The oxidation resistance of Nb-base alloys is a concern since layered, porous unadherent scales form in oxidizing environments at elevated temperatures. This type of oxide leads to rapid metal loss and reduced mechanical properties. The poor oxidation behavior of Nb-base alloys can be understood if pure Nb is considered.

The oxidation of pure Nb exhibits two stages. The first stage results from an oxide based on NbOx, NbO and NbO<sub>2</sub> that grows parabolically with time. This stage is not the problem as protective behavior is observed. The second stage is breakaway or linear oxidation that is associated with Nb<sub>2</sub>O<sub>5</sub> formation (3). The reasons why Nb<sub>2</sub>O<sub>5</sub> causes poor behavior could be any of the following: 1)  $\sqrt{VNb_2O_5}/\sqrt{VNb}=2.68$ ; 2) a stable monoclinic structure for Nb<sub>2</sub>O<sub>5</sub>; and 3) Nb<sub>2</sub>O<sub>5</sub> is a poor oxygen diffusion barrier. The time at which the transformation from the parabolic to linear stage occurs decreases with temperature. The oxidation rate of pure Nb is so high at ~1200°C and ~1atm O<sub>2</sub> that combustion can occur. In addition to scaling, the high solubility of oxygen in Nb can lead to interstitial embrittlement. The poor oxidation behavior of Nb requires that alloying or coating be considered

Alloying has been shown to improve the oxidation resistance of Nb. In an early binary alloy study, a Ti addition to Nb was the most effective way to reduce oxidation and oxygen dissolution (4). Other additions that had some benefit were Cr, Mo, V and Zr. Although these additions slowed the oxidation rate, it was clear that better protection could be obtained by forming continuous Al<sub>2</sub>O<sub>3</sub> or SiO<sub>2</sub> scales on Nb-alloys. Chromia scales are not an alternative as they volatilize at high temperature and Nb and Ti oxides are more stable. Silica can be formed by producing silicide coatings on the surface of the alloy, however, these coatings crack under repeated use. A more workable solution might be alloying to form Al<sub>2</sub>O<sub>3</sub> scales as is discussed below.

In mapping the oxidation behavior of the Nb-Al system, it is found that NbAl<sub>3</sub> can form an Al<sub>2</sub>O<sub>3</sub> scale upon exposure to high temperature oxidizing environments. At intermediate temperatures (760-870°C), however, NbAl<sub>3</sub> spalls and pests. A GEAE study showed that Ti added in amounts greater than 25 weight percent could stop spallation and pesting. Other elements were tried in the study and the best composition studied was Nb-25Ti-47Al-11Cr-0.4Si (5). In a follow on study, it found that a Ti-Al alloy with a maximum of Nb in solution (Ti-50Al-18Nb) had the best resistance to oxidation at 1370°C (6). Chromium additions to Ti-50Al-18Nb reduced spallation and allowed alumina to form at lower temperatures (1240°C), but reduced the mechanical properties and melting point. The oxidation resistance of these alloys decreased between 1000-1300°C due to the formation of a mixed TiO<sub>2</sub> + Al<sub>2</sub>O<sub>3</sub> scale similar to what has been observed in more recent work on gamma Ti-aluminides (7). This early GEAE work indicated that Nb-Ti-Al-Cr alloys might be useful.

A more recent study was directed at the possibility of making Nb-alloys alumina formers (8). In this study, elements that affected the transition from internal to external oxidation were added to Nb-Al binaries. Some elements added were: 1) V, Si, Ti, Ru, Re, Mn, Cr, Mo and W to decrease oxygen solubility; 2) Hf, Zr, Ti, V and Cr to decrease oxygen diffusivity; and 3) Ti, Fe, Cr, V and more Al to increase the diffusivity of Al. These workers found that Nb-Ti-Al

alloys could form alumina in air at  $T > 1400^{\circ}\text{C}$ . Titanium stabilized the bcc phase which increases Al diffusivity and solubility. The best alloys in this study had compositions near Nb-25Ti-37Al-3Cr-4V-5Si and could form alumina in air at temperatures as low as  $1100^{\circ}\text{C}$ . At temperatures lower than  $1100^{\circ}\text{C}$ , nonprotective oxides formed and linear oxidation rates were observed.

In the current study, the oxidation behavior of developmental Nb-Ti base alloys at temperatures between  $760$  and  $800^{\circ}\text{C}$  were examined in conjunction with mechanical properties. This is a critical temperature range for uncoated Nb-alloys since less protective Nb and Ti-oxides are the only defense against oxidation. The specimens examined were rendered from the forged pancakes which were also used to produce the mechanical property specimens. The surfaces were prepared with fine 600grit SiC abrasive and ultrasonic cleaning in a solvent. The first cyclic oxidation test was performed in a low velocity oxidation rig at  $800^{\circ}\text{C}$  in burnt natural gas and has been previously described (9). The second cyclic oxidation test was performed in static air in a CM Rapid Temp furnace. The samples were grit blasted, cleansed in solvent and placed into the furnace inside high purity 50ml alumina crucibles. The test consisted of a 5-minute heat up from  $28^{\circ}\text{C}$  to  $760^{\circ}\text{C}$ , an isothermal hold at  $760^{\circ}\text{C}$  for 1hr, followed by a fan quench to  $28^{\circ}\text{C}$  for 10 minutes. This cycle was repeated 201 times with microstructural and weight change data taken every 20hr. In this second test, emphasis was placed on comparing the developmental Nb-Ti alloys to other alternative materials like Cb-752, alpha-2 (Ti-24.5Al-12.5Nb-1.5Mo), gamma (Ti-48Al-2Cr-2Nb), Beta21S alloy 3899-3, which is an experimental Nb alloy containing Ti, Al, Cr, V, Hf, and René 41.

## Results and Discussion

The  $800^{\circ}\text{C}$  low velocity oxidation testing results for most of the alloys are shown in Figure 4.25 and Table 4.6. To make trends in the data more discernible, Figure 4.26 is a bar chart summarizing kinetic and microstructural observations on selected alloys. Alloys that showed large weight losses in short times like WC 3009, CB 752 and Alloy 15 had little indication of a case layer under the oxide scale. In these systems, external oxide formation or spallation was more rapid than interstitial dissolution. In 3899-3, Alloy 12 and Alloy 9, only moderate weight changes after 140 hours were observed. The external oxides on these alloys were adherent enough during thermal cycling to allow interstitials to dissolve into the substrate. These behaviors resulted in the cyclic oxidation kinetics isolated in Figure 4.27. In order to compare the Nb-Ti alloys with other classes of high temperature materials another bar chart was made in Figure 4.28. The chart shows that developmental Nb-Ti alloys represent a compromise between brittle oxidation resistant systems like NiAl or ceramic matrix composites (CMC) and systems with poor oxidation resistance like carbon/carbon or Cb 752. The individual behavior of the samples will be discussed in the following paragraphs according to their composition.

The Ni-Cr superalloy, René 41, was more oxidation resistant than the Nb-alloys. The René 41 exhibited a continuous chromia scale during oxidation which resulted in slow oxidation kinetics with no spallation. Figure 4.29 shows a cross section of René 41 after testing. Some TCP precipitation and grain boundary carbides are observed as well as a  $1\mu\text{m}$  continuous external scale.

The commercial Nb alloys, Cb 752 and WC 3009, showed oxide and metal spallation at short times. The Cb 752 formed white, unadherent layered scales resulting in a loss of  $138\text{mg}/\text{cm}^2$  after only 5 hours of testing. Figure 4.30 shows the structure of Cb 752 after oxidation. The grain size of the alloy was about  $20\mu\text{m}$ . The WC 3009, shown in Figure 4.31, was comparatively better losing only  $18.5\text{mg}/\text{cm}^2$  after 115 hours of testing. The spallation on the WC 3009 occurred as tiny chips on the surface of the alloy. The size of the chips may correlate to the coarse grain size that was observed for the alloy.

Several experimental Nb-Ti alloys with Al+Cr additions were oxidized and displayed good kinetics, one of these alloys was 3899-3 (Nb-37.5Ti-5Hf-5V-5Cr-5Al-0.5Zr-0.3C). Figure 4.32 shows that the external scale ( $\sim 7.5\mu\text{m}$ ) on the sample is smaller than the interstitial case layer ( $\sim 27.5\mu\text{m}$ ) indicating that the scale was adherent. The figure shows a large amount of precipitation at grain boundaries and fine precipitates in the bulk.

The best performing Cr containing Nb-Ti alloy was Alloy 2 which contained 15Mo and is shown in Figure 4.33. The external scale is about  $22\mu\text{m}$  thick with no obvious case. This had good oxidation kinetics, unfortunately the mechanical properties of this alloy are unknown because of difficulties in fabrication.

Figures 4.34-4.37 show cross sections of Nb-Ti alloys containing Cr, Alloys 3-6. These alloys exhibited brown porous, layered, flaky scales that were  $\sim 65\mu\text{m}$  thick. Underneath the external oxide, an equivalently thick interstitial layer is visible. In this layer, there is a volume expansion from interstitial dissolution which cracks second phase precipitates in Alloys 3 and 6 by placing them in tension.

Figures 4.38 and 4.39 show alloys with C additions, Alloys 7 & 8. The micrographs indicate that the oxidation morphology is similar and the major change is the presence of carbide stringers in the alloy. The carbides did not appear to crack like the second phase precipitates.

Alloys 9 and 10 containing Cr+Si also performed favorably in weight gain, although it exhibited a cracked external scale which was  $\sim 30\text{-}35\mu\text{m}$  with a thicker interstitial layer ( $\sim 40\text{-}55\mu\text{m}$ ). The second phase precipitates in the interstitial layer were cracked from volume expansion. These microstructures are shown in Figures 4.40 and 4.41.

The kinetics for Al containing Nb-Ti alloys were misleading because of Nb segregation. The segregation manifested itself as striations of white-yellow oxide indicative of Nb oxidation. Segregation or recrystallization related banding is observed particularly in Alloys 11 and 12. In some cases, the oxide extended through the 3mm diameter pin and created a visible hole. In more typical areas, the scales had a blue color with a white overgrowths and appeared protective. The cross sections of Alloys 11, 12, 13 and 14 are shown in Figures 4.42-4.45. The typical oxide scale on these samples was layered and ~40  $\mu\text{m}$  thick with an equivalently thick interstitial layer.

Figure 4.46 shows Alloy 17 (Cr+Ta) after testing. There is no clear indication of an external scale indicating that spallation is dominating the cyclic oxidation behavior. This would be expected given the large weight loss for the Alloy in Table 4.6 and the metal loss observed at the tip of the sample.

Alloy 19 represents another Al+Cr containing alloy and is shown in Figure 4.47. The layered, porous external scale was ~30 $\mu\text{m}$  thick with a ~10 $\mu\text{m}$  interstitial layer. The alloy contains at least 3 phases in the bulk. This alloy visually appeared to be one of the best for the first 100 hours of oxidation testing, after 100 hours, however, the scale turned brown and spallation was evident.

Alloy 20 was a Nb-Ti alloy with Al+W and is shown in Figure 4.48. The kinetics of this sample were tough to characterize as the pin broke in half. It was not clear if the break was caused by oxidation attack.

#### Oxidation Summary

The Nb-Ti alloys developed here had much better oxidation resistance than the commercial Nb-alloys Cb 752 and WC 3009. Internal work on similar alloys at the same temperature indicates that the better behavior occurs because of mixed niobium and titanium oxides such as (Nb,Ti)O<sub>2</sub> or TiNb<sub>2</sub>O<sub>7</sub> or NbAlO<sub>4</sub> in the case of Al containing systems. These oxides are more adherent and grow more slowly than the Nb<sub>2</sub>O<sub>5</sub> found on the commercial Nb-alloys. The Nb-Ti and Nb alloys, however, do not exhibit levels of oxidation resistance found in a Ni-base superalloy.

#### 4.6 Summary of Screening Alloys

Several of the alloys and alloy families studied in this screening effort show promise for improving the combinations of oxidation resistance and mechanical properties. The families of alloys that are promising are the Nb-Ti-Cr-Mo alloys, Nb-Ti-Cr-Si alloys, and the Nb-Ti-Al alloys. Alloy 19 looked good in oxidation initially but started to spall after 100 hours. Of the promising alloys, the Nb-Ti-Cr-Mo alloys were very difficult to process and additional

investigation, beyond the scope of this contract, is needed to determine improved alloy compositions and process routes. This leaves the Nb-Ti-Cr-Si alloys and the Nb-Ti-Al alloys. These were chosen for study in larger ingots, along with the alloy Nb-32Ti-10Cr-6Al, which was chosen for scaleup previously as a baseline alloy. The Cr-Al and Cr-Si alloys could be the base for future Nb-Ti alloys, while the Nb-Ti-Al is expected to help in developing an understanding of alloys in this system.

Table 4.1 Screening Alloy Forging Conditions

Alloy	Forging Parameters	
	Temperature °C	Crosshead mm/s
1) 31Nb-29Ti-25Mo-15Cr	1300	0.09
2) 31Nb-29Ti-15Mo-25Cr	1300	0.09
3) 50Nb-20Ti-30Cr	1300	0.09
4) 55Nb-30Ti-15Cr	1300	0.09
5) 65Nb-20Ti-15Cr	1300	0.09
6) 40Nb-30Ti-30Cr	1300	0.09
7) 55Nb-28.5Ti-15Cr-1.5C	1300	0.09
8) 55Nb-27Ti-15Cr-3C	1300	0.09
9) 54Nb-28Ti-15Cr-3Si	1300	0.09
10) 53Nb-27Ti-15Cr-5Si	1300	0.09
11) 50Nb-40Ti-10Al	1150	0.9
12) 45Nb-40Ti-15Al	1150	0.9
13) 45Nb-35Ti-20Al	1150	0.9
14) 41Nb-39Ti-20Al	1150	0.9
15) 86Nb-12Cr-2Ni	1300	0.09
16) 80Nb-20W		
17) 65Nb-20Ta-15Cr	1600	0.09
18) 55Nb-30Ta-15Cr		
19) 37Nb-30Ti-15Cr-15Al-3Si	1300	0.09
20) 37Nb-30Ti-15W-15Al-3Si	1300	0.09

Table 4.2 Screening Heat Treatment Conditions

Alloy	Heat Treatment Parameters			
	Solution		Age	
	Temperature °C	Time Hour	Temperature °C	Time Hour
1) 31Nb-29Ti-25Mo-15Cr	1300	4	1000	24
2) 31Nb-29Ti-15Mo-25Cr	1300	4	1000	24
3) 50Nb-20Ti-30Cr	1300	4	1000	24
4) 55Nb-30Ti-15Cr	1300	4	1000	24
5) 65Nb-20Ti-15Cr	1300	4	1000	24
6) 40Nb-30Ti-30Cr	1300	4	1000	24
7) 55Nb-28.5Ti-15Cr-1.5C	1300	4	1000	24
8) 55Nb-27Ti-15Cr-3C	1300	4	1000	24
9) 54Nb-28Ti-15Cr-3Si	1300	4	1000	24
10) 53Nb-27Ti-15Cr-5Si	1300	4	1000	24
11) 50Nb-40Ti-10Al	1150	4	900	24
12) 45Nb-40Ti-15Al	1150	4	900	24
13) 45Nb-35Ti-20Al	1150	4	900	24
14) 41Nb-39Ti-20Al	1150	4	900	24
15) 86Nb-12Cr-2Ni	1300	4	1000	24
16) 80Nb-20W				
17) 65Nb-20Ta-15Cr	1300	4	1000	24
18) 55Nb-30Ta-15Cr				
19) 37Nb-30Ti-15Cr-15Al-3Si	1300	4	1000	24
20) 37Nb-30Ti-15W-15Al-3Si	1300	4	1000	24



Table 4.3 Final Heat Treatment Conditions

Alloy	Heat Treatment Parameters			
	Solution		Age	
	Temperature °C	Time Hour	Temperature °C	Time Hour
1) 31Nb-29Ti-25Mo-15Cr				
2) 31Nb-29Ti-15Mo-25Cr	1300	4	1000	24
3) 50Nb-20Ti-30Cr	1300	4	1000	24
4) 55Nb-30Ti-15Cr	1300	4	1000	24
5) 65Nb-20Ti-15Cr	1300	4	1000	24
6) 40Nb-30Ti-30Cr	1300	4	1000	24
7) 55Nb-28.5Ti-15Cr-1.5C	1300	4	1000	24
8) 55Nb-27Ti-15Cr-3C	1300	4	1000	24
9) 54Nb-28Ti-15Cr-3Si	1300	4	1000	24
10) 53Nb-27Ti-15Cr-5Si	1300	4	1000	24
11) 50Nb-40Ti-10Al	1050	4	700	24
12) 45Nb-40Ti-15Al	1050	4	800	24
13) 45Nb-35Ti-20Al	1150	4	950	24
14) 41Nb-39Ti-20Al	1150	4	950	24
15) 86Nb-12Cr-2Ni	1400	4	1000	24
16) 80Nb-20W				
17) 65Nb-20Ta-15Cr	1300	4	1000	24
18) 55Nb-30Ta-15Cr				
19) 37Nb-30Ti-15Cr-15Al-3Si	1300	4	1000	24
20) 37Nb-30Ti-15W-15Al-3Si	1300	4	1000	24

Table 4.4a; Results Of Creep Testing

Alloy No.	Temperature		Rupture				Comments
			Stress		Time	def.	
			MPa	Ksi	hours	%	
°C	°F						
3	871	1600	138	20	20.2	22.1	
4	871	1600	138	20	16.8	29.1	
5	871	1600	138	20	56.2	15.1	
6	871	1600	138	20	4.6	6.2	
7	871	1600	138	20	19.5	15.6	
8	871	1600	138	20	22.8	18.1	
9	871	1600	138	20	19.2	10.6	
10	871	1600	138	20	24.2	13.4	
11	649	1200	172, 207, 241	25,30,35			Stopped
12	649	1200	172, 207, 241	25,30,35			Stopped
13	649	1200	172	25	90.3	0.44	Broke while remounting
14	649	1200	172	25	1	0.04	
15	871	1600	138	20	21.9	4.1	
17	871	1600	138	20	19.5	1.6	
19	649	1200	172	25			Broke during mounting
20	871	1600	138	20	123.6	8.1	*
* 365 h at 1600°F / 2Ksi before 1600°F / 20Ksi							
3	1093	2000	28	4			
4	1093	2000	28	4	19.7	30.4	
5	1093	2000	28	4	25.3	13.4	
6	1093	2000	28	4	35.7	34.8	
7	1093	2000	28	4	22.2	25.2	
8	1093	2000	28	4	20.7	35.1	
9	1093	2000	28	4	17.4	38.3	
10	1093	2000	28	4	25.6	36	
11	871	1600	28	4	253.8	66	
12	871	1600	28	4	425	28.1	
13	871	1600	28	4	493.6	0.99	
14	871	1600	28, 34, 41	4,5,6			Stopped
15	1093	2000	28	4	47.2	4.5	
17	1093	2000	28	4			No Specimen
19	871	1600	28, 34, 41	4,5,6			Stopped
20	1093	2000	28	4			No Specimen

Table 4.4b; Results Of Tensile Testing at 20°C

Alloy No.	0.2% YS		UTS		Elong %	RA %	Density g/cc
	Ksi	MPa	Ksi	MPa			
2	<0.2% strain		48.4	333.7	2.0	0.3	7.26
3	Thread failure						7.36
4	Thread failure						7.16
5	<0.2% strain		103.4	712.9	0.7	3.9	7.57
6	<0.2% strain		118.9	819.8	1.5	radius	6.95
7	103.2	711.6	118.9	819.8	2.7	6.3	7.14
8	106.1	731.6	117.3	808.8	2.5	4.9	7.12
9	111.0	765.3	126.2	870.1	4.4	10.1	7.07
10	115.7	797.8	121.5	837.7	3.0	6.0	6.95
11	87.4	602.6	93.4	644.0	21.7	51.0	6.37
12	125.5	865.3	134.1	924.6	15.1	20.4	6.08
13	Broke during mounting					5.99	
14	<0.2% strain						5.82
15	94.2	649.5	130.7	901.2	4.7	2.0	8.44
17	104.4	719.8	112.6	776.4	3.6	2.9	10.17
19	Thread failure		41.0	282.7			6.10
20	<0.2% strain		26.2	180.6	1.2	1.3	7.91
21	60.0	413.7	82.0	565.4	21.0		9.01

Alloy 21 is Cb752 which is added for comparison.

Table 4.4c; Results Of Tensile Testing at 870°C

Alloy No.	0.2% YS		UTS		Elong %	RA %	Density g/cc
	Ksi	MPa	Ksi	MPa			
2	<0.2% strain		60.1	414.4	2.0	3.9	7.26
3	55.8	384.7	64.9	447.5	1.3	6.2	7.36
4	<0.2% strain		62.4	430.2	3.0	4.0	7.16
5	63.1	435.1	63.5	437.8	2.3	1.7	7.57
6	42.6	293.7	58.3	402.0	6.5	5.6	6.95
7	52.5	362.0	58.4	402.7	4.4	10.4	7.14
8	53.5	368.9	65.8	453.7	5.1	5.5	7.12
9	46.1	317.9	59.3	408.9	8.8	9.4	7.07
10	48.9	337.2	67.7	466.8	5.5	2.1	6.95
11	19.9	137.2	28.5	196.5	45.9	76.9	6.37
12	17.0	117.2	25.1	173.1	51.4	66.7	6.08
13	Broke during mounting						5.99
14	<0.2% strain						5.82
15	59.4	409.6	77.1	531.6	4.1	3.4	8.44
17	<0.2% strain		75.8	522.6	1.9	3.5	10.17
19	<0.2% strain		35.9	247.5	0.6	0.1	6.1
20	Broke during mounting						7.91
21	38.0	262.0	58.0	399.9	10.0		9.01

Alloy 21 is Cb752 which is added for comparison.

Table 4.4d: Results Of Tensile Testing at 1095°C

Alloy No.	0.2% YS		UTS		Elong %	RA %	Density g/cc
	Ksi	MPa	Ksi	MPa			
2	Broke during mounting						7.26
3	15.3	105.5	31.3	215.8	28.2	33.8	7.36
4	15.3	105.5	23.9	164.8	63.0	84.5	7.16
5	22.9	157.9	36.7	253.0	7.5	11.3	7.57
6	10.4	71.7	21.1	145.5	66.0	56.3	6.95
7	19.1	131.7	26.4	182.0	42.6	43.3	7.14
8	18.4	126.9	31.8	219.3	50.6	57.1	7.12
9	15.3	105.5	28.2	194.4	77.2	89.1	7.07
10	14.4	99.3	29.7	204.8	59.8	73.9	6.95
11	4.5	31.0	9.6	66.2	103.9	87.9	6.37
12	4.0	27.6	8.4	57.9	101.9	88.0	6.08
13							5.99
14	6.4	44.1	8.6	59.3	54.9	78.7	5.82
15	35.7	246.2	45.1	311.0	34.5	84.9	8.44
17	<0.2% strain		42.7	294.4	Oxid.	22.5	10.17
19	9.8	67.6	22.7	156.5	77.5	39.2	6.1
20	Broke during mounting						7.91
21	37.0	255.1	43.0	296.5	21.0		9.01

Alloy 21 is Cb752 which is added for comparison

Table 4.5 Compositions For Alloys 11 - 14

Aim Alloy Composition At.%	Measured Composition					
	Aluminum		Niobium		Titanium	
	Wt. %	At. %	Wt. %	At. %	Wt. %	At. %
11) 50Nb-40Ti-10Al	3.9	10.5	66.8	48.9	28.3	40.6
12) 45Nb-40Ti-15Al	5.96	15.2	64.3	45.4	28.9	39.4
13) 45Nb-35Ti-20Al	8.16	19.9	65.1	45.1	26.0	35.0
14) 41Nb-39Ti-20Al	8.36	19.8	60.8	40.9	30.0	39.3

Table 4.6 Summary Of Weight Gains For The Screening Alloys

Alloy	Weight Change/Area mg/cm <sup>2</sup>	Time Hours
1) 31Nb-29Ti-25Mo-15Cr		
2) 31Nb-29Ti-15Mo-25Cr	0.57	140
3) 50Nb-20Ti-30Cr	-0.25	90
4) 55Nb-30Ti-15Cr	1.51	140
5) 65Nb-20Ti-15Cr	1.18	140
6) 40Nb-30Ti-30Cr	-24.80	90
7) 55Nb-28.5Ti-15Cr-1.5C	1.88	140
8) 55Nb-27Ti-15Cr-3C	1.63	140
9) 54Nb-28Ti-15Cr-3Si	2.95	140
10) 53Nb-27Ti-15Cr-5Si	2.81	140
11) 50Nb-40Ti-10Al	-16.81	140
12) 45Nb-40Ti-15Al	-2.50	140
13) 45Nb-35Ti-20Al	-13.10	140
14) 41Nb-39Ti-20Al	1.55	140
15) 86Nb-12Cr-2Ni	-8.40	90
16) 80Nb-20W		
17) 65Nb-20Ta-15Cr	135.20	40
18) 55Nb-30Ta-15Cr		
19) 37Nb-30Ti-15Cr-15Al-3Si	0.36	140
20) 37Nb-30Ti-15W-15Al-3Si	-3.20	40
Cb 752	-278.40	20
René 41	0.03	140
3899-3	2.41	140
WC 3009	-18.51	15

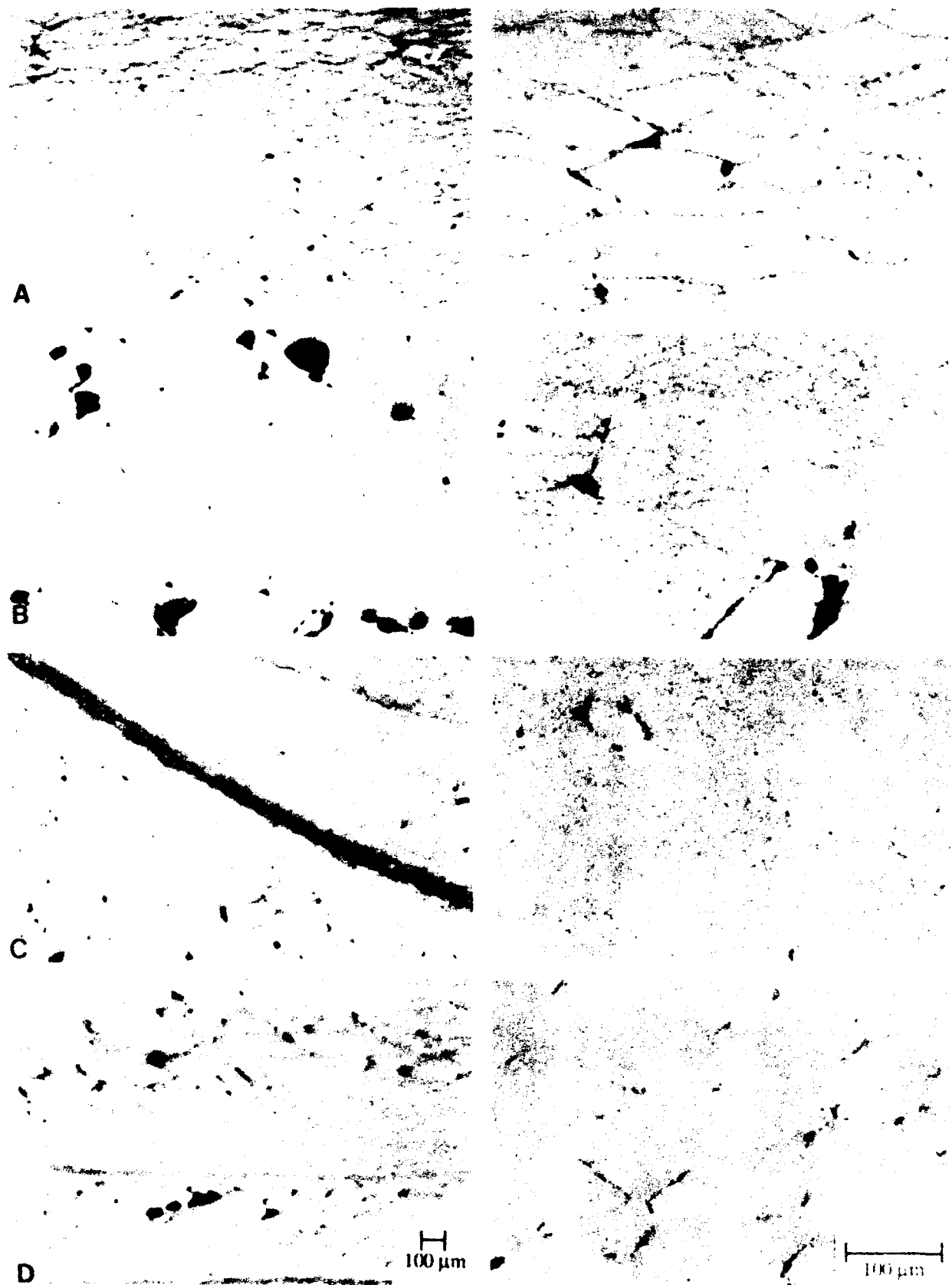


Figure 4.1 Optical micrographs of the microstructure of alloy 2 in the a) as-forged, b) solution treated, c) solution treated and aged, and d) direct aged conditions.



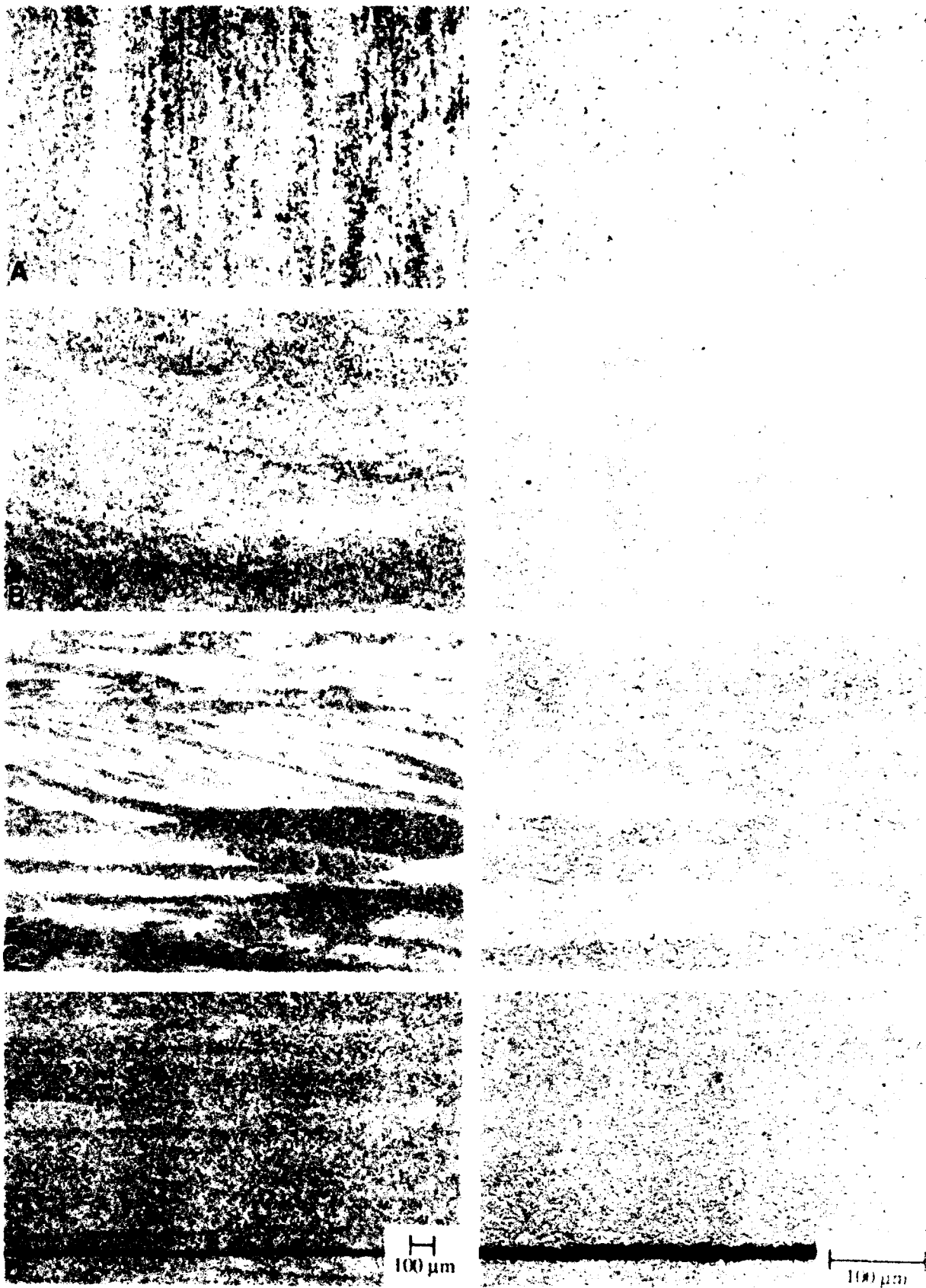


Figure 4.2 Optical micrographs of the microstructure of alloy 3 in the a) as-forged, b) solution treated, c) solution treated and aged, and d) direct aged conditions.

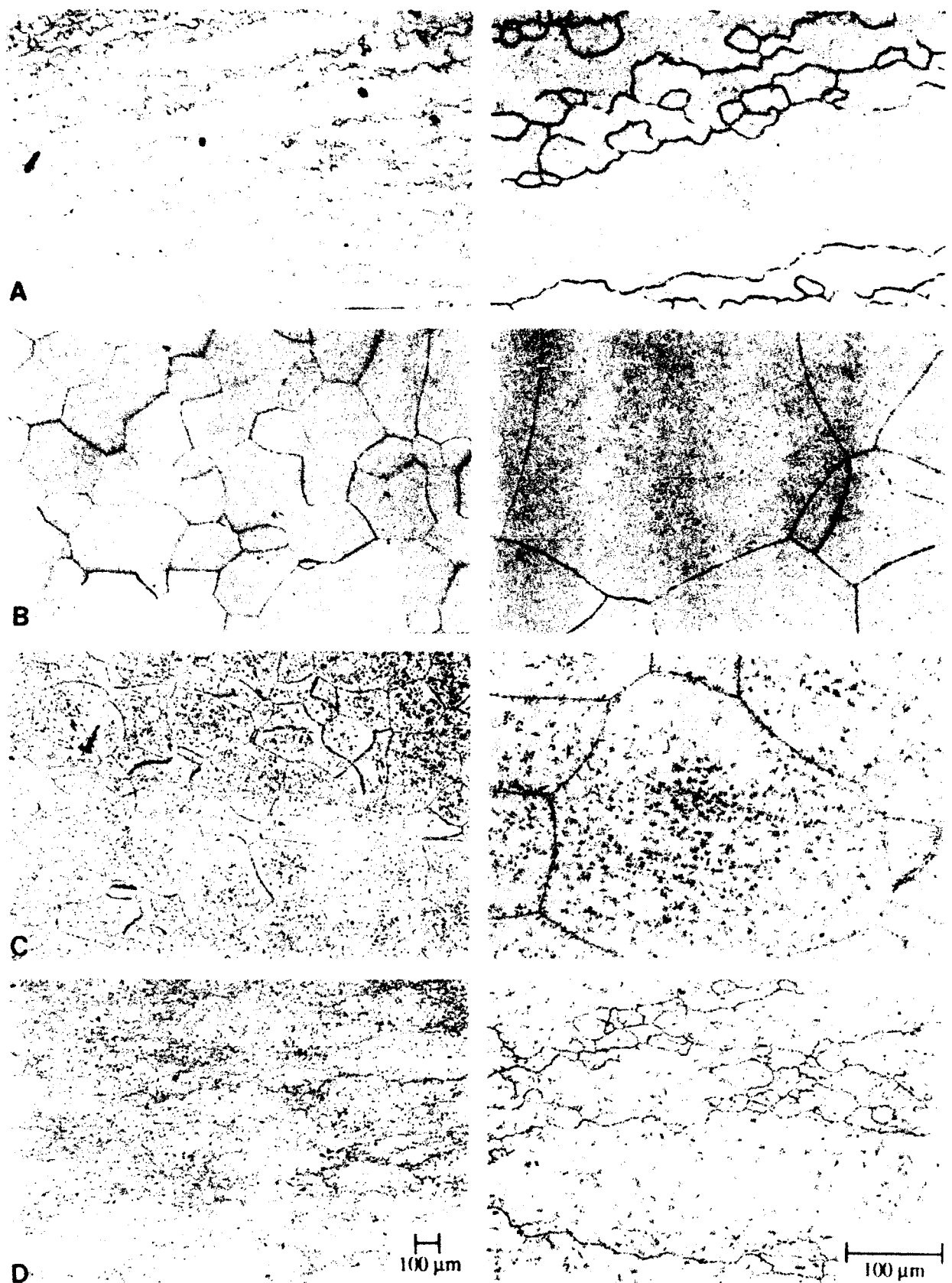


Figure 4.3 Optical micrographs of the microstructure of alloy 4 in the a) as-forged, b) solution treated, c) solution treated and aged, and d) direct aged conditions.

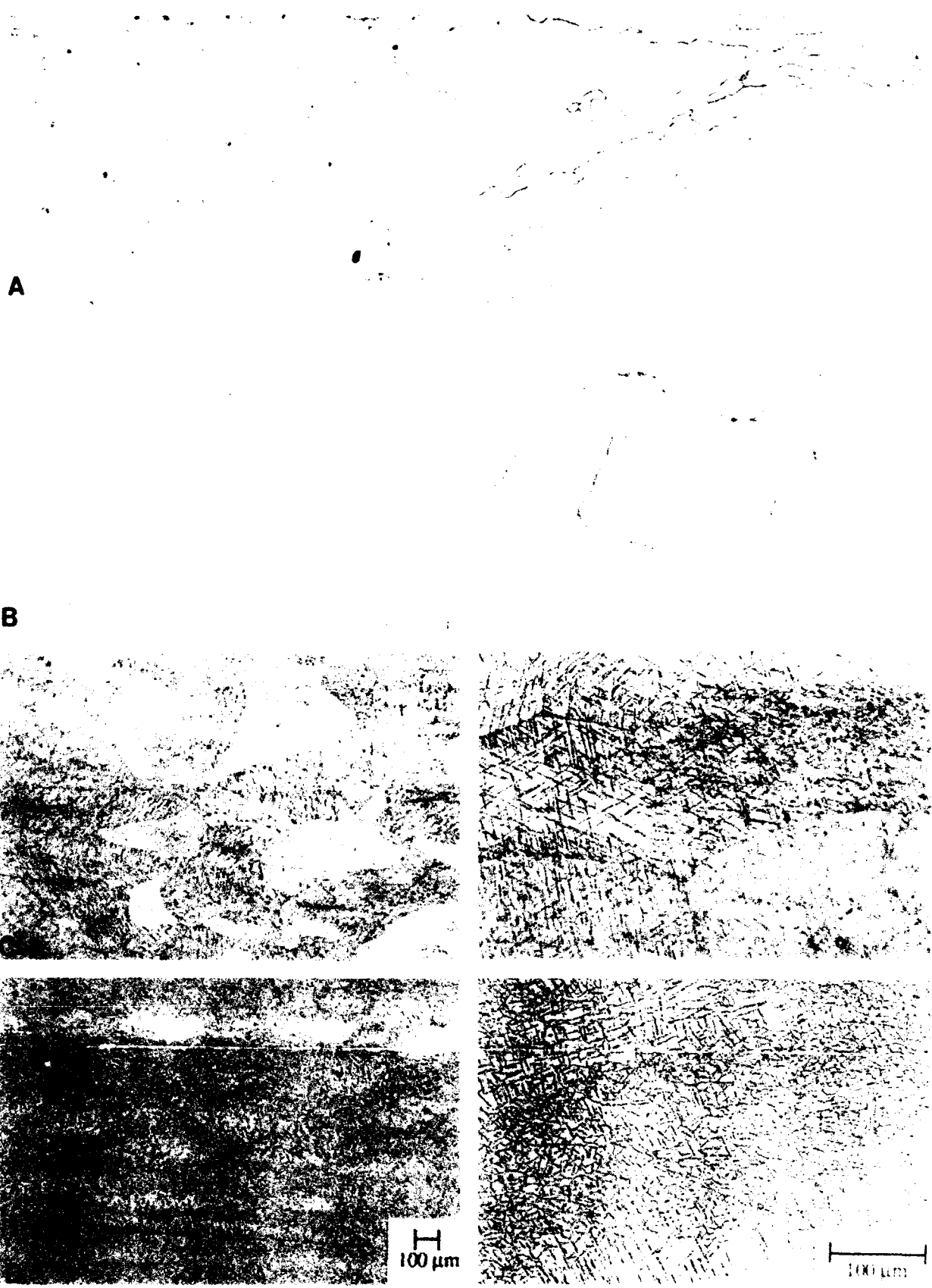


Figure 4.4 Optical micrographs of the microstructure of alloy 5 in the a) as-forged, b) solution treated, c) solution treated and aged, and d) direct aged conditions.

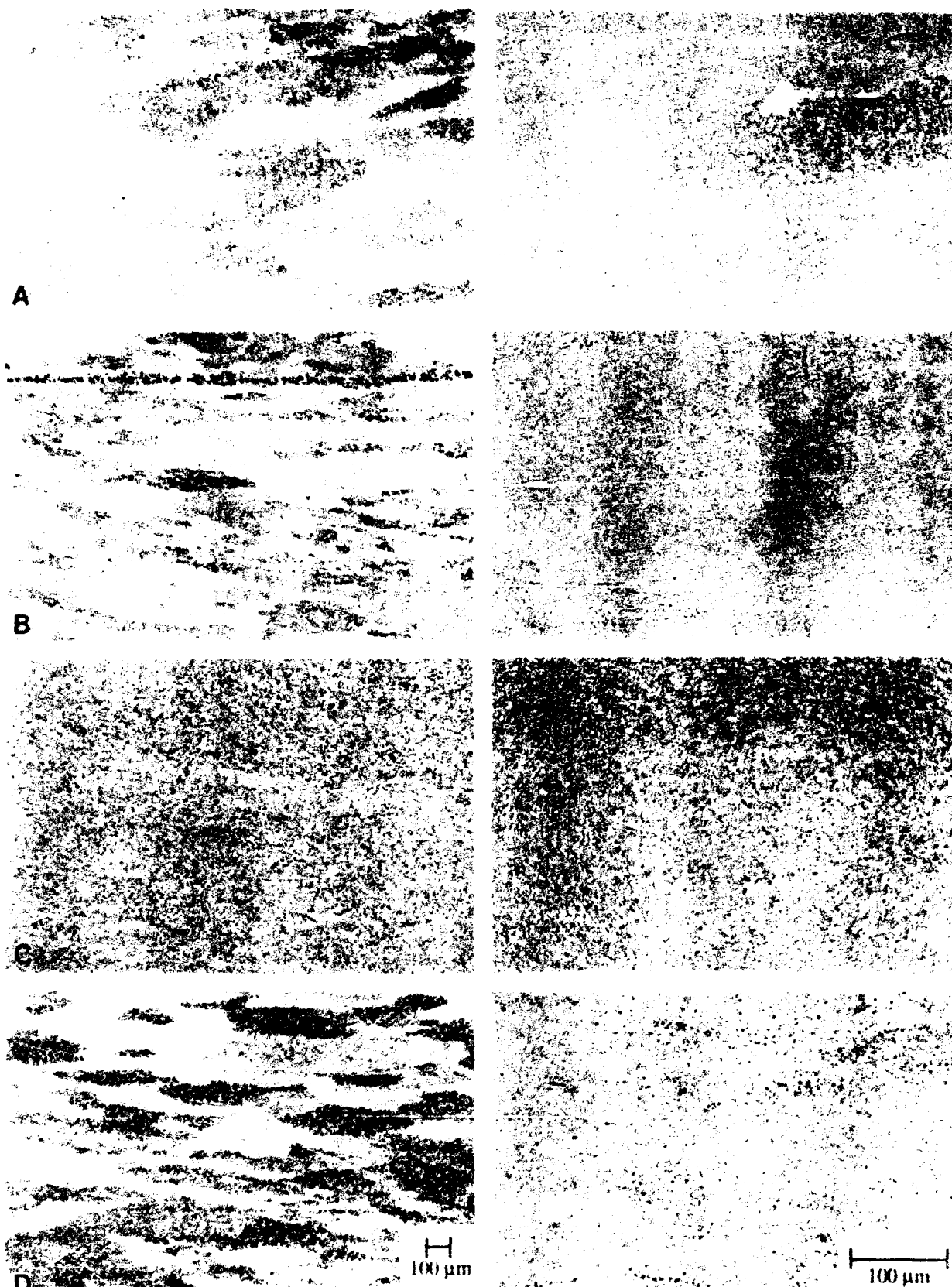


Figure 4.5 Optical micrographs of the microstructure of alloy 6 in the a) as-forged, b) solution treated, c) solution treated and aged, and d) direct aged conditions.

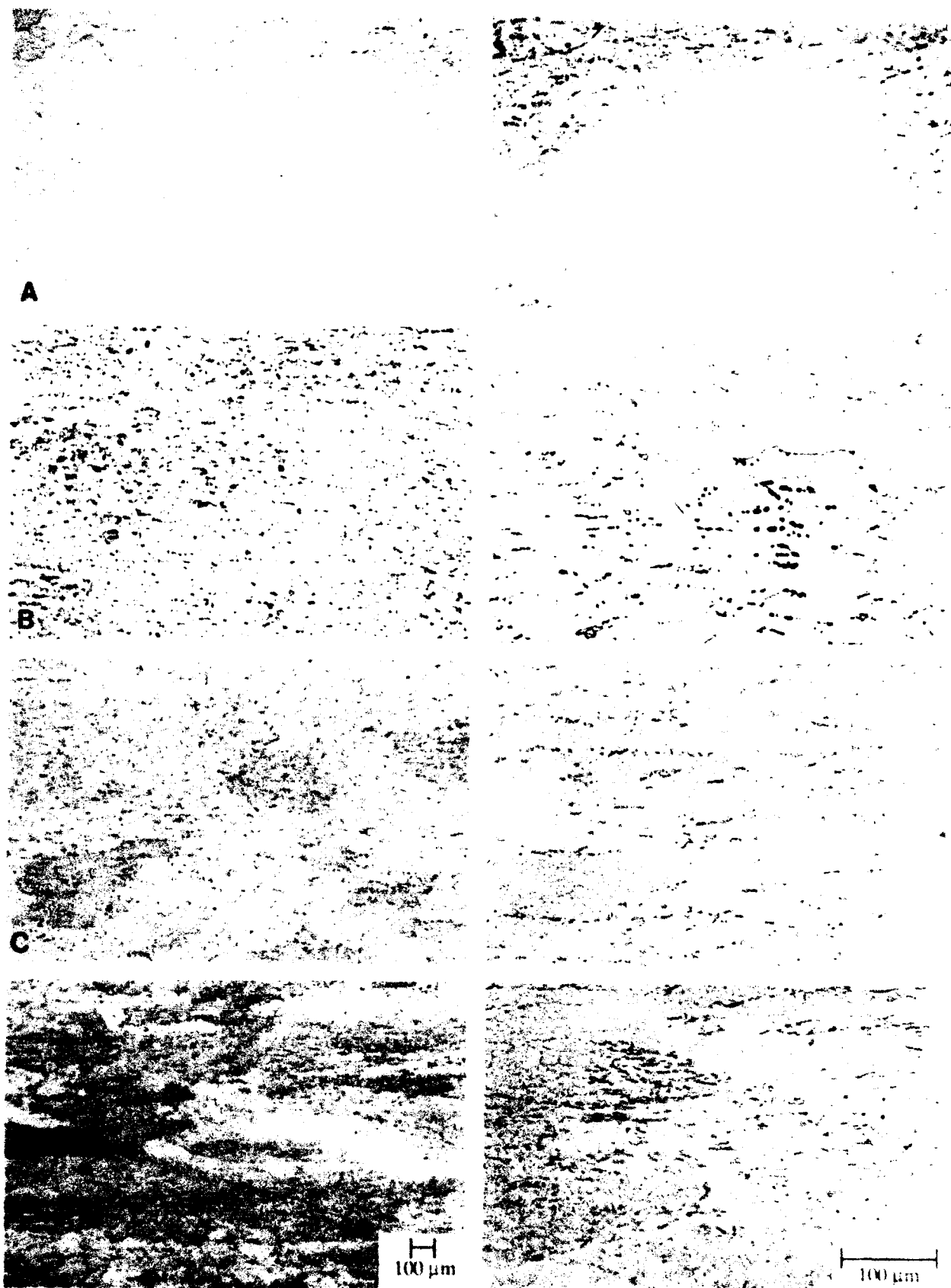


Figure 4.6 Optical micrographs of the microstructure of alloy 7 in the a) as-forged, b) solution treated, c) solution treated and aged, and d) direct aged conditions.

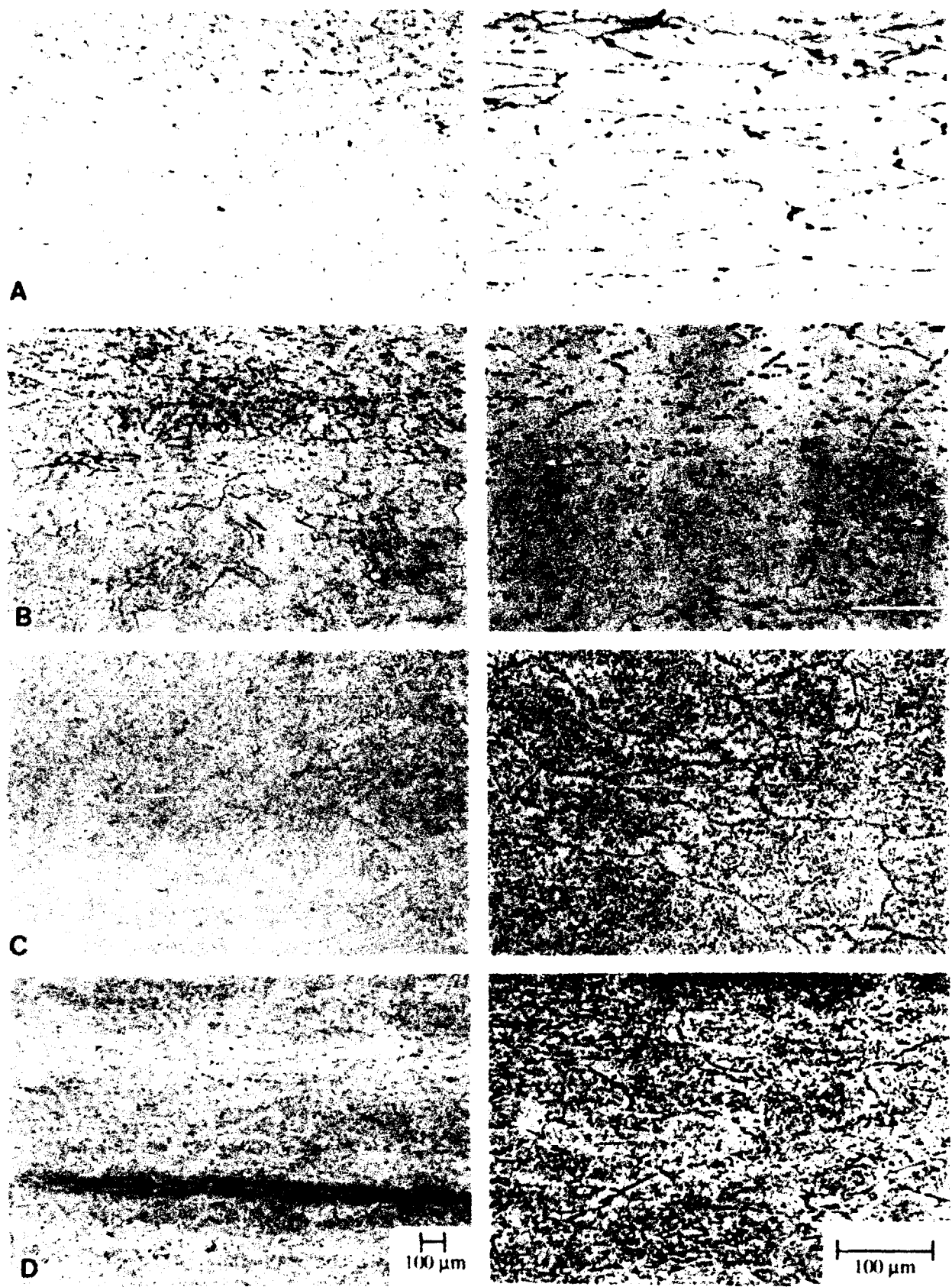
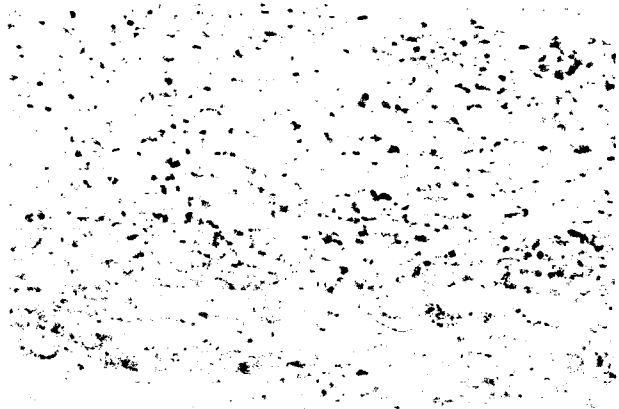
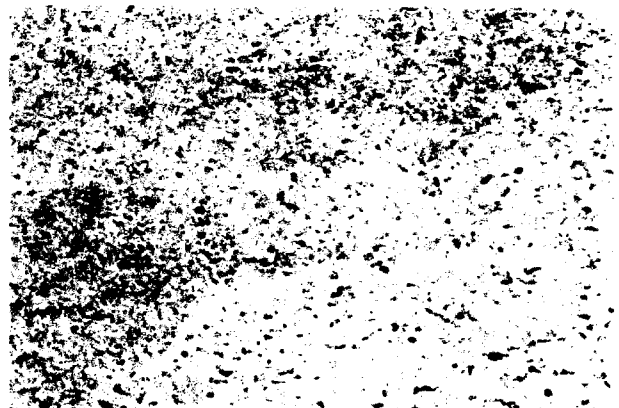


Figure 4.7 Optical micrographs of the microstructure of alloy 8 in the a) as-forged, b) solution treated, c) solution treated and aged, and d) direct aged conditions.

**A**



**B**



**C**

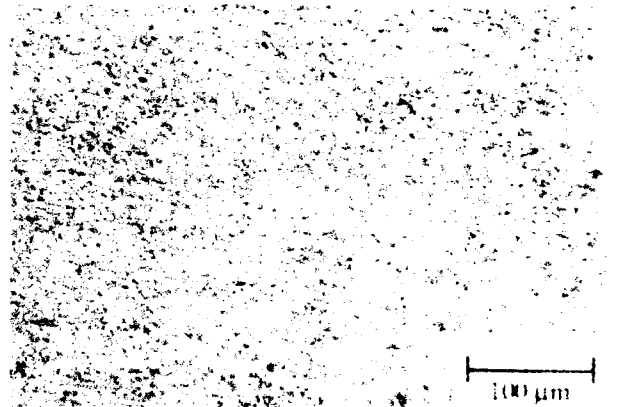
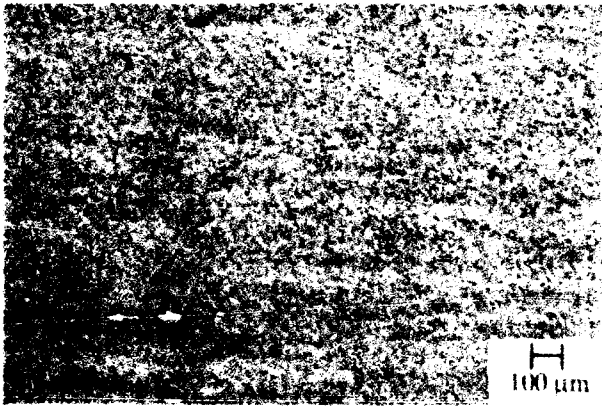


**Figure 4.8** Optical micrographs of the microstructure of alloy 9 in the a) as-forged, b) solution treated, c) solution treated and aged, and d) direct aged conditions.



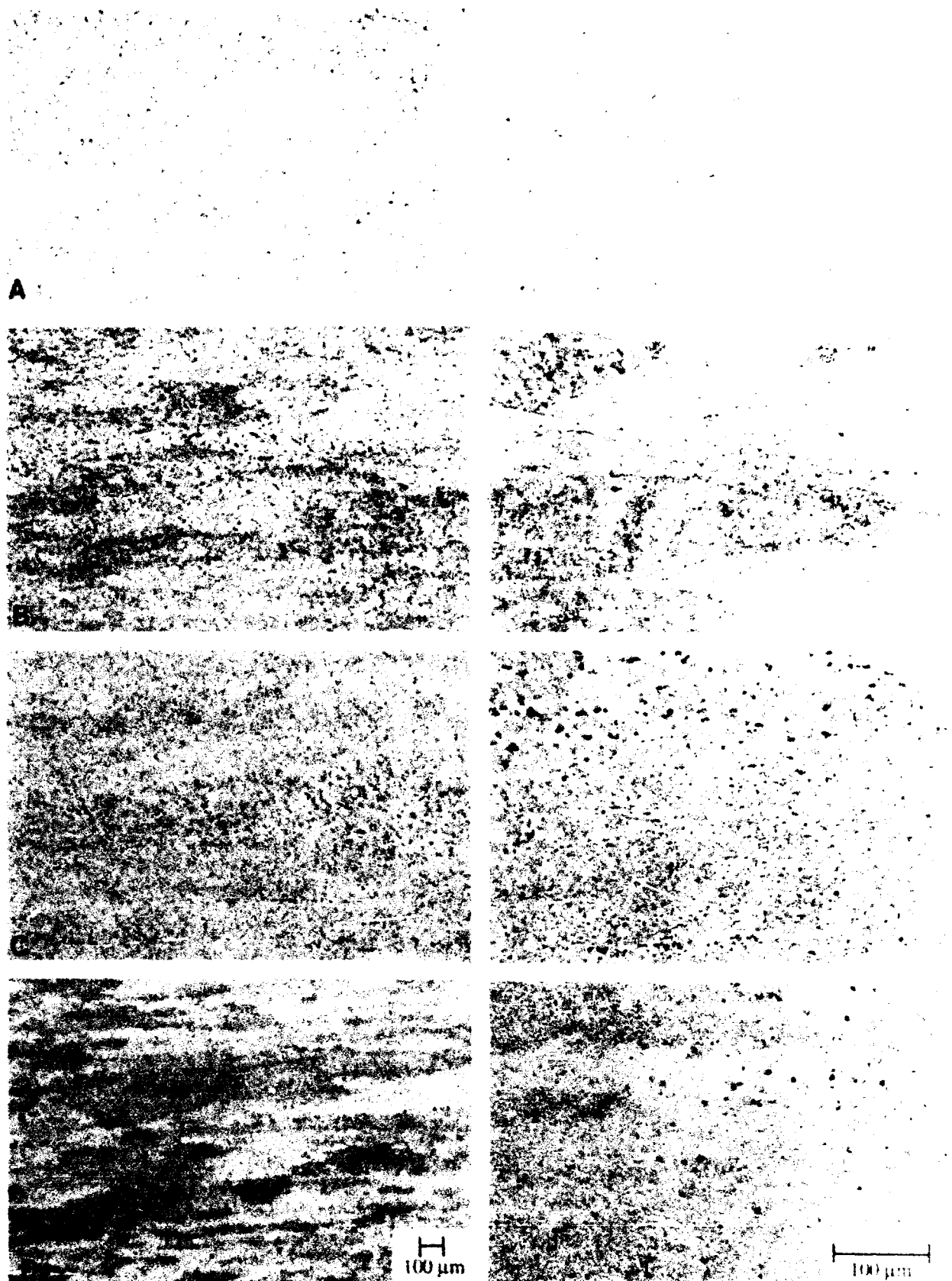
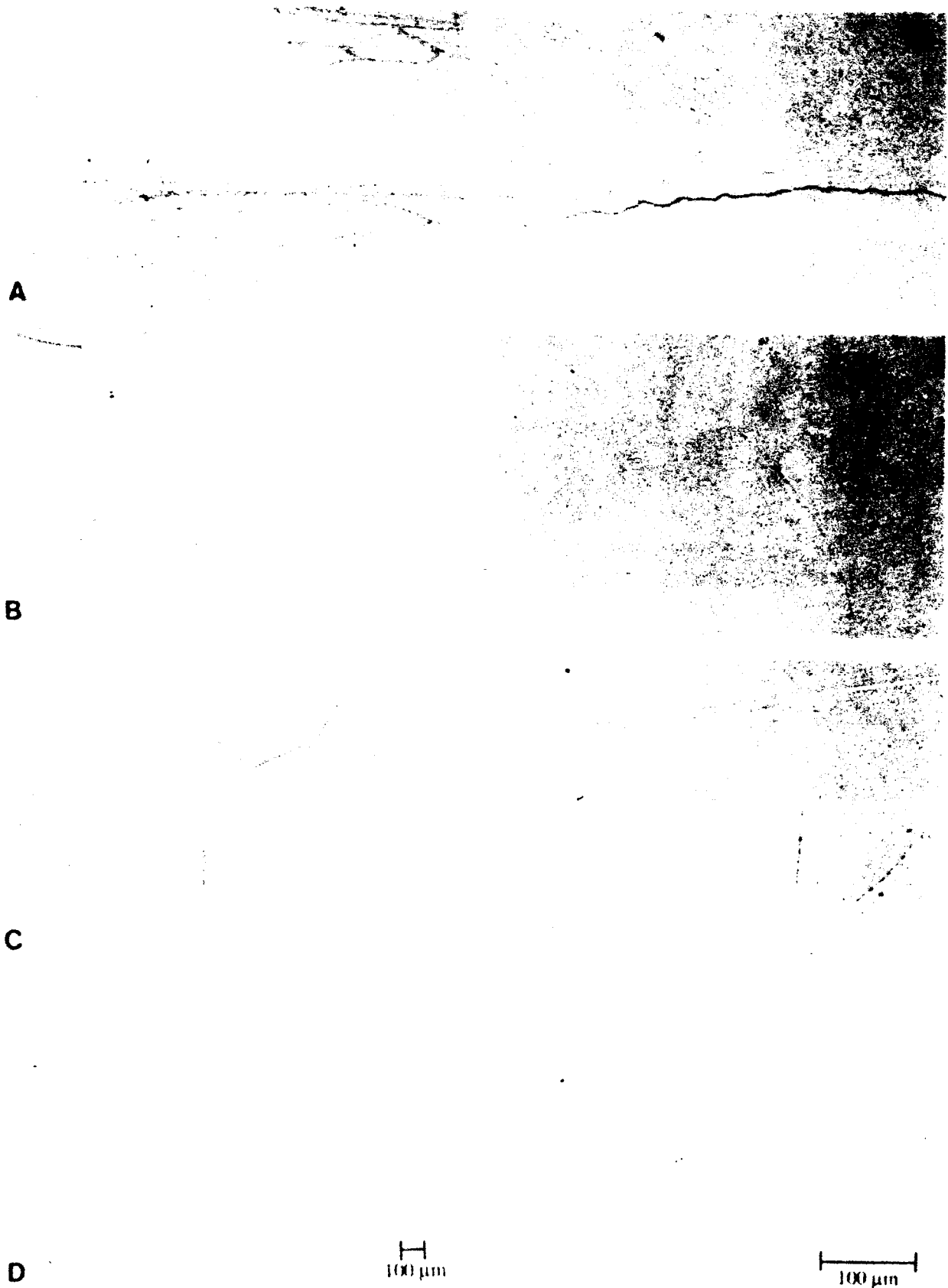


Figure 4.9 Optical micrographs of the microstructure of alloy 10 in the a) as-forged, b) solution treated, c) solution treated and aged, and d) direct aged conditions.





**Figure 4.10** Optical micrographs of the microstructure of alloy 11 in the a) as-forged, b) solution treated, c) solution treated and aged, and d) direct aged conditions.

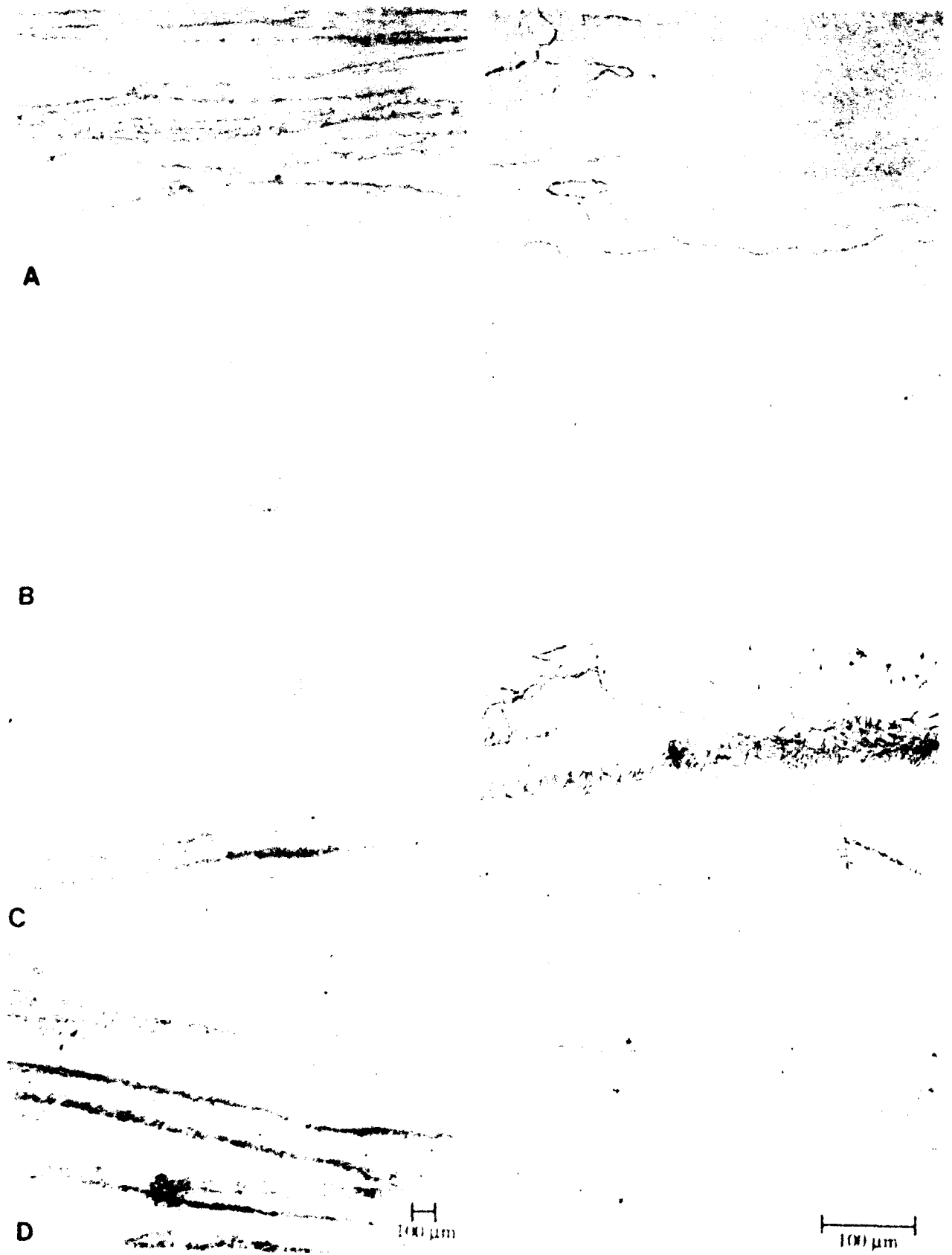


Figure 4.11 Optical micrographs of the microstructure of alloy 12 in the a) as-forged, b) solution treated, c) solution treated and aged, and d) direct aged conditions.

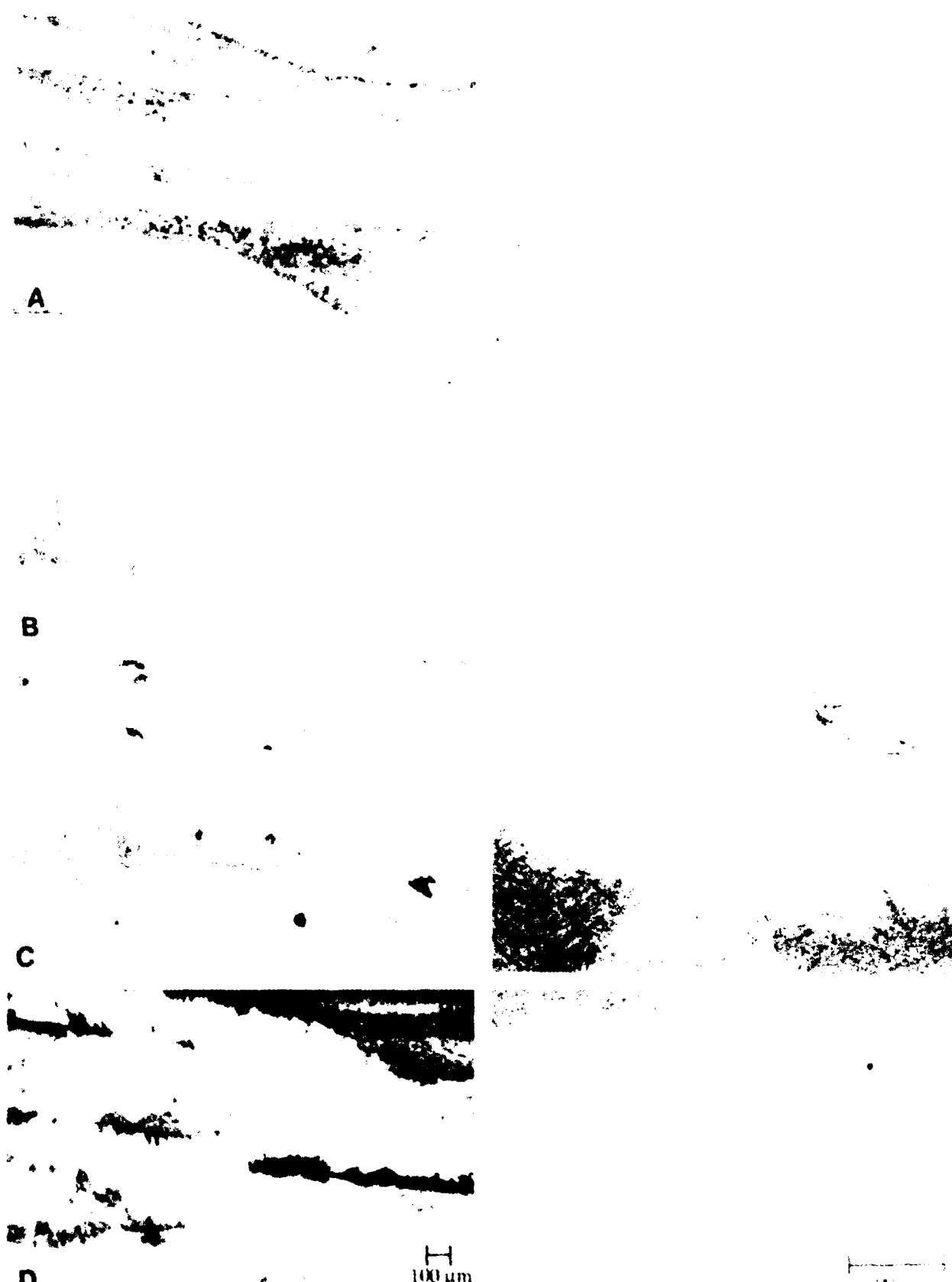


Figure 4.12 Optical micrographs of the microstructure of alloy 13 in the a) as-forged, b) solution treated, c) solution treated and aged, and d) direct aged conditions.

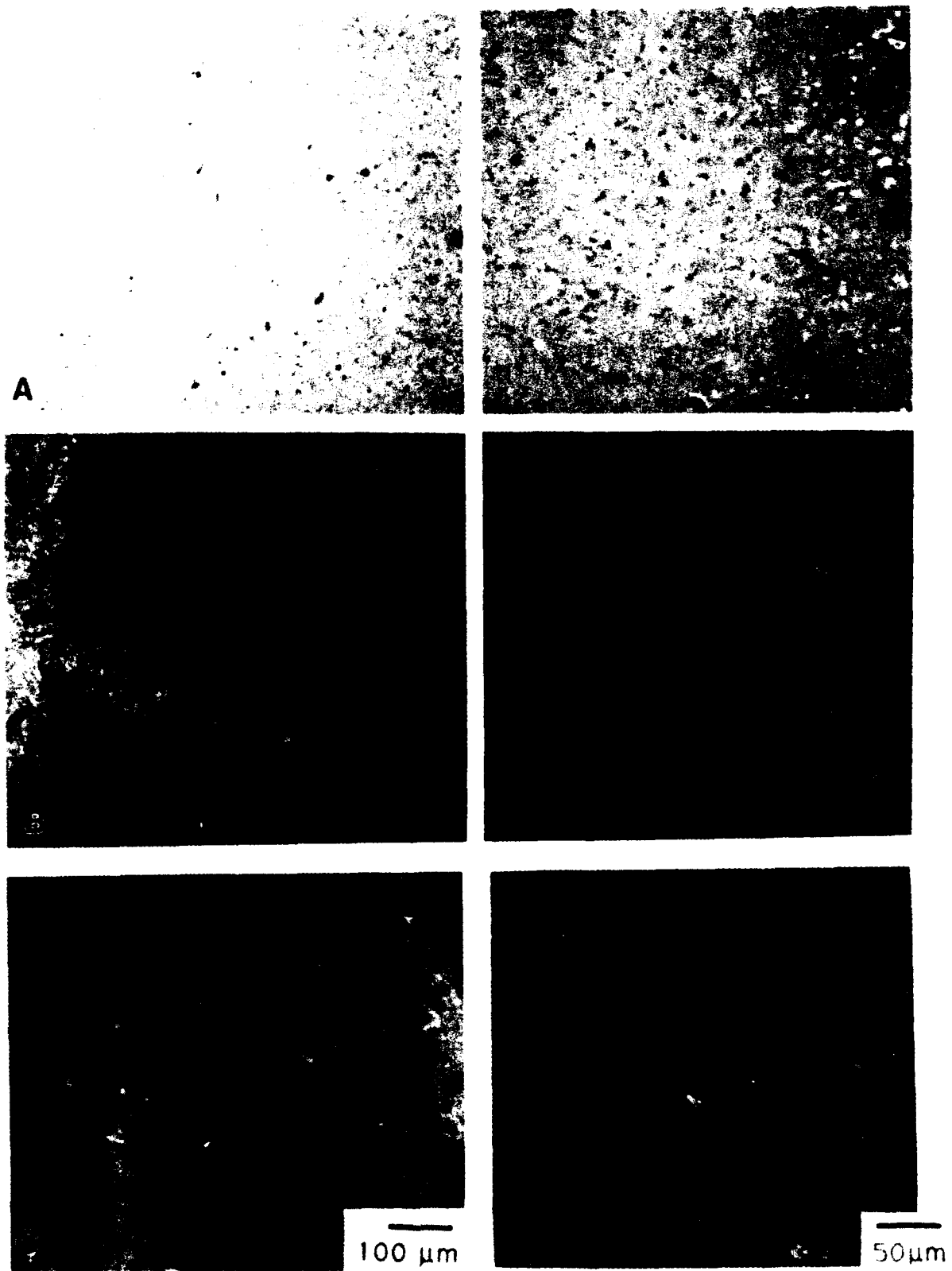


Figure 4.13 Optical micrographs of the microstructure of alloy 14 in the a) solution treated, b) solution treated and aged, and c) direct aged conditions.

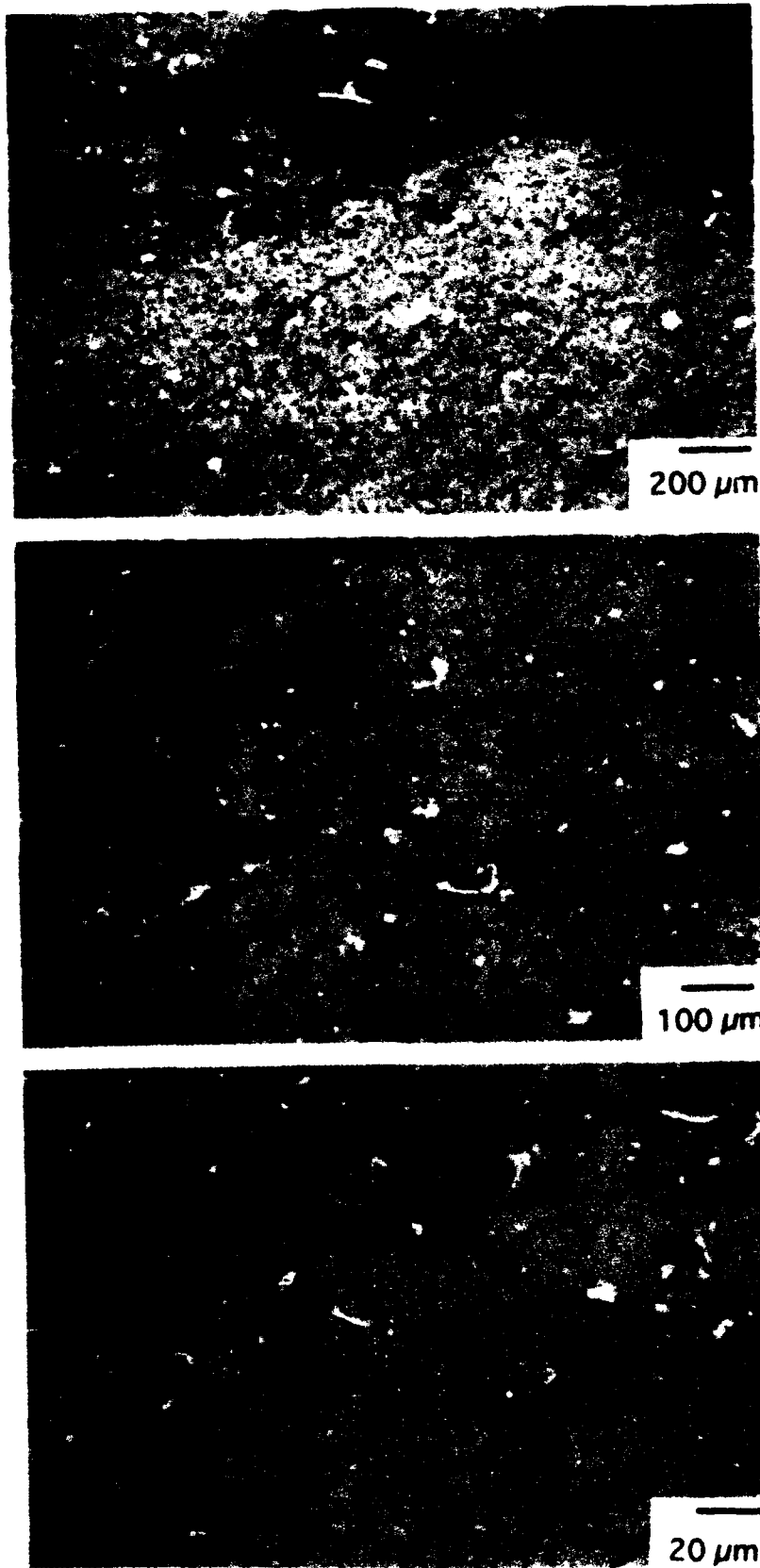


Figure 4.14 Actual microstructure of alloy 11 as observed in the room temperature tensile test. Specimen was solution heat treated at 1050°C / 4h and aged at 700°C / 24h.

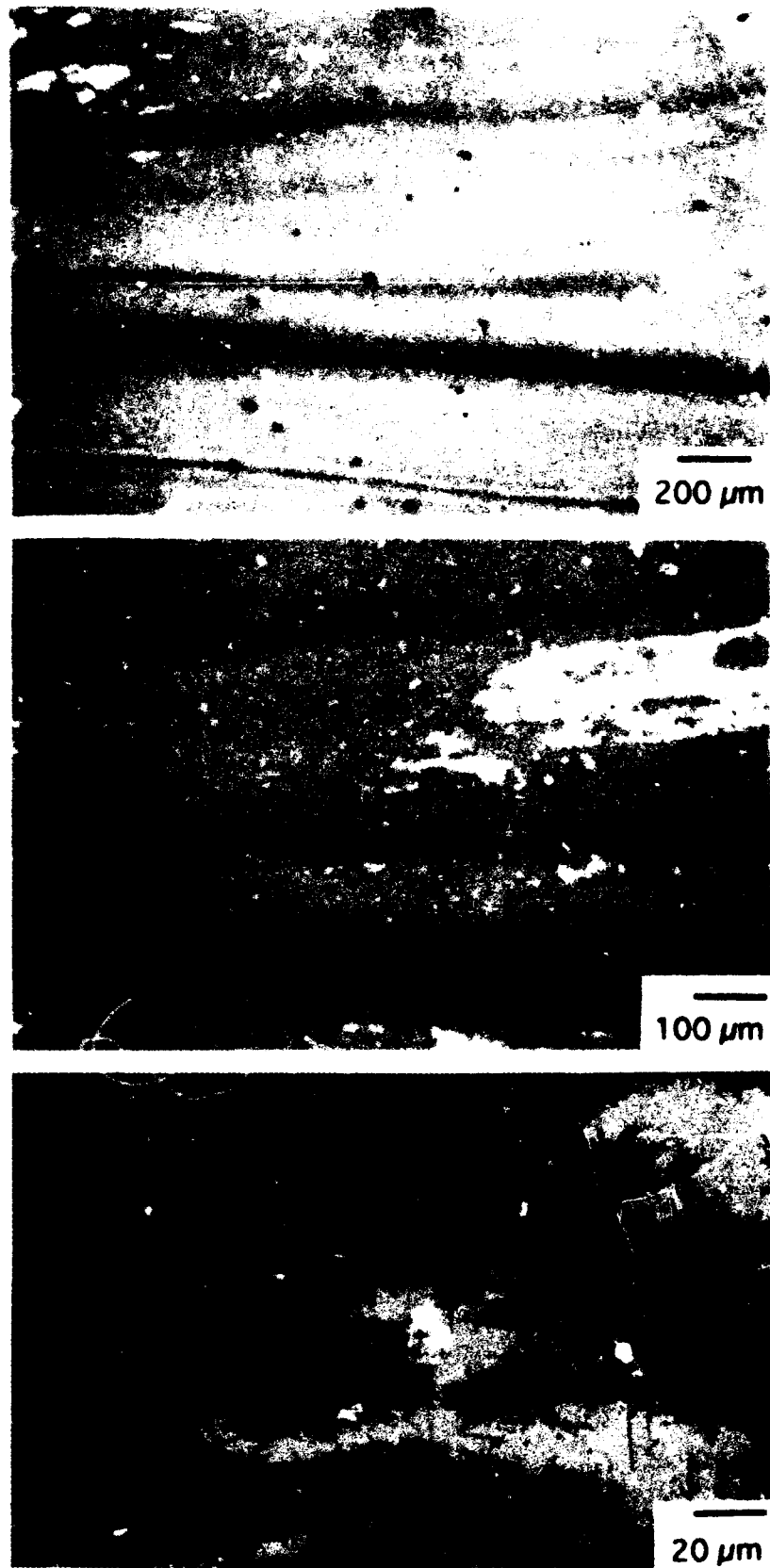


Figure 4.15 Actual microstructure of alloy 12 as observed in the room temperature tensile test. Specimen was solution heat treated at 1050°C / 4h and aged at 800°C / 24h.

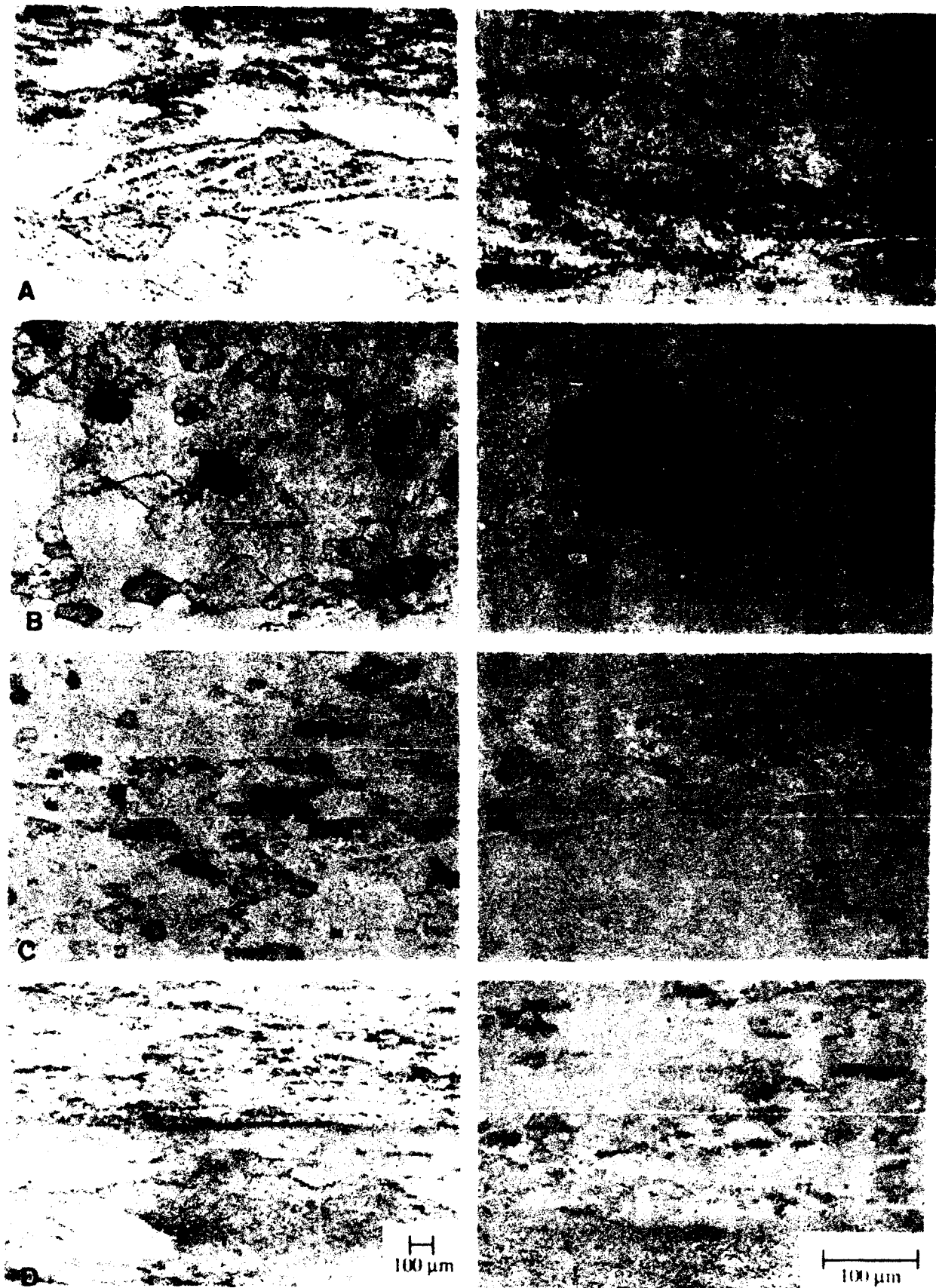


Figure 4.16 Optical micrographs of the microstructure of alloy 15 in the a) as-forged, b) solution treated, c) solution treated and aged, and d) direct aged conditions.

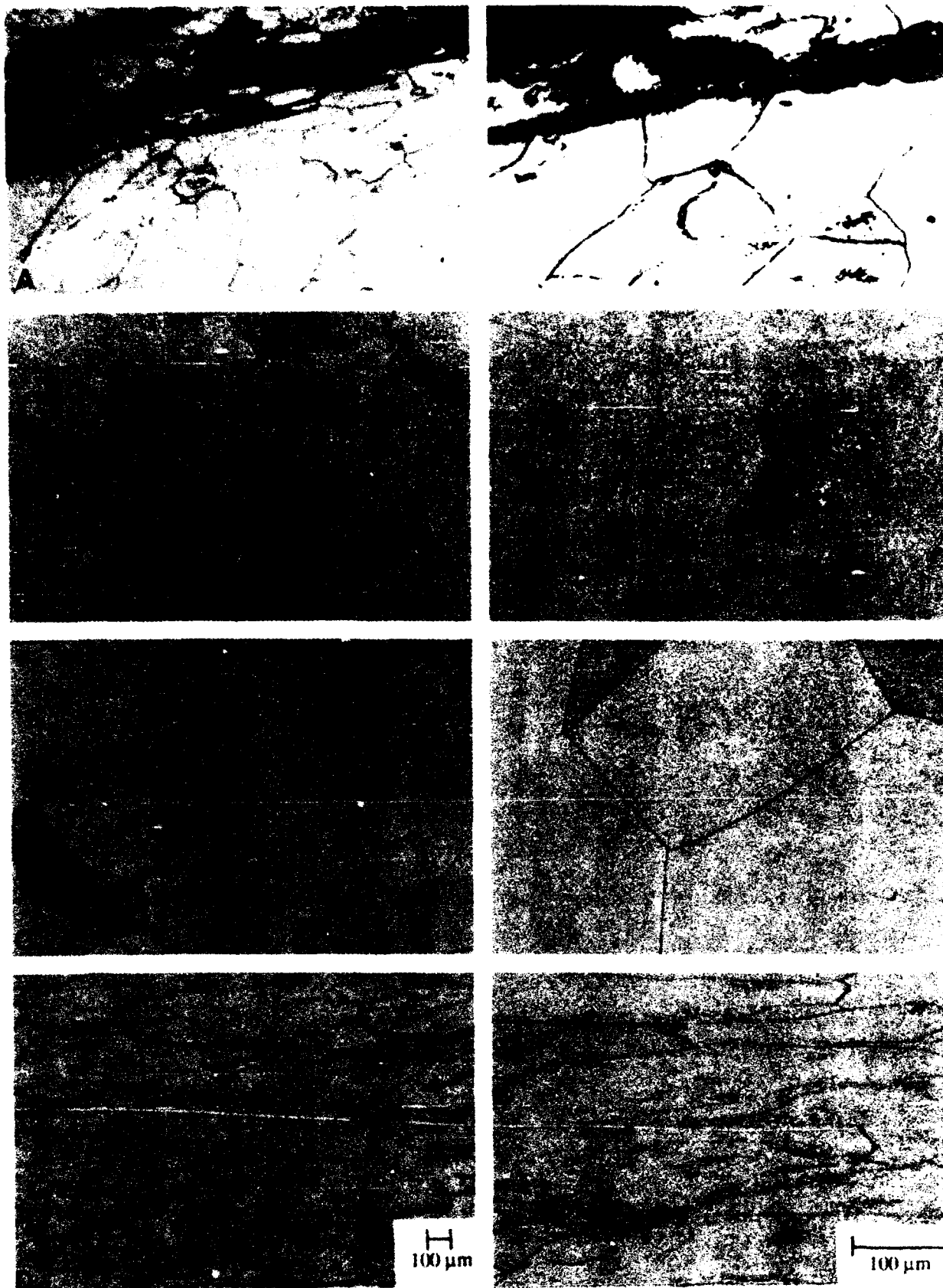


Figure 4.17 Optical micrographs of the microstructure of alloy 17 in the a) as-forged, b) solution treated, c) solution treated and aged, and d) direct aged conditions.



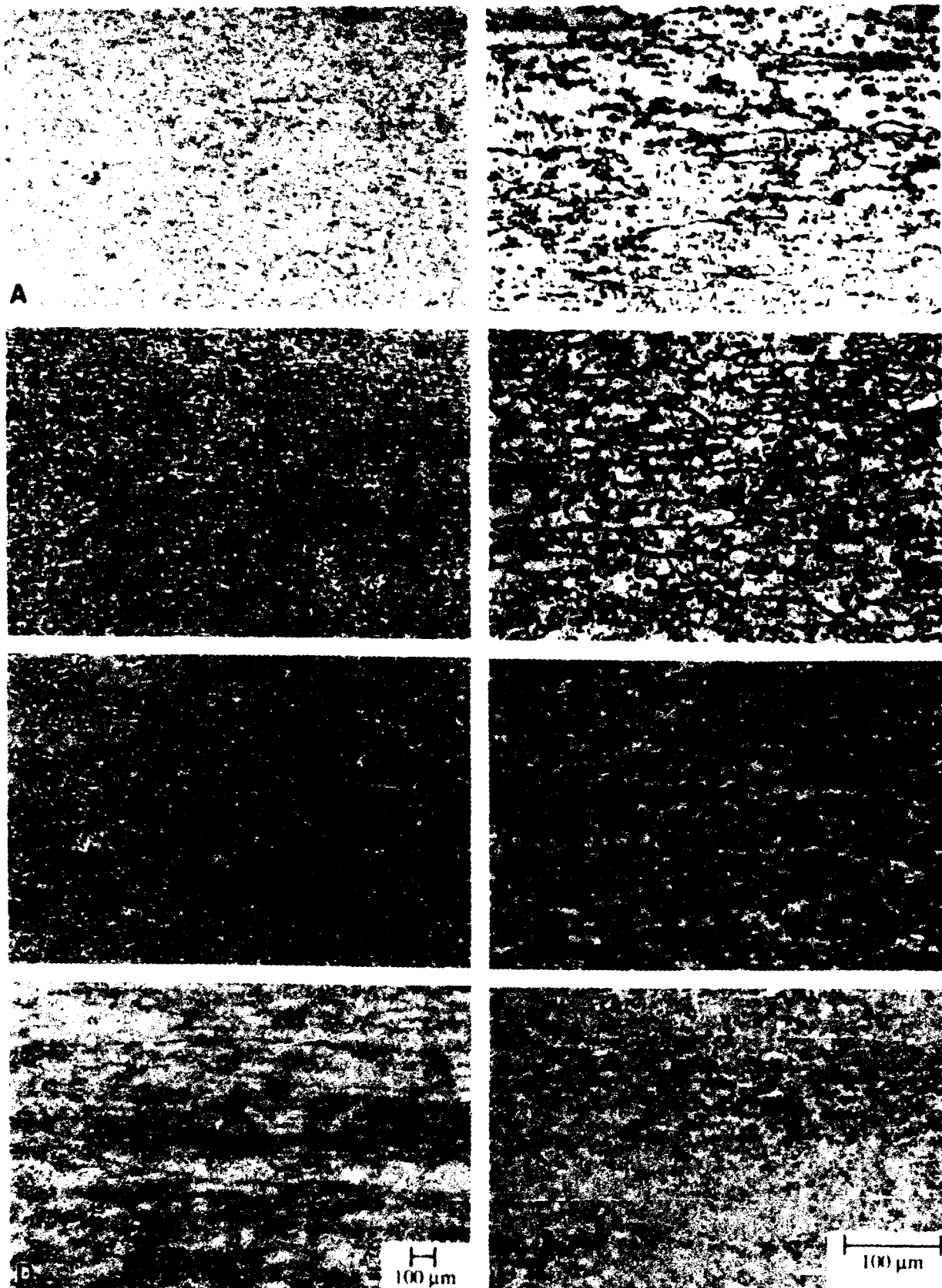


Figure 4.18 Optical micrographs of the microstructure of alloy 19 in the a) as-forged, b) solution treated, c) solution treated and aged, and d) direct aged conditions.

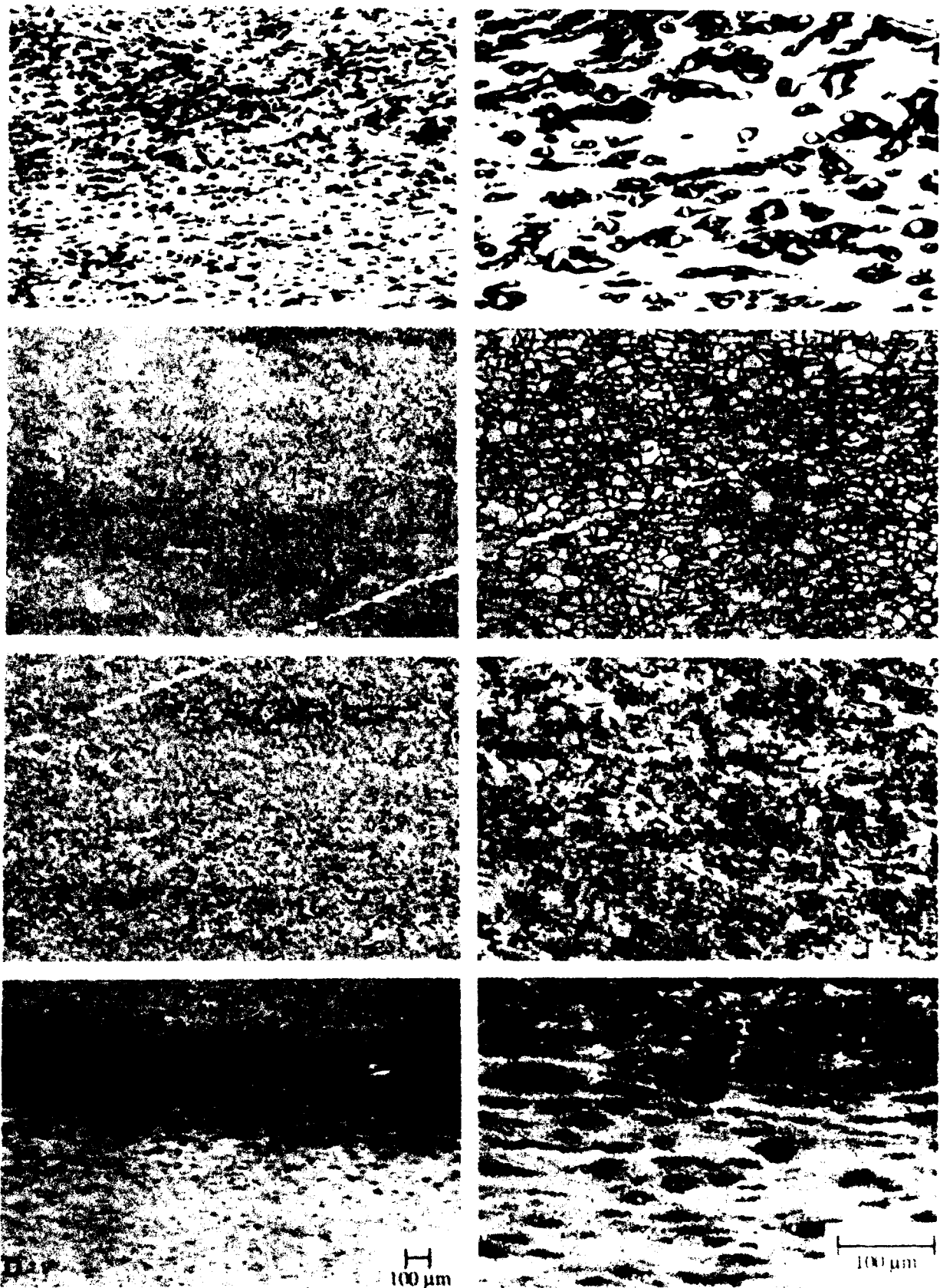


Figure 4.19 Optical micrographs of the microstructure of alloy 20 in the a) as-forged, b) solution treated, c) solution treated and aged, and d) direct aged conditions.

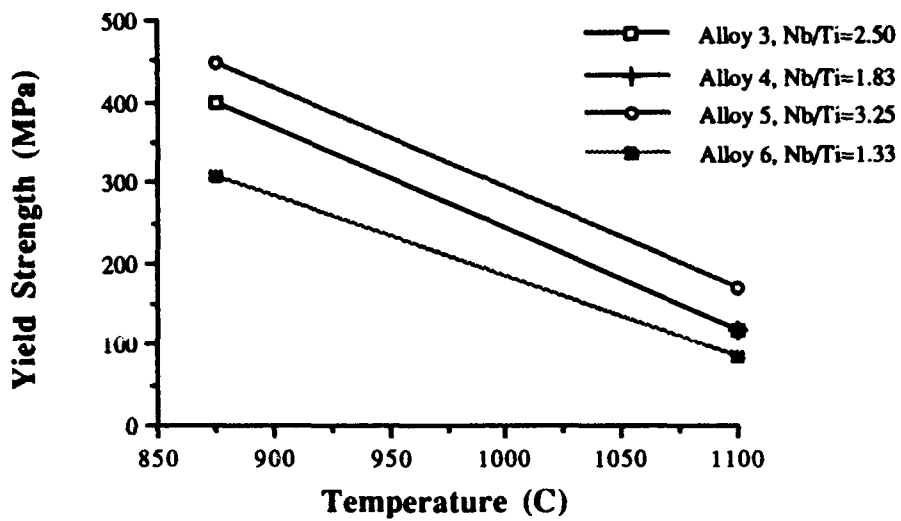


Figure 4.20 Comparison of the elevated temperature yield strengths for Alloys 3-6.

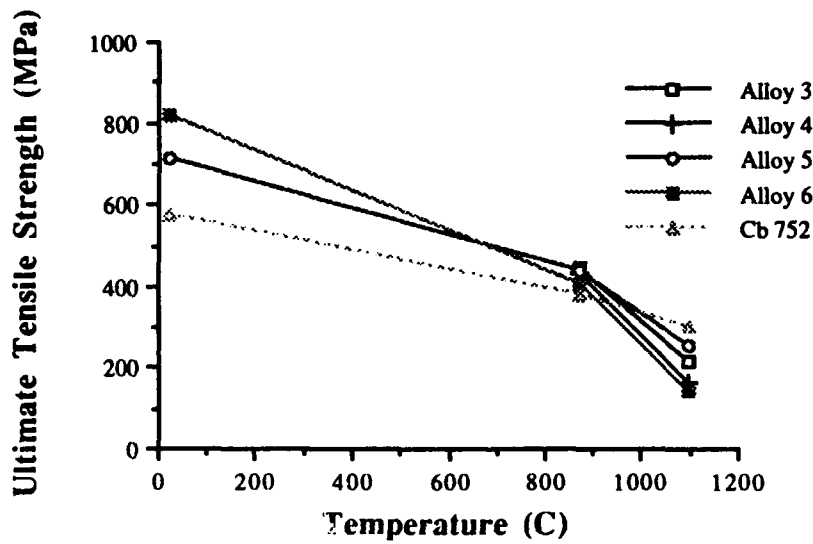


Figure 4.21 Comparison of ultimate tensile strength of contract alloys with the conventional niobium alloy Cb752.

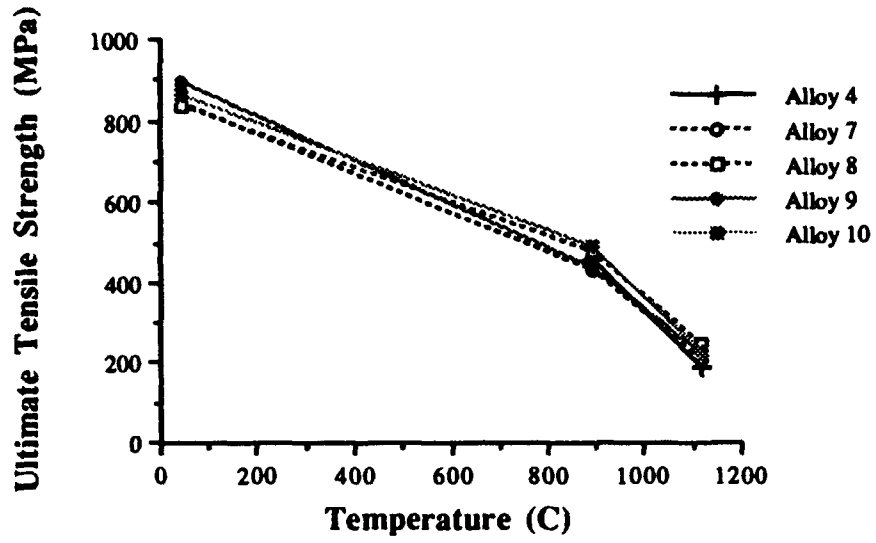
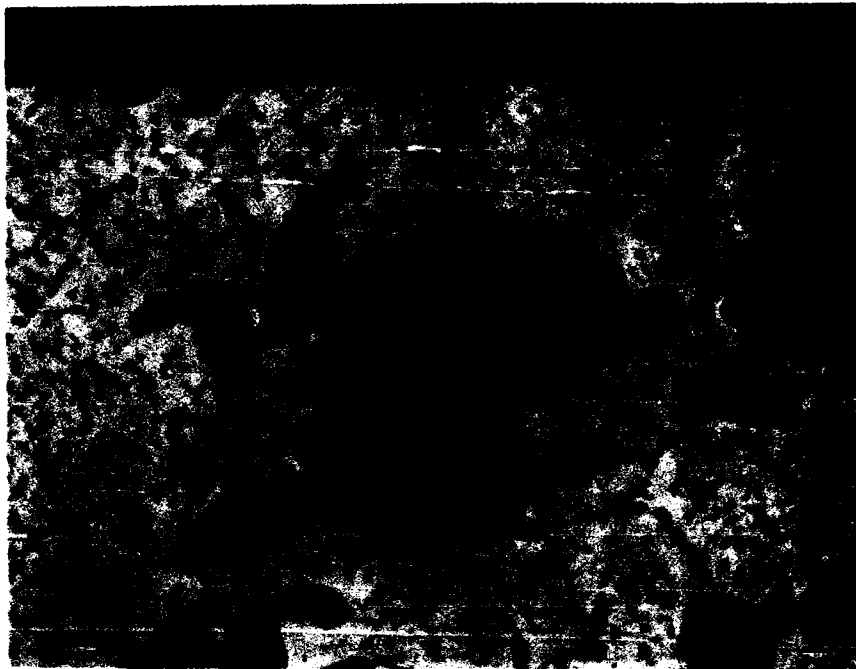
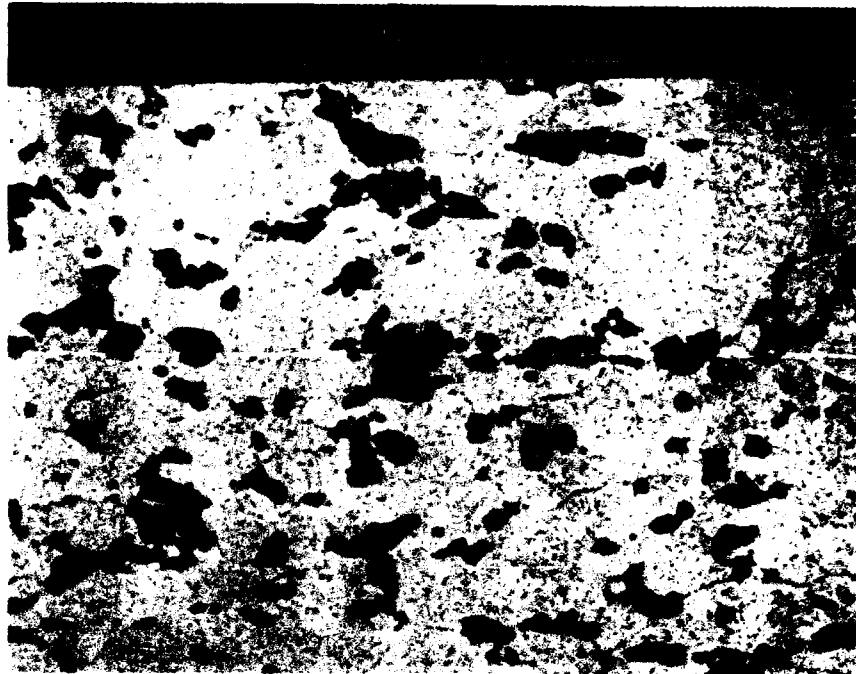


Figure 4.22 Comparison of the ultimate tensile strength of the C and Si modified alloys based on Alloy 4 with the unmodified Alloy 4.



**Figure 4.23** Backscattered electron images of Alloy 10 following tensile testing at room temperature showing fracture of the large primary phase, either Laves or Silicide, away from the fracture surface.

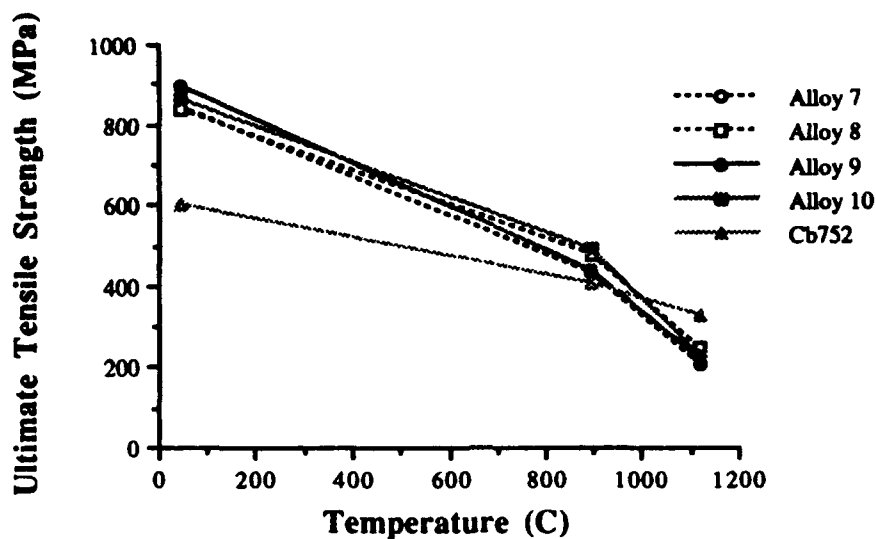


Figure 4.24 Comparison of the ultimate tensile strength of the C and Si modified alloys based on Alloy 4 with the conventional niobium alloy Cb752.

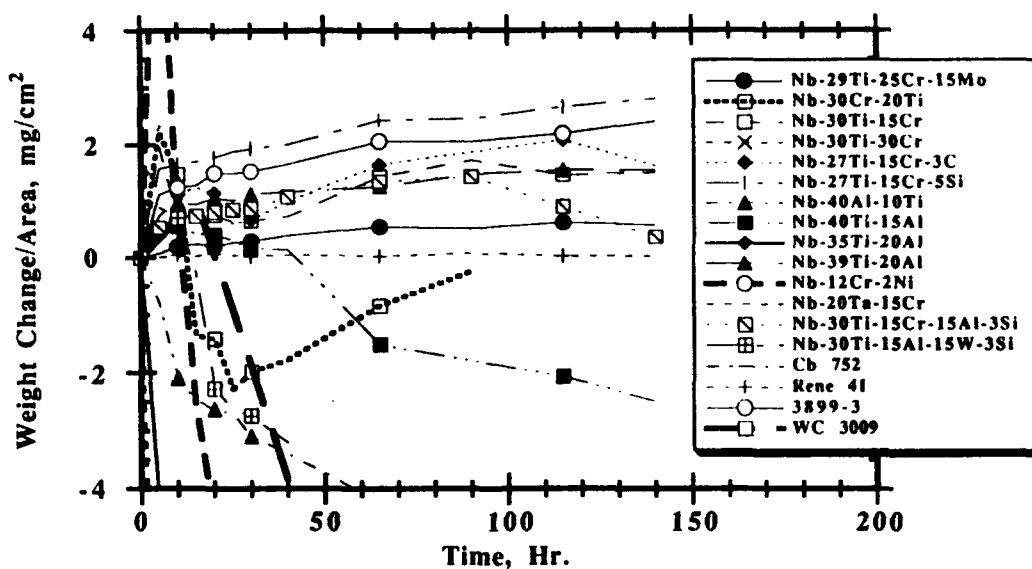


Figure 4.25 Graph showing the weight change / area versus time for Nb-Ti alloys, commercial Nb alloys and Rene'41 during the 800°C cyclic oxidation test. The test was performed in a low velocity oxidation rig that burnt natural gas / air mixtures and rapidly cycled the samples three times an hour to room temperature.

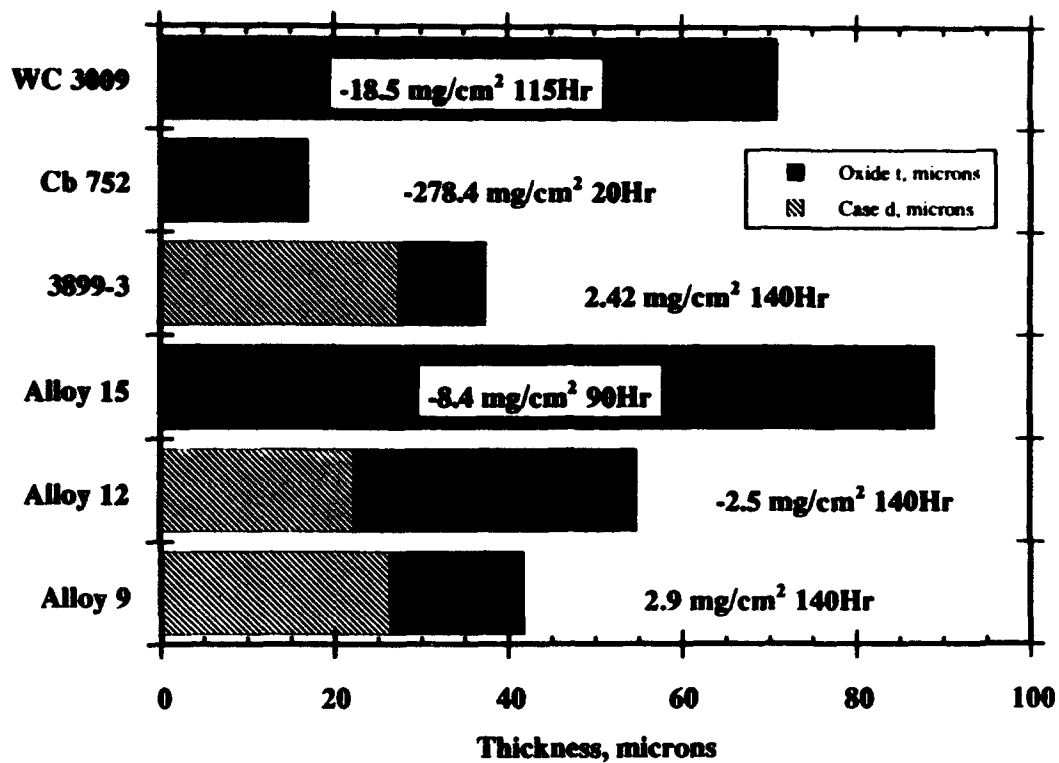


Figure 4.26 Bar chart summarizing microstructural and kinetic observations for downselected Nb-Ti alloys and commercial Nb alloys. Systems that lost weight rapidly had little evidence of a layer enriched with interstitials, while alloys with moderate weight change had the layer present.

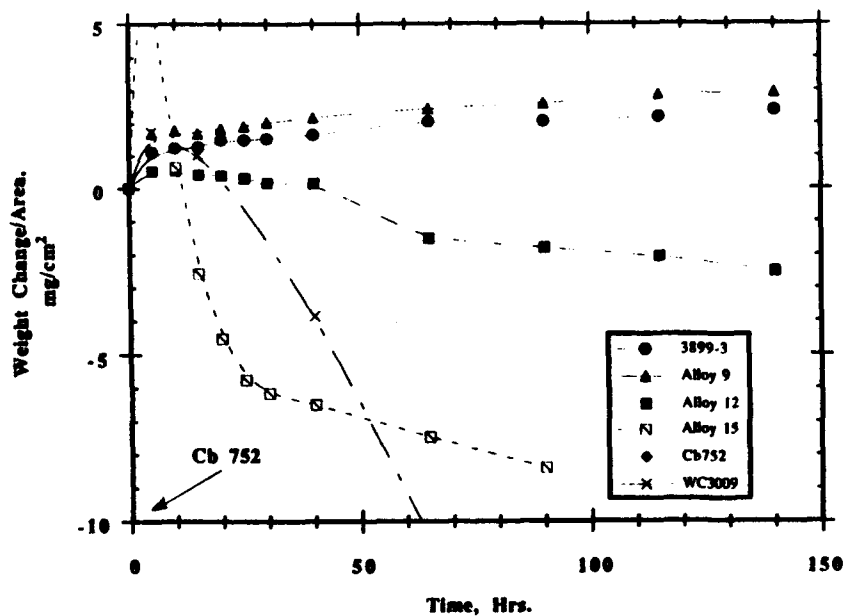


Figure 4.27 Cyclic oxidation weight change curves as a function of time for the alloys examined in Figure 4.26.

### Oxidation of High Temp Materials 20Hr/1475°F/Air

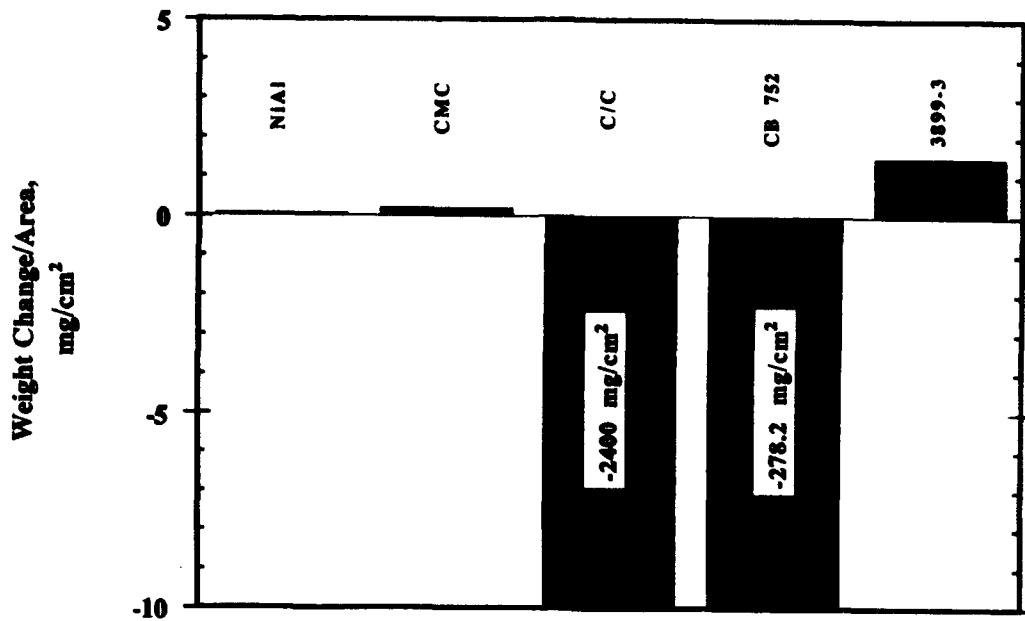


Figure 4.28 Bar chart comparing the cyclic oxidation resistance of various high temperature materials. The Nb-Ti alloys represent a compromise in properties with better oxidation resistance than Nb alloys.

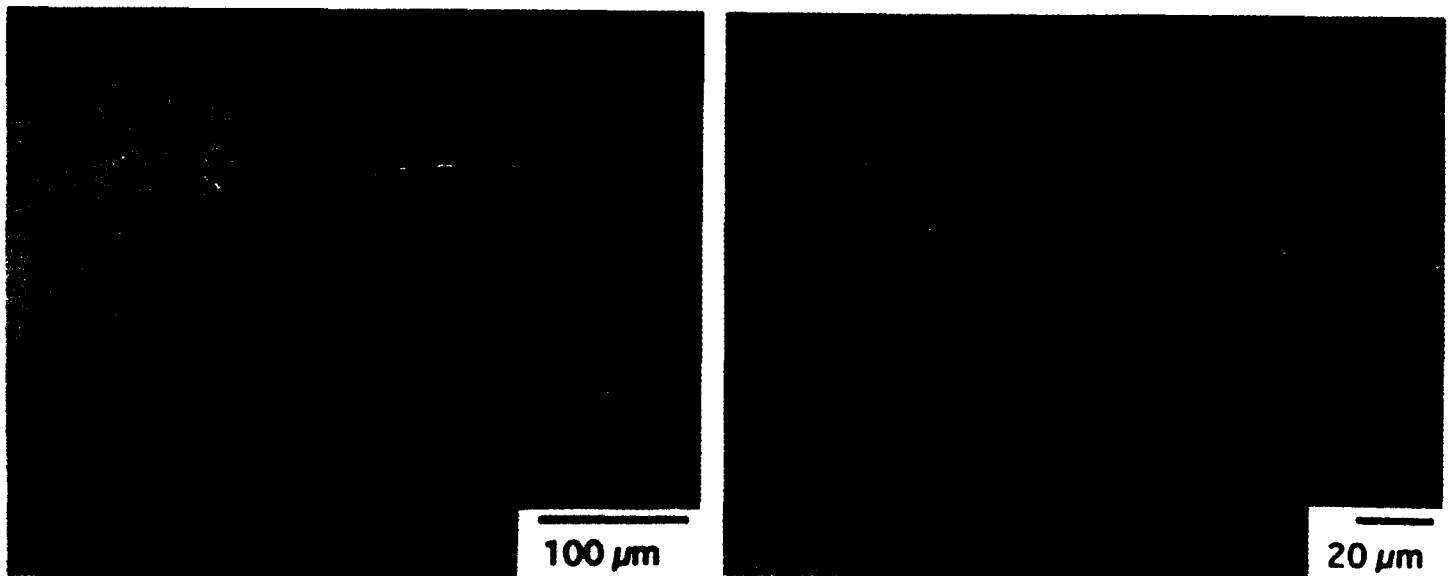


Figure 4.29 Cross sectional optical micrographs of Rene'41 after cyclic oxidation at 800°C for 140h. a thin continuous chromia scale is observed on the surface.



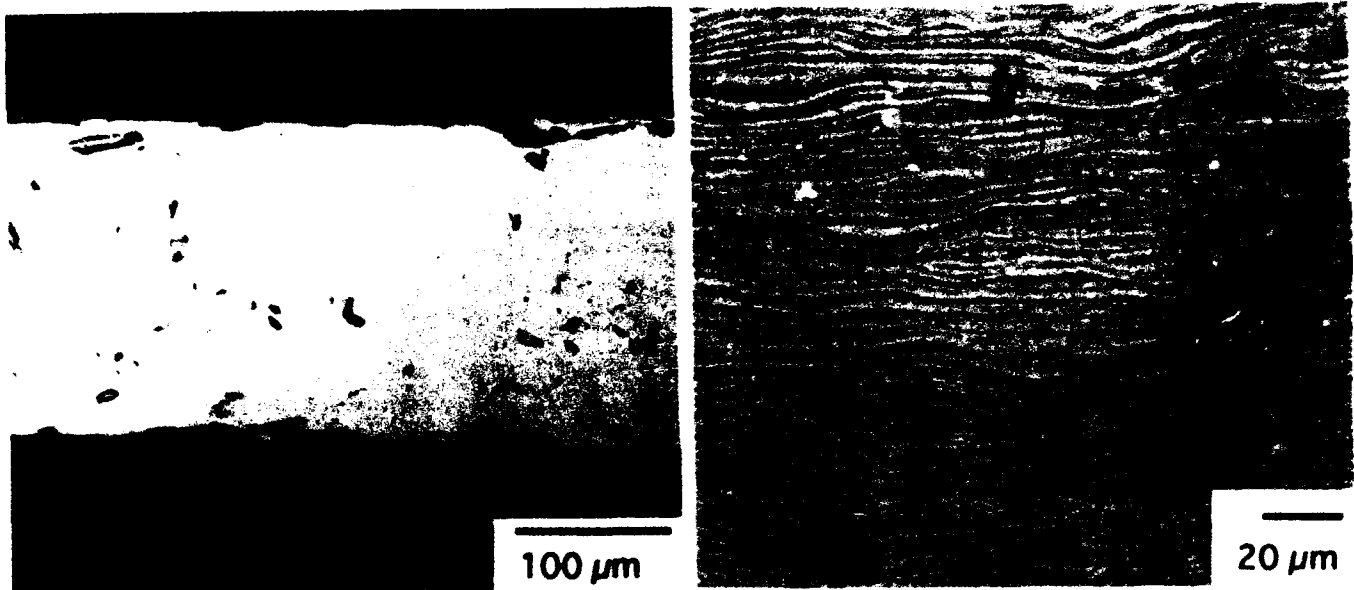


Figure 4.30 Cross sectional optical micrographs of Cb752 after cyclic oxidation at 800C° for 20h. An unadherent, flaky white scale was observed on a heavily cold worked substrate.

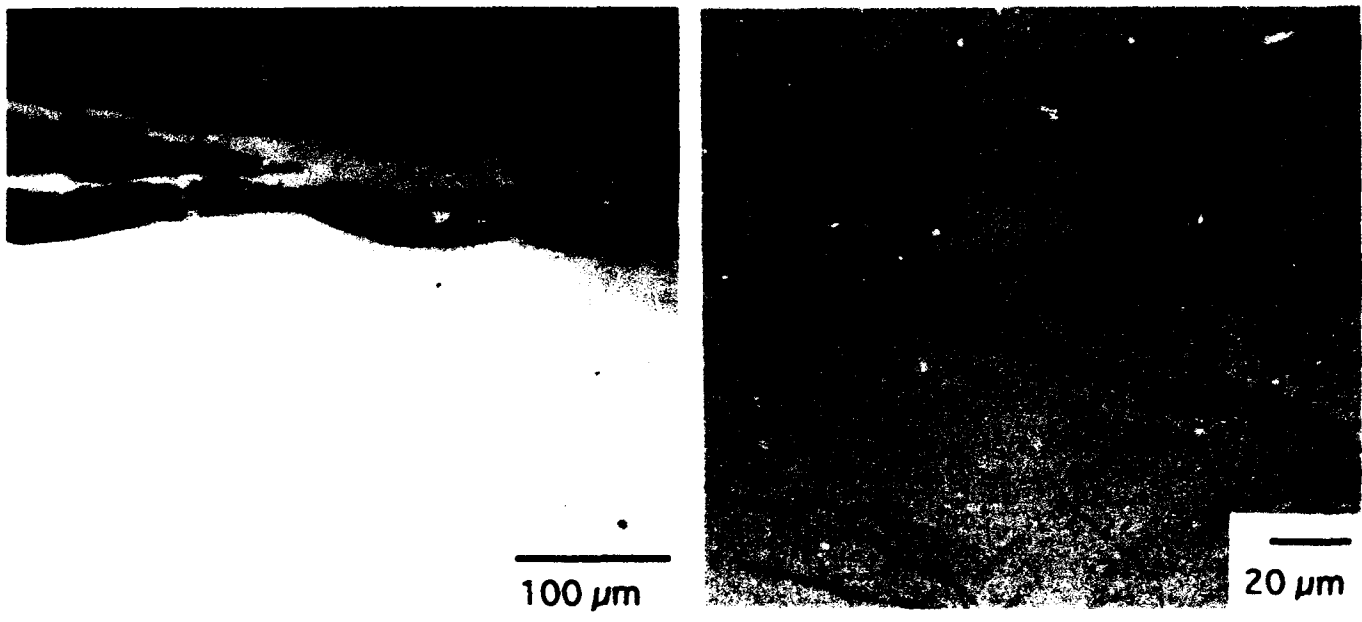


Figure 4.31 Cross sectional optical micrographs of WC3009 after cyclic oxidation at 800°C for 115h. Spallation was observed on the sample in the form of chips.

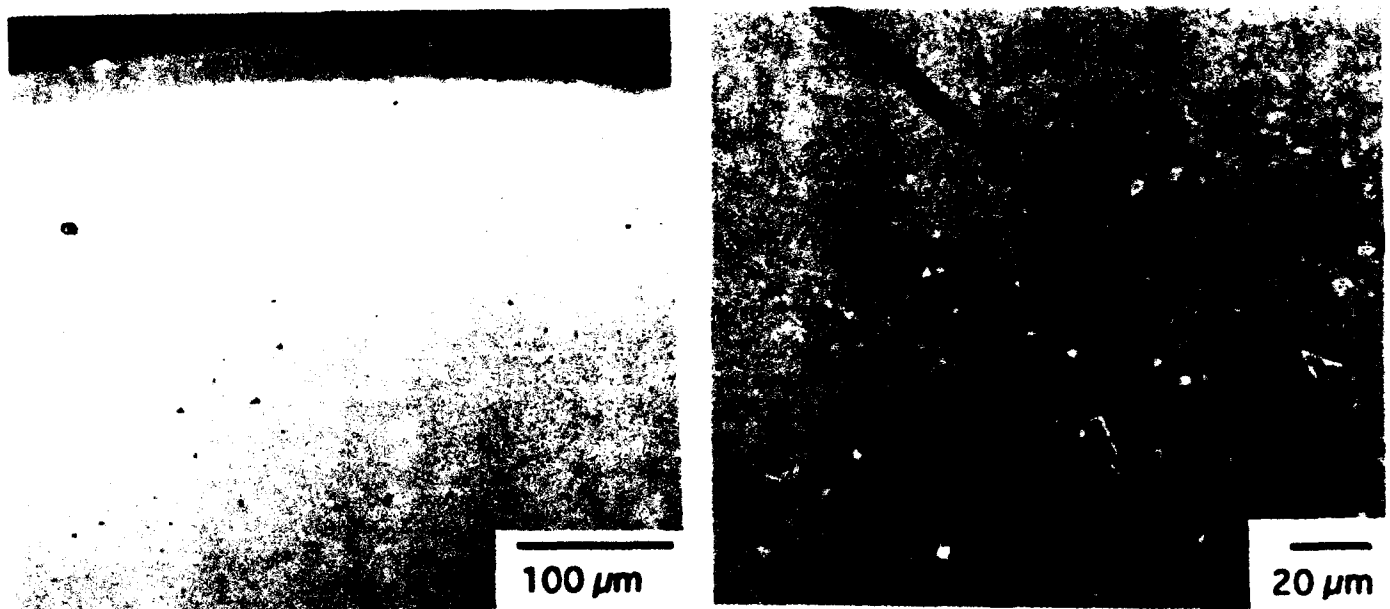


Figure 4.32 Cross sectional optical micrographs of 3899-3 ( Nb-37.5Ti-5Hf-5V-5Cr-5Al-0.5Zr-0.3C ) after cyclic oxidation at 800°C for 140h. The oxide was adherent and a layer enriched in interstitials is apparent.

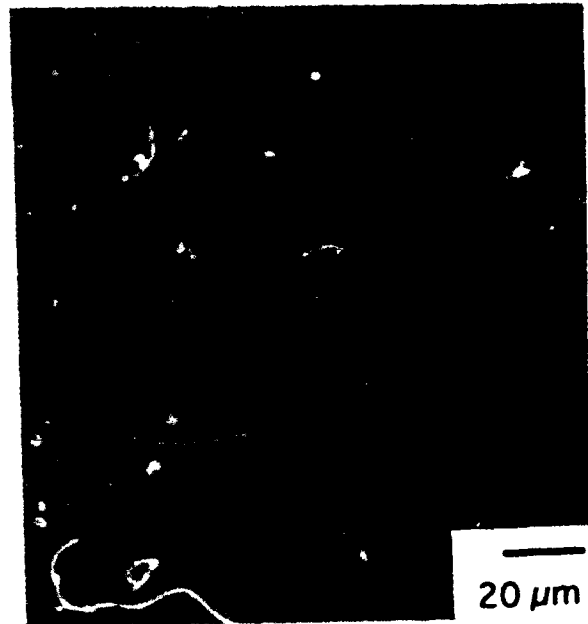
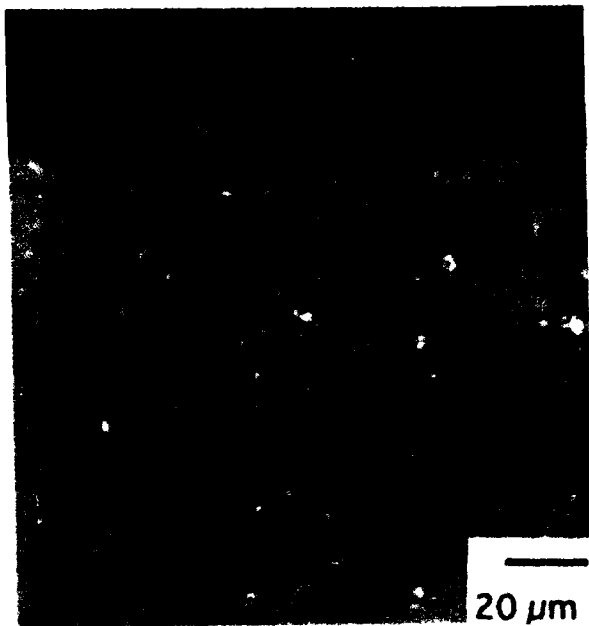
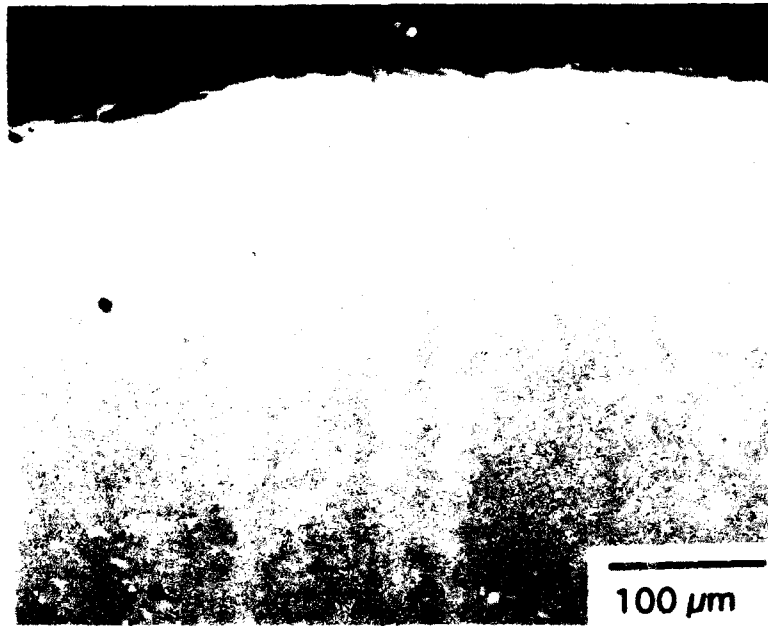


Figure 4.33 Cross sectional optical micrographs of alloy 2 ( Nb-29Ti-25Cr-15Mo ) after cyclic oxidation at 800°C for 140h. The alloy had good oxidation resistance but was difficult to fabricate.

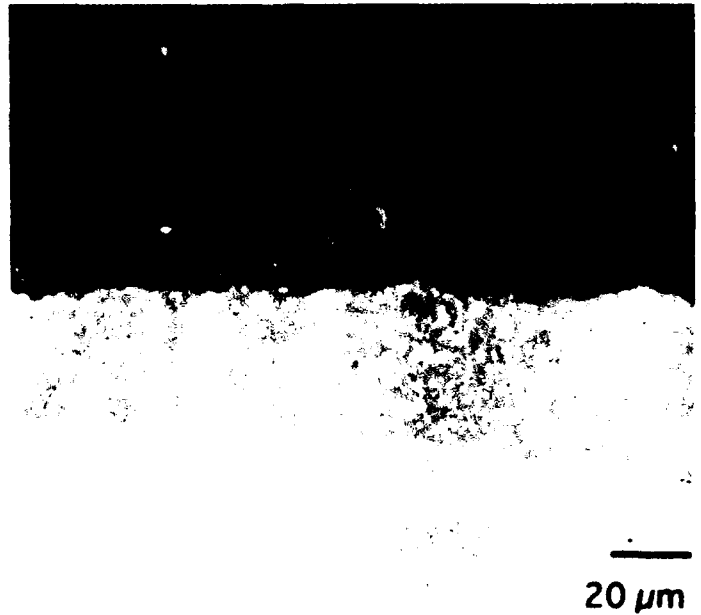
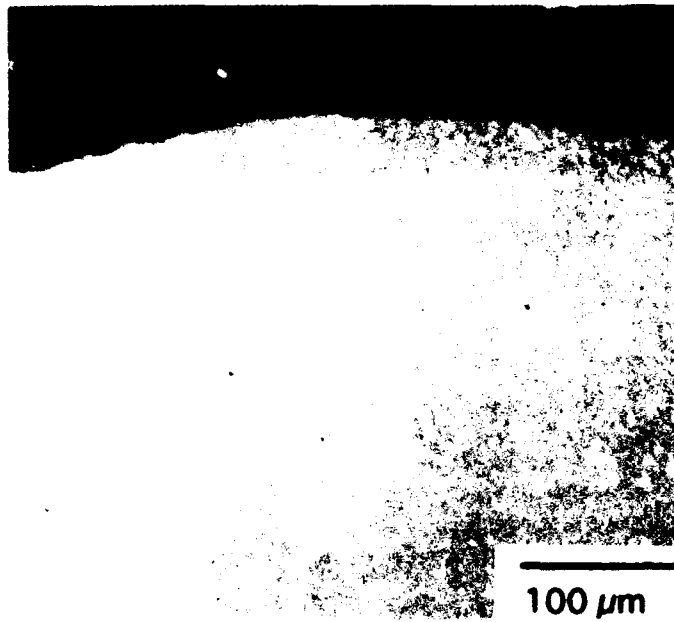


Figure 4.34 Cross sectional optical micrographs of Alloy 3 ( Nb-20Ti-30Cr ) after cyclic oxidation at 800°C for 90h. Brown, layered porous scales were relatively non-protective. A thick case developed underneath the external oxide scale.

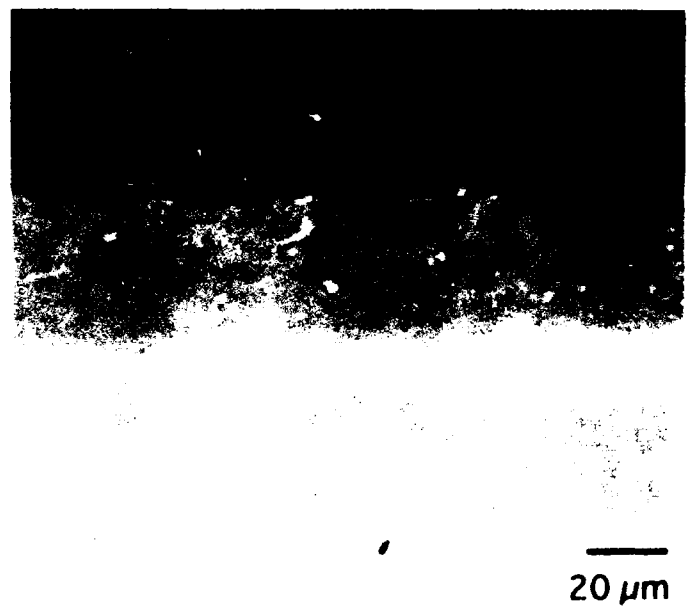
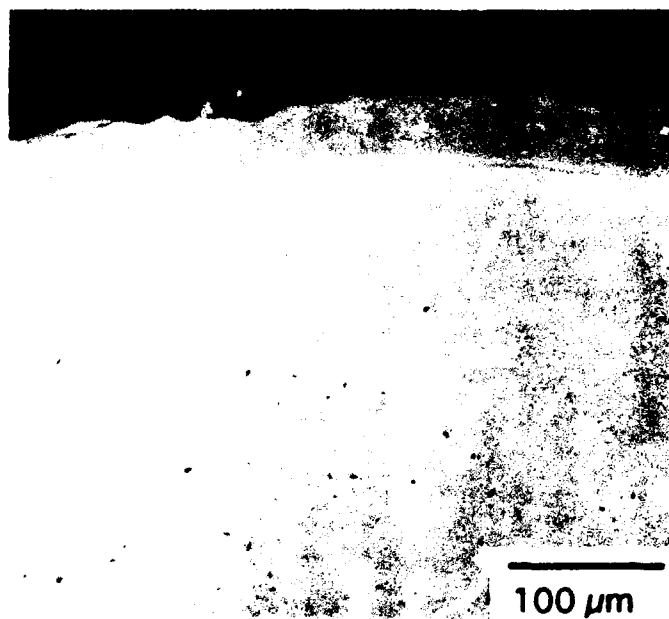


Figure 4.35 Cross sectional optical micrographs of alloy 4 ( Nb-30Ti-15Cr ) after cyclic oxidation at 800°C for 140h. Brown, layered porous scales were relatively non-protective. A thick case developed underneath the external oxide scale.

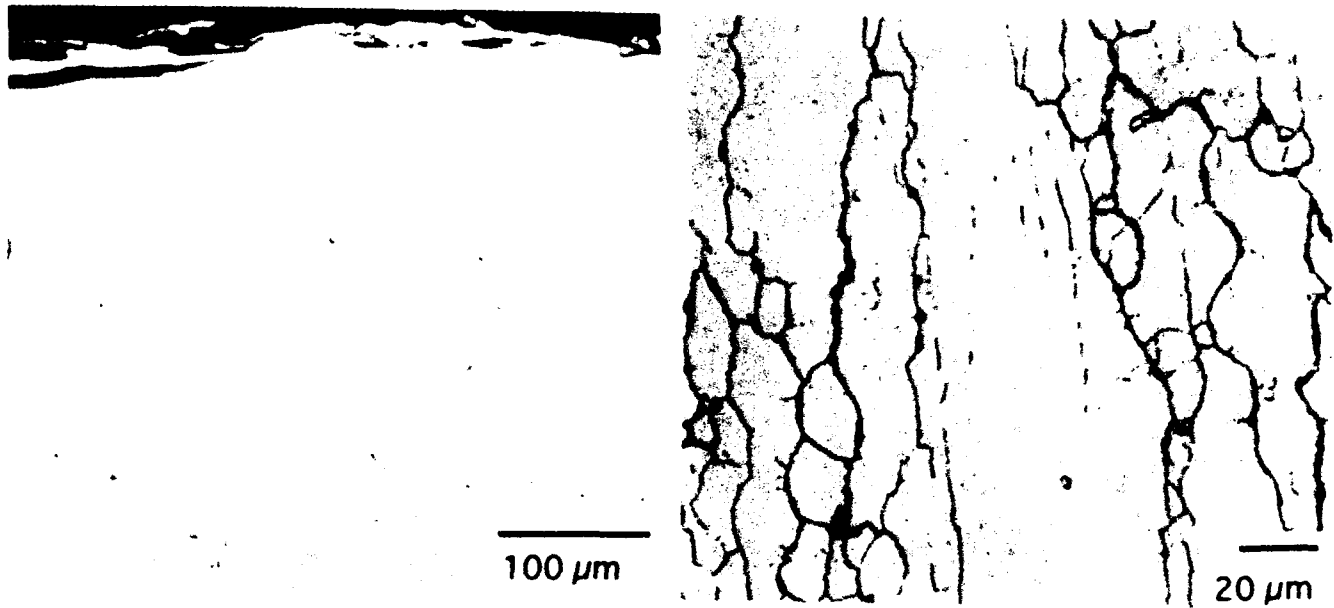


Figure 4.36 Cross sectional optical micrographs of alloy 5 ( Nb-20Ti-15Cr ) after cyclic oxidation at 800°C for 140h. Brown, layered porous scales were relatively non-protective. A thick case developed underneath the external oxide scale.

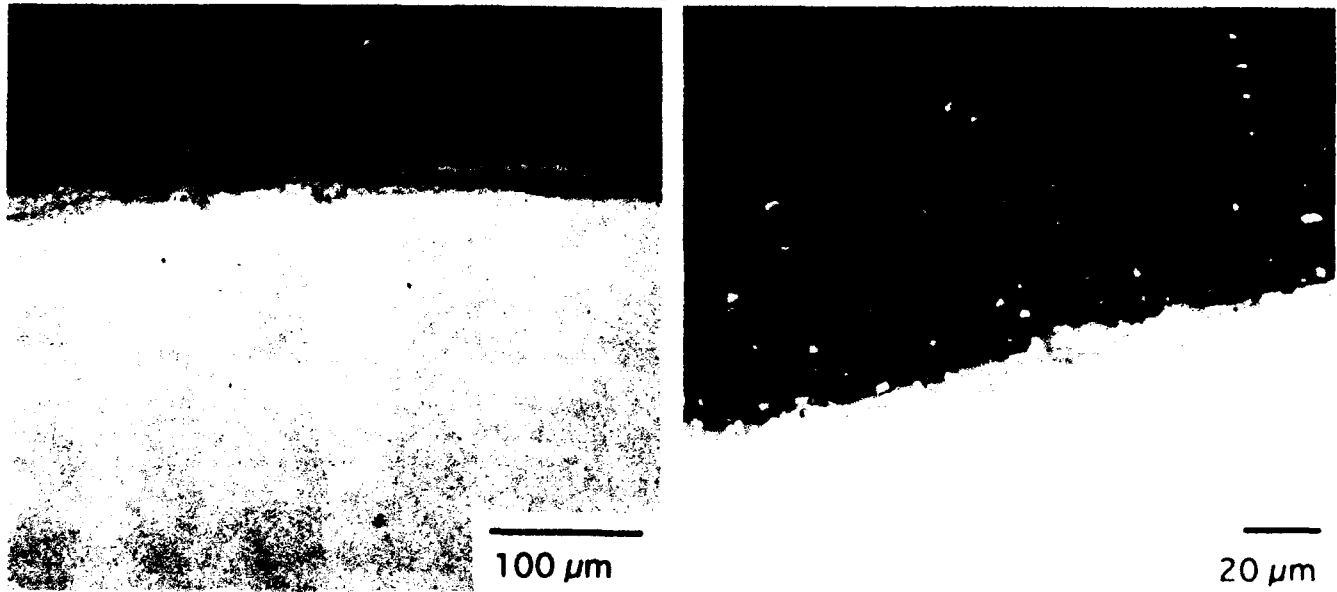


Figure 4.37 Cross sectional optical micrographs of alloy 6 ( Nb-30Ti-30Cr ) after cyclic oxidation at 800°C for 140h. Brown, layered porous scales were relatively non-protective. A thick case developed underneath the external oxide scale. The high Cr resulted in massive spallation.

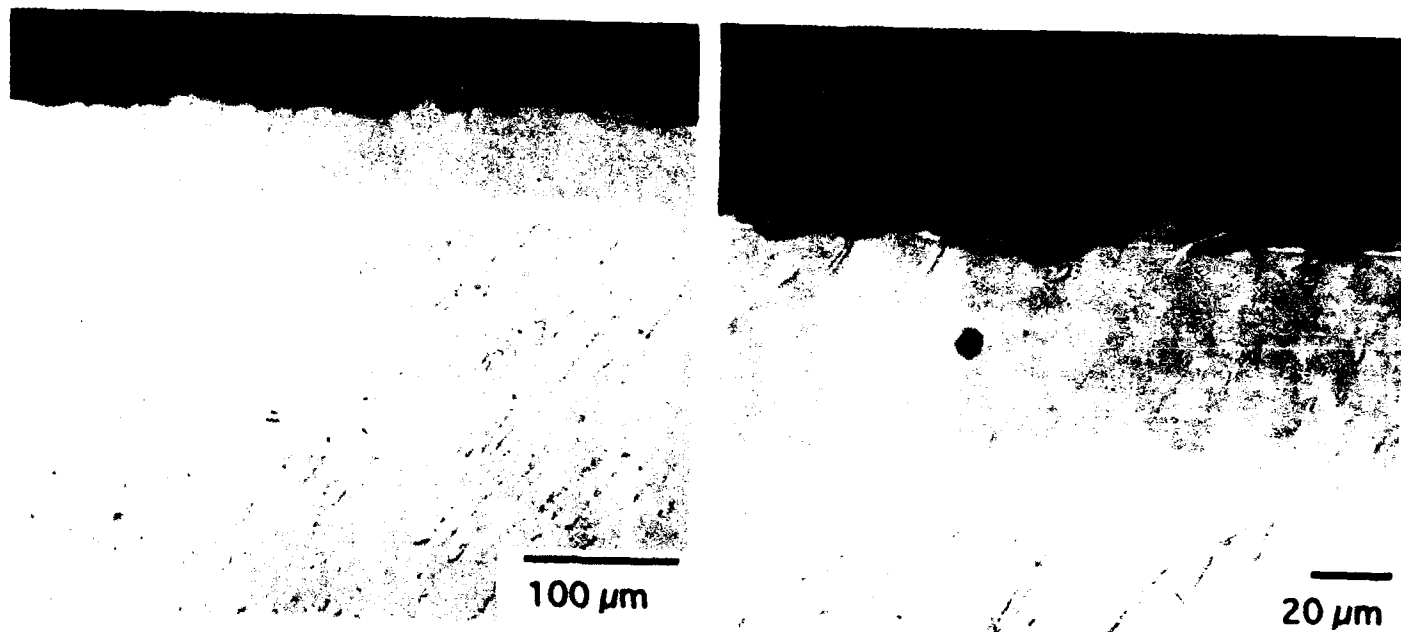


Figure 4.38 Cross sectional optical micrographs of alloy 7 ( Nb-29Ti-15Cr-1.5C ) after cyclic oxidation at 800°C for 140h. Brown, layered porous scales were relatively non-protective. A thick case developed underneath the external oxide scale.

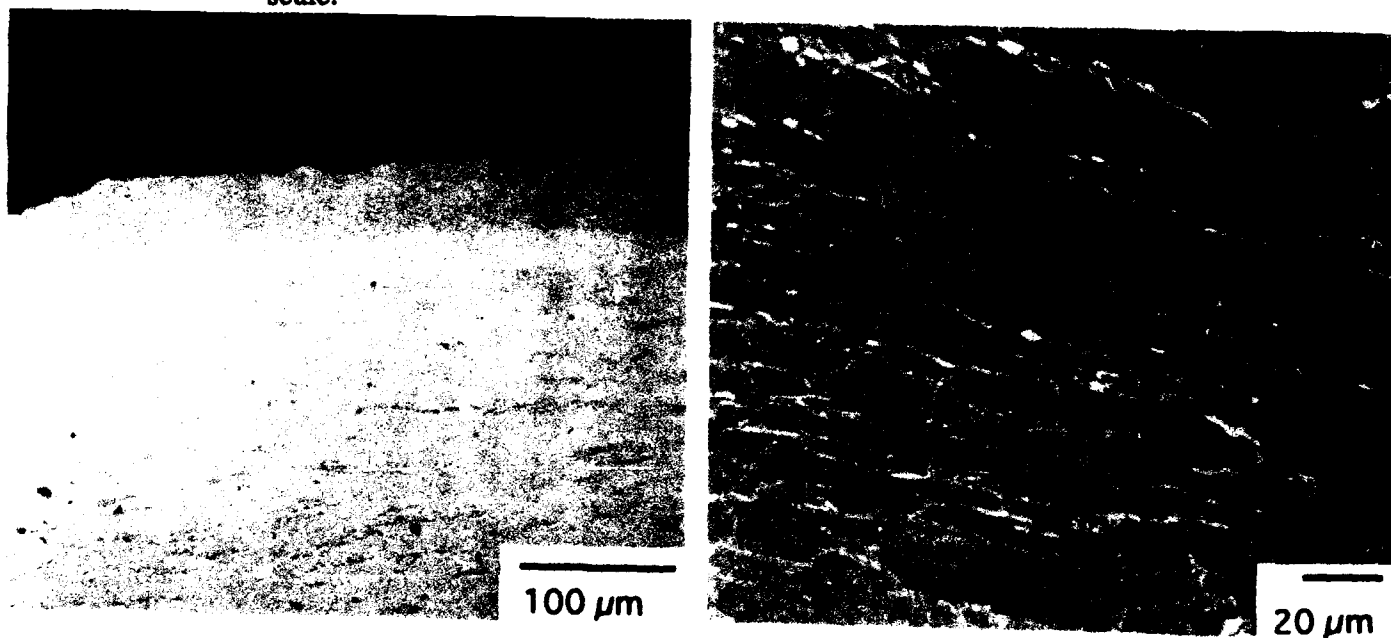


Figure 4.39 Cross sectional optical micrographs of alloy 8 ( Nb-29Ti-15Cr-3C ) after cyclic oxidation at 800°C for 140h. Brown, layered porous scales were relatively non-protective. A thick case developed underneath the external oxide scale.

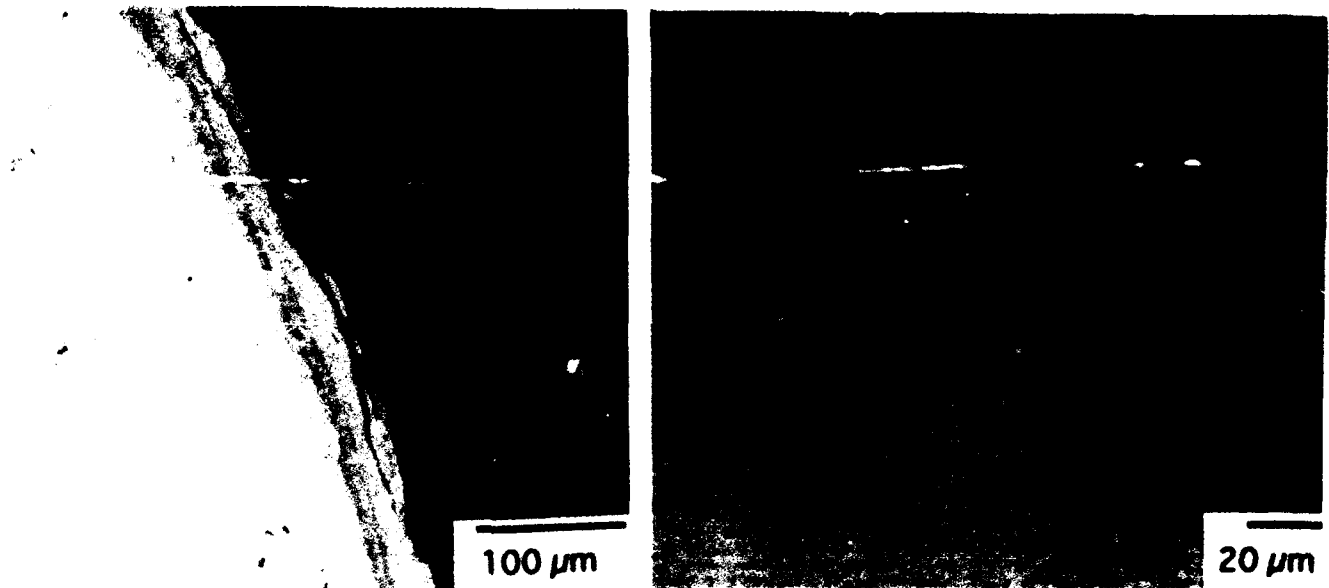


Figure 4.40 Cross sectional optical micrographs of alloy 9 ( Nb-28Ti-15Cr-3Si ) after cyclic oxidation at 800°C for 140h. The alloy had good oxidation resistance with a large volume fraction of a second phase.

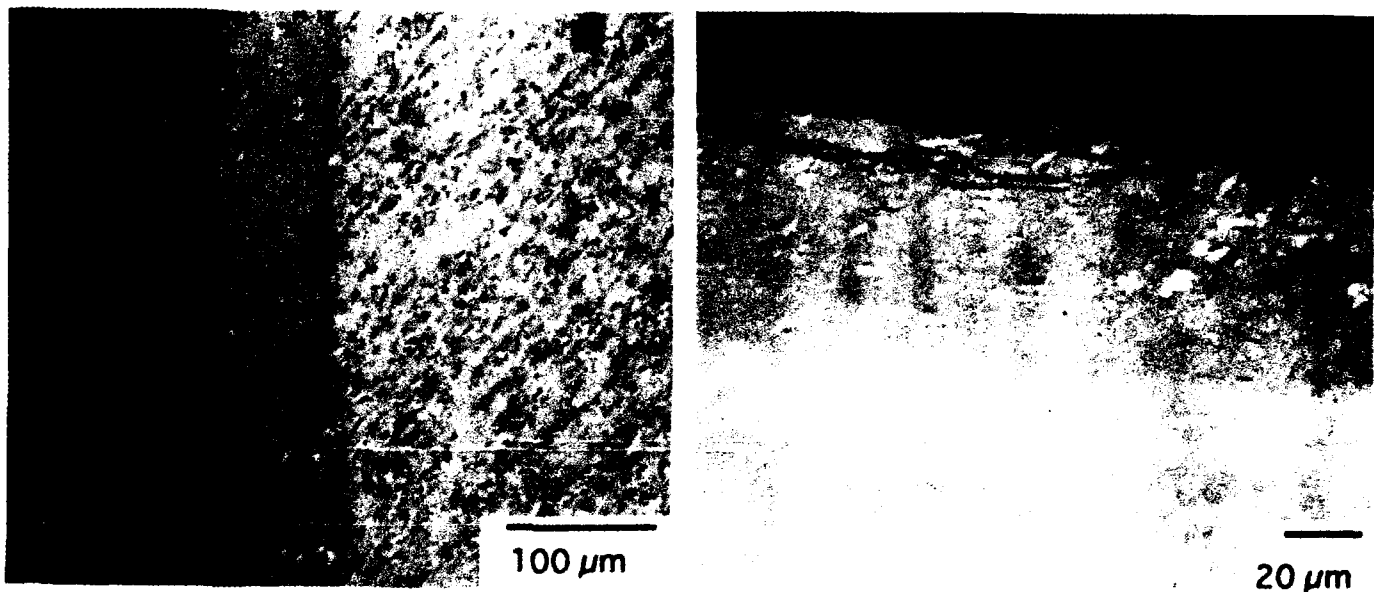


Figure 4.41 Cross sectional optical micrographs of alloy 10 ( Nb-28Ti-15Cr-5Si ) after cyclic oxidation at 800°C for 140h. The alloy had good oxidation resistance with a large volume fraction of a second phase.

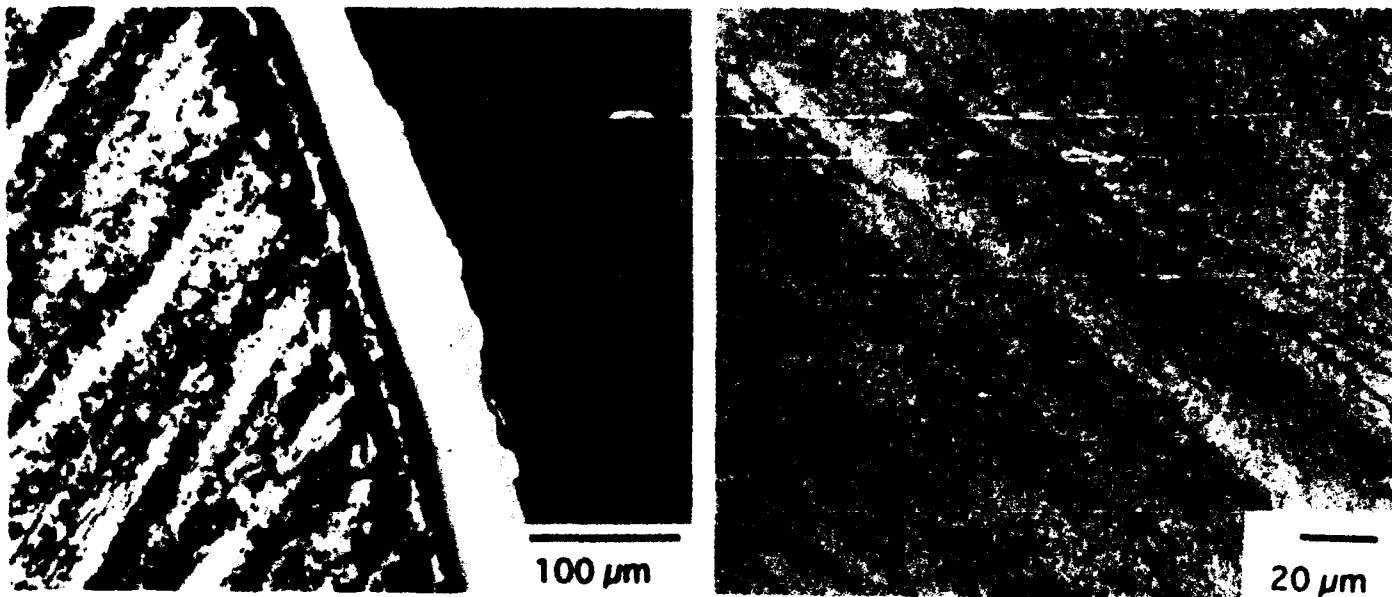


Figure 4.42 Cross sectional optical micrographs of alloy 11 ( Nb-40Ti-10Al ) after cyclic oxidation at 800°C for 140h. The alloy had good oxidation resistance but segregation affected oxidation kinetics.

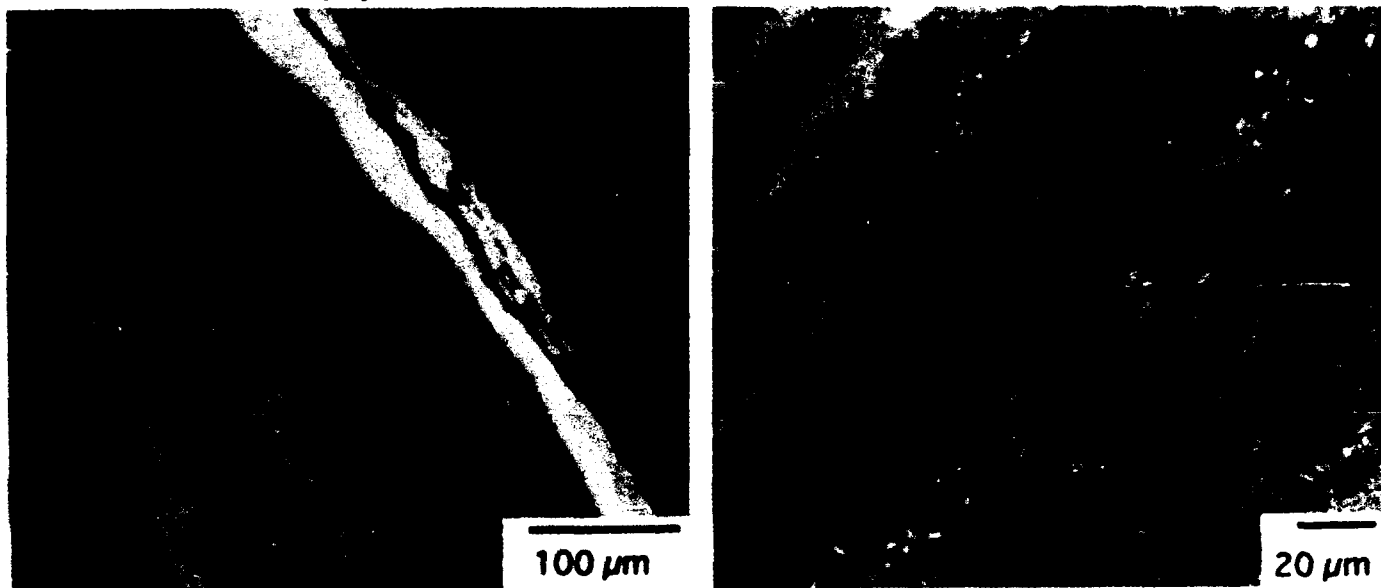


Figure 4.43 Cross sectional optical micrographs of alloy 12 ( Nb-40Ti-15Al ) after cyclic oxidation at 800°C for 140h. The alloy had good oxidation resistance but segregation resulted in a hole being oxidized through the pin.



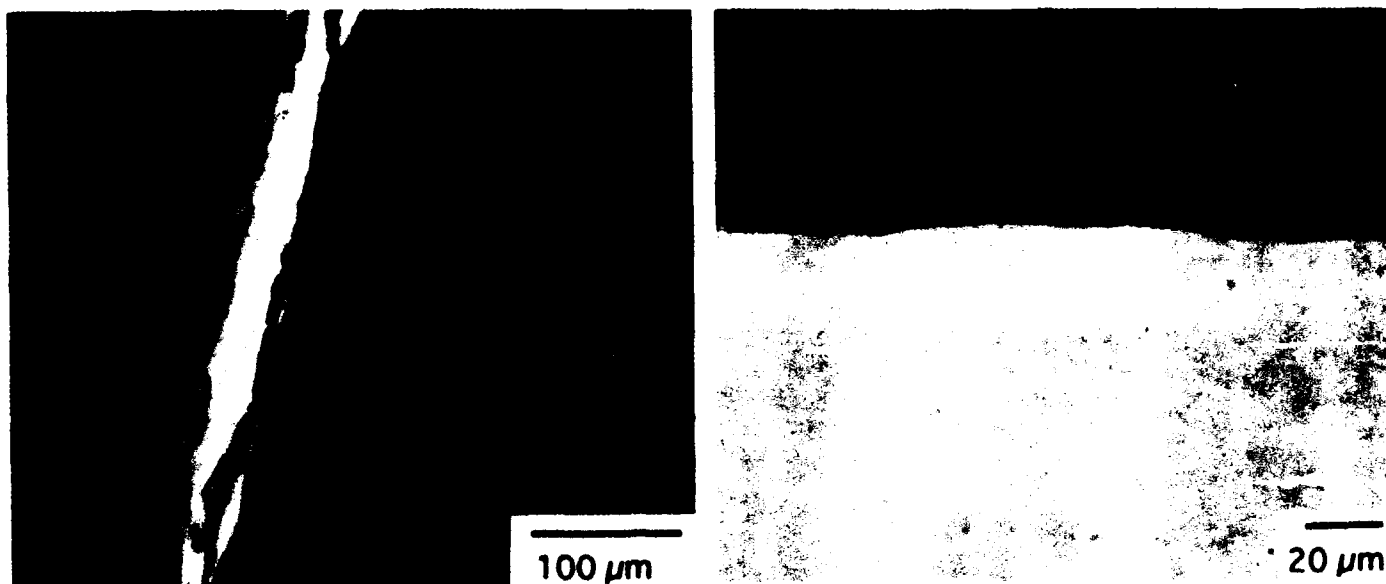


Figure 4.44 Cross sectional optical micrographs of Alloy 13 ( Nb-35Ti-20Al ) after cyclic oxidation at 800°C for 140h. The alloy had good oxidation resistance but segregation affected oxidation kinetics.

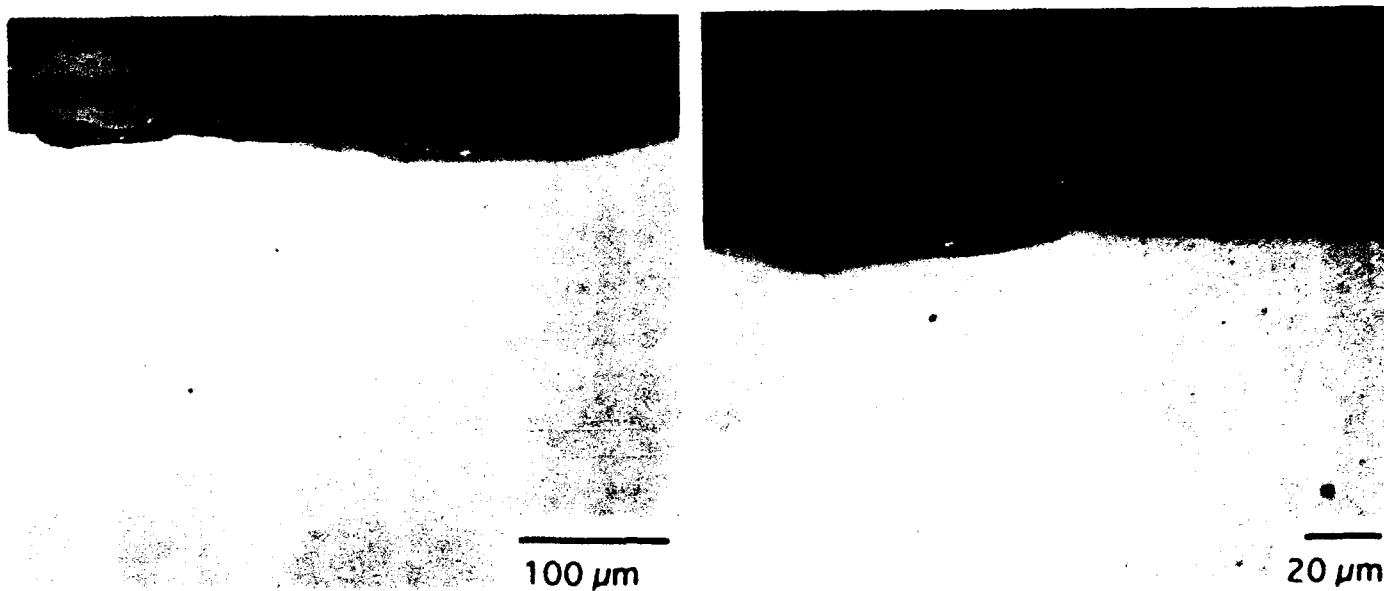
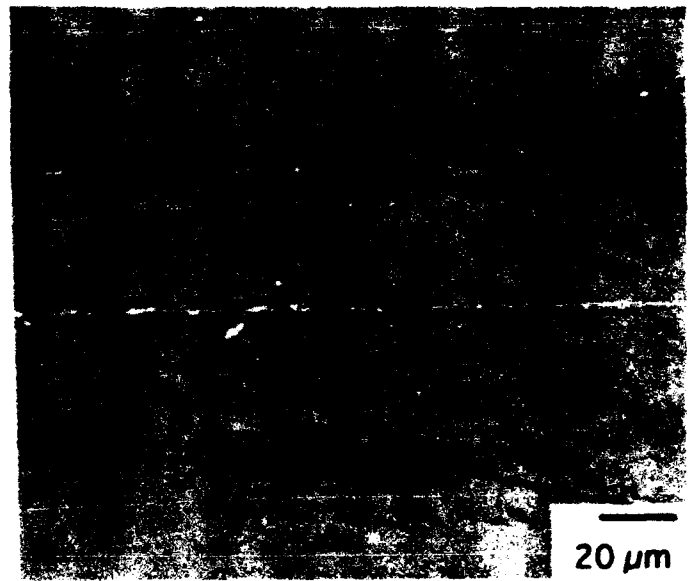
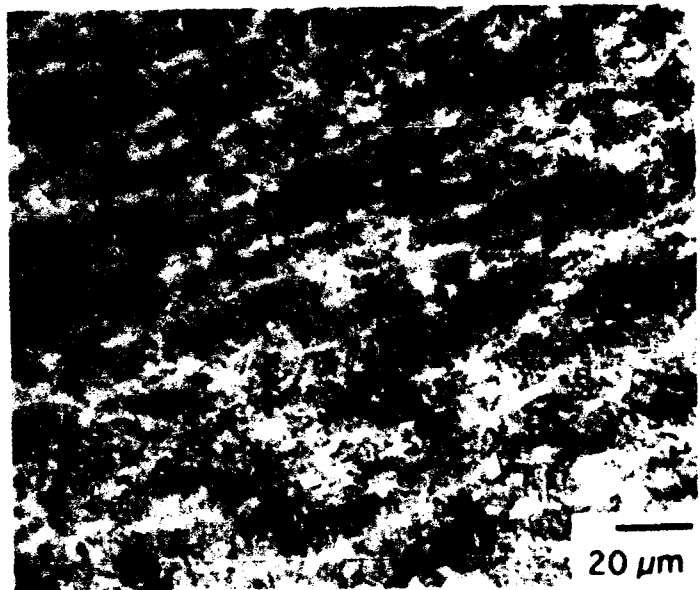
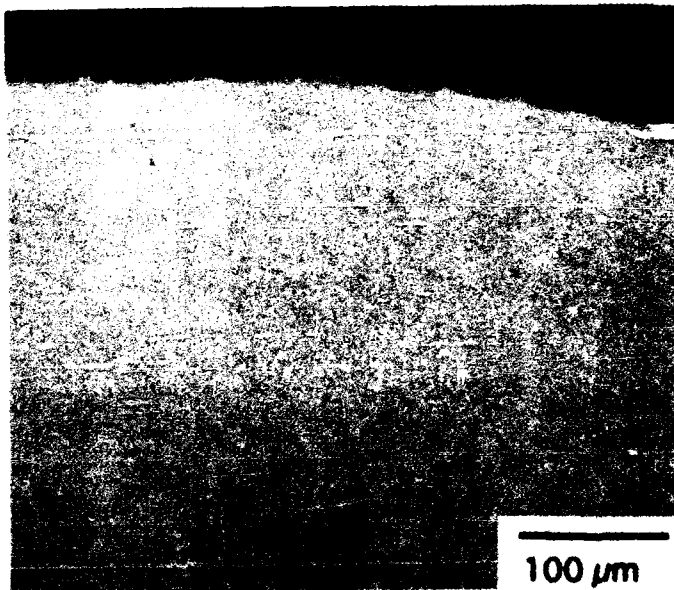


Figure 4.45 Cross sectional optical micrographs of Alloy 14 ( Nb-39Ti-20Al ) after cyclic oxidation at 800°C for 140h. The alloy had good oxidation resistance and segregation was not as apparent as in Alloys 11-13.



**Figure 4.46** Cross sectional optical micrographs of Alloy 17 ( Nb-20Ta-15Cr ) after cyclic oxidation at 800°C for 140h. The lack of Ti in the alloy harms oxidation resistance and resulted in massive spallation.



**Figure 4.47** Cross sectional optical micrographs of Alloy 19 ( Nb-30Ti-15Cr-15Al-3Si ) after cyclic oxidation at 800°C for 140h. Visually the pin looked good for the first 100h and then turned brown and spalled.

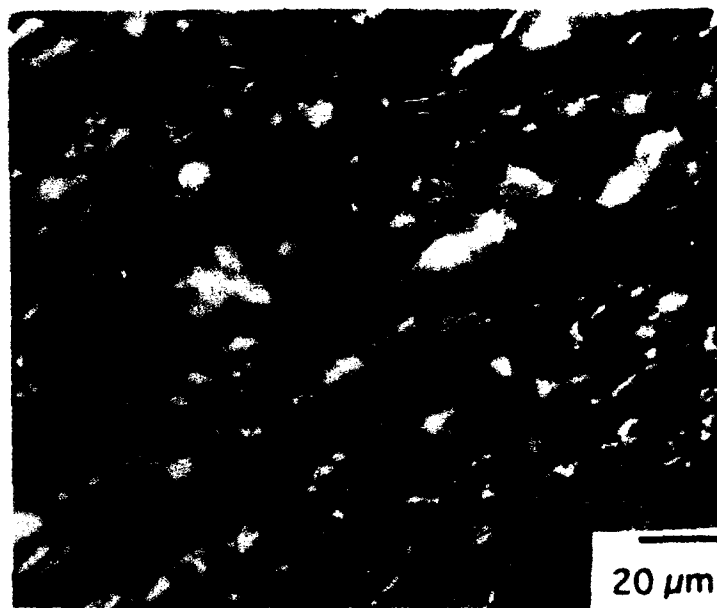
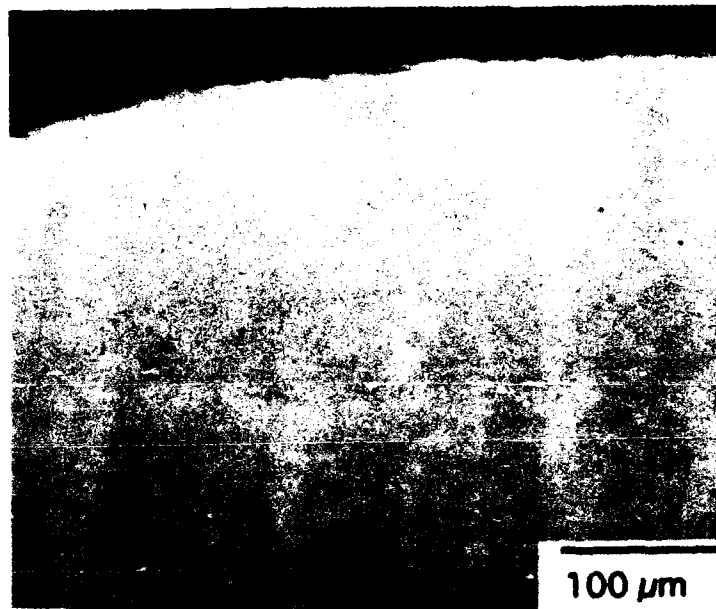


**Figure 4.48** Cross sectional optical micrographs of Alloy 20 ( Nb-30Ti-15W-15Al-3Si )  
**after** cyclic oxidation at 800°C for 140h. The pin had a heterogeneous surface with  
some areas displaying a thin oxide and others a thick oxide. The pin broke  
during the test which affected kinetic measurements.

## 5.0 Scale up of Ingot Alloys

Based on the results of the Task I screening effort, both RS & Ingot, three alloys were chosen for scaleup in Task II and property determination in Task III. The alloys chosen are given in Table 5.1. Alloy 1 was based on previous work which had been done at GE-CRD on quaternary alloys in the Nb-Ti-Cr-Al system and is expected to be a solid solution strengthened alloy similar to P5. Alloy 2 was based on the results from Alloys 9 and 10 in the screening and Alloy 3 was based on the results from Alloys 11-14 in the screening. In Alloy 2 the Si content was reduced to 1.5% compared to the screening alloy since it was felt that this may allow for a higher ductility while still retaining the fine grain size. In Alloy 3 the Mo was added to try and improve the strength and creep resistance of the ternary Nb-Ti-Al alloy. The Al was held midway between that for Alloys 11 and 12 to try to increase the strength while maintaining high ductility. The high ductility was expected to be reduced by the addition of the Mo.

Mechanical properties were determined under a range of test conditions. Most tensile tests were performed in air, although one set of specimens was tested in inert atmosphere. Attempts were made to determine times to various strain levels during the creep tests. In some instances the test was extremely short and only the failure time was recorded. Several of the specimens for Alloy 3 were removed from creep testing after 100 hours and tensile tested at room temperature. Fatigue testing was performed using 20CPM and  $R=0$  for LCF and 29Hz and  $A=0.67$  for HCF. Both Charpy impact and short rod toughness testing was performed.

## Test Plan

### 5.1 Alloy 1 Results

#### 5.1.1 Alloy 1 Processing / Microstructure Results

Alloy 1 was produced as a 7.5-cm-diameter ingot casting by triple VAR. The ingot was sealed in a stainless steel can and extruded to ~ 2.5-cm-diameter bar. The yield was very good with more than enough material to perform all of the planned mechanical testing. The microstructure of the extruded bar exhibited some segregation as shown in the backscattered electron images shown in Figure 5.1. The light and dark streaks in the backscattered electron images correspond to differences in the atomic number, with the lighter areas being higher in high atomic number elements, Nb or Cr, and the darker areas being higher in low atomic number elements, Ti or Al. The difference in the composition corresponding to the contrast difference is shown in the EDS spectra shown in Figure 5.2. A small study of the effect of thermal treatment on microstructure was performed. Small specimens of the extruded bar were heat treated at 1100 or 1150°C for 1 or 4 hours. The results of the heat treatment on the microstructure are shown in Figure 5.3.

Increasing the time and the temperature reduced the level of segregation although some segregation was present in even the highest temperature and longest time treatment. The effect of the heat treatment on the grain size can also be seen in the optical micrographs shown in Figure 5.4. The structure at the grain boundaries in Figures 5.3 and 5.4 is believed to be an etching artifact. Based on the presence of segregation and the results of the heat treat study, the heat treatment which was chosen was 1150°C for 4 hours in argon followed by a slow cool. This heat treatment was expected to remove most of the segregation while maintaining a reasonably small grain size

#### 5.1.2 Alloy 1 Mechanical Property / Microstructure Results

The mechanical property test results for Alloy 1 are given in Table 5.2. The material to be tested was expected to be solid solution strengthened with approximately 100 micron equiaxed grains. There was expected to be some segregation left over from the casting as was seen in the analysis of the ingot. As shown in Figure 5.5, which is the structure shown in the gauge section of the room temperature tensile specimen, the aim microstructure was achieved.

#### Tensile Testing In Air

The fracture surface of specimens tested at room temperature showed both cleavage and intergranular fracture, Figure 5.6a. The cleavage appeared to be the initial mechanism as shown by the direction of the crack indicated by the river markings on the cleavage facets. The final fracture was intergranular with some dimples present on the intergranular facets, Figure 5.6b. There was no visible reduction of area in the gauge section and the ductility at this temperature was very low. The cross section micrograph showed the presence of slip within the grains through which fracture had occurred, with almost no slip in grains away from the fracture surface.

The fracture surface of the specimen tested at 370°C showed dimples of various sizes, Figure 5.7a. The elongation was above 20% and necking of the specimen was observed. There was a significant amount of slip throughout the specimen, as seen in the cross section micrograph, Figure 5.7b. This fracture appears to be completely ductile.

The fracture surface of the 870°C tested specimen showed cleavage at the initiation site, Figure 5.8a, with the majority of the fracture occurring by intergranular fracture, Figure 5.8b. The low magnification micrograph of the gauge section showed the presence of fractures in the gauge section at the surface of the specimen, Figure 5.8c, with the cracks being perpendicular to the stress axis. An unusual feature of the initiation site at this temperature was the presence of beachmarks. The beachmarks appear to begin after the initiation, i.e., away from the specimen surfaces, and are present throughout the first grain of the fracture. The ductility at this

temperature dropped to an average of 12% elongation and the yield and ultimate strength were equal because of the presence of a load drop in the load - displacement curve at this temperature. The stress did increase after the yield point drop, but did not get as high as the yield point. The microstructure of the specimen consisted of equiaxed grains with very little slip seen in any of the grains, Figure 5.8d.

Tensile testing at 980 and 1200°C resulted in severely oxidized specimens which necked down to a point. The grains were significantly elongated and there was little slip seen in the cross section microstructure of the specimens. The load-displacement curve did exhibit a load drop for these temperatures; however, the work hardening increased the required load to levels above the yield point.

Based on the properties seen in this alloy as a function of temperature it appears that the ductile to brittle transition lies between room temperature and 370°C. The presence of the gauge section cracks and the beach markings on the 870°C specimen suggests an interaction with the environment. The interaction with the environment occurs in approximately 1/2 hour during the heat up, soak and actual running of the tensile test. A thin surface layer of the gauge section is expected to be embrittled by this interaction with the environment such that while the bulk of the specimen is capable of significant elongation, the surface layer fractures shortly after the specimen becomes plastic. Depending on the rate of further oxidation, these cracks can then reoxidize and retrack to grow in a stepwise fashion, if diffusion is fast enough. Alternatively, the surface layer crack can occur once and then the fracture will be dominated by the behavior of the bulk material. It could be that the beach marks are an indication of the first scenario, although the high ductility of the alloy suggests that the ductility of the matrix is controlling the final fracture. Further study would be needed to clarify this failure mechanism. By the same reasoning the diffusion of the embrittling species may be fast enough at the higher temperatures, 980 and 1200°C, and have a lesser effect on the deformation, such that the alloy has high ductility again at the higher temperatures.

#### **Tensile testing in inert atmosphere**

The fracture surface of specimens tested in an inert environment at 870°C showed a large reduction of area with significant amounts of ductile tearing, Figure 5.9a, but no evidence of dimples. There also was no evidence of either the cracks along the gauge section or the beachmarkings which were seen in the air tested specimens, Figure 5.9b. Cracks were present at the surface of the specimen, but these appear to be associated with grain boundary fractures. The ductility (22% elongation) was double that seen for the specimens tested at the same temperature in air (11% elongation).

The results of the inert tensile test appear to substantiate the role of the environment in the fracture in air at 870°C. The lack of cracks in the gauge section and beachmarkings combined with the good ductility and ductile fracture surface appearance for the inert test supports the suggestion that the air is responsible for the properties and the fracture surface appearance in the 870°C air test.

Another comparison between the inert test and the air test is the presence of both cleavage and intergranular failure in the air tests compared with ductile tearing in the inert test. The fracture in the inert test appears to be by grain boundary fracture following large amounts of deformation, Figure 5.9c. The presence of intergranular failure throughout the air fracture surface suggests that diffusion of either O or N along the grain boundaries is fast enough to embrittle the boundaries through the specimen thickness.

### **Tensile testing following thermal exposure**

Tensile testing of exposed specimens was performed to determine the metallurgical stability of the alloy. Thus, the rough specimen blanks were heat treated and exposed at 870°C for 100 hours. These specimen blanks were then finish machined to tensile specimens. The final machining removed any layers which were altered by an environmental interaction during the exposure. Tensile testing following the thermal exposure resulted in complete intergranular failure at room temperature, and nearly complete intergranular failure at 870°C, Figures 5.10 a and b. The fracture surfaces following thermal exposure are different from those seen without thermal exposure. The room temperature test of the as-heat treated material exhibited transgranular cleavage over approximately half the fracture surface and a ductile appearing intergranular fracture over the other half. The room temperature test following exposure exhibited intergranular fracture over the entire surface with no indications of ductility. At 870°C the as-heat treated specimen exhibited gauge section cracks, transgranular cleavage fracture, intergranular fracture and pronounced beachmarkings, while the exposed material exhibited similar features but predominantly intergranular fracture.

Micrographs taken from the cross section of the gauge section showed the presence of a precipitate which was aligned along the specimen axis, Figure 5.10c. The alignment of the precipitates is believed to correlate with the segregation patterns which were seen in the original extrusion. The identity of the precipitate has not been determined although it is probably the laves phase based on the Cr level in the alloy.

Two possible explanations for the presence of large amounts of intergranular fracture in these specimens are that the alloy has undergone precipitation at the grain boundaries or that O or N has diffused along the grain boundaries, similar to what was described above. No conclusive evidence for a grain boundary film could be observed in any of the micrographs. Further

analysis of the grains using analytical techniques, such as TEM would be required to answer the question of what caused the change to predominantly intergranular fracture. The lower strength of the alloy may also be associated with the presence of the precipitate. Since the alloy is solid solution strengthened, the loss of solid solution strengthening elements to form the precipitate may cause a reduction in the overall strength of the alloy if the precipitate does not increase the strength of the alloy. Based on the relatively large size of the precipitate, approximately 1-5 microns, it is expected that the precipitate is in the overaged condition and would not increase the strength of the alloy. Thus, the loss in strength is believed to be associated with the loss in solid solution strengtheners which indicates that the alloy is unstable.

### **Tensile testing with a notch**

The fracture surface of the notch tensile test at room temperature consisted of transgranular cleavage only, Figure 5.11a. The 870°C test had similar fracture features to those seen in the other 870°C tests, i.e., initiation, beachmarkings, cleavage and intergranular fracture, Figures 5.11b and c

The notch strength ratio was 2.4 at room temperature and 1.5 at 870°C. The notch ratio at room temperature is high because the full strength was not reached due to the low ductility of the alloy. Using the strength at 370°C as the denominator, the low temperature notch ratio becomes 1.5.

### **Creep**

It appears from the creep specimens which were tested at 870°C that the stress for a reasonable creep time at this temperature is below 205 MPa. Because of the low times to failure in these specimens a comparison can be made between these creep specimens and the tensile testing done in air. The first comparison is the size of the surface cracks seen in the three tests. The cracks are fewer and much larger in the tensile test while the number of cracks increases and the individual crack sizes get smaller as the test time increases, Figure 5.12. Also the beachmarkings proceed further into the specimen as the time to failure increases, Figure 5.13. The fracture surface appearance is different in the three tests. In the tensile test at room temperature the fracture is predominantly transgranular cleavage with some intergranular failure. For the short time creep test, 10-5, Figure 5.14a, the amount of cleavage is reduced, although still being the fracture feature at the initiation, while the amount of intergranular fracture is increased. Finally, the fracture surface for specimen 10-6, Figure 5.14b, appears to be more ductile with dimples being present with some intergranular fracture. The microstructure of the specimens changes with time from no precipitation in the tensile test to a small amount of precipitation in the two creep tests, Figures 5.15a and b.



Based on the presence of beachmarkings and surface cracks it is believed that the failure mechanism for creep is similar to that seen in the tensile test. The change in fracture surface characteristics may be related to a strain rate effect although this cannot be determined since the final strain for these specimens was not determined. An alternate explanation could be that the strength and ductility of the alloy are changing during the test due to the precipitation. This precipitation may lead to an increase in the ductility of the material, as was seen in the exposed tensile results for specimen 10-10, thus resulting in a more ductile appearing fracture surface.

## **Fatigue**

Both LCF fractures initiated at the surface and proceeded by transgranular cleavage through most of the specimen. The initiation cause was not determined. Final fracture was by intergranular failure, Figure 5.16a and b. There was no evidence of beachmarkings on the fracture surface or gauge section surface cracks on any of the fatigue specimens. Both of the LCF tests were very short, lasting for approximately 2-3 minutes only, at the 20 CPM testing rate. The HCF specimens were not examined.

## **Impact / Toughness**

The impact data show an increase between room temperature and 870°C. The energy absorption is lower at 870°C than expected based on the tensile ductility found at that temperature. The toughness value was higher than expected based on the low ductility observed in the tensile test at room temperature. Both of these results are not understood at present.

## **Summary**

This alloy appears to be brittle at room temperature based on the tensile, exposed tensile and impact results, however the notch tensile and toughness results are better than might be expected for materials such as intermetallics. The 870°C data showed an interaction with the air environment which may have affected the strength and ductility of the alloy. The higher temperature properties were affected by the poor oxidation resistance of the alloy which will be discussed in Section 5.3.4.

## **5.2 Alloy 2 Results**

### **5.2.1 Alloy 2 Processing / Microstructure Results**

The actual composition for Alloy 2 is Nb-28.5Ti-15Cr-1.5Si. This ingot was produced by triple VAR. The ingot was solution treated at 1350°C for 6 hours and then forged using process conditions of 1300°C and 1.25-cm-per-second crosshead rate. The choice of forging as

compared to extrusion, which was used for Alloy 1, was because this alloy was produced at a different subcontractor. The objective was to achieve a 75% reduction in the ingot diameter; however, the ingot fractured, with multiple cracks appearing at the top and bottom of the ingot, after a very small deformation was achieved. The structure of the ingot was characterized in three places, near a crack at the bottom, near a crack at the top, and general structure near the side of the ingot. The microstructure of the ingot consisted of grains with a second phase, precipitating both within the grains and at the grain boundaries, as seen in Figure 5.17. Either the porosity or the grain boundary phase, may have caused the cracking. As shown in Figure 5.18a, the crack at the bottom appears to have occurred through the linking of porosity which was present in the ingot. A HIP following the ingot production may have removed this failure mechanism. The crack at the top, Figure 5.18b, appears to be following a grain boundary. All grain boundaries had a high volume fraction of second phase which would be either a NbCr<sub>2</sub> type or a silicide phase, either of which would be expected to be brittle. Therefore, it is believed that the fracture may have been related to the presence of the grain boundary phase. Alternate thermal treatments prior to forging may have produced a structure which was more amenable to working into billet. Because of the extensive cracking of this material further work was abandoned.

### 5.3 Alloy 3 Results

#### 5.3.1 Alloy 3 Processing / Microstructure Results

The actual composition for Alloy 3 was 45Nb-41Ti-12.5Al-1.5Mo. This ingot was produced by triple VAR in an 8.25cm diameter mold. The reduction of the ingot to billet was by forging which was done after holding the ingot at 1150°C for 1.5 hours. The processing consisted of upsetting and squaring through five steps to a final billet which measured 3 x 24 x 15 cm. A picture of the resulting billet is shown in Figure 5.19.

A heat treatment study was performed to determine a heat treatment for the billet. Initial studies were performed on residual material from screening Alloys 11 and 12. The heat treatment matrix for the material from these two alloys is shown in Table 5.3.

The 800°C solution heat treatment for Alloy 11 resulted in retention of an elongated grain structure which had presumably recovered but has not recrystallized, Figure 5.20a. Aging the 800°C structure at 500 and 600°C, Figure 5.20b and c, resulted in inhomogeneous precipitation on what appear to be subboundaries. Aging at 700°C, Figure 5.20d, did not show precipitation; however, this may have been a sampling artifact since the tensile tested specimen, which received a similar aging treatment, did show precipitation in the unrecrystallized regions. The transus for this alloy is between 700 and 800°C based on the lack of precipitation at 800°C and low volume fraction of precipitation seen in the unrecrystallized regions following an age at 700°C.

The 900 and 950°C solution treatments of Alloy 12 resulted in the retention of elongated grains. There does appear to be some precipitation at subboundaries in the 900°C treated structure, Figure 5.21a, but no precipitation in the 950°C treatment structure, Figure 5.21b, indicating that the transus for this alloy is between 900 and 950°C. The 1000°C heat treatment did result in a low volume fraction of recrystallized grains, Figure 5.22a, surrounded by unrecrystallized regions. Aging of the 1000°C structure at 500°C, Figure 5.22b, 600°C, Figure 5.22c, and 700°C, Figure 5.22d, resulted in significant precipitation in the unrecrystallized regions, with a low volume fraction of precipitation in the recrystallized regions. The volume fraction of precipitation increased in both the recrystallized and unrecrystallized regions with increasing age temperature, from high volume fractions of precipitate in the 500°C age to complete precipitation in the 700°C age for unrecrystallized regions, and no precipitation in the 500°C age to some precipitation in the 700°C age for recrystallized regions. Based on the results from Alloys 11 and 12, it appears that higher temperature solution and age heat treatments should be investigated for Alloy 3.

The heat treatment study for the actual composition focussed on determining three treatments, i) a solution treatment which would not recrystallize the structure but would allow for recovery, ii) a solution treatment which would allow for a fully recrystallized structure, and iii) a direct age treatment which would allow for full precipitation. The final Alloy 3 composition was subjected to the heat treat matrix shown in Table 5.4.

The as-forged structure consists of elongated grains with no evidence of precipitation, Figure 5.23. The 950°C solution treatment for 1 hour appears to have resulted in a very low volume fraction of recrystallized grains with no precipitation, but presumably a recovered structure, Figure 5.24. The recrystallization is indicated in the age treatments following this solution treatment, for example, the 650°C age following the 950°C solution is shown in Figure 5.25a where the precipitation appears to have occurred at subboundaries with a very low volume fraction of recrystallized grains as shown by the precipitation free regions. Each of the other solution heat treatments resulted in some degree of partial recrystallization with the 1100°C / 4 hours solution heat treatment coming closest to achieving a completely recrystallized structure as shown in Figure 5.25b. Based on these results the two solution treatment possibilities are i) solution treat at temperatures below 950°C for approximately 1 hour to recover the structure but avoid recrystallization, and ii) heat treat at 1100°C for greater than 4 hours or at higher temperatures to provide a fully recrystallized structure. The most promising aging treatments which could be applied following these solution treatments are the 700°C or 750°C treatments as shown for the 950°C / 1 hour solution treatment in Figures 5.26a and b. The 650°C treatment results in a finer structure but appears to be very inhomogeneous as was seen in Figure 5.25a. The 800°C age results in a very low volume fraction of second phase in all treatments, Figure 5.27.

The direct age treatment resulted in complete precipitation for all aging temperatures, Figure 5.28 a-d. The transus for this alloy appears to be near 800°C based on the low volume fraction of second phase present in all specimens from that thermal treatment. The structure which appears to be outlining the grains in the direct age at 700°C has been determined to be a specimen preparation artifact. The direct age treatment was chosen to be the 750°C age for the reason that it was the highest temperature age which resulted in full precipitation. For similarity, the age for the solution and age treatment was also chosen to be 750°C although for a longer time. The choice of a longer time for the solution and age treatment was because of the slower precipitation kinetics seen in that structure. A small heat treatment matrix was performed to ensure that the times and temperatures selected for the solution and age heat treatment would provide the desired structures. The heat treatments were 1100°C / 8 hours solution with a 750°C age for either 50 or 100h, Figure 5.29a and b. The 1100°C solution treatment followed by a 750°C age for 50 hours provides the desired structure.

Because of the lack of testing on Alloy 2, two heat treatments were selected for Alloy 3 testing. The primary treatment was considered a direct age and consisted of forging plus heat treating at 750°C, for 25 hours followed by a furnace cool. The alternate treatment was forging followed by an 1100°C / 8 hour solution treatment and age at 750°C, for 50 hours and furnace cooling. The longer time in the age for the alternate heat treatment was required due to the slower precipitation in the fully recrystallized structure. The direct age was used for most of the testing and the solution and age was used for a limited test matrix. The direct age structure consisted of elongated matrix grains which contained a large volume fraction of a fine precipitate as shown in Figure 5.28c. The grains were plate shaped and were elongated in the plane of the deformation, which resulted in the long axis of the grains lying parallel to the stress direction in the uniaxial tests. The solution and age structure consisted of equiaxed grains of the matrix with a fine precipitate as was shown in Figure 5.29a. The precipitate in the solution and age structure appeared to be coarser than that seen in the direct age structure.

### 5.3.2 Alloy 3 Mechanical Property / Microstructure Results for Heat Treatment 1

#### **Tensile testing**

The mechanical property test results for Alloy 3 are given in Table 5.5. The tensile failures at room temperature exhibited large amounts of deformation with grain flow evident on the specimen surface, Figure 5.30a. The fracture surface exhibited dimple failure, Figure 5.30b, as would be expected from the high ductility of the alloy at this temperature. The fracture surface exhibited some tendency for alignment of the dimples which is believed to be associated with the fine laths contained in the underlying microstructure.

The failures at 260, 565, and 650°C were similar to the room temperature failure except that the dimple size was larger in the high temperature cases as shown in the comparison of the micrographs from the 260°C and room temperature tests shown in Figure 5.31. The 565 and 650°C tests exhibited fractures on the gauge section which were perpendicular to the stress axis as shown in the micrograph for the 650°C specimen, Figure 5.32. It is believed that the small fractures on the gauge section occur because of an embrittlement of the surface by the environment during the testing. The large strain in the neck region causes the fracture of this embrittled surface region during the final failure.

The 980°C test specimen exhibited significant oxidation of the material. The specimens necked down to a point consistent with the high elongations observed, Figure 5.33a. The microstructure of this specimen consisted of elongated grains with serrated grain boundaries, Figure 5.33b, the lack of precipitate indicates that this test was performed above the beta transus for this material.

Alloy 3 exhibited good combinations of tensile strength and ductility as a function of temperature. The concentration of the testing at the lower temperatures was done because of the tensile results which were obtained in the screening studies on Alloys 11 and 12 indicating low strengths at high temperatures. These low strengths were born out by the 980°C test results. At all temperatures studied the failure appears to have been by normal ductile failure modes. The only exception was the surface cracking on the gauge section seen in the tests at 565 and 650°C which was attributed to an environmental interaction. It should be noted that while the surface cracking was observed in this alloy, there was no observation of the beachmarks, cleavage fracture or intergranular fractures seen in scaleup Alloy 1. This difference may be attributed to differences in oxidation rate, test temperature, or material mechanical properties.

### **Inert testing**

The properties determined in inert testing are very similar to those seen in the air testing. The fractures exhibited similar features to those seen in the air test, such as reduction of area, (compare figure 5.34a with 5.32a), and dimples on the fracture surface, (compare Figure 5.34b with 5.34c). The one difference between the two fractures was the absence of the surface cracks along the gauge section on the inert specimens while such cracks were seen in the air test specimens. This again suggests that the surface cracks are caused by interaction with the environment. The similarity in the properties for the inert and air tests also indicates that the surface cracks have little to do with the tensile properties for the alloy, although they may affect other properties, especially cyclic properties.

### **Exposed testing**

These specimens were cut to specimen blanks, heat treated, exposed at 650°C for 100 hours and final machined into specimens. Thus, this exposure measures the metallurgical stability of the

alloy. As seen in the data table both the room temperature and elevated temperature strength properties were increased for the exposed specimens over the as - heat treated specimens. A comparison using backscattered electron imaging in the SEM of the structure seen in specimen 1B with that seen in specimen 5B, Figure 5.35, does seem to indicate some slight coarsening of the structure. Another indication of the difference in microstructures is seen in the fracture surface where the dimple size for the 650°C test is smaller following the thermal exposure than that seen in the test following the heat treatment, compare Figure 5.36 with 5.31. The dimple size seen in the room temperature tests was comparable although both were smaller than that seen for testing at elevated temperatures.

The strengthening of the alloy following the thermal exposure indicates that the original heat treatment selected does not result in a completely stable structure or properties. The improvement in strength and decrease in ductility implies that the original heat treatment produced material which was not in the peak aged condition. Further investigation of the deformation - heat treatment - properties relationships for this alloy would be needed to determine the optimum heat treatment conditions for specific applications using this alloy.

### **Notched tensile testing**

The notched tensile results show that the material notch strengthens, as expected for a material with this level of ductility. The notch strength ratio was about 1.5 for both 20 and 650°C. The fracture surfaces showed the same types of failures seen in the smooth bar air tensile tests.

### **Creep testing**

Of the five specimens which were creep tested, three failed within 10 hours, and two were stopped at 100 hours, Table 5.5. Of the three failed specimens, 7T and 7M failed with what appears to be a bimodal fracture surface. The fracture in both specimens appears to have initiated by cleavage failure, Figure 5.37, while the final fracture was by ductile failure mechanisms as shown by the presence of dimples. There was no significant difference observed in the microstructure of these specimens, compared to the tensile specimens, which would cause the observed change in fracture mechanism from ductile failure as shown by dimples to cleavage fracture initiation in the creep test. The brittle region of the fracture surface was tinted, indicating that it had been exposed to the atmosphere longer than the ductile fracture region. At this point the cause of the brittle fracture surface region is not understood. The possibilities are some sort of environmental interaction or a hold time crack growth phenomena. Further investigation would be required to clarify this point. The creep testing which was done at 980°C was similar to the tensile testing done at very high temperature in that the creep test also necked down to a point with high elongations.

Most of the creep conditions were chosen such that a comparison with previous data would be possible. Thus, the 650°C tests at 175MPa and 385MPa allow for a comparison with previous data. Comparing the data for this alloy with data presented in the Very High Temperature Titanium Base Materials final (10) contract report for the orthorhombic alloys the following comparisons can be made. The time to 0.2% creep for the 650°C / 175 MPa test done in both cases shows a time of 31.8 hours for the alloy in this contract versus a time of 6 hours for the orthorhombic alloy. Comparing 650°C / 385MPa shows 0.7 hours for this alloy compared to 0.5 hours for the orthorhombic alloy. Based on these comparisons it appears that the alloy developed under this contract has creep capability above that of the orthorhombic alloy. However, it should be stressed that these data are very limited and the comparison is for the orthorhombic alloy in a single heat treatment.

Although there had been no plan to perform testing following a stressed exposure, the two unfailed specimens provided the opportunity to do this type of testing. Therefore, the two unfailed specimens were sent back for tensile testing to failure at room temperature to get an indication of the effect of the stressed exposure on properties. Both a 650°C / 175 MPa and a 760°C / 105MPa specimen were available for this testing. The surface condition of the specimens prior to testing is shown in Figure 5.38, and as expected both surfaces were oxidized with the surface of the 760°C specimen being more oxidized than the surface of the 650°C specimen. The results of the tensile testing are shown in the data table. Specimen 6M exhibited approximately a 50MPa drop in both the yield and ultimate strength with a drop in the elongation from about 12% to about 7%. The fractured specimen exhibited grain deformation and reduction of area, Figure 5.39a, in the gauge section. Fractures on the specimen surface perpendicular to the stress axis, and dimples on the fracture surface, Figure 5.39b, were observed. All of these features are similar to features which were seen in the tensile testing which was done in air. Specimen 6B broke during setup, however, an analysis of the fracture surface indicates that the fracture was very similar to that seen in the test done on specimen 6M including dimples on the fracture surface which would indicate a ductile fracture, Figure 5.39c and d. SEM micrographs of the microstructure of both specimens did not reveal any indications of unusual structure which could be expected to significantly affect the properties, Figure 5.40. It appears that the alloy is not seriously degraded by a stressed exposure, at least at temperatures up to 650°C.

### **Fatigue testing**

Both of the specimens used for LCF testing had inhomogeneities in the gauge section which were found after the LCF test. It is believed that these inhomogeneities were unmelted Nb particles. The fracture of both specimens was associated with the inclusions; however, it could not be determined if the inclusions were the initiation site. The fracture surfaces exhibit dimples on specimen 13T and striations on 13B, Figures 5.41a and b, respectively. The difference in fracture surface between the two specimens is expected to be due to a difference in the location of

the analysis, in the fatigue crack growth region for 13B and in the overload region for 13T. Further analysis would be expected to show examples of both types of fracture surface features on both specimens.

Both of the HCF tests were performed on good material. One of the specimens, 14T, went to runout of 10 million cycles. The other specimen failed at 126,038 cycles at an A ratio of 1.0 and a mean stress of 279MPa as shown in the data table. The fracture initiated at the surface, grew across approximately half the specimen and then failed by ductile overload, Figure 5.42.

Because of the presence of the Nb inclusions, the cycles to failure for the LCF specimens are considered to be minimums for the alloy. This was the only instance of problems with the melt practice which affected the results of the mechanical testing. Based on comparison with fatigue data on other alloys, the fatigue capability of this alloy is comparable to other titanium aluminides such as alpha-2 or orthorhombic and high temperature titanium alloys such as AF2. Even without the inclusion problem, the fatigue testing of the alloy was very limited and further data should be obtained to determine the fatigue capability of the material.

### **Impact testing**

The results of the impact testing varied significantly both at a given temperature and as a function of temperature. Some of this variation was related to the orientation of the grains with respect to the crack direction. As stated previously the grains are elongated within the plane of the forging. If the crack front direction was perpendicular to the long axis of the grains the toughness was highest while if the crack front direction was parallel to the long axis the toughness was lowest. There was fairly good correlation between the crack direction and toughness, especially at the two lower temperatures.

The impact results at -40°C indicate that the DBTT for this material is below -40. The dip in impact at room temperature is not understood at this time, but may be associated with a grain orientation effect. The effect of the grain orientation was not expected and further testing of the alloy would be needed to completely determine the effect of orientation on impact energy. The further analysis would be to carefully orient the grains in relation to the crack direction and determine the properties in the three directions.

### **Toughness testing**

Both of the toughness tests were invalid because of the high toughness of the alloy. The short rod toughness specimen, which was used for this test, was designed for low toughness materials. Because of the toughness of this alloy the specimen could not be fractured without



significant plasticity. Therefore, it is expected that these toughness values are minimums for this alloy. Compact tension specimens would be required to obtain valid toughness values.

## **Summary**

This alloy shows good combinations of strength and ductility. The creep and fatigue strength of the alloy are comparable to orthorhombic base material reported in the Very High Temperature Titanium Base Material final report (10). However, the ductility, notch tensile ratio, post creep tensile, impact and toughness properties are all better than that seen in the intermetallic materials such as alpha-2 or orthorhombic. The tensile strength of this alloy was lower than that of the intermetallic materials. However, as shown by the exposed tensile test results it was possible to produce material which has higher strength than the material studied here. Based on the properties measured for this alloy it does not appear to be capable of being used at the very high temperatures envisioned in this contract.

### **5.3.3 Alloy 3 Mechanical Property / Microstructure Results for Heat Treatment 2**

As stated previously the second heat treatment consisted of a solution and age which was expected to result in an equiaxed grain structure with precipitate within the grains. The testing which was done consisted of tensile and creep testing, with post creep tensile testing being done on unfailed creep specimens.

#### **Tensile testing**

As shown in Table 5.6, the tensile strength of Alloy 3 in this heat treatment condition was lower at all temperatures tested than was measured in heat treatment 1. The ductility was higher than that measured in heat treatment 1. The microstructure of the alloy is shown in Figure 5.43 from which it can be seen that the grains are equiaxed and contain a precipitate. The precipitation has not gone to completion as shown by the precipitate free regions. It is expected that higher strengths could be achieved with this heat treatment had the precipitation gone to completion. There is evidence of grain boundary failure away from the fracture surface in the room temperature test as shown in Figure 5.44. This grain boundary failure away from the fracture surface was not observed in heat treatment 1; however, the observation of such fractures in heat treatment 1 may have been complicated by the elongation of the grains in that heat treatment, such that it was difficult to find grain boundaries which were properly oriented and near the fracture surface. Other features of the fracture at various temperatures, such as dimples, and cracks in the gauge section are similar for the two heat treatments.

## Creep testing

The only creep specimen which went to failure was the test at 980°C / 14MPa. As described in the tensile test section for heat treatment 1, this test temperature was above the transus for the alloy and thus the microstructure consisted of a single phase structure. The heavy oxidation of the alloy caused a significant reduction in the cross section of the specimen through spallation and an increase in the surface oxygen content of the alloy during the test, Figure 5.45.

The properties of the alloy in this heat treatment were below those of the alloy in heat treatment 1. The times to 0.2% creep were shorter and total creep elongations in a given time ( 100 hours ) were higher for heat treatment 2 than were measured in heat treatment 1. This result may be due to the lack of complete precipitation observed for this heat treatment.

Similar to heat treatment 1, it was possible to perform two tests of tensile properties following creep testing on this heat treatment. These two specimens were the same conditions as those used for heat treatment 1, 650°C / 175MPa, and 760°C / 105MPa. The surfaces of these specimens were similar to those observed on heat treatment 1 specimens as shown in Figure 5.46. The fracture surfaces of these two specimens exhibited more intergranular failure than was seen in the tensile specimens, Figure 5.47. Compared to the tensile test on as-heat treated material, specimen 18T had a lower ductility and higher strength while specimen 18M exhibited roughly the same properties as the as-heat treated tensile test. The lower ductility measured in specimen 18T correlated with more intergranular failure than that seen in 18M which had both more transgranular failure and higher ductility. The fracture surfaces still appeared ductile with tear ridges which conformed to the shape of the plates which were in the microstructure, Figure 5.48. It appears that there may be some effect of a stressed exposure on the mechanical properties of the alloy in this heat treatment condition, however, further investigation would be required to confirm this observation.

## Summary

It was hoped that the larger equiaxed grain size of the alloy in this heat treatment would provide improved creep resistance. The lack of complete precipitation made the efficacy of this approach difficult to determine.

### 5.3.4 Oxidation Testing of Scaleup Alloys

Cyclic oxidation results at 760°C for downselected Nb-Ti alloys and other materials are shown in Figures 5.49 and 5.50. In decreasing order, the oxidation resistance of the various classes was such that the Ni-Cr superalloy ( René 41 ) > Ti-48Al-2Cr-2Nb (gamma) ~ Ti-24.5Al-12.5Nb-1.5Mo (alpha-2) > Titanium beta alloy (beta 21S) > Ti-Nb orthorhombic alloys > Nb-Ti alloys

>> Cb 752. The higher Nb/Al content of the Nb-Ti alloys degraded oxidation resistance when compared to the Ti-aluminides and Ti-Nb orthorhombic alloys. The higher Nb/Al resulted in more rapid oxygen uptake and spallation. The Nb-Ti alloys were far superior to Cb 752 which disintegrated before the first inspection period. X-ray diffraction showed that the Cb 752 was totally converted into  $Nb_2O_5$  which explains the catastrophic oxidation. The René 41 was superior to the other alloys as expected from the oxidation screening test.

Surface micrographs of the alloys taken following the oxidation test are shown in Figures 5.51-5.56. Figure 5.51 shows the René 41. A continuous dark grey chromia scale is observed on the surface with no spallation.

Figure 5.52 shows the Ti-48Al-2Cr-2Nb and Ti-24.5Al-12.5Nb-1.5Mo. The gamma alloy exhibits a scale with little spallation, while the alpha-2 alloy shows spallation (white regions) and dark oxide patches where oxide has healed after a spallation event. Also present on the alpha-2 are machining marks from the low stress grind process used during sample processing.

Figure 5.53 shows the beta 21S and the Ti-Nb orthorhombic alloys which both exhibited some spallation. The beta 21S exhibited a heterogeneous dark grey and yellowish-green scale. The Ti-20Al-23Nb and the Ti-22Al-27Nb alloys appeared off white with patchy oxide formation that may result from locally thick oxide, loosely adherent oxide or the grain structure.

Figures 5.54 and 5.55 shows the Nb-Ti Alloy 1, Nb-32Ti-10Cr-6Al, Alloy 2, Nb-28Ti-15Cr-1.5Si, Alloy 3, Nb-39Ti-12.5Al-1.5Mo, and 3899-3 which was described in Section 4.5. Alloys 1 and 2 appeared orange brown with thick scales that were spalling. The spalling resulted in the negative weight changes shown in Figure 5.49. Alloy 3 and the 3899-3 alloy exhibited thick scales with Alloy 3 having a white scale that spalled profusely, while the 3899-3 alloy was dark brown and had some spallation.

Figure 5.56 shows the Cb 752 after the first inspection at 21 hours. The sample was reduced to layered white flakes and was totally disintegrated. The oxidation resistance advantage of the Nb-Ti alloys over Cb 752 is obvious.

A hardness profile underneath the oxide scale is shown in Figure 5.57 and indicates the extent of interstitial embrittlement for the tested alloys. The Nb-Ti alloys all exhibit a hard distinguishable layer underneath the external oxide scale. Table 5.7 shows the extent of this layer and the peak hardness value. Under this layer, the hardness decays to baseline values in ~100 microns as measured from the surface. The beta 21S and the Ti-Nb alloys show hardening at the external surface (~500 KHN) and decay to baseline hardnesses in ~80 microns. The Ti-aluminide alloys did not show an embrittled layer, although one is likely present. The René 41 shows softening underneath the chromia scale as a result of losing solid solution and precipitation strengtheners to

oxide scale formation. Optical micrographs of cross sections where the hardness readings were taken are shown in Figures 5.58-5.67.

Figure 5.58 shows a barely visible chromia scale on René 41 with an 8-micron denuded region. The hardness indent under the region is much larger than others showing the softening behavior in this area.

Figure 5.59 shows the Ti-48Al-2Cr-2Nb gamma alloy. A thin 3-micron external scale is observed above a 12-micron sublayer. Other work has shown this layer to be alpha-2 caused by interstitial enrichment or Al denudation. The indents were not made in these layers and, therefore, no hardening was observed.

Figure 5.60 shows the Ti-24.5Al-12.5Nb-1.5Mo alpha-2 alloy. The micrographs show a darker etching region next to the surface, but hardness readings do not indicate extensive interstitial enrichment over readings made in the center of the alloy. An indent made near the surface, however, caused cracking indicating that an embrittled layer may exist. No external scale is observed, therefore, this may be a region where the oxide has spalled.

The cross section of the beta 21S alloy is shown in Figure 5.61. A precipitate outlines grain boundaries and does not suffer preferential oxidation attack. The surface shows an 8-micron external scale with a white imaging layer underneath that may be alpha case. The indents miss these layers, but hit the darker etching region that shows some elevated hardness.

The cross sections of Ti-20Al-23Nb and Ti-22Al-27Nb are shown in Figures 5.62 and 5.63. Ti-20Al-23Nb shows an external scale of 20 microns and a dark etching region of 30 microns. The indent that hits the bottom of the etched region shows an increase in hardness. The Ti-22Al-27Nb alloy shows similar features with the exception of an oblate primary phase. The external oxide was only ~8 microns thick possibly due to spallation, while the darker etching region was 28 microns. Hardness readings again indicated that this region had elevated hardness.

Figures 5.64-5.67 show the Nb-Ti alloys after oxidation and hardness testing. Immediately obvious in all the cross sections is a distinguishable interstitial layer underneath an external oxide scale already characterized in Table 5.7. Indents show cracking and, therefore, the brittle nature of the layer. In the case of the 3899-3 alloy, internal oxides precipitated in the alloy underneath the layer. The external oxide thicknesses showed variability as a result of the greater propensity for these alloys to spall. The microstructures for Alloys 1 and 3 show etching features that might indicate segregation or nonuniform deformation that might affect oxidation performance.

**Table 5.1 Compositions (Atm.%) Of Alloys Selected For Scale-Up**

<b>Alloy Number</b>	<b>Composition (Atm. %)</b>
1	Nb-32Ti-10Cr-6Al
2	Nb-28.5Ti-15Cr-1.5Si
3	Nb-41Ti-12.5Al-1.5Mo

**Table 5.2 Mechanical Property Results For Alloy 1.**

**Tensile In Air**

Spec. ID	Test Temperature		Atm	Exposure Temperature °C	Yield Stress		Ultimate Stress		Elong. %
	°F	°C			MPa	Ksi	MPa	Ksi	
9-1	70	21	Air			*	543	77.8	0.7
9-2	70	21	Air			*	547	78.3	1.1
9-3	700	371	Air		668	95.6	818	117.1	23.3
9-4	700	371	Air		664	95.1	827	118.4	23.9
9-5	1600	871	Air		455	65.2	455	65.2	9.8
9-6	1600	871	Air		422	60.4	422	60.4	13.9
9-7	1800	982	Air		201	28.8	224	32.0	57.9
9-8	1800	982	Air		225	32.2	225	32.2	66.4
10-1	2200	1204	Air			**			
10-2	2200	1204	Air		53	7.6	66	9.4	***

**Tensile In Inert Atmosphere**

10-3	1600	871	Inert		370	52.9	419	60.0	21.0
10-4	1600	871	Inert		418	59.9	460	65.8	24.0

**Tensile Following 100 Hour Thermal Exposure Of Unmachined Specimen Blanks**

9-9	70	21	Air	871		**			
9-10	70	21	Air	871		**			
10-9	1600	871	Air	871	349	50.0	377	54.0	7.3
10-10	1600	871	Air	871	324	46.4	370	52.9	22.4

**Notched Tensile**

**NSR**

7-1	70	21	Air				1349	193.1	2.4
7-2	70	21	Air				1259	180.2	
7-3	1600	871	Air				659	94.3	1.5
7-4	1600	871	Air				698	99.9	

\* Failed before reaching 0.2% offset

\*\* Thread failure

\*\*\* Too oxidized to obtain reading

Table 5.2; cont.

Creep

Spec ID	Test Temperature		Atm	Creep Stress		Time To Failure (Hours)
	°F	°C		MPa	Ksi	
10-5	1600	871	Air	275	40	0.3
10-6	1600	871	Air	205	30	1.7
10-7	1800	982	Air	140	20	0.5
10-8	1800	982	Air	100	15	1.2

Fatigue

LCF	20CPM, R=0			Total Strain	Cycles To Failure		RT Modulus			
3-1	1600	871	Air	1.20%	43		14.7			
3-2	1600	871	Air	1.00%	59		15.3			
HCF	29Hz			Cycles to Failure	Maximum Stress		Mean Stress		Alternating Stress	
					MPa	Ksi	MPa	Ksi	MPa	Ksi
4-1	1600	871	Air	Tens. at mean	870.3	124.6	521.1	74.6	349.3	50.0
4-2	1600	871	Air	30,856	348.6	49.9	208.9	29.9	139.7	20.0

Charpy Impact Testing				J	Ft/Lbs
1-1	-40	-40	Air	2.7	2
1-2	-40	-40	Air	2.7	2
2-1	70	21	Air	2.7	2
2-2	70	21	Air	2.7	2
8-1	1600	871	Air	12.2	9
8-2	1600	871	Air	12.2	9

Short Rod Toughness Testing				MPa√m	Ksi√in
11-1	70	21	Air	54.2	49.3
11-2	70	21	Air	54.7	49.8

### Table 5.3 Aging Studies

Aging Studies performed on screening Alloys 11 and 12 to help define heat treatment conditions for Alloy 3, Nb-41Ti-12.5Al-1.5Mo

Alloy	Solution Treatment		Aging	
	Temperature	Time	Temperature	Time
	°C	Hour	°C	Hour
11) 50Nb-40Ti-10Al	800	4		
	800	4	500	24
	800	4	600	24
	800	4	700	24
12) 45Nb-40Ti-15Al	900	4		
	950	4		
	1000	4	500	24
	1000	4	600	24
	1000	4	700	24



Table 5.4 Heat Treatment Matrix For Alloy 3

Solution Treatment		Aging					
Temperature °C	Time Hour	Temperature					Time Hour
		No Age	650°C	700°C	750°C	800°C	
950	1	X	X	X	X	X	20
950	4	X	X	X	X	X	20
1000	1	X	X	X	X	X	20
1000	4	X	X	X	X	X	20
1100	1	X	X	X	X	X	20
1100	4	X	X	X	X	X	20

Table 5.5; Mechanical Property Results For Alloy 3.

<b>Tensile In Air</b>										
Spec. ID	Test Temperature		Atm		Yield Stress		Ultimate Stress		Elong %	R of A %
	°F	°C			MPa	Ksi	MPa	Ksi		
1T	70	21	Air		858	122.8	885	126.7	11.9	34.9
1M	70	21	Air		872	124.8	944	135.1	11.7	22.4
1B	500	260	Air		717	102.6	803	114.9	11.5	38.5
2T	500	260	Air		744	106.5	781	111.8	10.3	39
2M	1050	566	Air		681	97.5	747	106.9	10.6	37.3
2B	1050	566	Air		693	99.2	770	110.3	12.3	40.2
3T	1200	649	Air		593	84.9	776	111.1	9.5	29.4
3M	1200	649	Air		660	94.5	724	103.6	14.0	49.2
3B	1800	982	Air		55	7.9	78	11.1	96.4	96.3
4T	1800	982	Air		55	7.9	67	9.6	61.8	95.5
<b>Tensile In Inert Atmosphere</b>										
4M	1200	649	Inert		599	85.7	735	105.2	12.0	67
4B	1200	649	Inert		658	94.2	748	107.1	10.0	41
<b>Tensile Following 100 Hour Thermal Exposure Of Unmachined Specimen Blanks</b>										
	Test Temperature		Exposure Temp. (°C)							
5T	70	21	Air	649		127.3		133.7	10.7	22.8
5M	70	21	Air	649		141.8		153.3	10.0	27.3
5B	1200	649	Air	649	785	112.4	828	118.6	5.7	17.8
6T	1200	649	Air	649	749	107.2	805	115.3	7.1	18.4
<b>Notched Tensile</b>										<b>NSR</b>
8T	70	21	Air					1437	205.7	1.6
8B	70	21	Air					1437	205.7	
9T	1200	649	Air					1157	165.7	1.5
9B	1200	649	Air					1147	164.2	

Table 5.5; cont.

Creep										
Spec. ID	Test Temperature		Atm	Creep Stress		Time To Failure (Hour)	Time to (%) Creep (Hour)		Total Creep %	
	°F	°C		MPa	Ksi		0.20%	1.00%		
7T	1000	538	Air	560	80	3.1	0.8		2.8	
6M	1200	649	Air	175	25	100*	31.8		0.392	
7M	1200	649	Air	385	55	8.8	0.7	3.7	3.7	
6B	1400	760	Air	105	15	100*	4.5	58.9	1.513	
7B	1800	982	Air	14	2	10.7	0.1		72.3	
Post Creep Tensile Test										
Spec. ID	Test Temperature		Atm	Yield Stress		Ultimate Stress		Elong %	R of A %	
	°F	°C		MPa	Ksi	MPa	Ksi			
6M	70	21	Air	816	116.8	824	118	7.10	13.6	
6B	70	21	Air	Specimen failed during setup						
Fatigue Tests										
LCF				Total Strain		Cycles to Failure				
13T	1200	649	Air	1.00%		324				
13B	1200	649	Air	0.70%		1444				
HCF				Cycles To	Maximum Stress		Mean Stress		Alternating Stress	
				Fracture	MPa	Ksi	MPa	Ksi	MPa	Ksi
14T	1200	649	Air	10,000,000	419.1	60.0	209.6	30.0	209.6	30.0
14B	1200	649	Air	126,038	558.8	80.0	279.4	40.0	279.4	40.0
Impact Tests					J	FtLbs				
10T	-40	-40	Air		66.4	49				
10B	-40	-40	Air		35.2	26				
11T	70	21	Air		33.9	25				
11B	70	21	Air		16.3	12				
12T	1200	649	Air		93.5	69				
12B	1200	649	Air		115.2	85				
Toughness Tests					MPa√m	Ksi√in				
15T	70	21	Air		72.3	65.8				
15B	70	21	Air		68.5	62.3				

\* Test terminated an specimen tensile tested at 21°C

Table 5.6; Mechanical Properties For Alternate Heat Treatment Of Alloy 3

Tensile In Air									
Spec ID	Test Temperature		Atm	Yield Stress		Ultimate Stress		Elong. %	R of A %
	°F	°C		MPa	Ksi	MPa	Ksi		
16T	70	21	Air	737	105.5	821	117.6	14.9	30.8
16M	70	21	Air	724	103.7	797	114.1	13.7	30.4
16B	500	260	Air	504	72.2	623	89.2	17.8	51.5
17T	500	260	Air	559	80.1	719	103.0	18.8	45.1
17M	1050	566	Air	515	73.7	613	87.7	13.7	32.5
17B	1050	566	Air	522	74.8	618	88.5	13.6	47.9

Creep											
Spec ID	Test Temperature		Atm	Creep Stress		Hour	Time to Failure				Total Creep %
							Time To Percent Creep (Hour)				
							0.1%	0.20%	0.50%	1.00%	
18T	1200	649	Air	175	25	100*	3.8	9.00	32.0		0.8
18M	1400	760	Air	105	15	113.7*	0.3	0.90	4.4	17.00	3.6
18B	1800	982	Air	14	2	11			0.6		25.9

Post Creep Tensile Test										
Spec ID	Test Temperature		Atm	Yield Stress		Ultimate Stress		Elong. %	R of A %	
	°F	°C		MPa	Ksi	MPa	Ksi			
18T	70	21	Air	796	113.9	838	120	2.90	4.2	
18M	70	21	Air	732	104.8	800	114.5	10.10	22.1	

\* Test terminated and specimen tensile tested at 21°C

**Table 5.7.**  
**Knoop Hardness of Interstitial Layer**

<b>Alloy</b>	<b>Layer Thickness, mm</b>	<b>Peak Knoop Hardness</b>
Nb-38Ti-12.5Al-1.5Mo	27.5	970
Nb-28Ti-15Cr-1.5Si	80	1141
Nb-32Ti-10Cr-6Al	70	1216
3899-3	50	1195

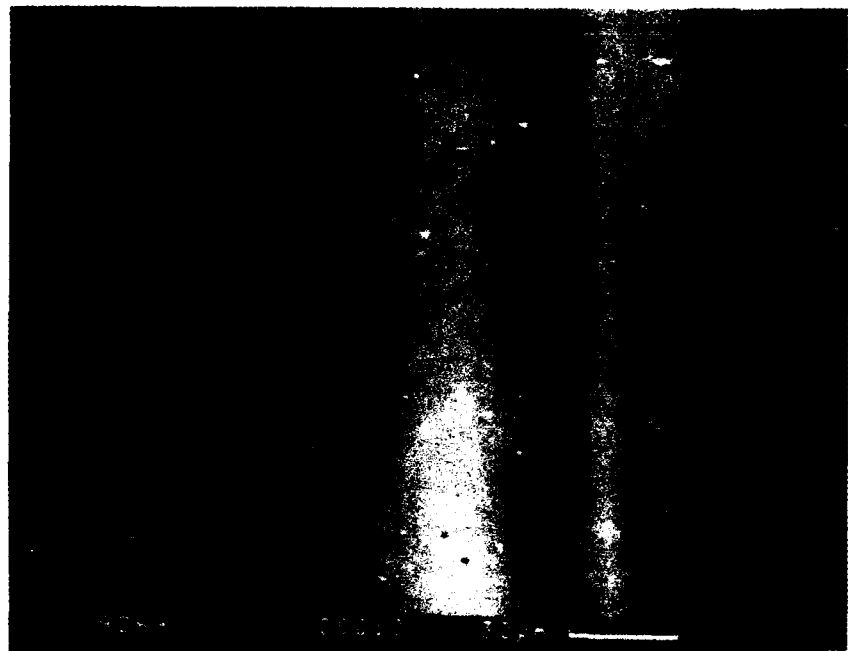
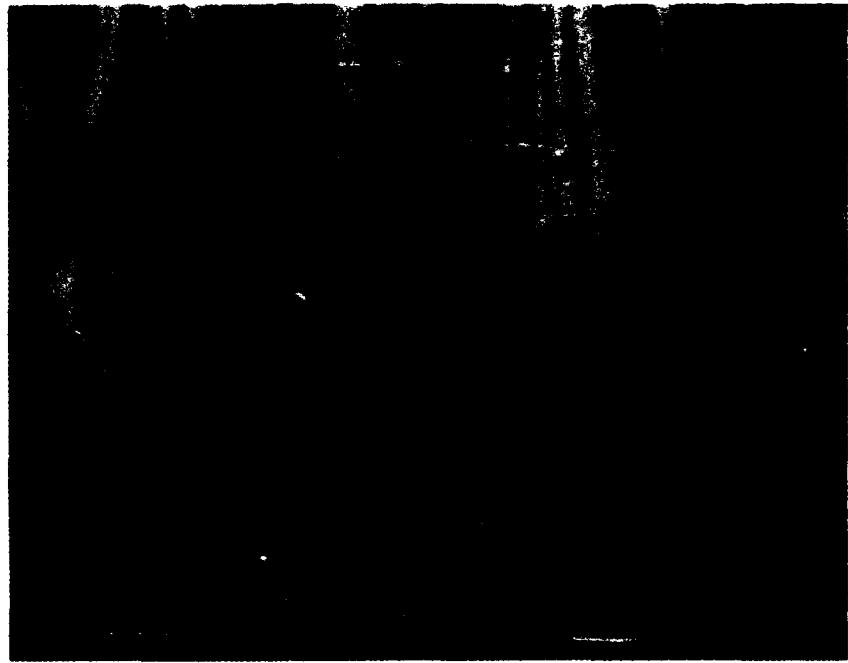
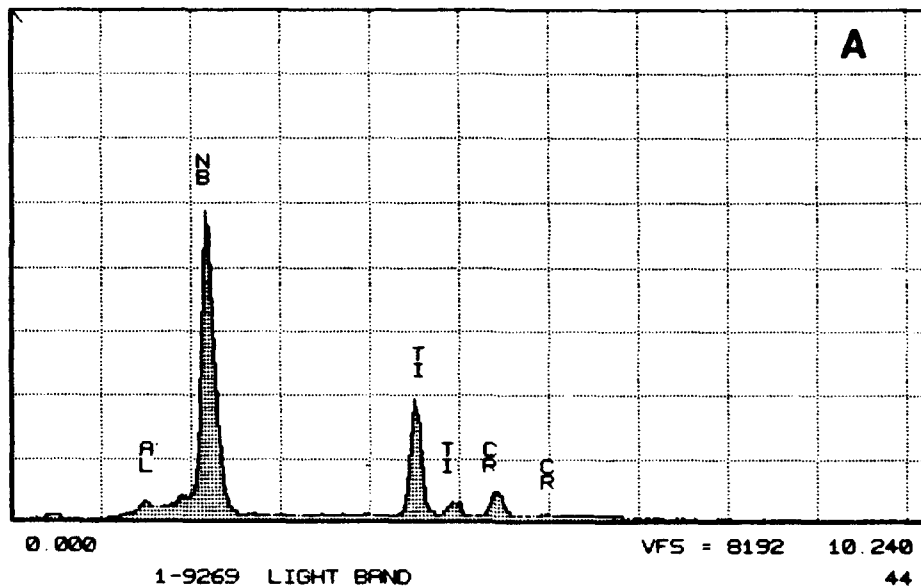


**Figure 5.1** Backscattered electron images of the as-extruded microstructure of scaled up Alloy 1

GERE / CamScan SEM / NORAN Series II EDS THU 24-OCT-91 07:22  
Cursor: 0.000keV = 0 ROI (10) 0 000:20.480



GERE / CamScan SEM / NORAN Series II EDS THU 24-OCT-91 07:24  
Cursor: 0.000keV = 0 ROI (10) 0 000:20.480

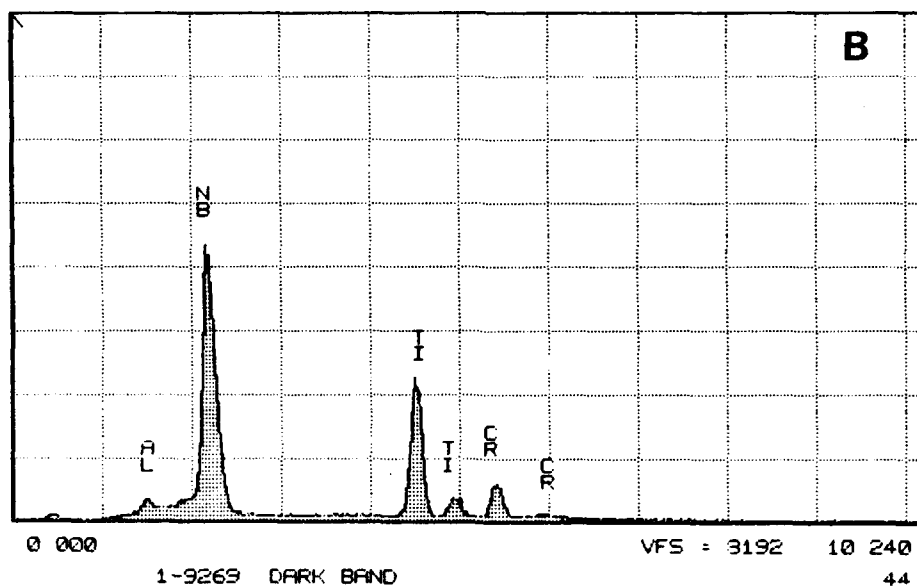


Figure 5.2 EDS spectra taken from the a) light and b) dark bands seen in Figure 5.1

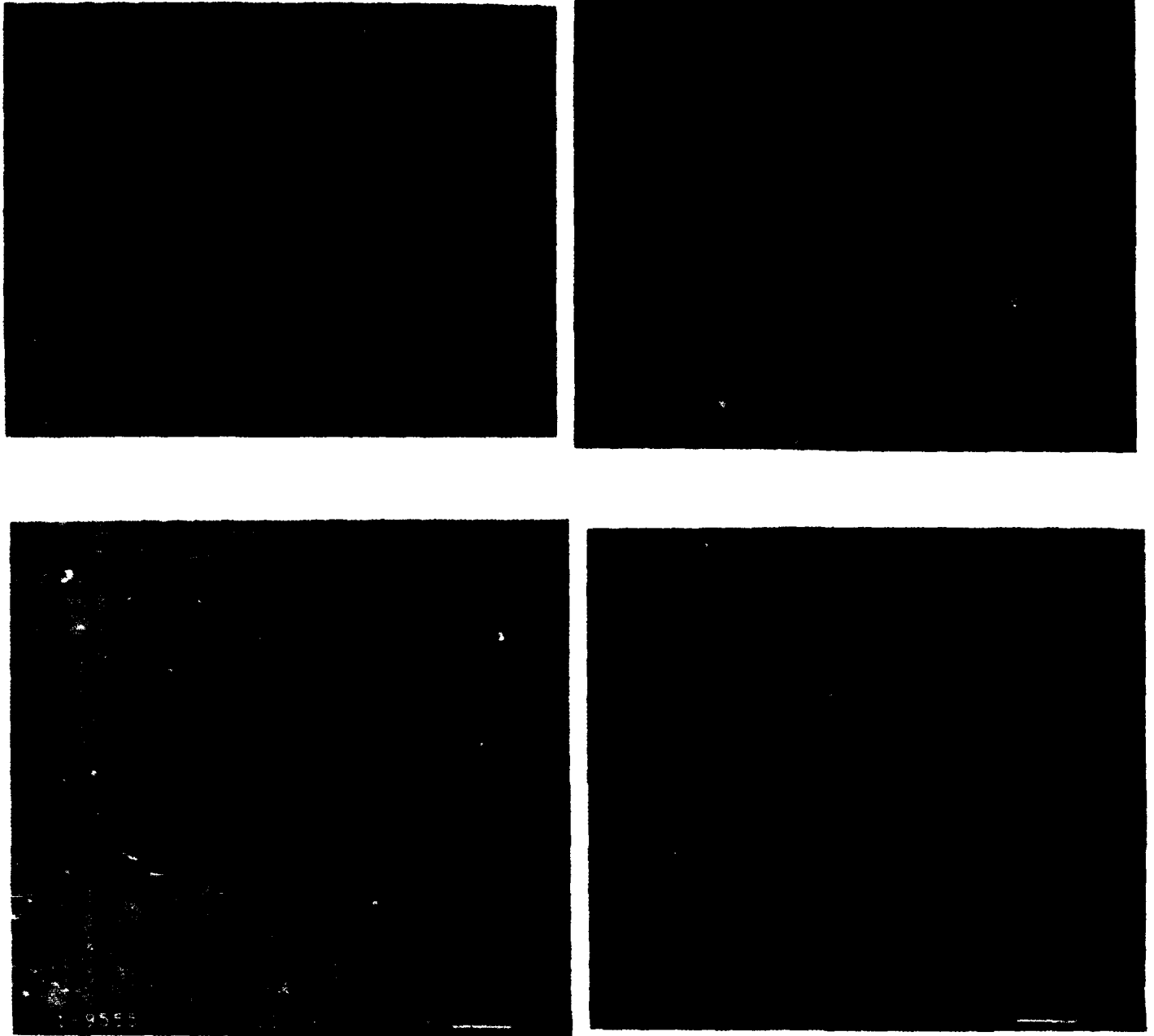
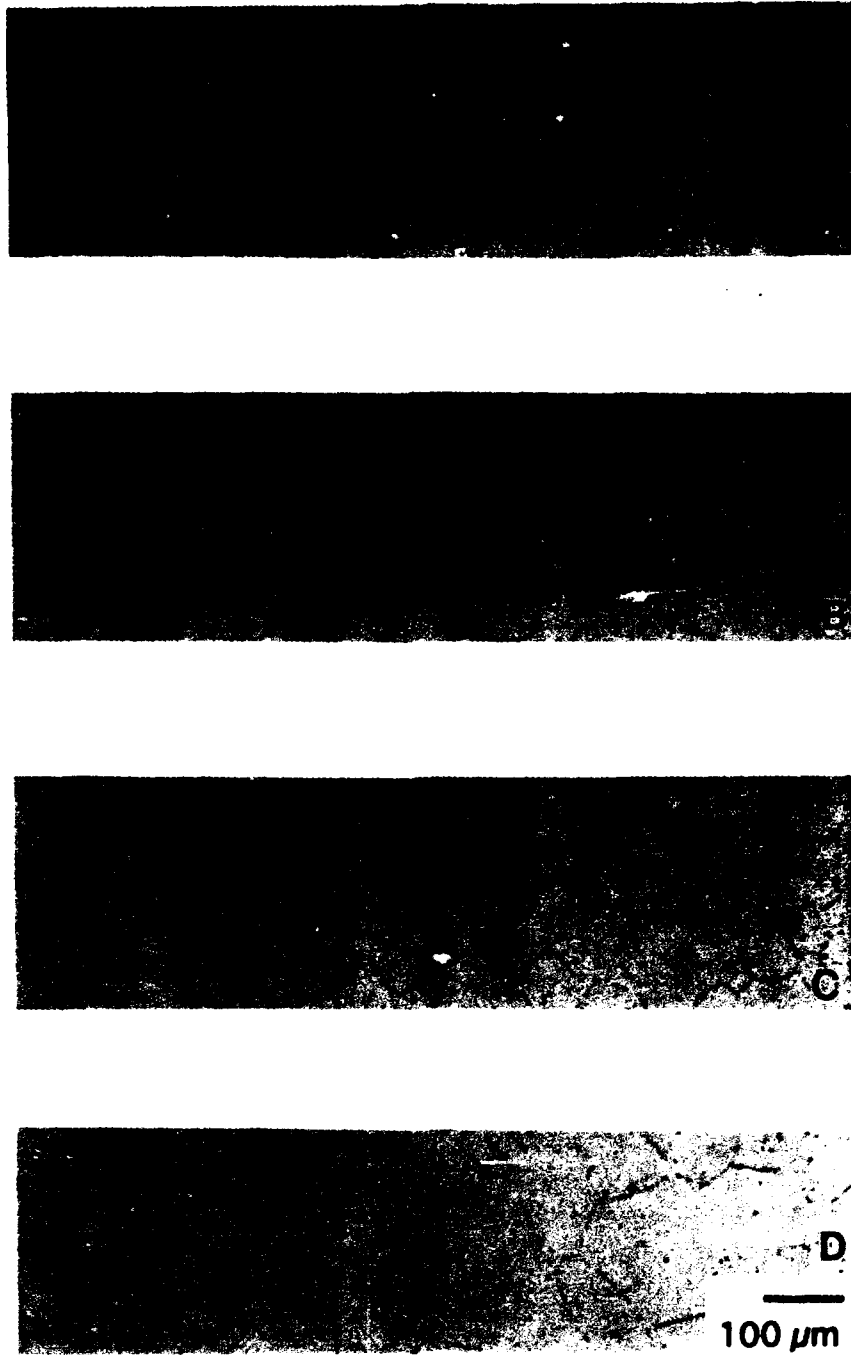
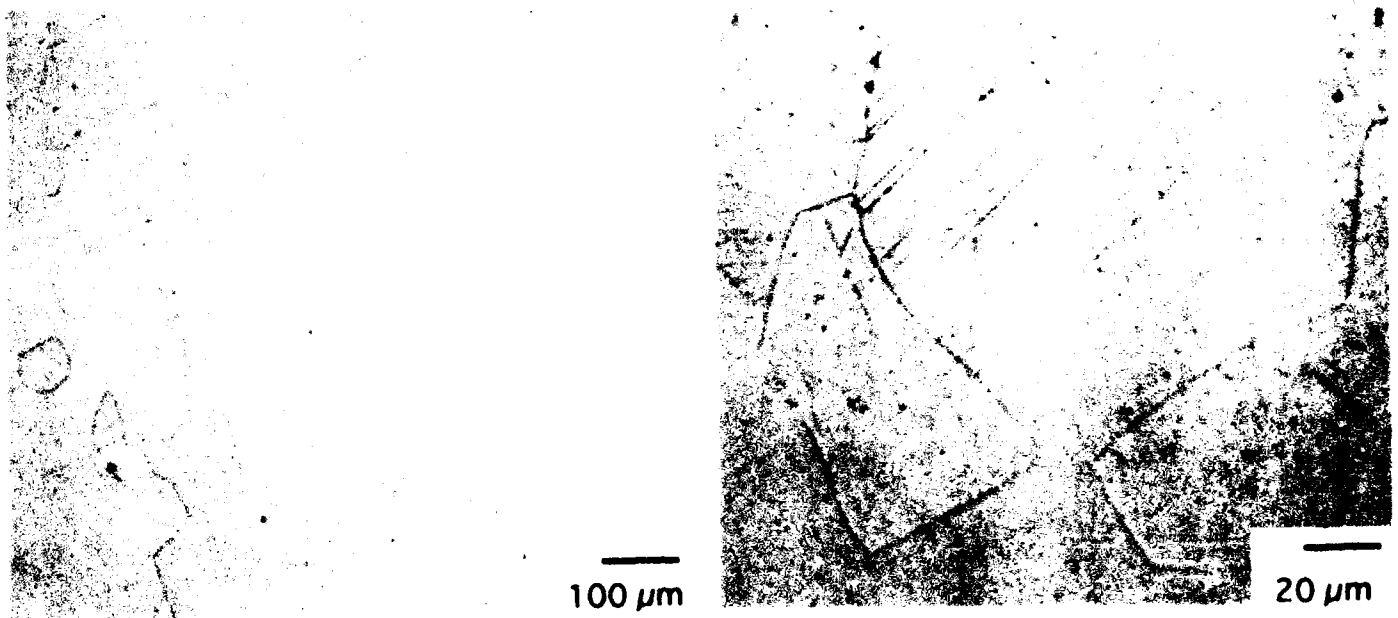


Figure 5.3 Backscattered electron images of alloy 1 following heat treatment at a) 1100°C / 1h, b) 1100°C / 4h, c) 1150°C / 1h, and d) 1150°C / 4h.





**Figure 5.4** Optical micrographs of Alloy 1 following heat treatment at a) 1100°C / 1h, b) 1100°C / 4h, c) 1150°C / 1h, and d) 1150°C / 4h.



**Figure 5.5** Optical micrograph of Alloy 1 taken from the room temperature tensile specimen indicating that the desired structure was achieved.



**Figure 5.6** Fracture surface from the room temperature tensile test taken at a) low magnification and b) high magnification showing intergranular failure with a small amount of dimple failure.

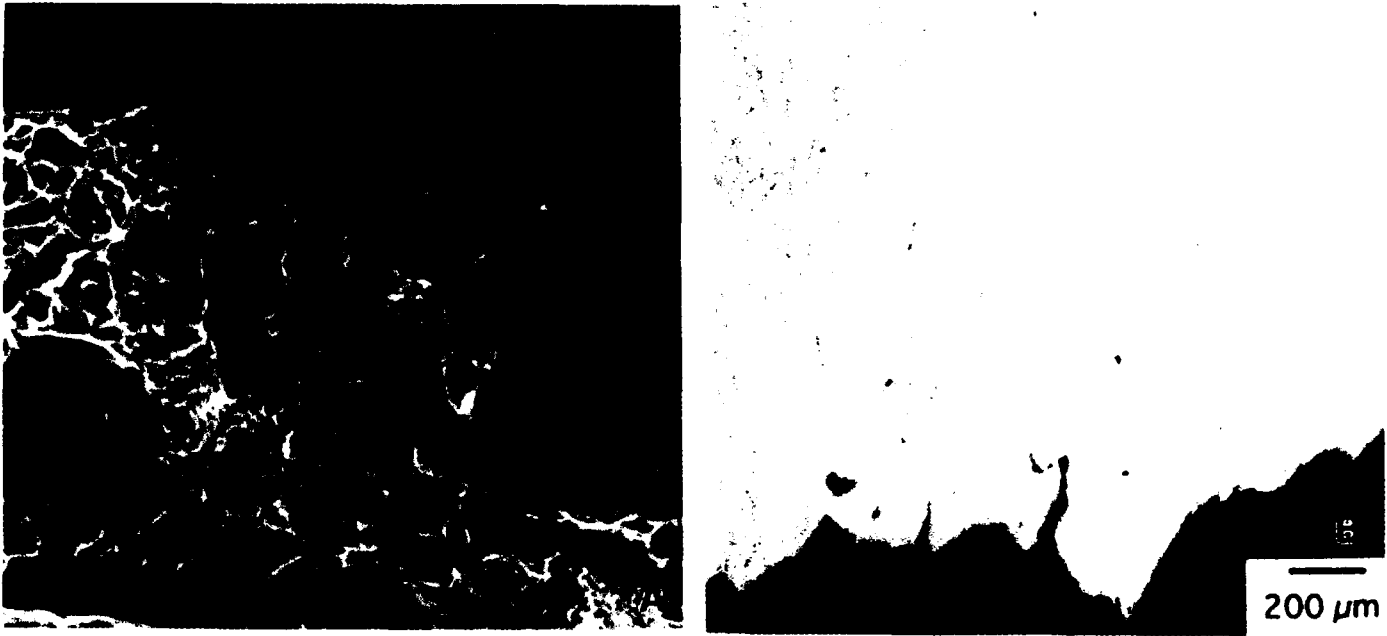


Figure 5.7 Micrographs taken from the 370°C tensile test specimen showing a) secondary electron image of dimples present on the fracture surface and b) microstructure of the material below the fracture surface.

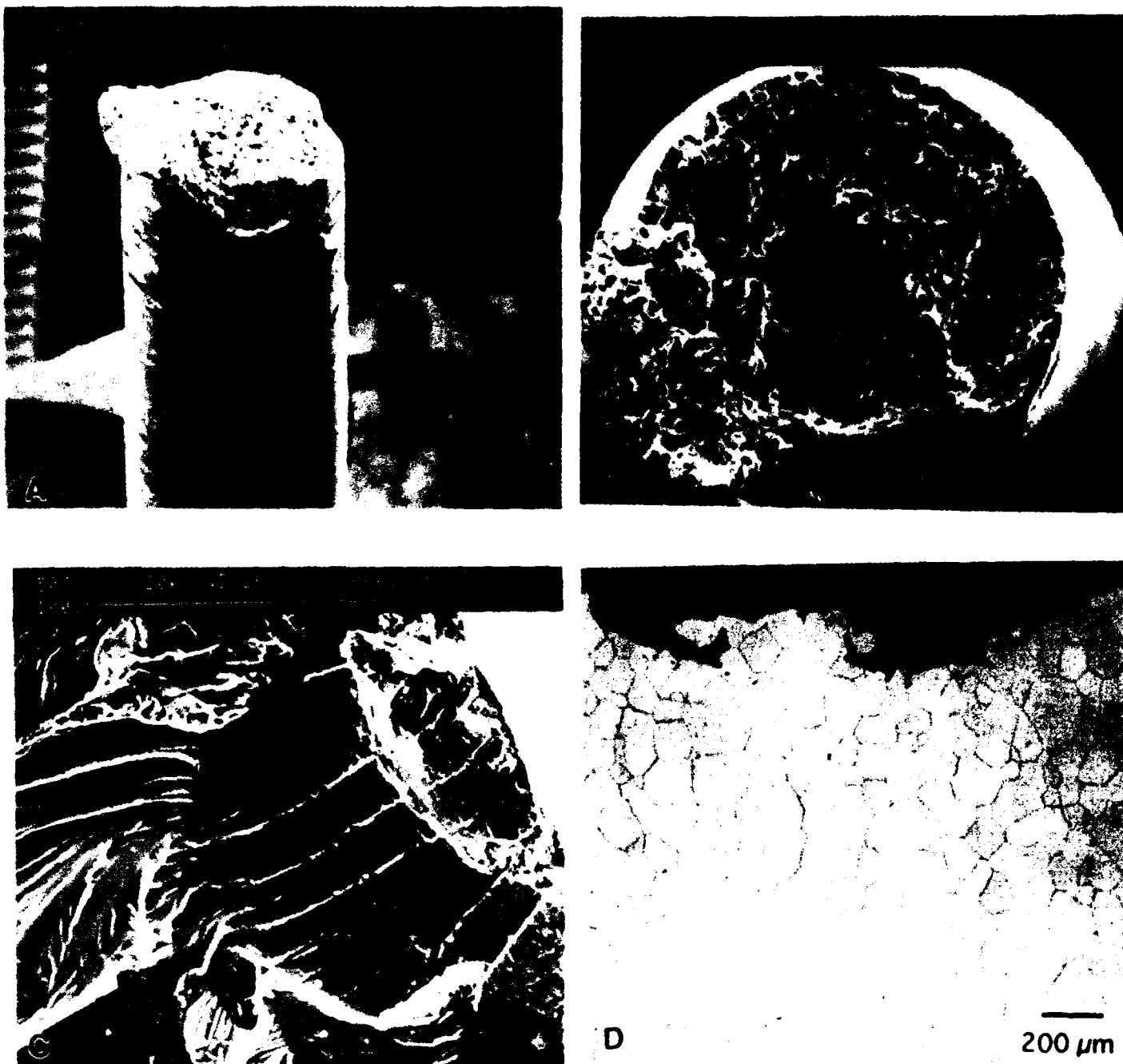


Figure 5.8 Micrographs taken from the 870°C tensile test specimen showing three magnifications of the fracture surface showing the presence of (a) surface cracks ( b ), cleavage initiation and intergranular fracture ( c ), and beachmarkings ( d ) and d) the microstructure of the specimen below the fracture surface.



Figure 5.9 Micrographs taken from the tensile specimen which was tested in inert environment at 870°C showing a) ductile fracture surface, b) lack of surface cracking and large amount of reduction of area, and c) microstructure below the fracture surface exhibiting the grain boundary failures.

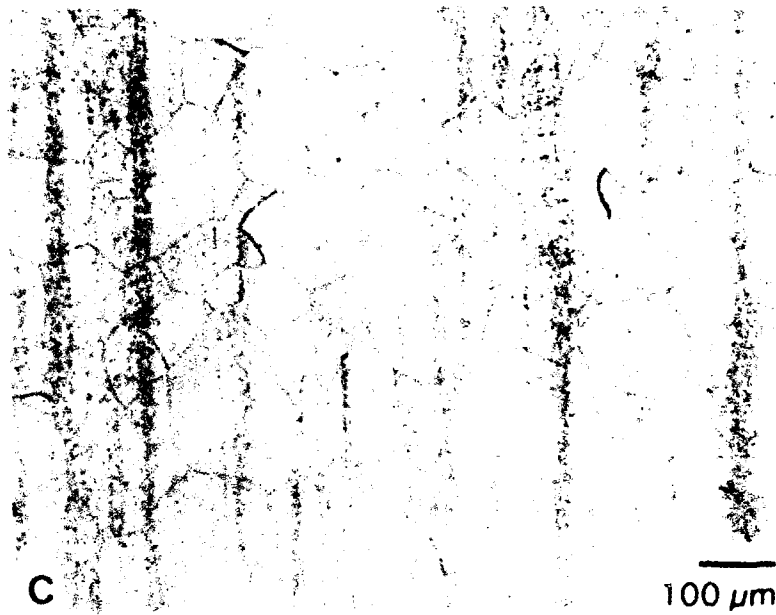
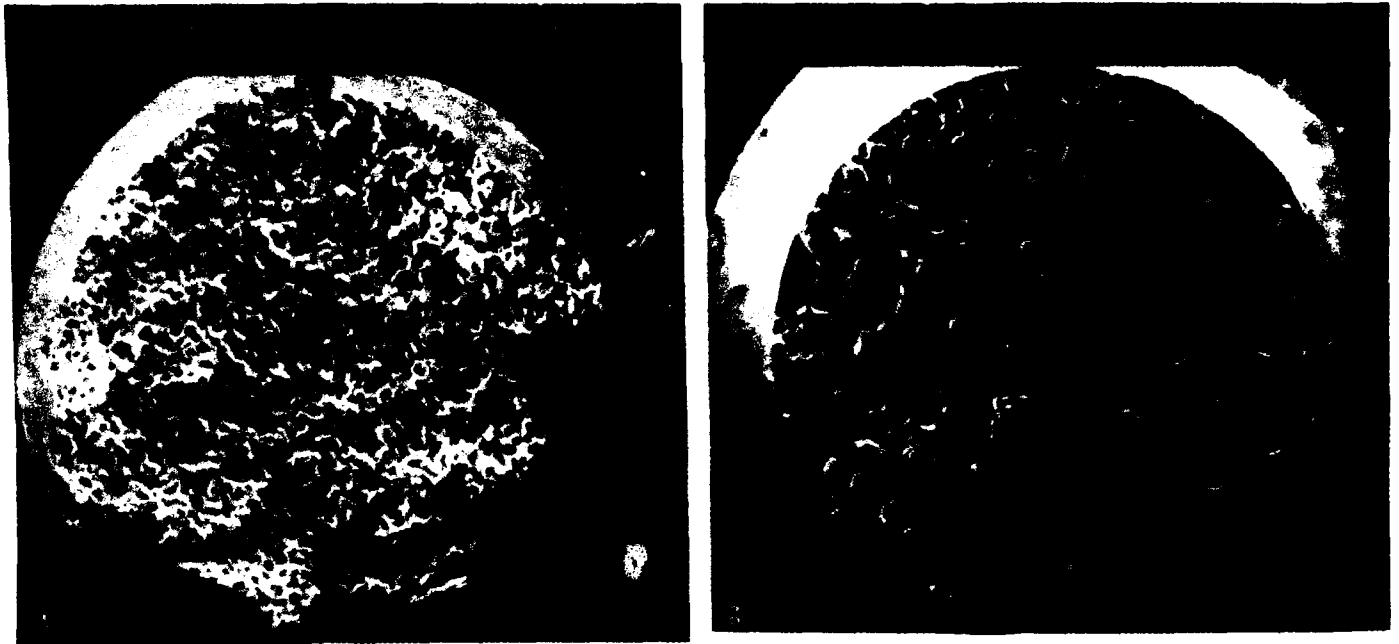


Figure 5.10 Micrographs taken from tensile specimens which had undergone thermal exposure prior to the test, a) exposed then tested at room temperature, b) exposed then tested at 870°C, and c) microstructure of the specimen below the fracture surface showing the presence of an aligned precipitate.



Figure 5.11 Micrographs taken from the notch tensile specimens tested at a) room temperature, b) 870°C, and c) high magnification of the 870°C test showing the beachmarkings and cleavage fracture.



Figure 5.12 Low magnification secondary electron images of specimens which were creep tested at a) 870°C / 275MPa, and b) 870°C / 205 MPa.

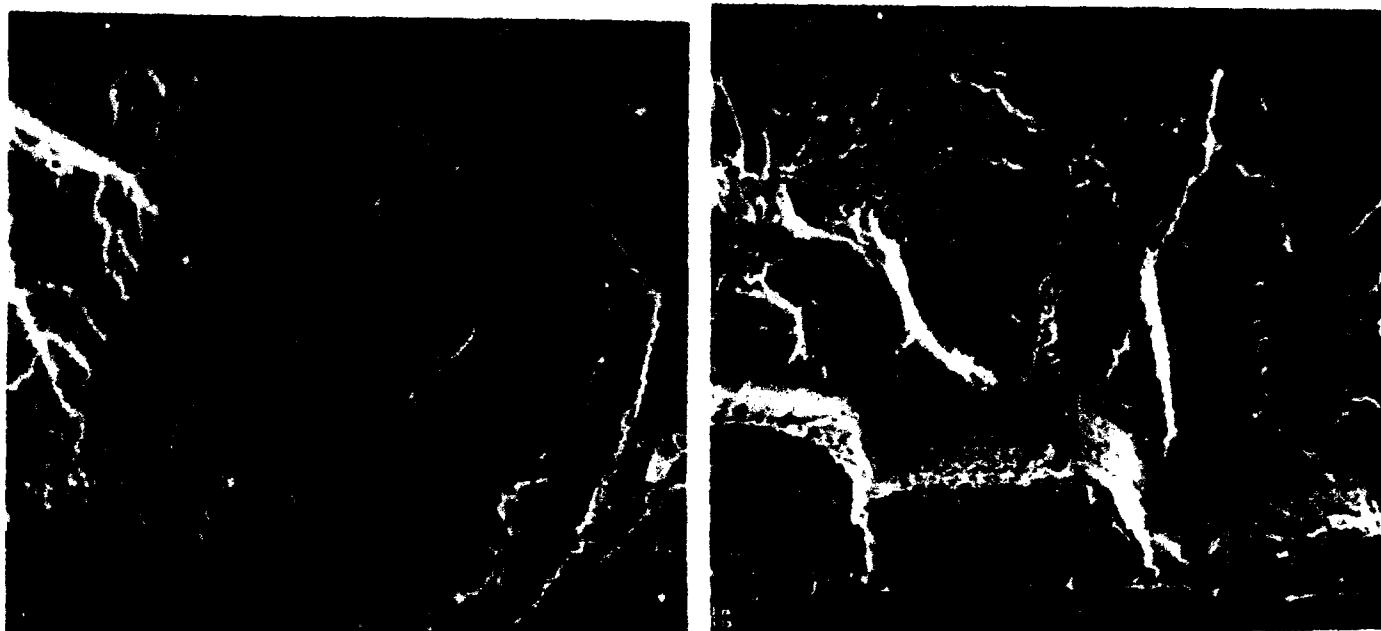


Figure 5.13 Micrographs taken from the fracture surface of specimens which were creep tested at a) 870°C / 275MPa, and b) 870°C / 205 MPa.



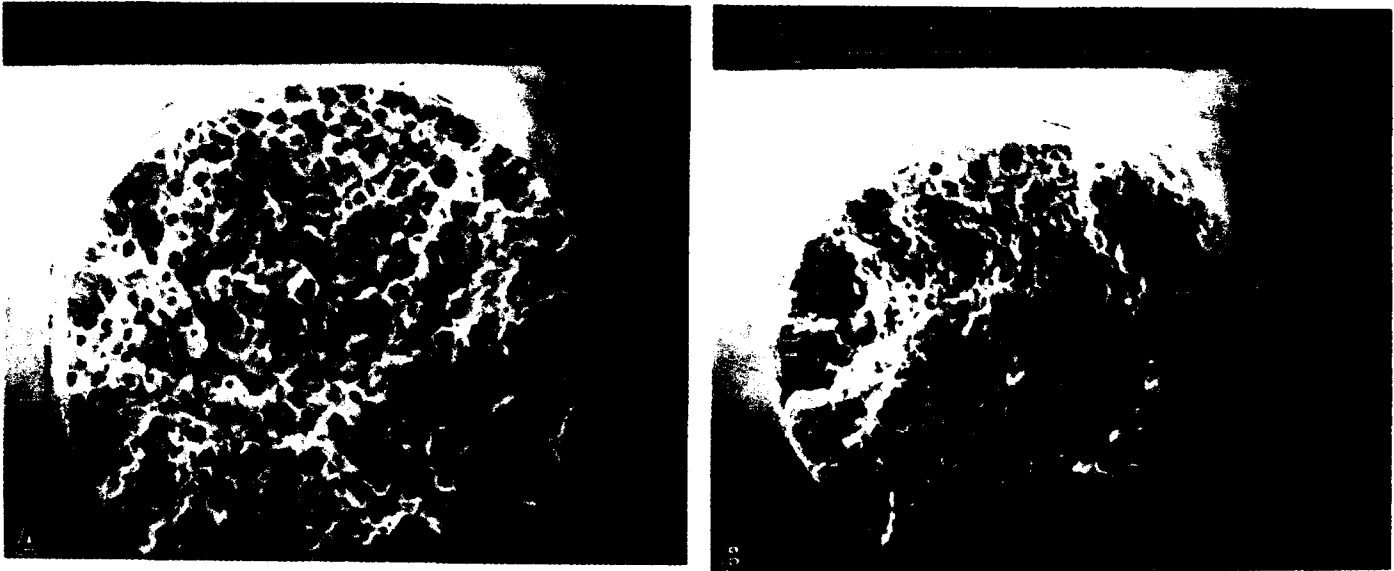


Figure 5.14 Secondary electron images of the fracture surface of specimens which were creep tested at a) 870°C / 275MPa, and b) 870°C / 205 MPa.

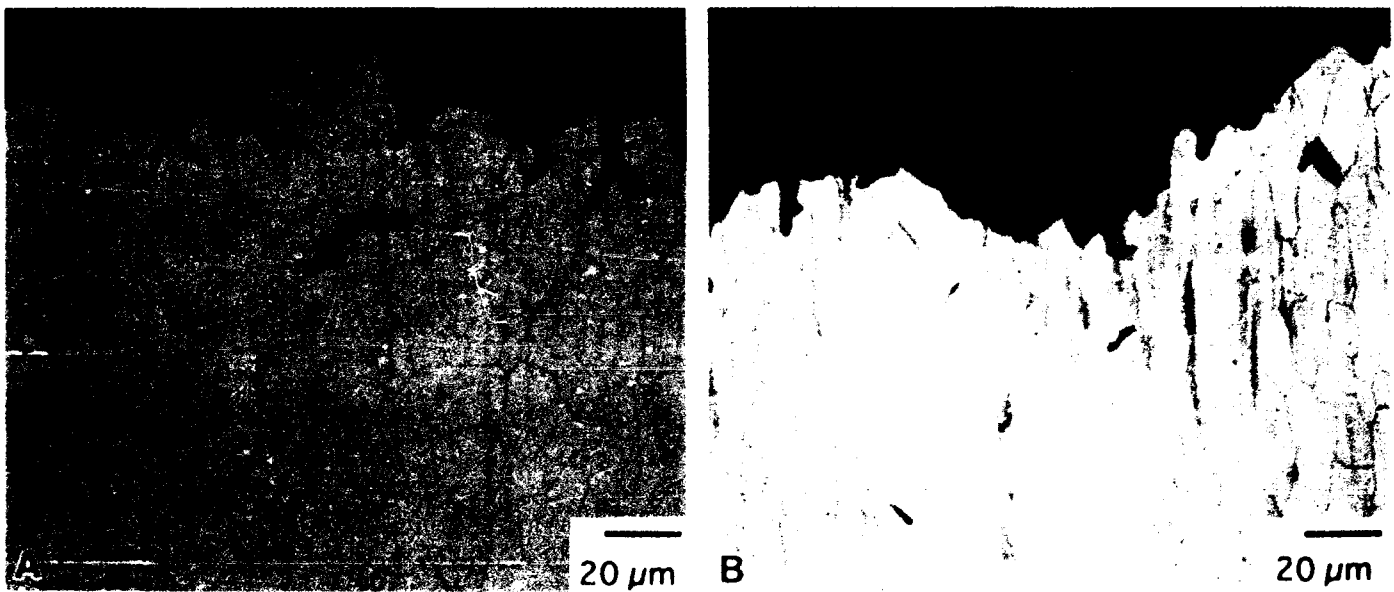


Figure 5.15 Optical micrographs of the microstructure below the fracture surface of specimens which were creep tested at a) 870°C / 275MPa, and b) 870°C / 205 MPa.

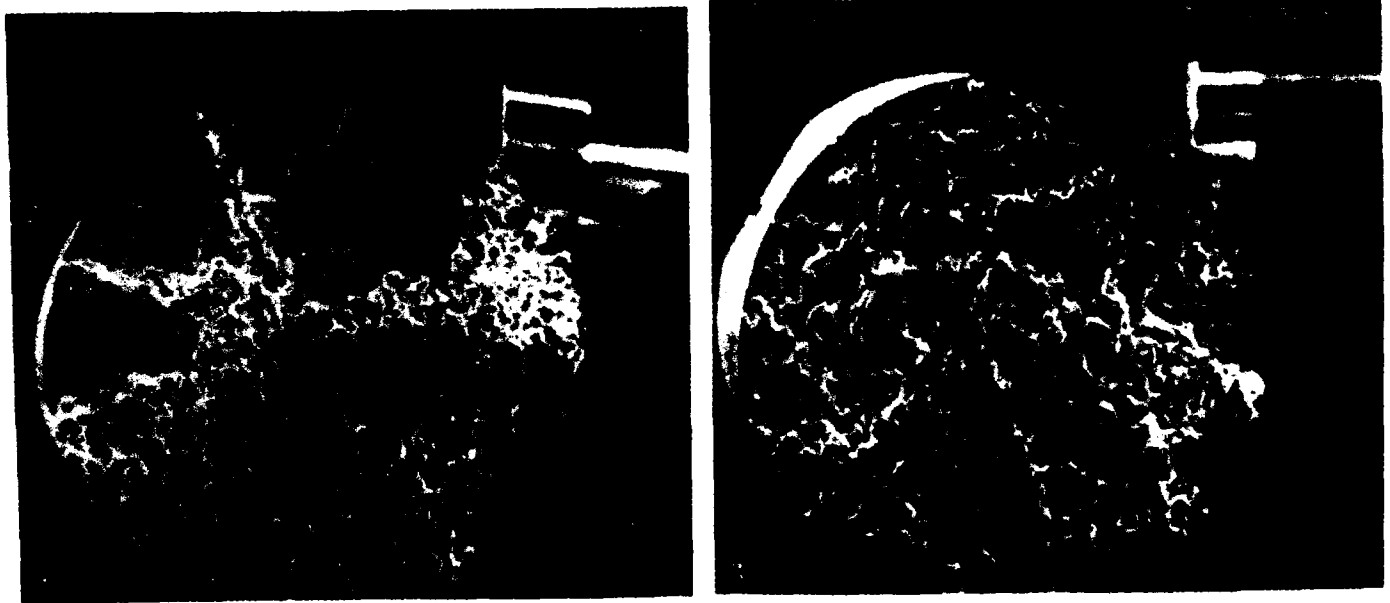


Figure 5.16 Secondary electron images of the fracture surface from LCF specimens showing cleavage fracture at initiation and intergranular final fracture, a) strained to 1.2% strain and b) strained to 1.0% strain

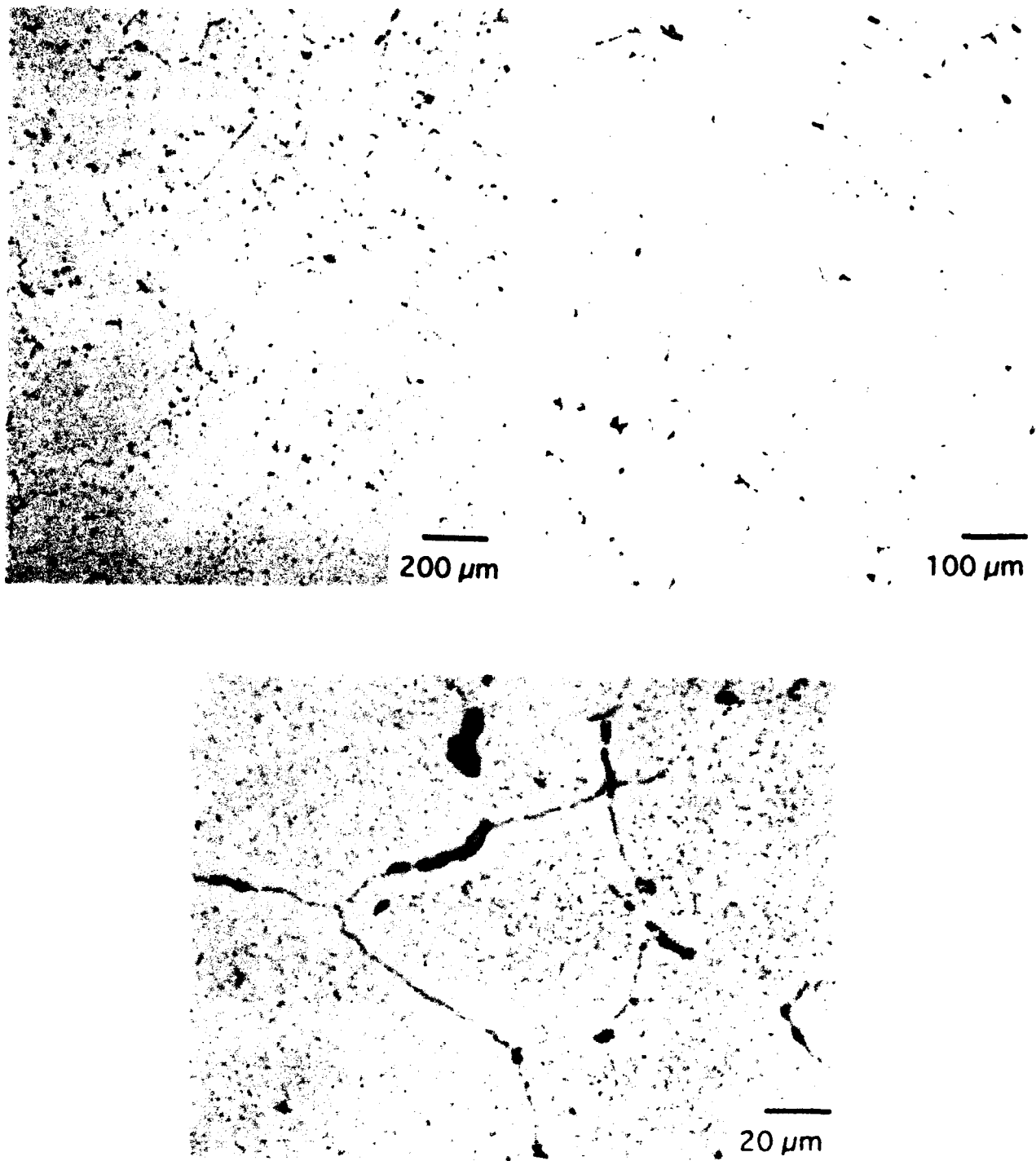


Figure 5.17 Optical micrographs of the structure present in the ingot of alloy 2 during the forging attempts. The structure consists of a grain boundary phase, a precipitate within the grains and porosity.

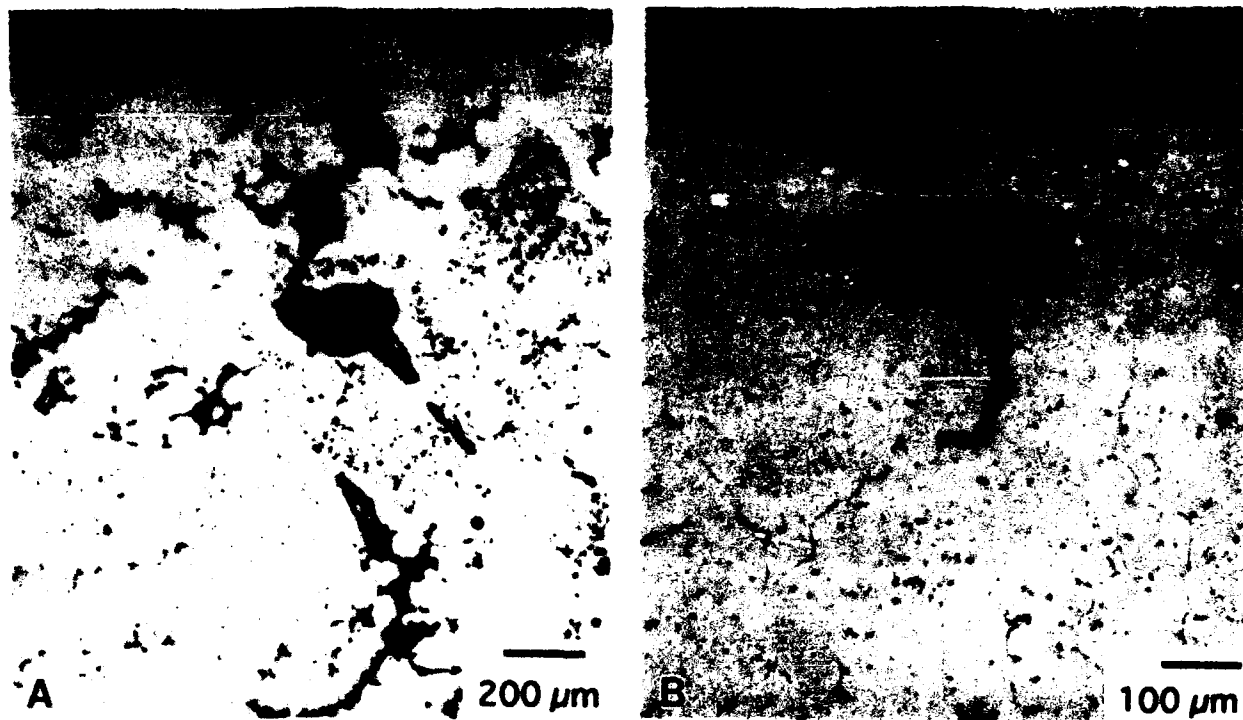


Figure 5.18 Optical micrographs of a) crack near the bottom of the ingot showing the cracking mechanism to be linking of the porosity, and b) crack near the top of the ingot showing the crack progressing along the grain boundaries.

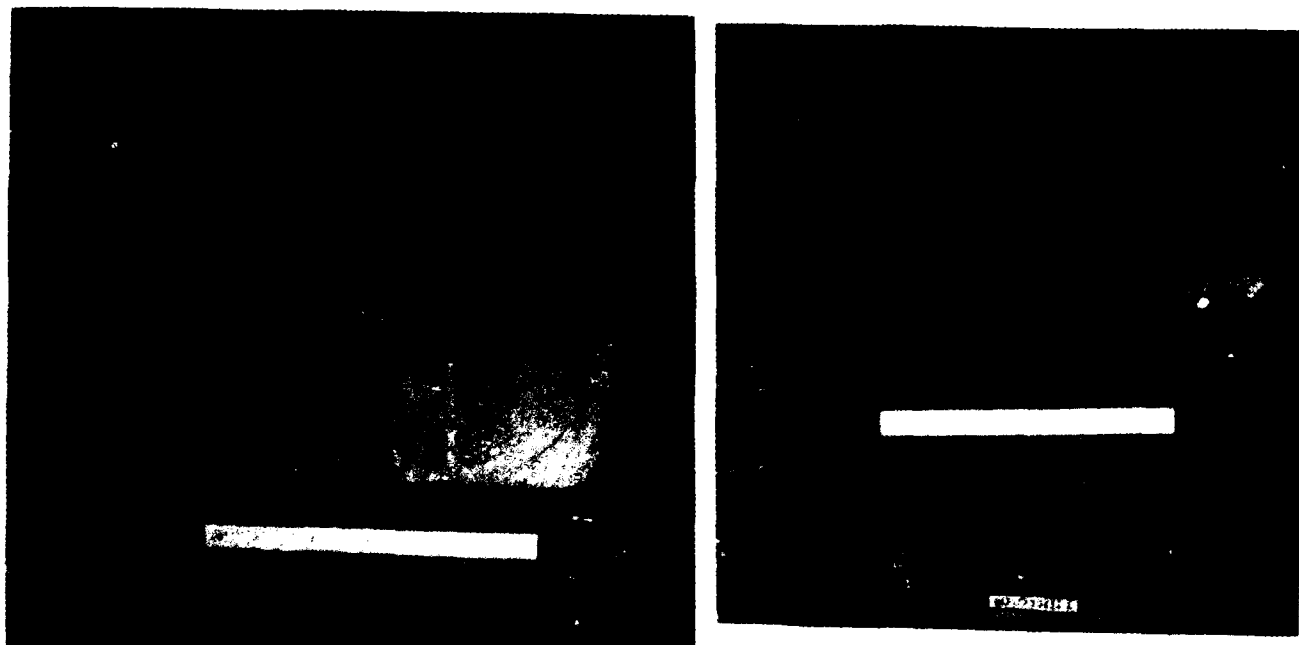


Figure 5.19 Picture of the as-received billet of Alloy 3.

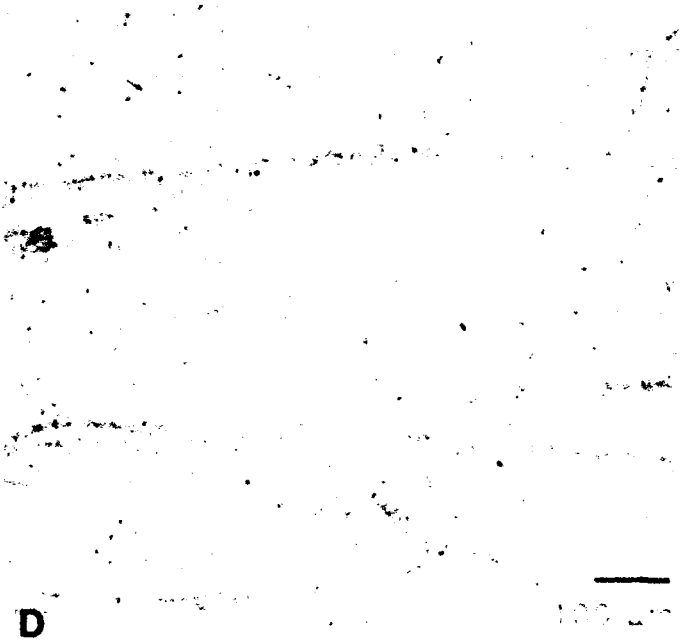
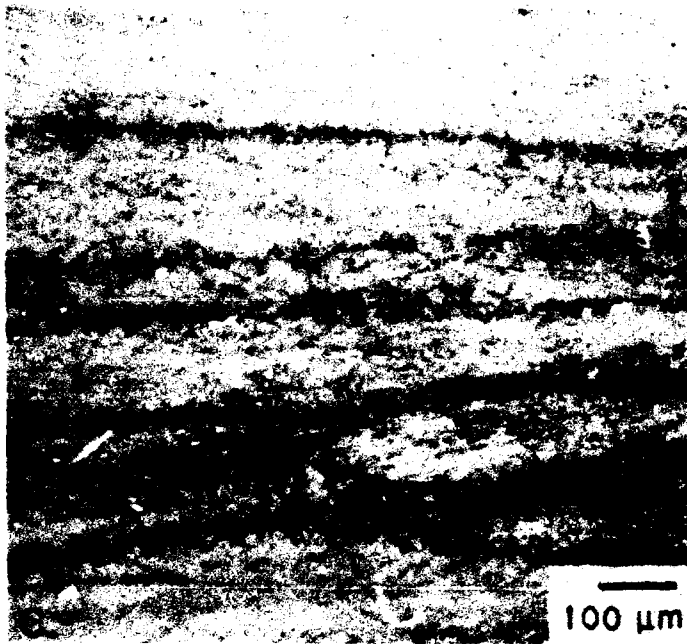
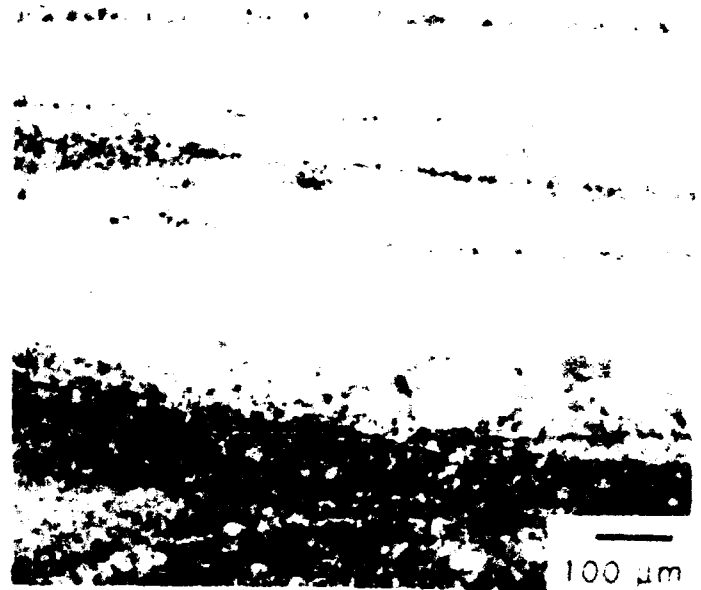
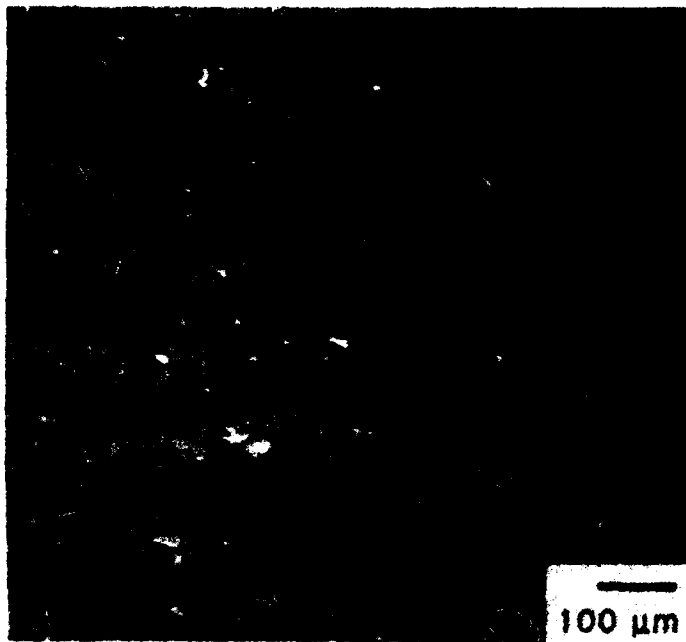


Figure 5.20 Optical micrographs of specimens from Alloy 11 which had been heat treated at a) 800°C / 4h, b) 800°C / 4h plus 500°C / 24h, c) 800°C / 4h plus 600°C / 24h, and d) 800°C / 4h plus 700°C / 24h.

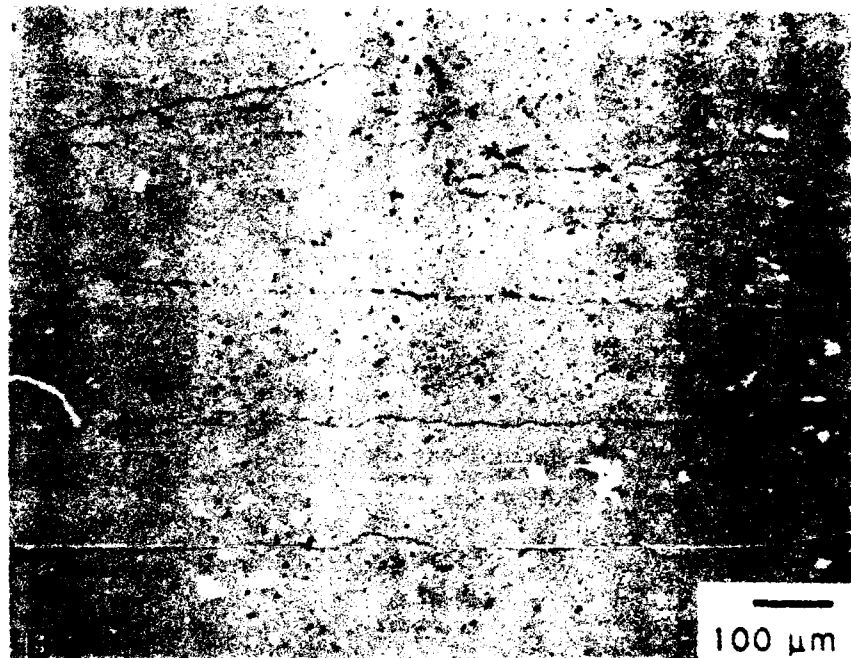
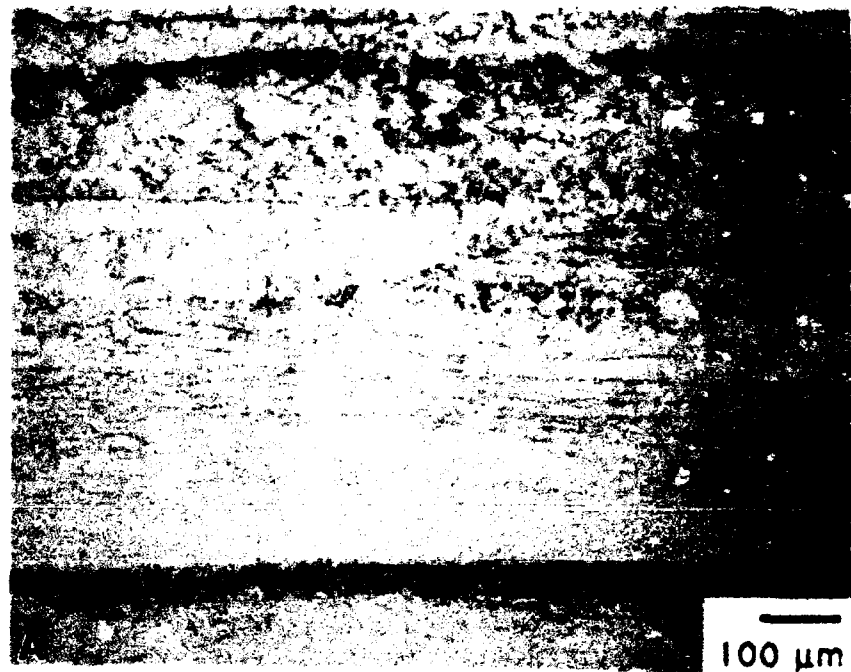


Figure 5.21 Optical micrographs of specimens from Alloy 12 which had been heat treated at a) 900°C / 4h, and b) 950°C / 4h.

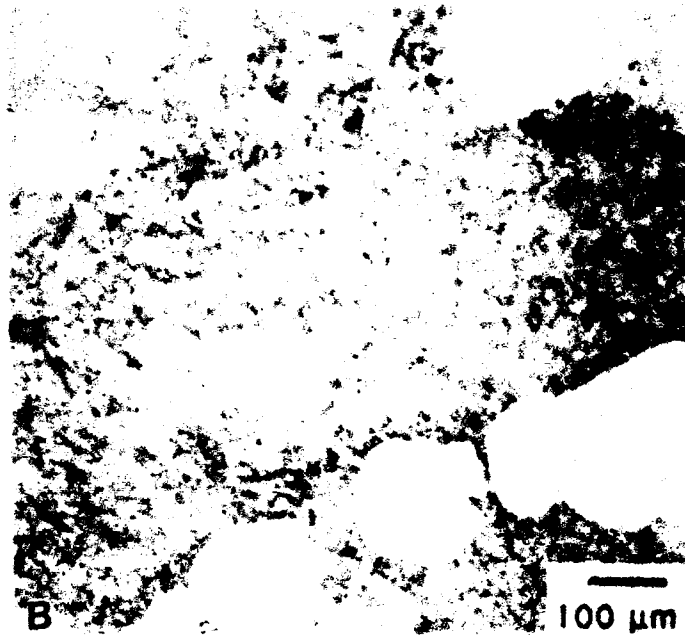
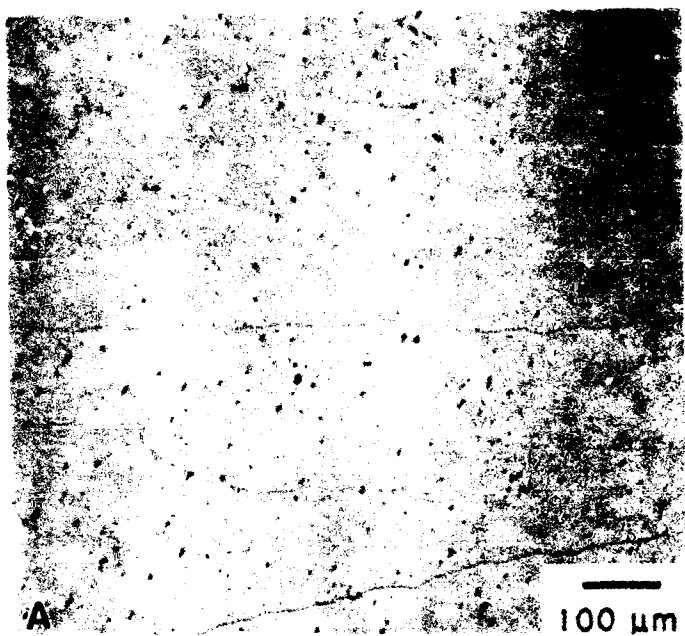
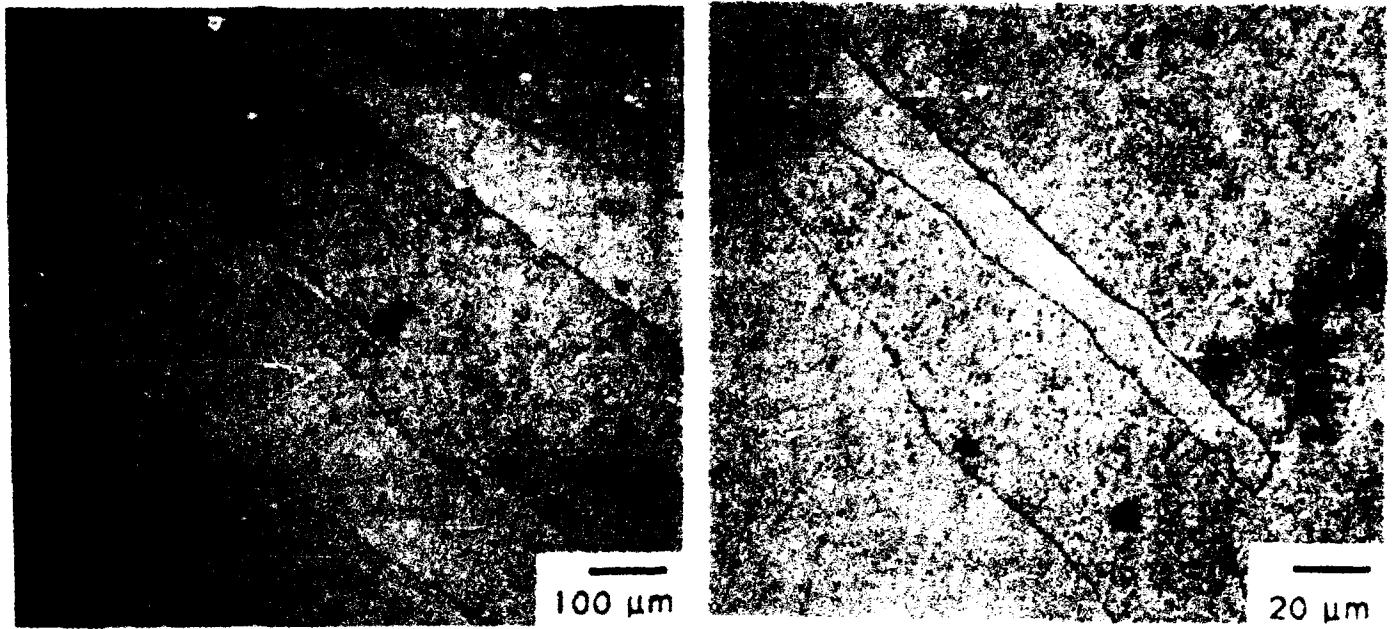
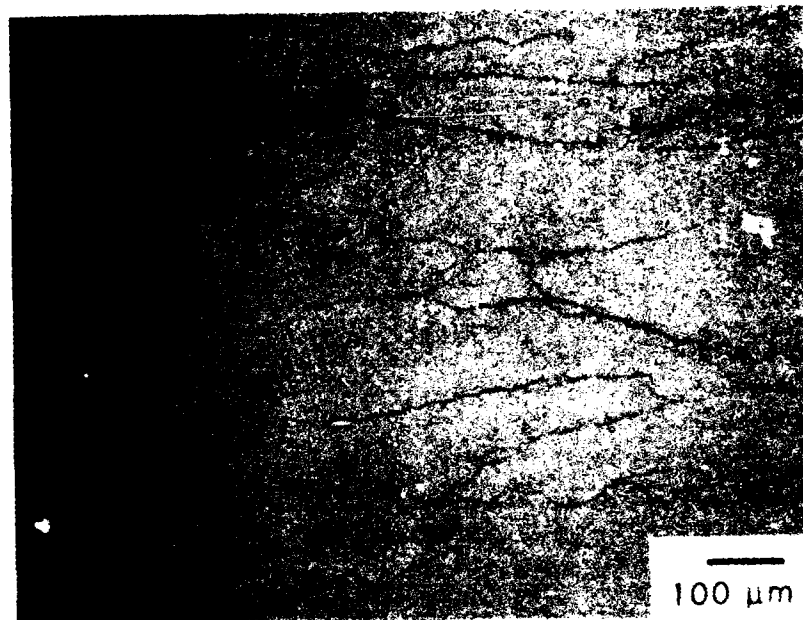


Figure 5.22 Optical micrographs of specimens from Alloy 12 which had been heat treated at a) 1000°C / 24h, b) 1000°C / 4h plus 500°C / 24h, c) 1000°C / 4h plus 600°C / 24h, and d) 1000°C / 4h plus 700°C / 24h.



**Figure 5.23** Optical micrographs of the as-forged structure present in the billet of Alloy 3.



**Figure 5.24** Optical micrograph of material from Alloy 3 which had been heat treated at 950°C/1h.



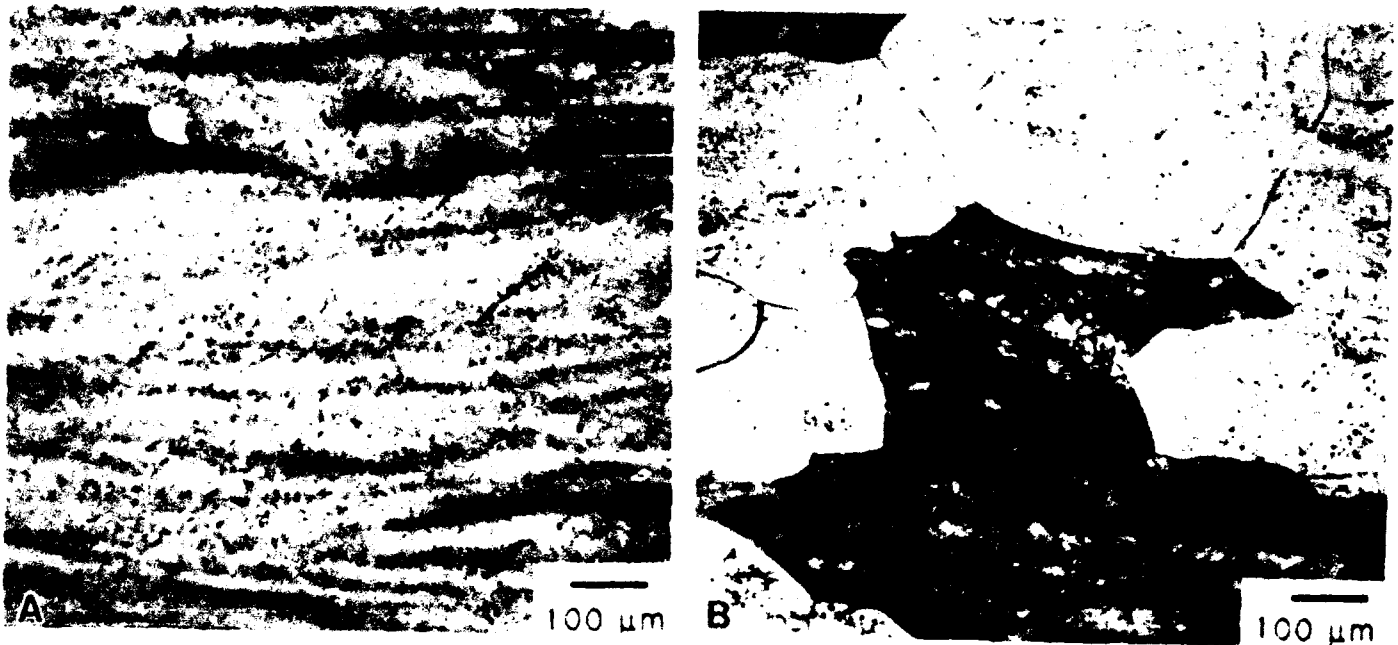


Figure 5.25 Optical micrograph of material which had been aged at  $650^{\circ}\text{C} / 20\text{h}$  following either an a)  $950^{\circ}\text{C} / 1\text{h}$  or b)  $1100^{\circ}\text{C} / 4\text{h}$  solution treatment showing the presence of both recrystallized and unrecrystallized regions in the microstructure.

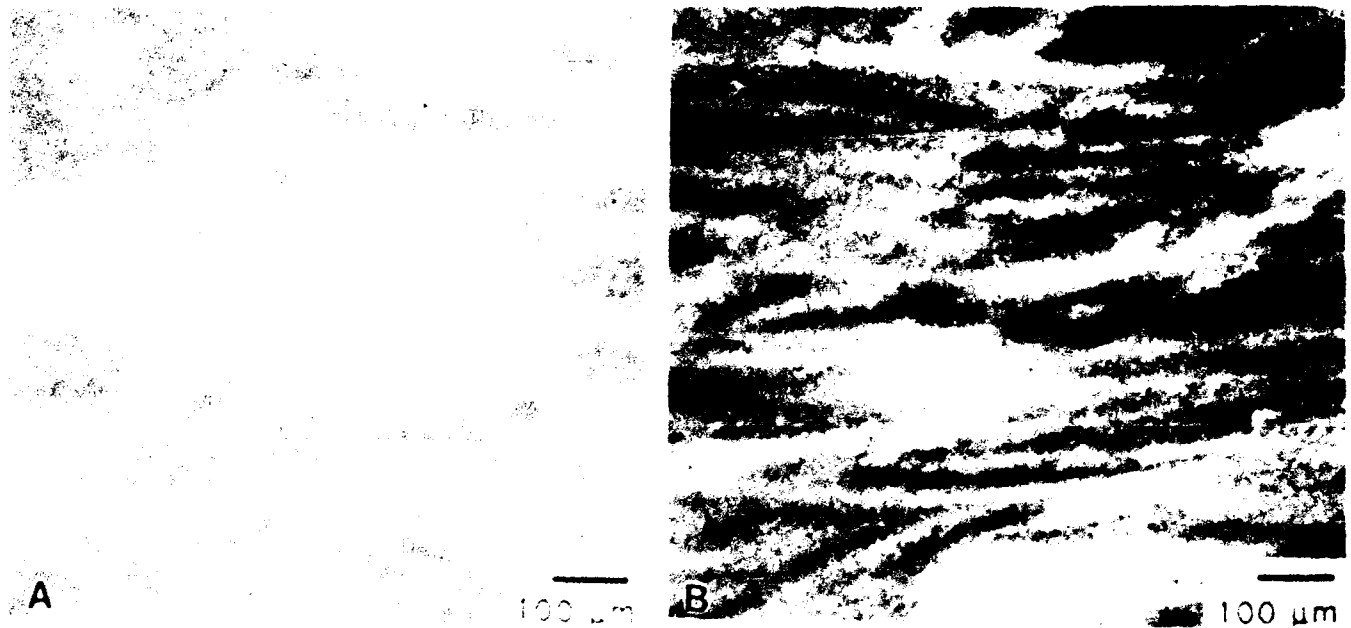


Figure 5.26 Optical micrographs of material which had been aged for either a)  $700^{\circ}\text{C} / 20\text{h}$  or b)  $750^{\circ}\text{C} / 20\text{h}$  following a solution treatment of  $950^{\circ}\text{C} / 1\text{h}$ .



Figure 5.27 Optical micrographs of material which had been aged at 800°C / 20h following a solution treatment of 950°C / 1h.

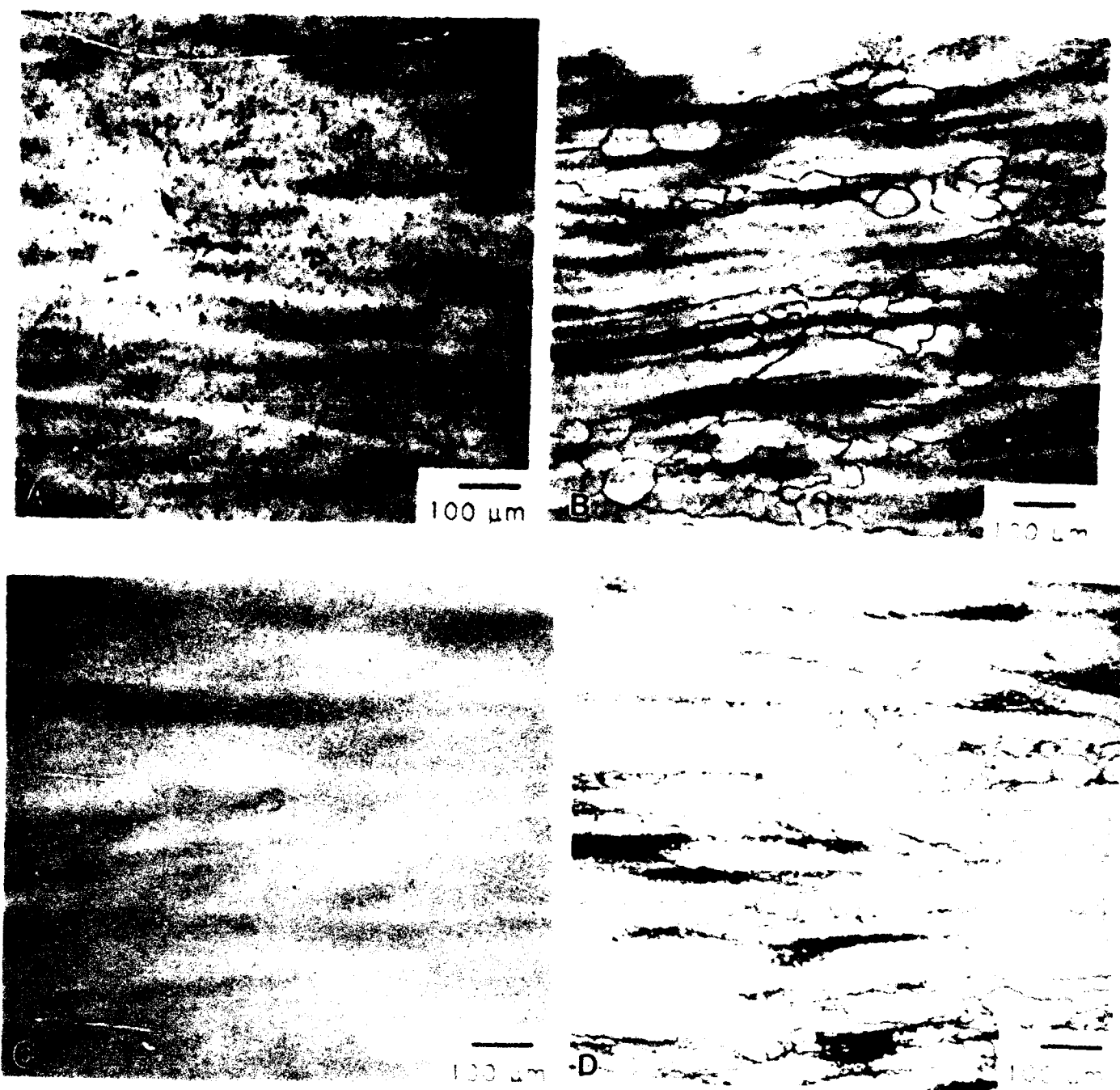


Figure 5.28 Optical micrographs of material which had been forged and then aged at a) 650°C / 20h, b) 700°C / 20h, c) 750°C / 20h, and d) 800°C / 20h.

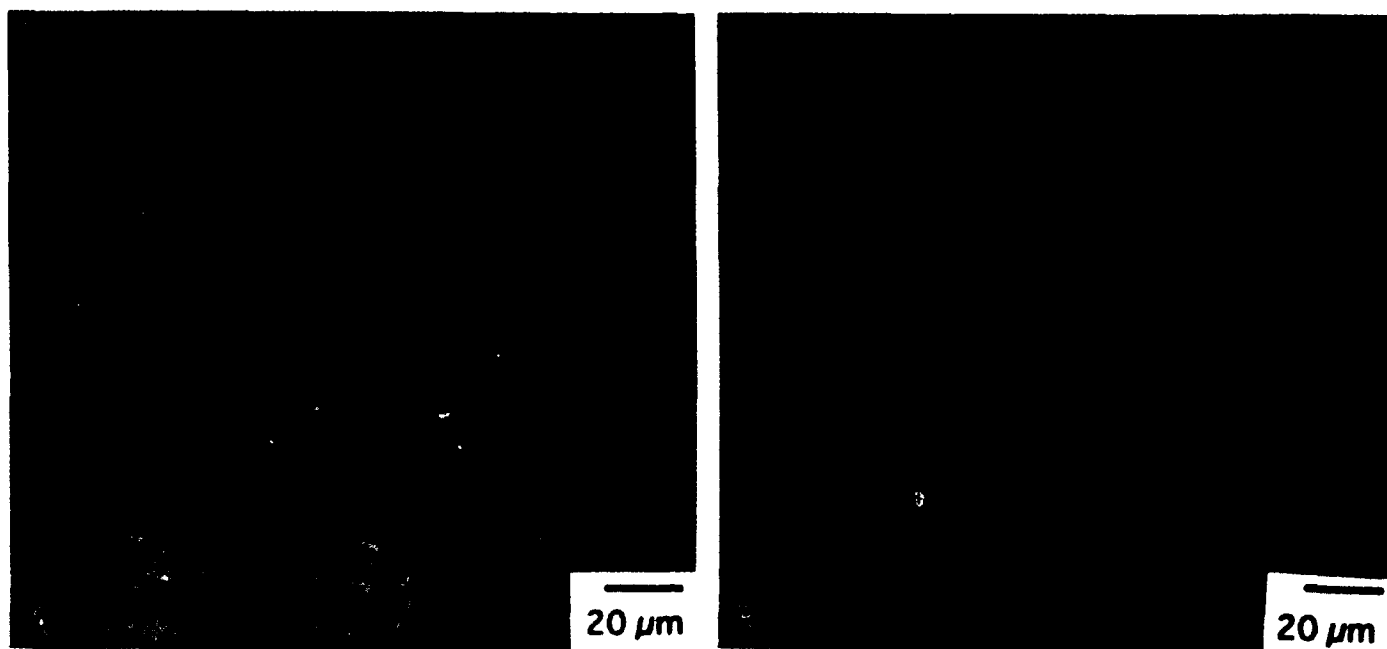


Figure 5.29 Optical micrograph of material which had been solution treated at 1100°C / 8 h followed by an age treatment of a) 750°C / 50h, and b) 750°C / 100h.

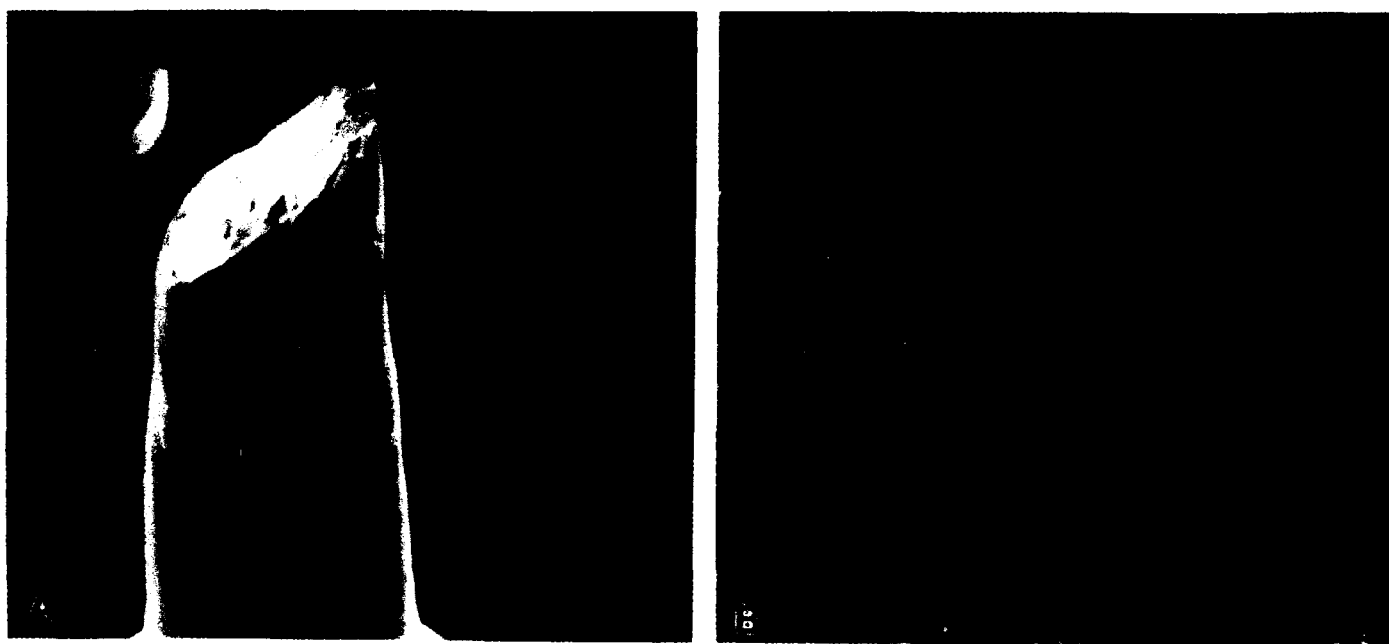


Figure 5.30 Secondary electron images taken at a ) low and b) high magnification of room temperature tensile specimen.

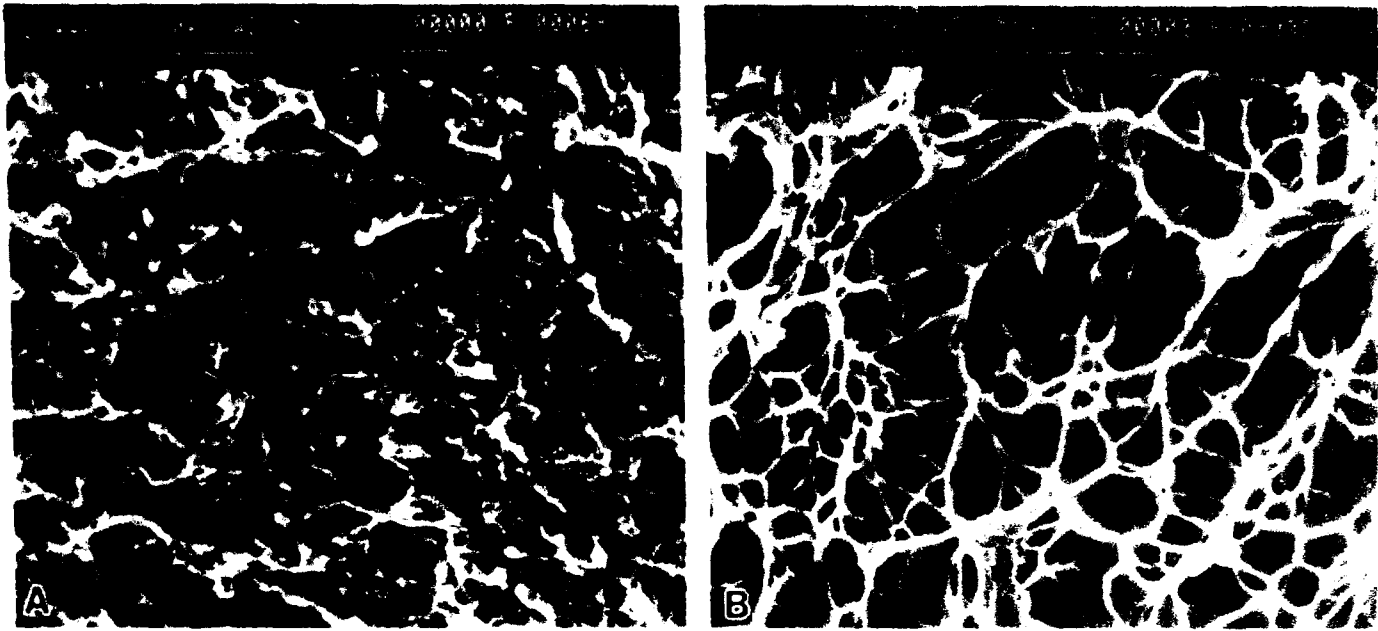


Figure 5.31 Comparison of the dimple size in a) room temperature and b) 260°C tensile tests.



Figure 5.32 Low magnification secondary electron images of a) specimen surface and b) fracture surface from a specimen which was tensile tested at 650°C.

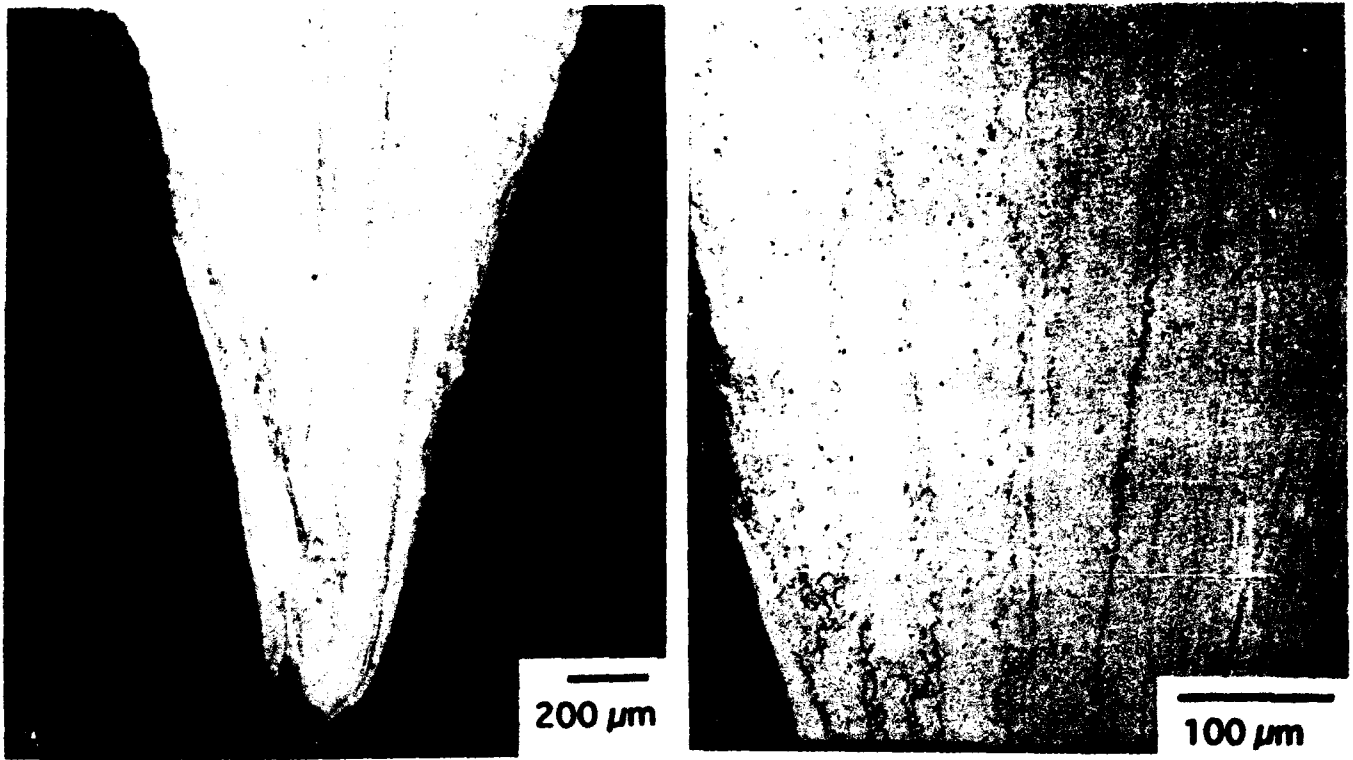


Figure 5.33 Optical micrographs taken at two magnifications showing a) necking to a point and oxidation, and b) grain structure in the specimen following the test.

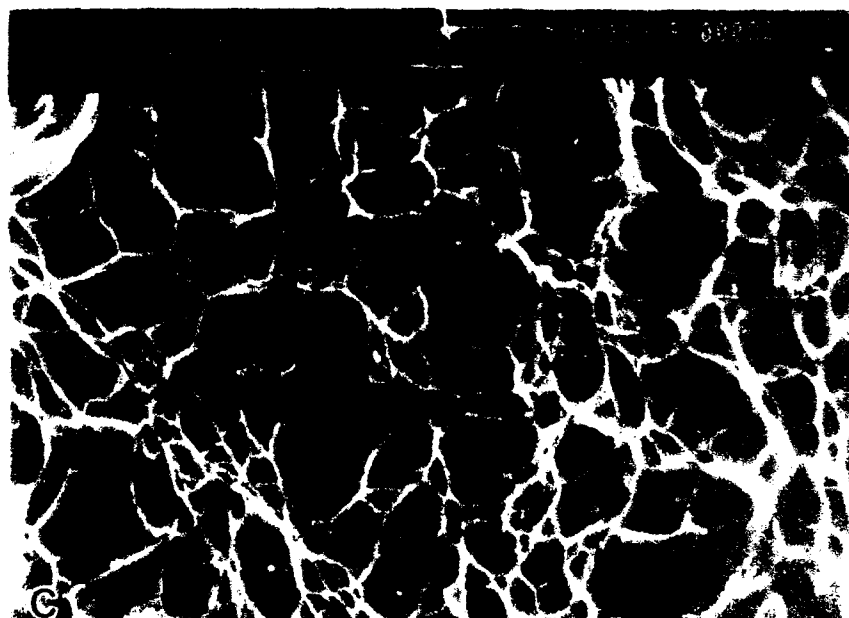


Figure 5.34 Secondary electron micrographs of a tensile specimen which was tested in inert environment at 650°C showing a) reduction of area and lack of surface cracks, and b) dimples present on the fracture surface following inert test for comparison with c) dimples on the fracture surface for a specimen which was tested in air.

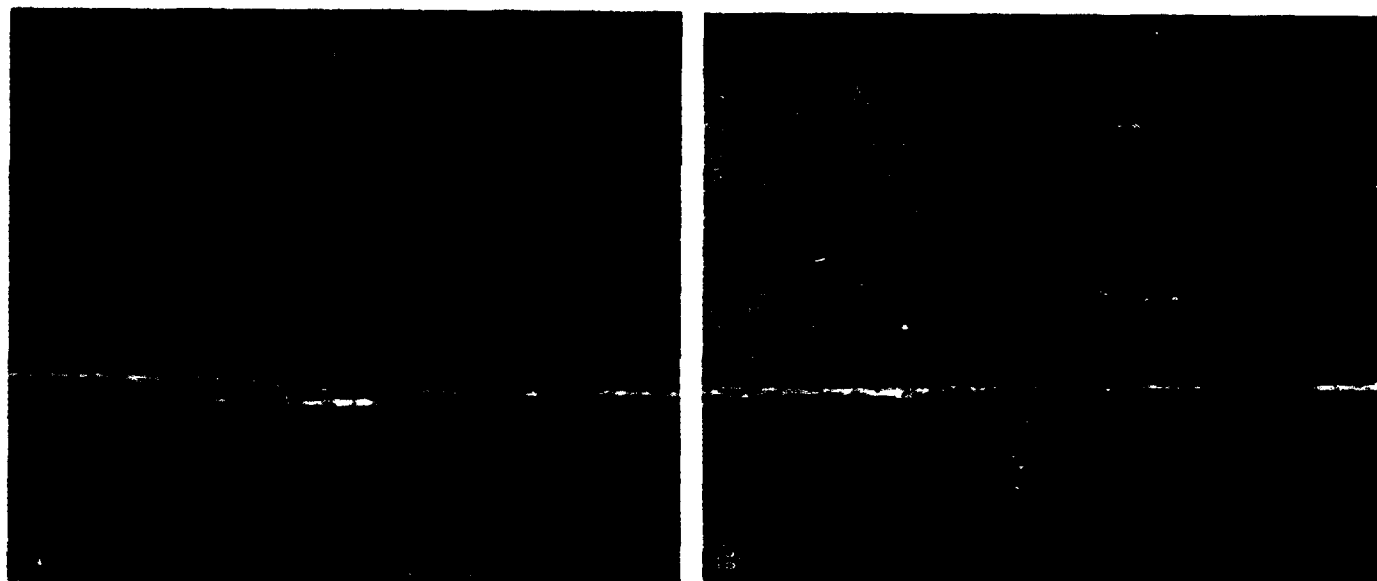


Figure 5.35 Comparison of backscattered electron images of material which had been tensile tested a) as-heat treated and b) following a thermal exposure at 650°C / 100h.

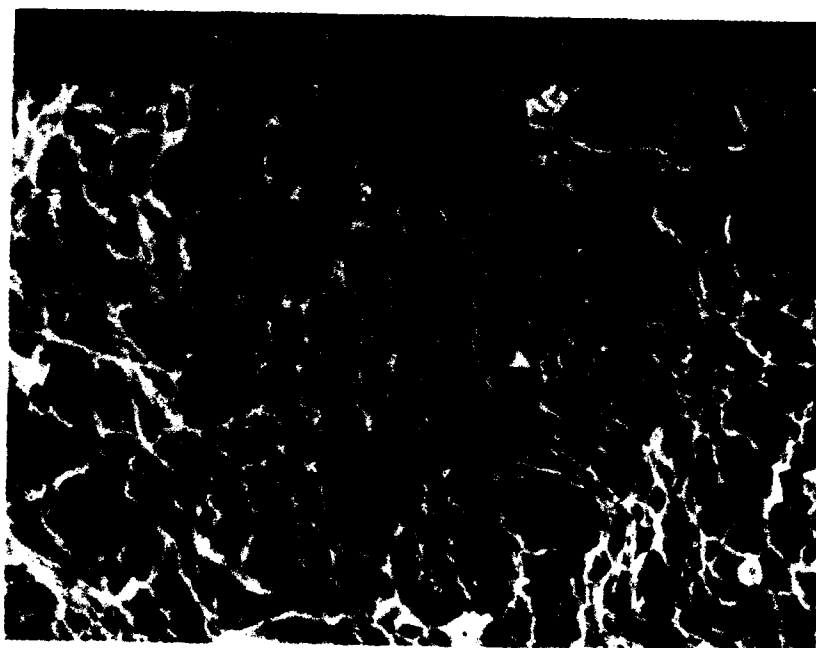


Figure 5.36 Secondary electron micrograph showing the dimple size in a specimen which had been tensile tested following thermal exposure at 650°C / 100h.



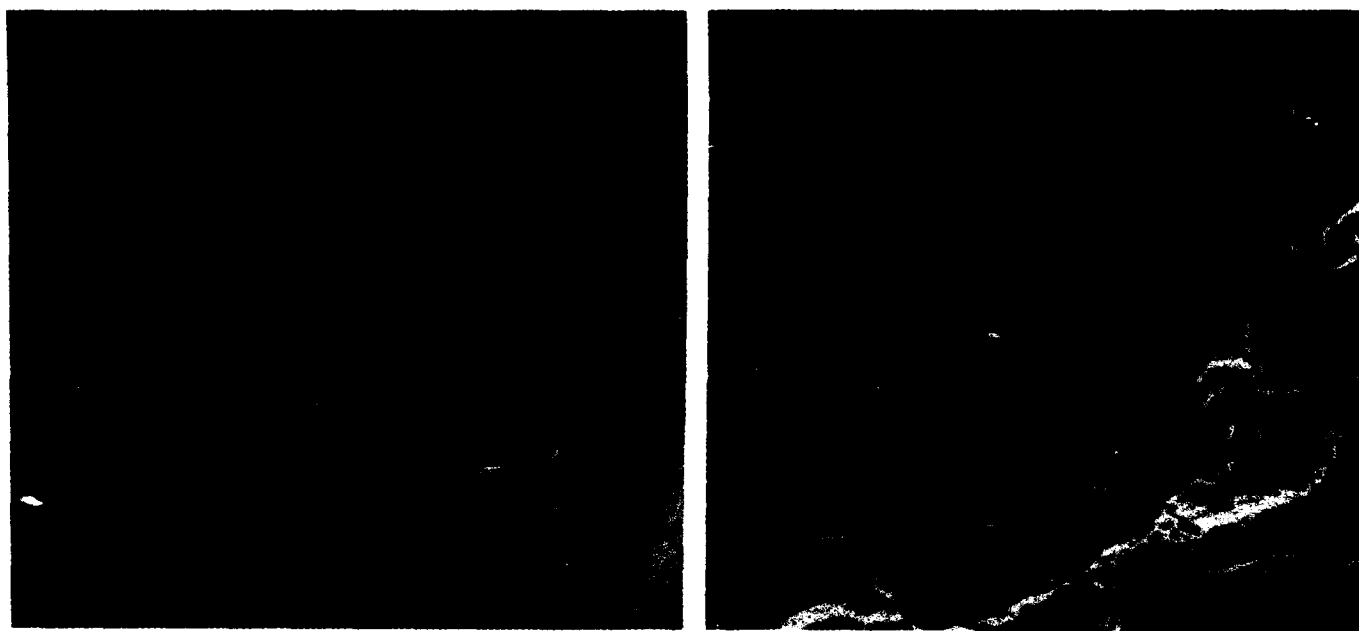


Figure 5.37 Secondary electron micrographs taken at three magnifications from a specimen which had been creep tested to failure in 3.1h at 540°C / 560MPa.

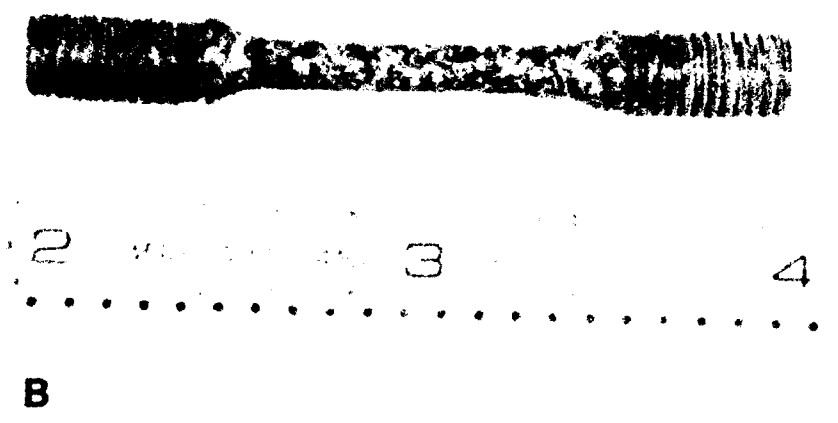
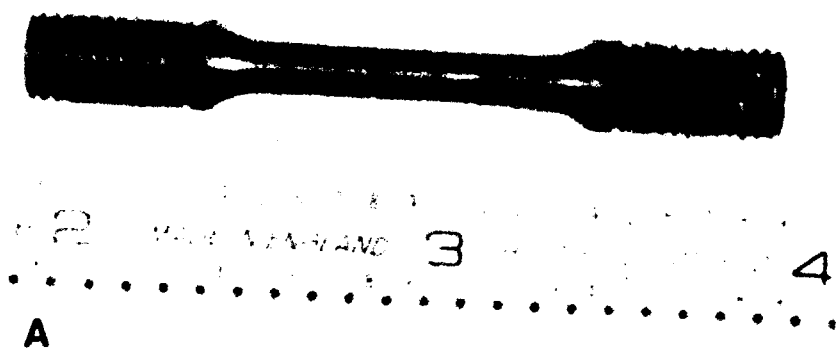


Figure 5.38 Optical micrographs of specimens following creep for 100 hr at a) 650°C and b) 760°C.

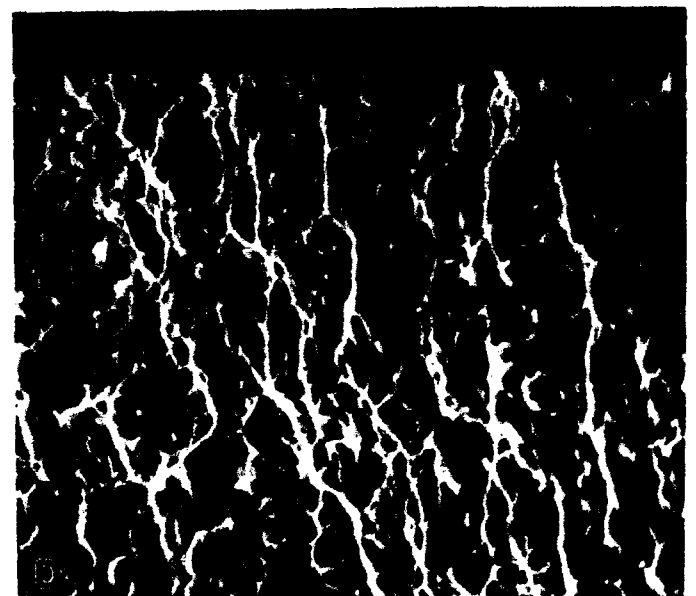
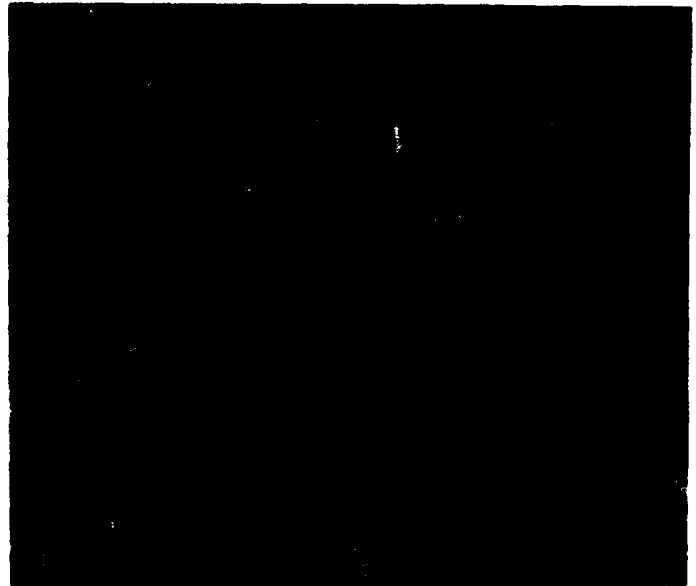
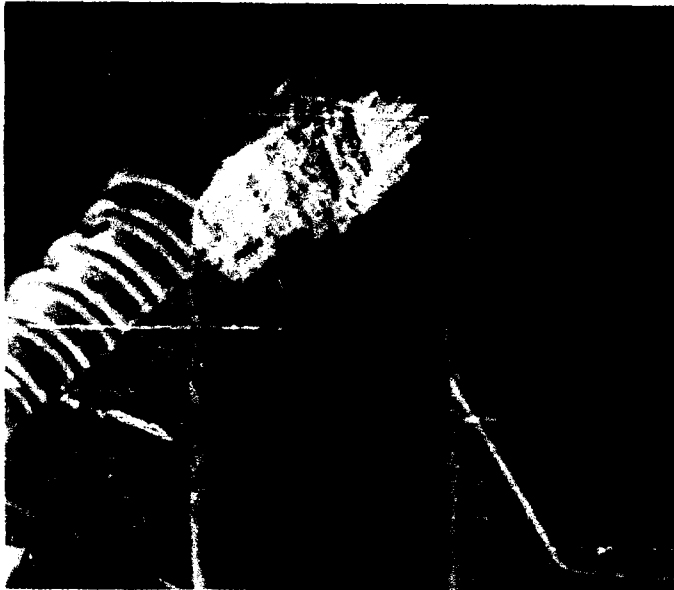


Figure 5.39 Secondary electron images of specimens which were tensile tested following creep for 100 hr at 650°C a) specimen surface, and b) fracture surface and for 100 hr at 760°C c) specimen surface, and d) fracture surface.

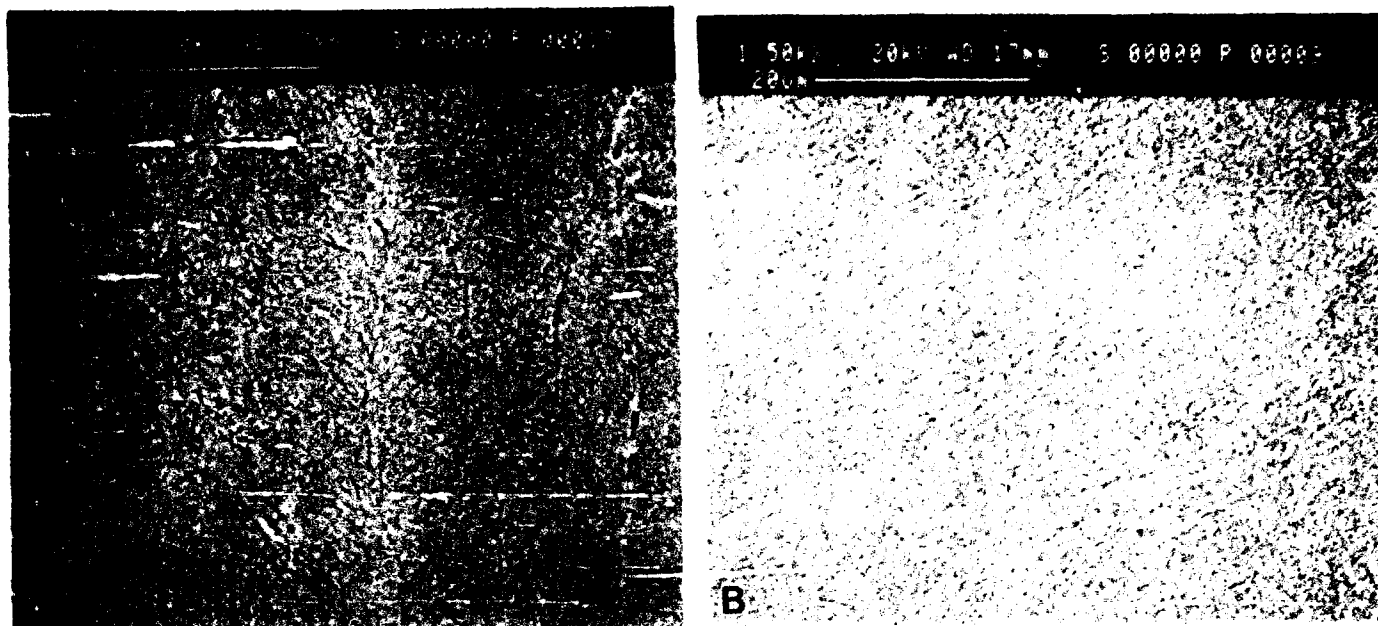


Figure 5.40 Backscattered electron images of the microstructure of specimens which were creep tested for 100h at a) 650°C and b) 760°C.

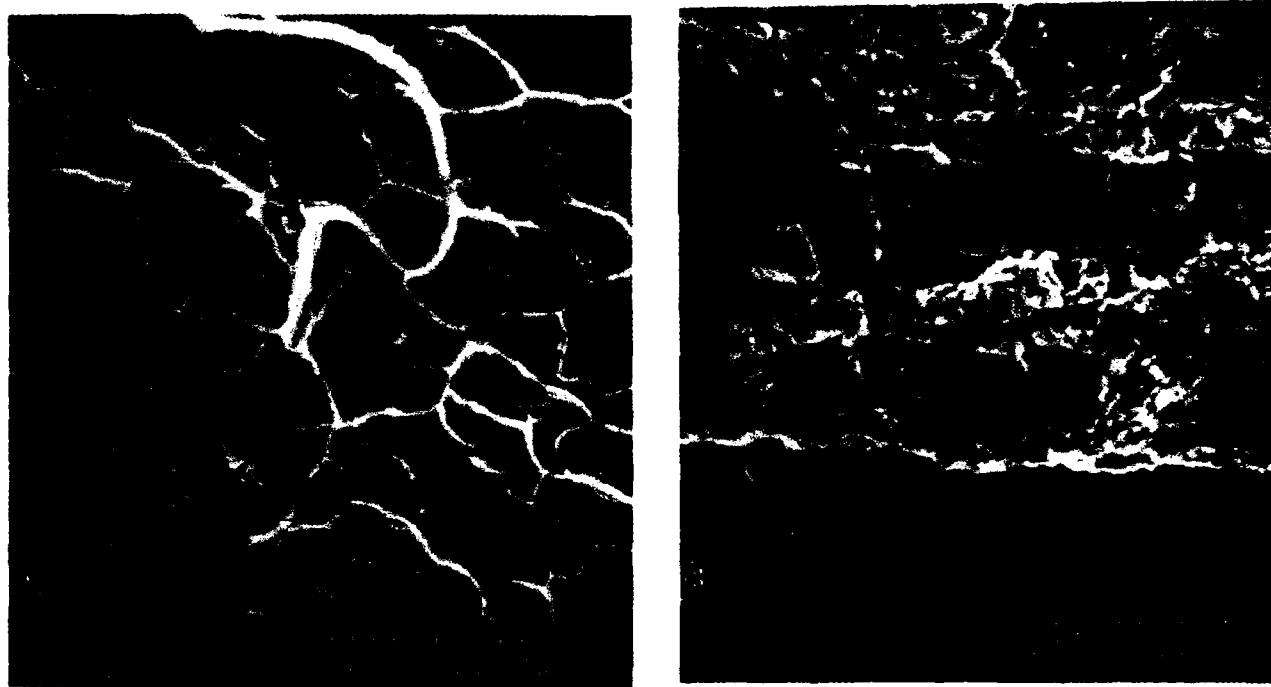


Figure 5.41 Secondary electron images of the fracture surface from LCF specimens showing a) dimples and b) striations.

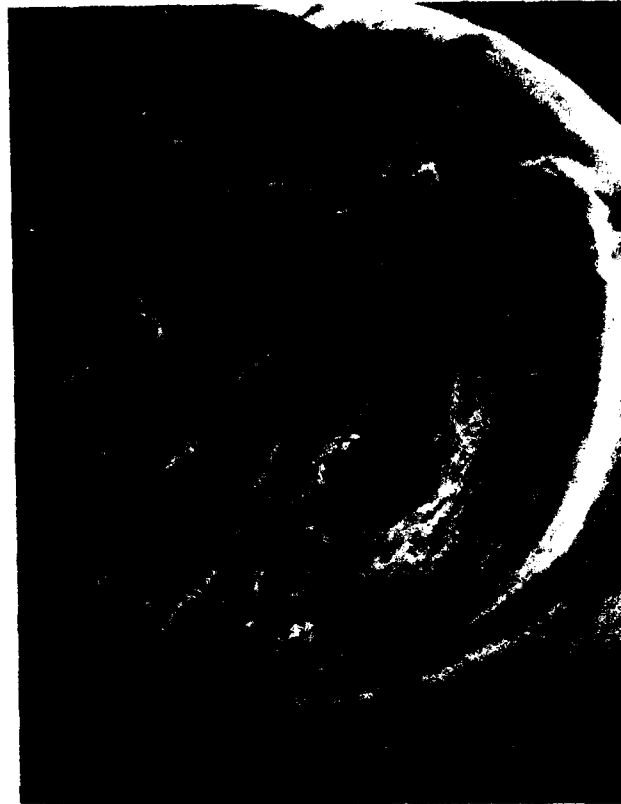


Figure 5.42 Secondary electron image taken from the fracture surface of an HCF specimen.

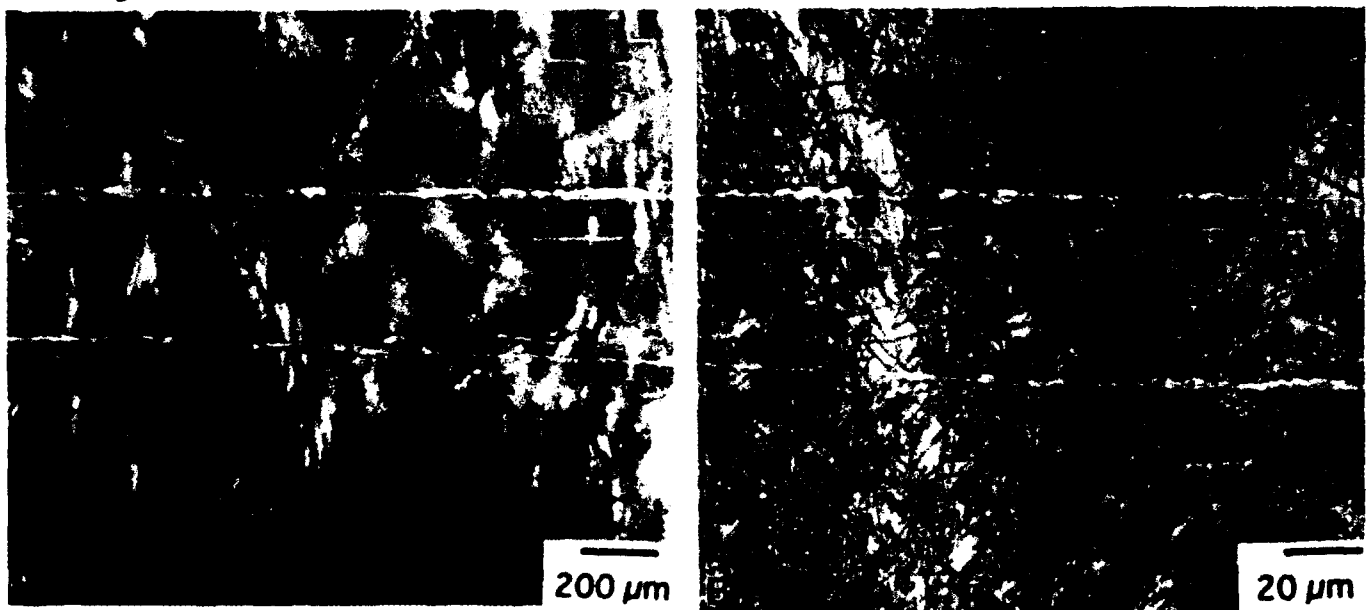


Figure 5.43 Optical micrographs of the microstructure below the fracture surface for a specimen from heat treatment 2 in alloy 3 which was tensile tested at room temperature a) low, and b) high magnification.

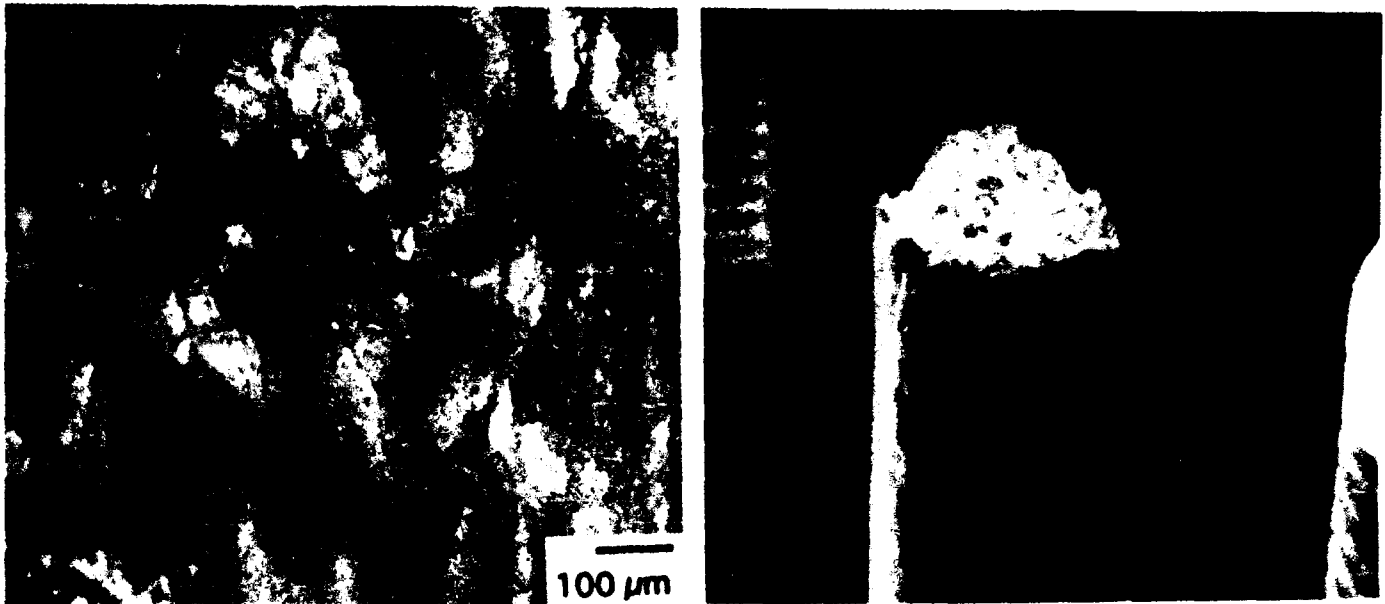


figure 5.44 Micrographs taken of a specimen from heat treatment 2 in alloy 3, a) optical micrograph showing the presence of grain boundary failures away from the fracture surface, and b) secondary electron images of the surface of the tensile specimen.

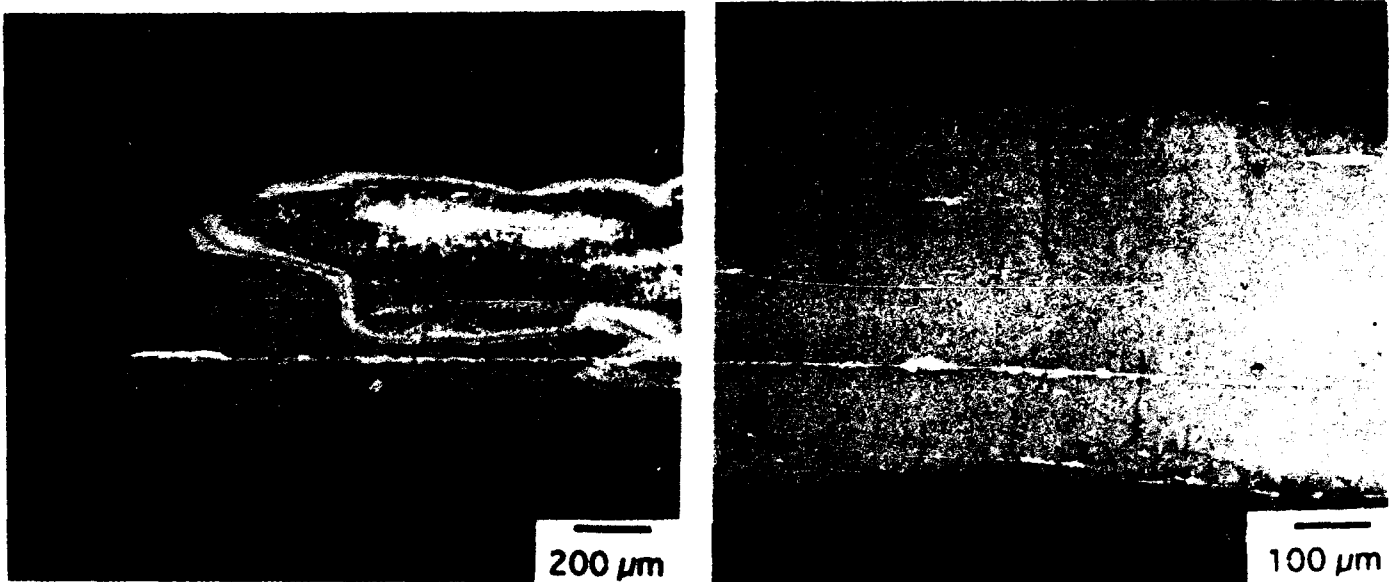
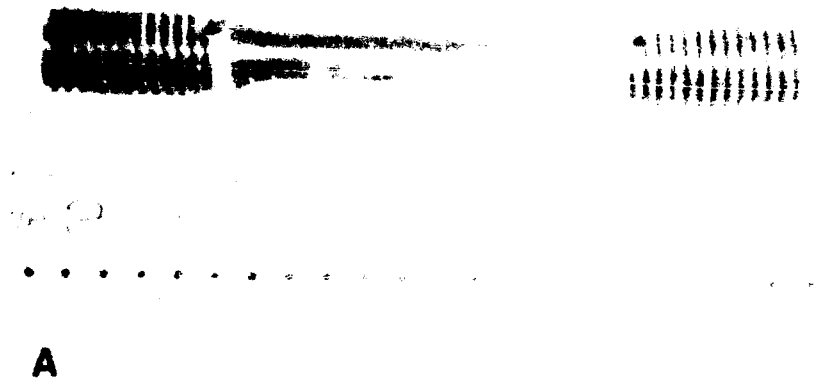
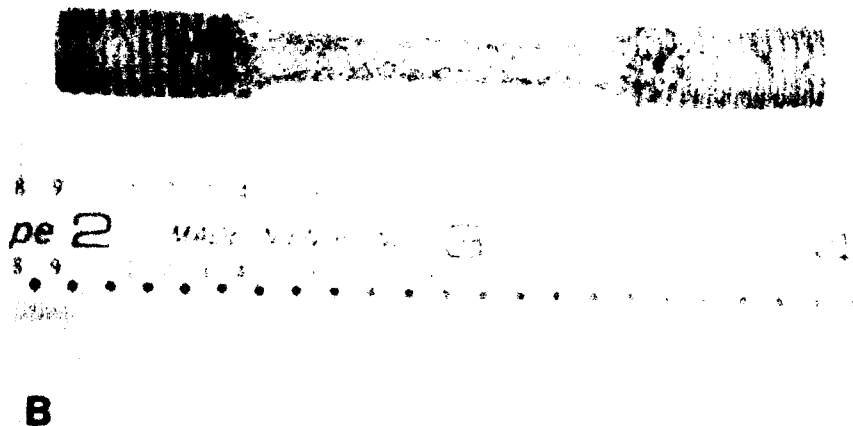


Figure 5.45 Optical micrograph of the microstructure of the specimen which was tested at 980°C.



**A**



**B**

Figure 5.46 Optical micrographs of specimens for heat treatment 2 following creep for 100 h at a) 650°C and b) 760°C.



Figure 5.47 Secondary electron images of the fracture surface of specimens which were tensile tested at room temperature following a creep exposure at a) 650°C / 100h, and b) 760°C / 114h.

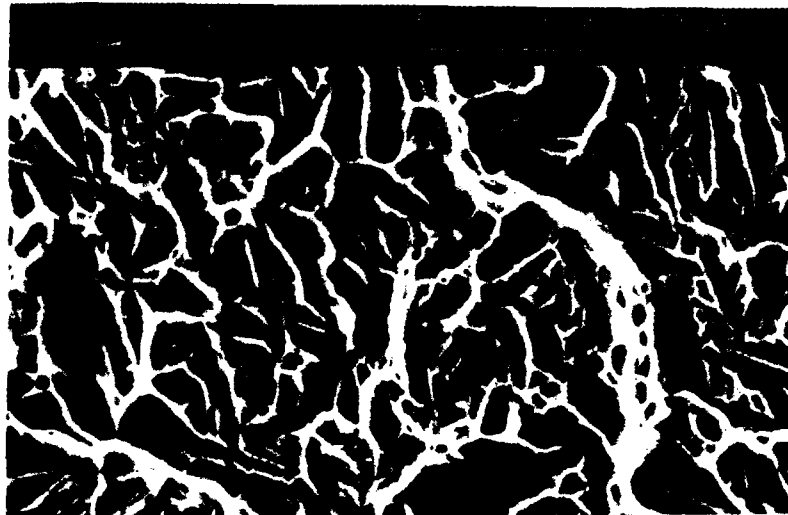


Figure 5.48 Secondary electron image of the fracture surface of a specimen which was tensile tested at room temperature following creep exposure at 650°C / 100h indicating the presence of tear ridges associated with the microstructural laths.



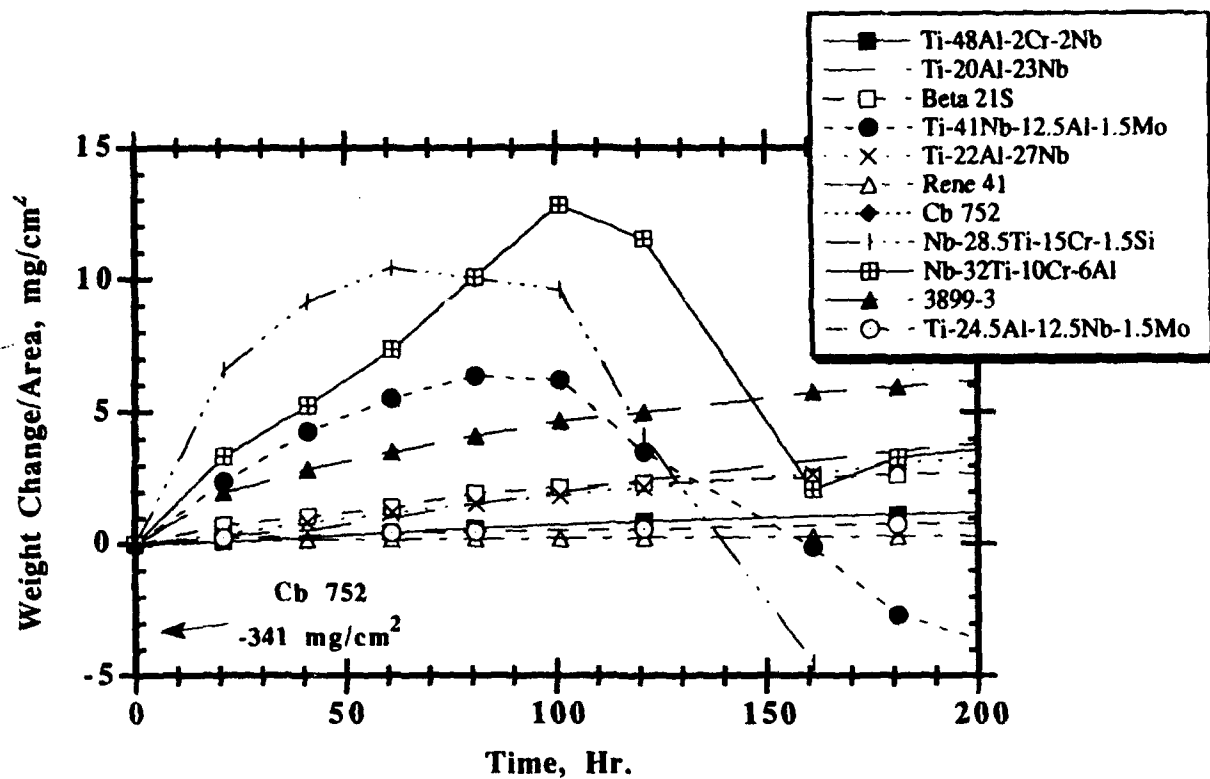


Figure 5.49 Weight change/area versus hot time data for various alloy systems during a 760°C cyclic oxidation test in air. The thermal cycle was 1h at temperature followed by a forced air cool down to room temperature for 10 minutes.

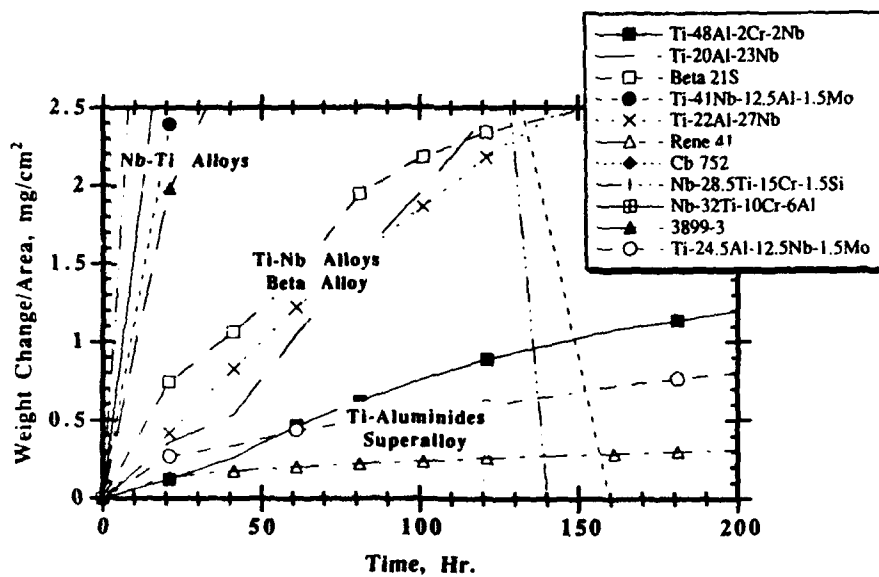


Figure 5.50 Weight change/area versus hot time data for various alloy systems during a 760°C cyclic oxidation test in air. The expanded y-axis shows the gap between Nb-Ti alloys and other alternative systems. The gap can be closed with further alloy development or the use of an environmental coating.

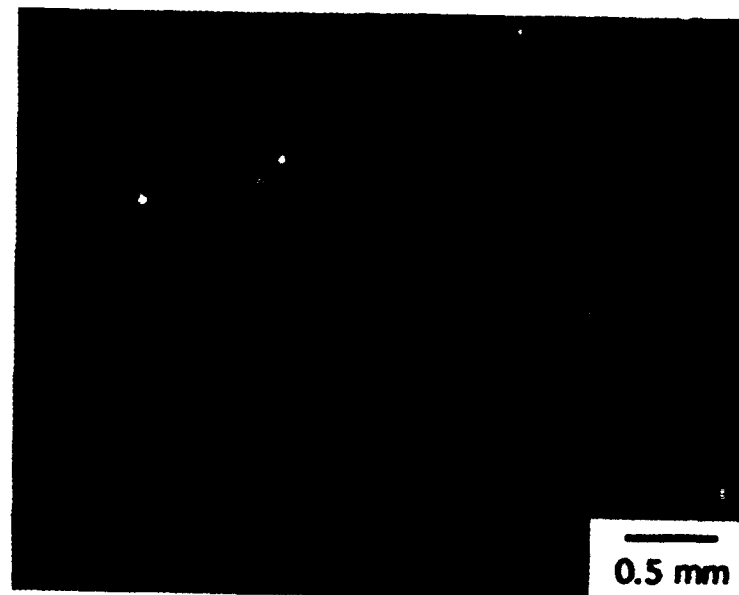


Figure 5.51 Low magnification surface micrograph of René 41 after 61hr of cyclic oxidation at 760°C in air. The surface shows no spalling and a continuous chromia scale.

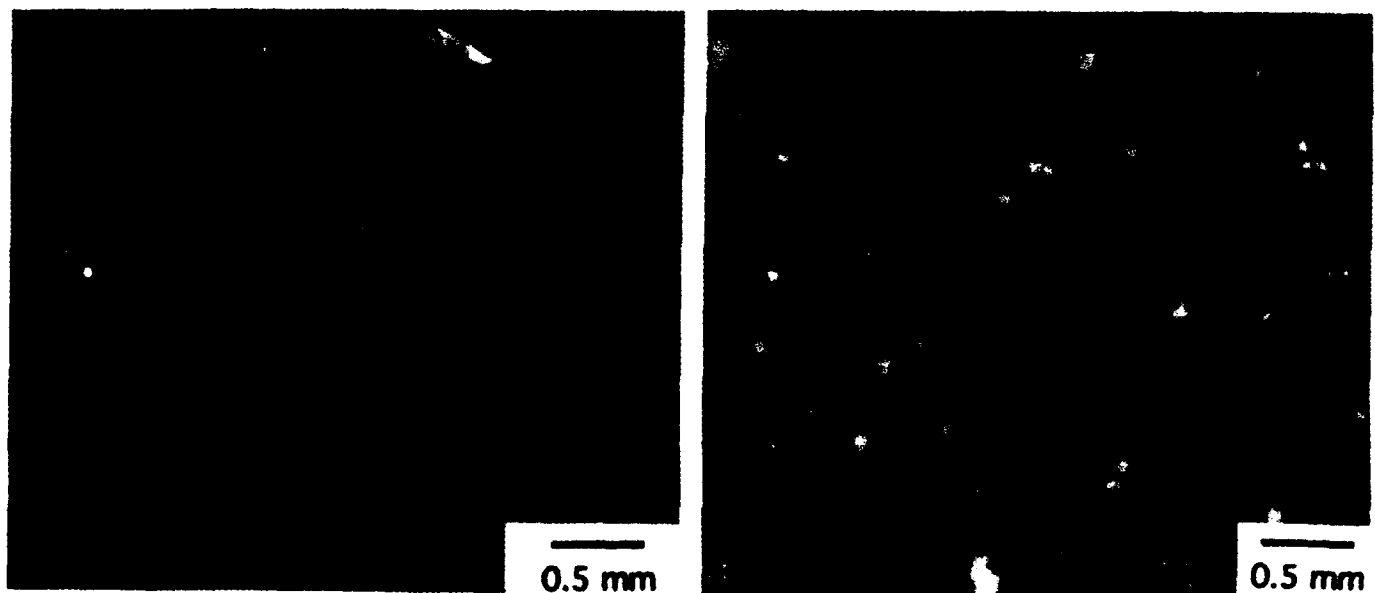


Figure 5.52 Low magnification surface micrograph of (a) Ti-48Al-2Cr-2Nb (b) and Ti-24.5Al-12.5Nb-1.5Mo after 61h of cyclic oxidation at 760°C in air. The 48-2-2 gamma alloy shows a thick oxide with little spallation, while the 12.5-1.5 alpha-2 alloy shows patchy spallation.

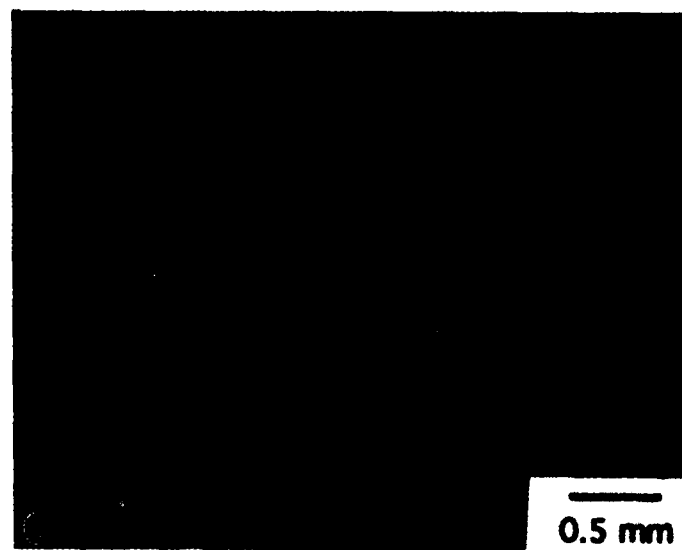
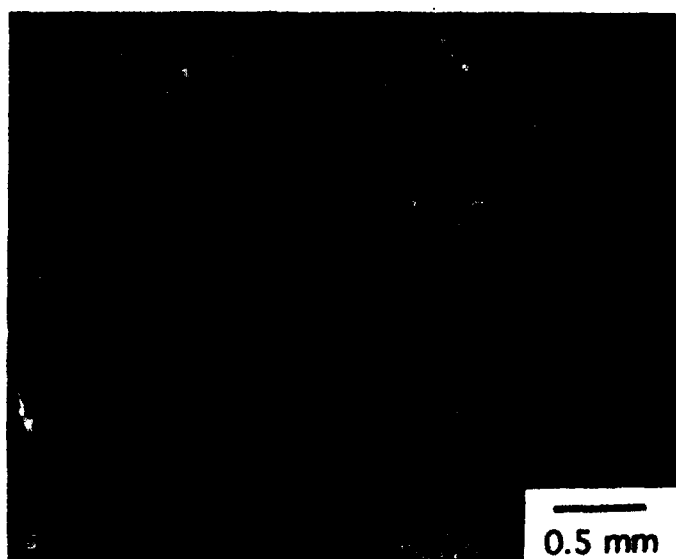
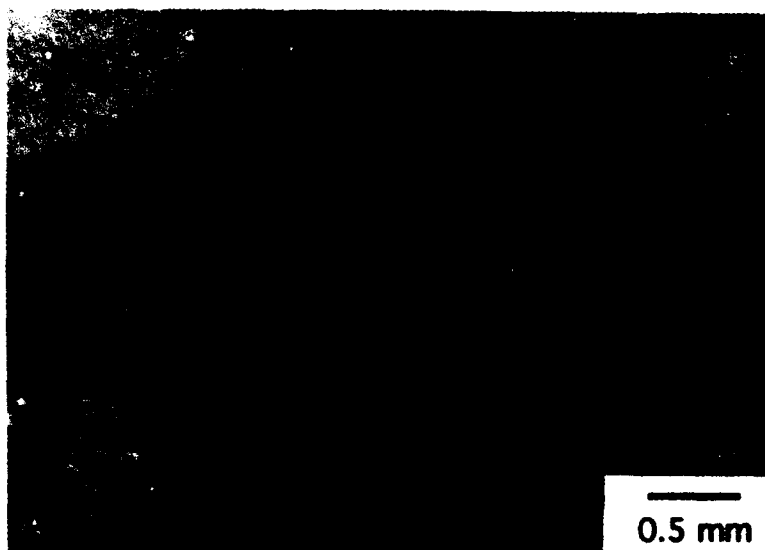


Figure 5.53 Low magnification surface micrograph of a) Beta 21S, b) Ti-20Al-23Nb and c) Ti-22Al-27Nb after 61h of cyclic oxidation at 760°C in air. These alloys all showed signs of spallation. The beta 21S had a heterogeneous oxide scale, while the Ti-Nb alloys had a more homogeneous white scale.

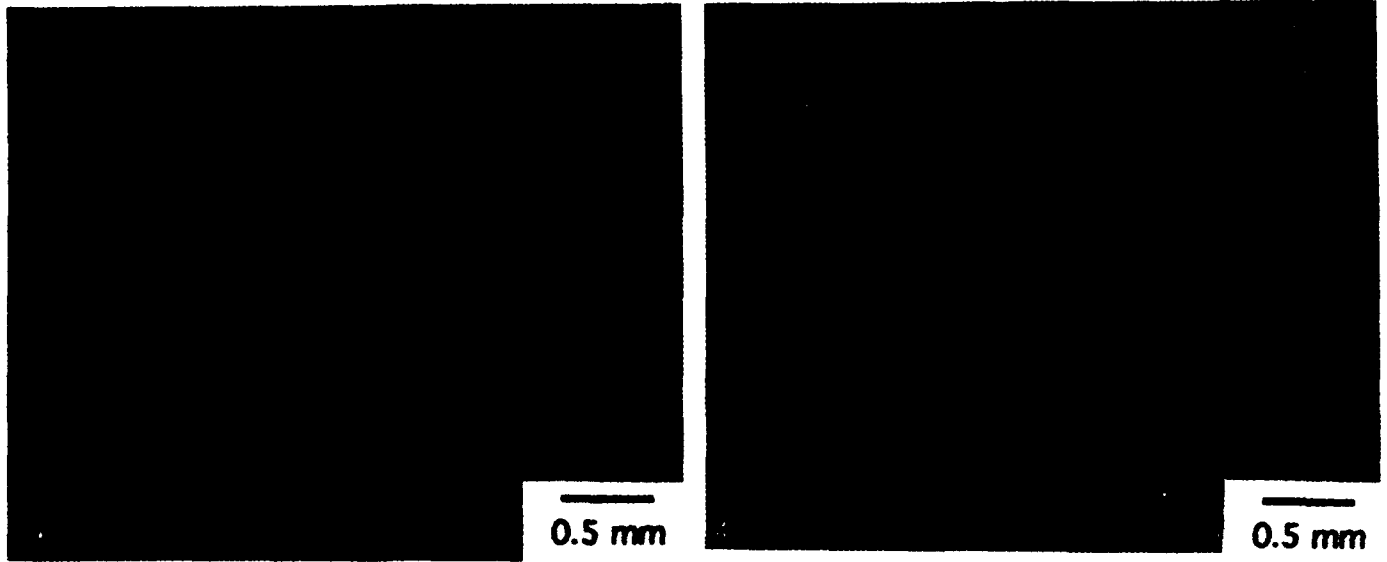


Figure 5.54 Low magnification surface micrograph of a) alloy 1 (Nb-32Ti-10Cr-6Al) and b) alloy 2 (Nb-28Ti-15Cr-1.5Si) after 61h of cyclic oxidation at 760°C in air. These alloys showed spallation and a dark orange brown scale.

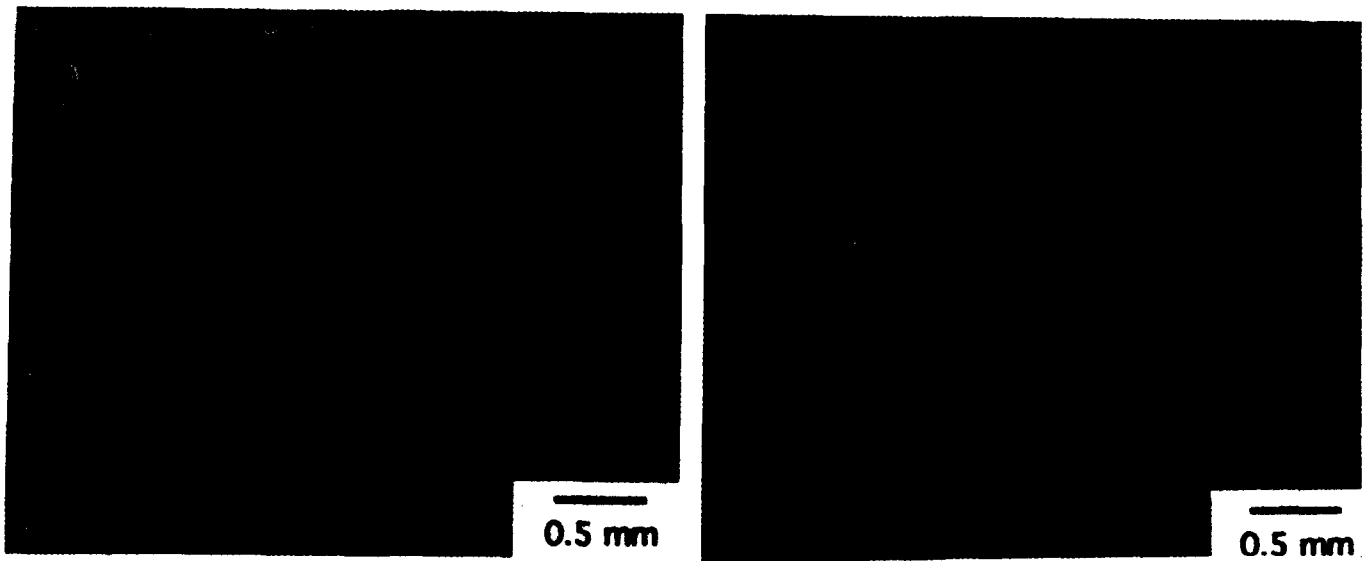


Figure 5.55 Low magnification surface micrograph of a) alloy 3 (Nb-41Ti-12.5Al-1.5Mo) and b) 3899-3 (Nb-37.5Ti-5Hf-5V-5Cr-5Al-0.5Zr-0.3C) after 61h of cyclic oxidation at 760°C in air. Alloy 3 showed white spalling scales, while the 3899-3 was brown grey with less spallation.

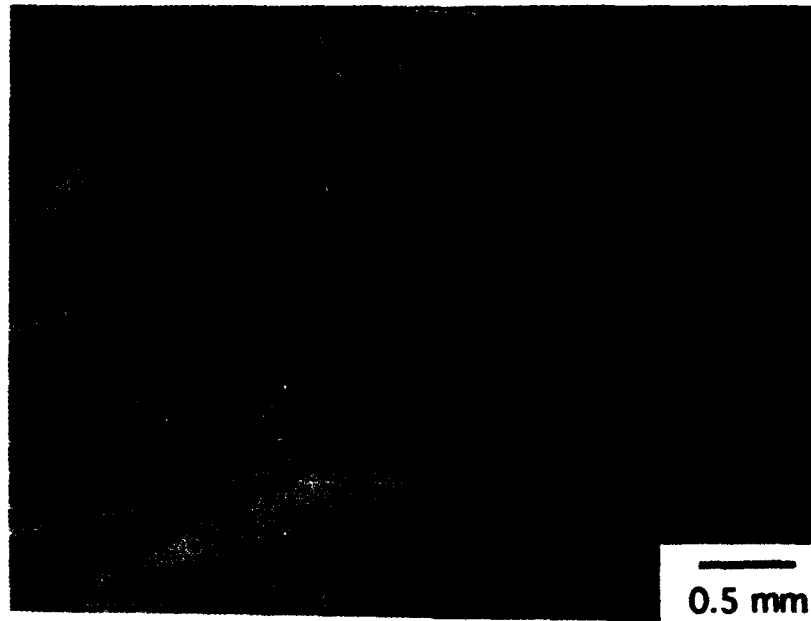


Figure 5.56 Low magnification surface micrograph of Cb752 after 21h of cyclic oxidation at 760°C. The 0.9mm thick sheet was totally oxidized into Nb<sub>2</sub>O<sub>5</sub>.

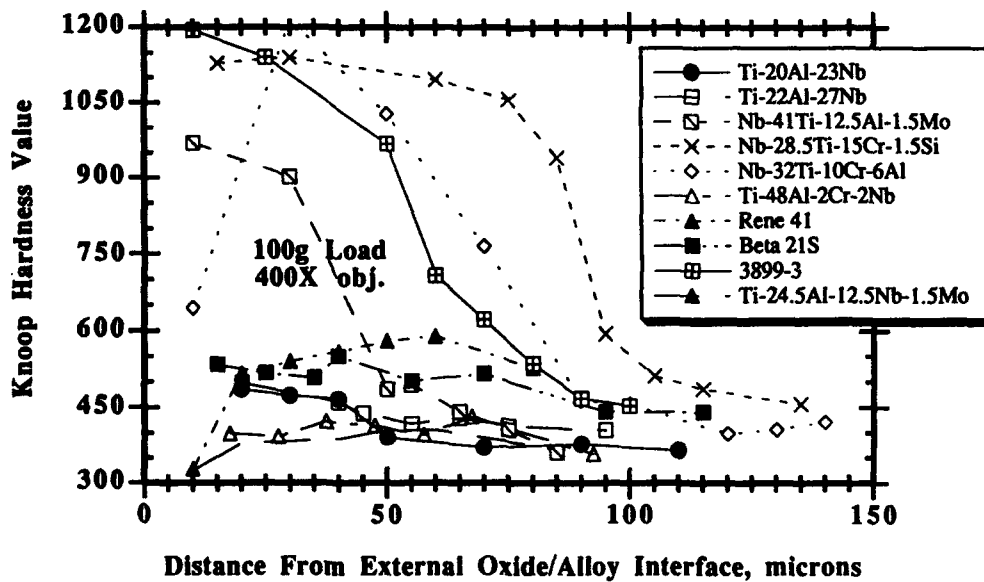
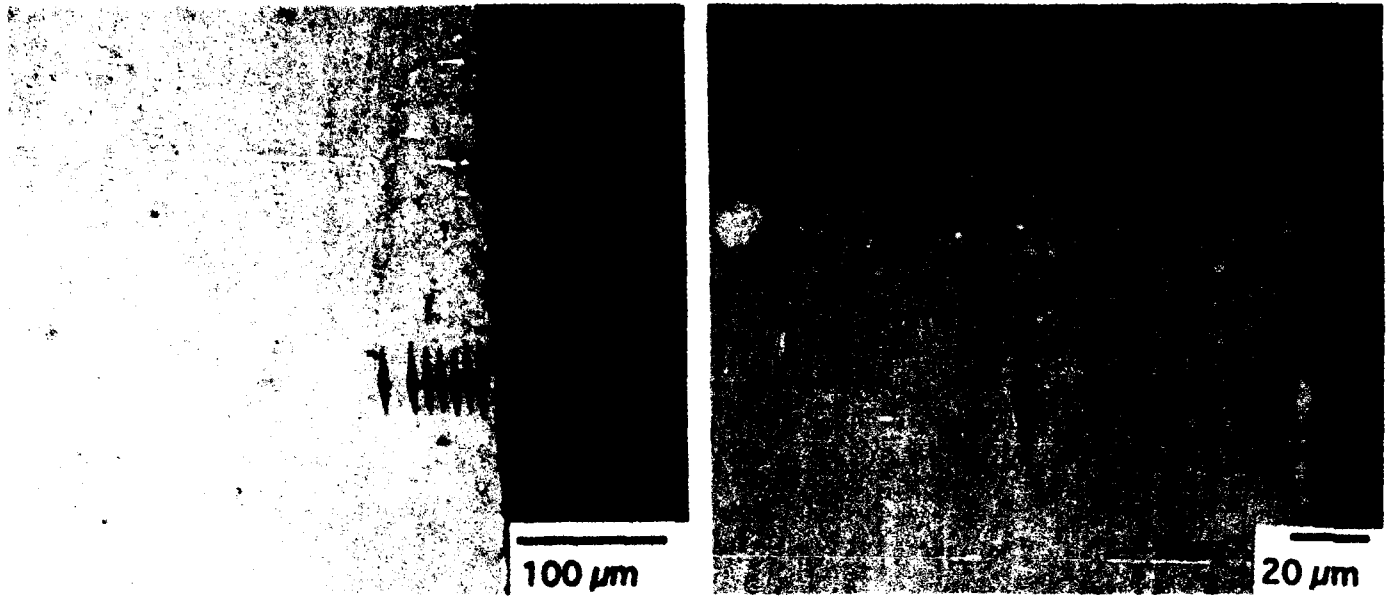
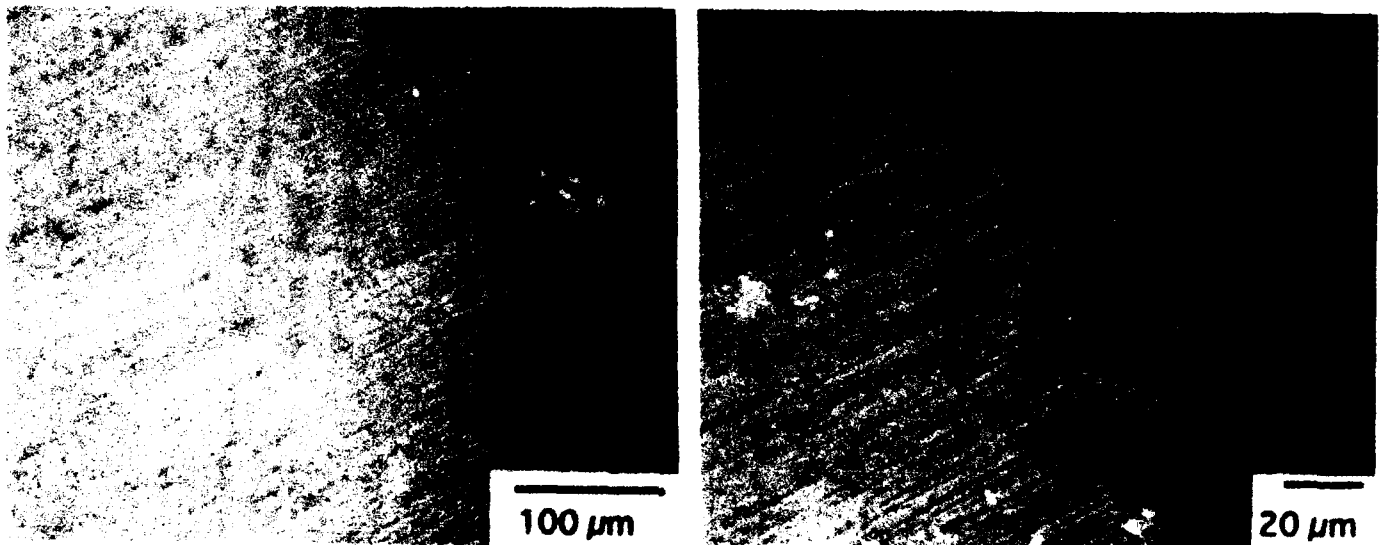


Figure 5.57 Hardness profiles of the various alloy stems after 760°C cyclic oxidation in air. The Nb-Ti alloys show a distinct case.



**Figure 5.58** Optical cross sectional micrographs of etched Rene'41 after 760°C cyclic oxidation and hardness testing. A denuded layer that is softer than the base alloy is observed under the Cr-rich scale



**Figure 5.59** Optical cross sectional micrographs of etched Ti-48Al-2Cr-2Nb after 760°C cyclic oxidation and hardness testing. No hardening was observed near the surface after test although a sublayer was not tested.

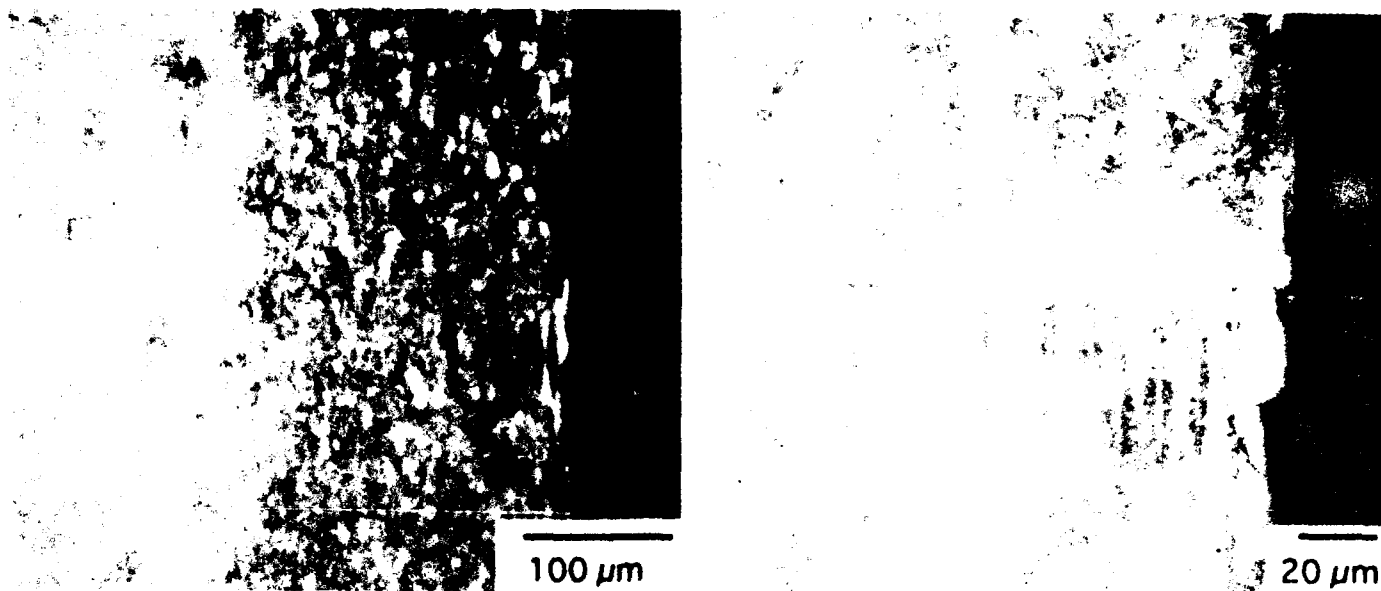


Figure 5.60 Optical cross sectional micrographs of etched Ti-24.5Al-12.5Nb-1.5Mo after 760°C cyclic oxidation and hardness testing. A dark etching layer was noted near the surface but hardness readings were not much different than the base

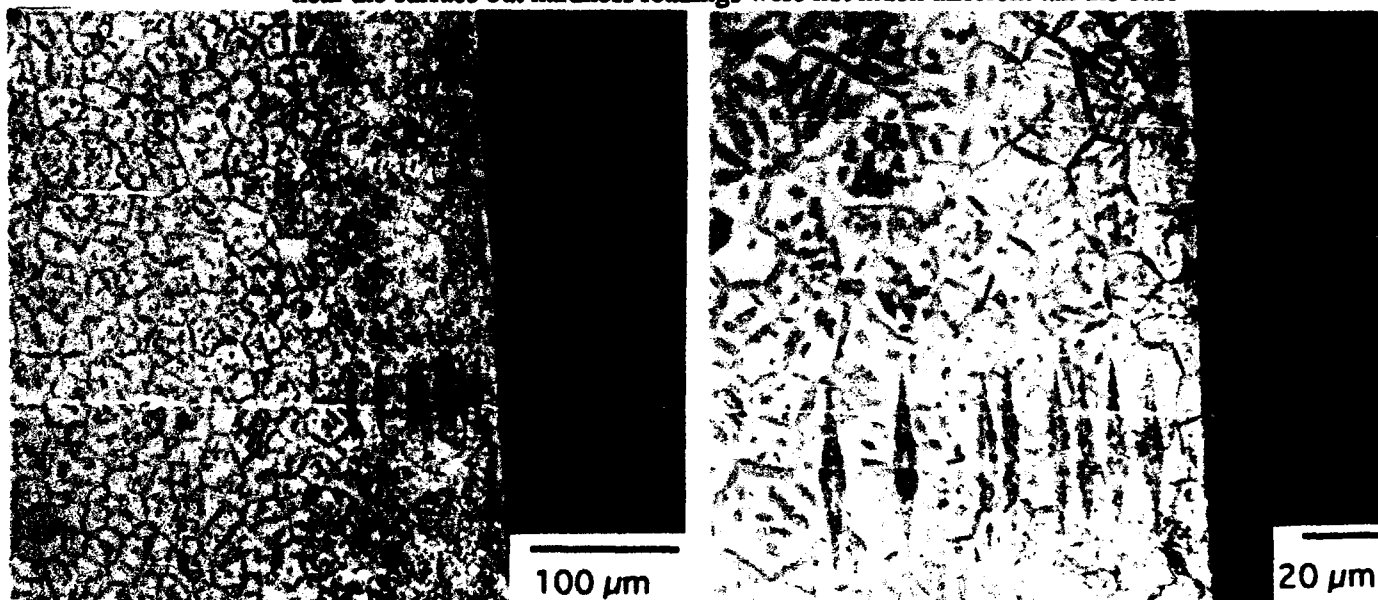
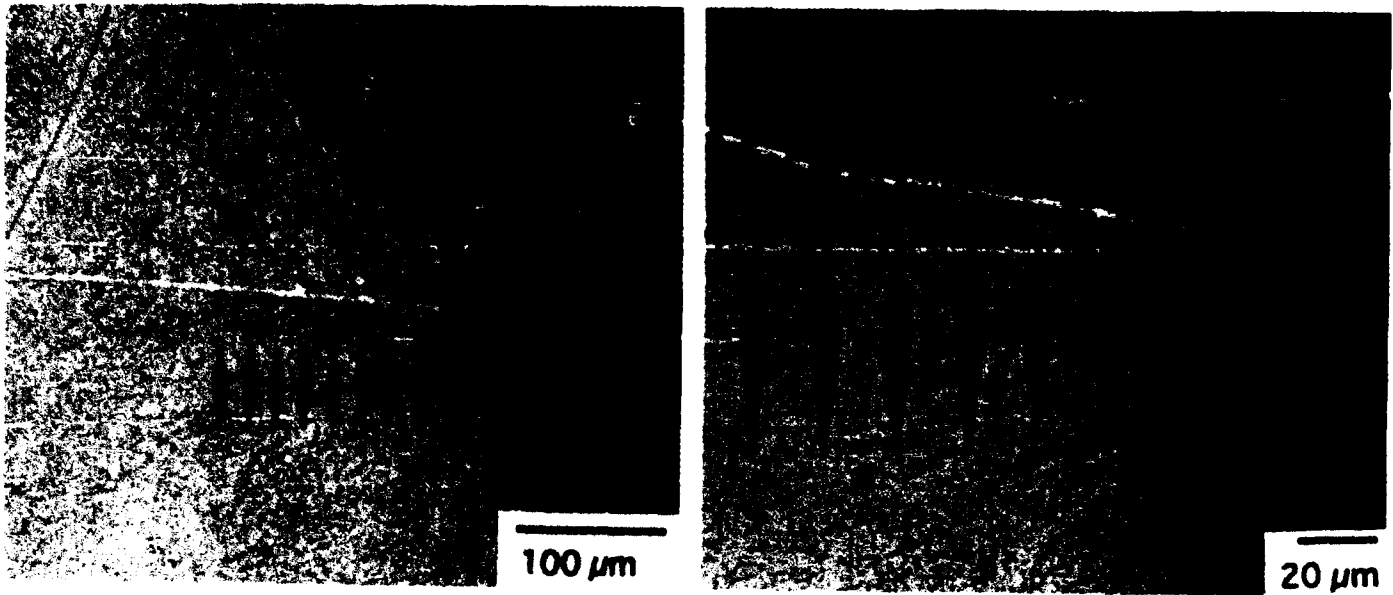
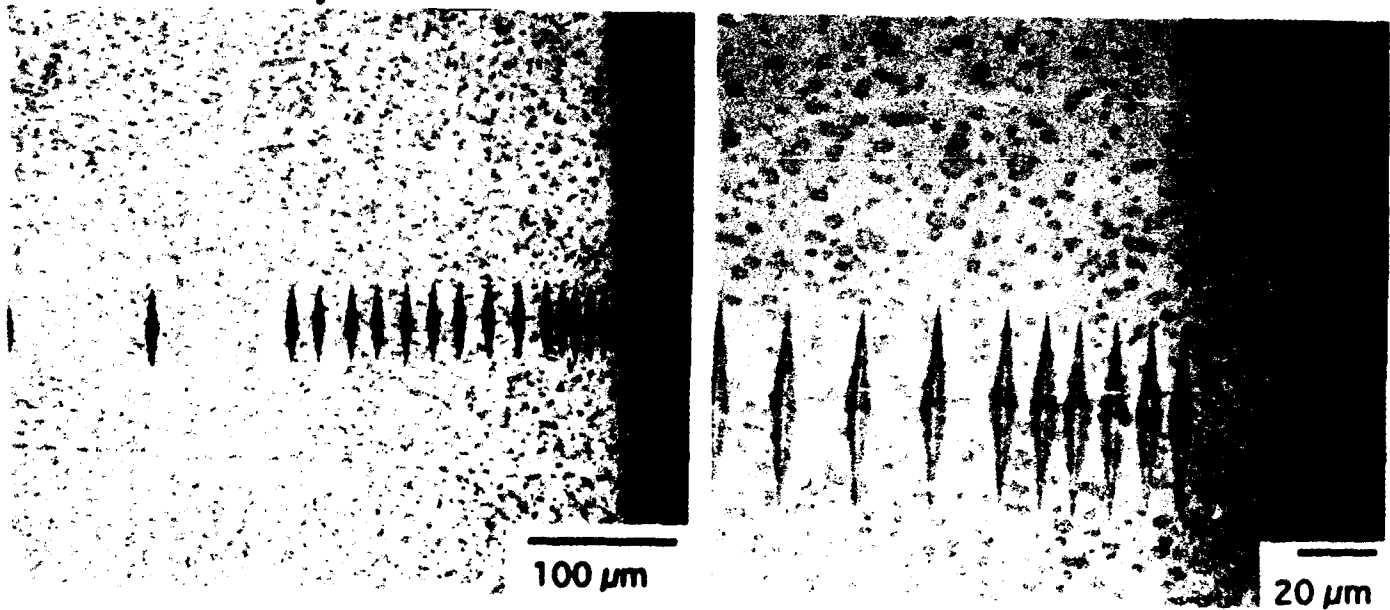


Figure 5.61 Optical cross sectional micrographs of etched Beta 21S after 760°C cyclic oxidation and hardness testing. A visible scale is noted as well as extensive grain boundary precipitates. A white imaging alpha case may be developed under the external scale.



**Figure 5.62** Optical cross sectional micrographs of etched Ti-20Al-23Nb after 760°C cyclic oxidation and hardness testing. A thick external scale and a dark etching hard layer are evident.



**Figure 5.63** Optical cross sectional micrographs of etched Ti-22Al-27Nb after 760°C cyclic oxidation and hardness testing. Little external scale was observed due to spallation or mounting procedures.



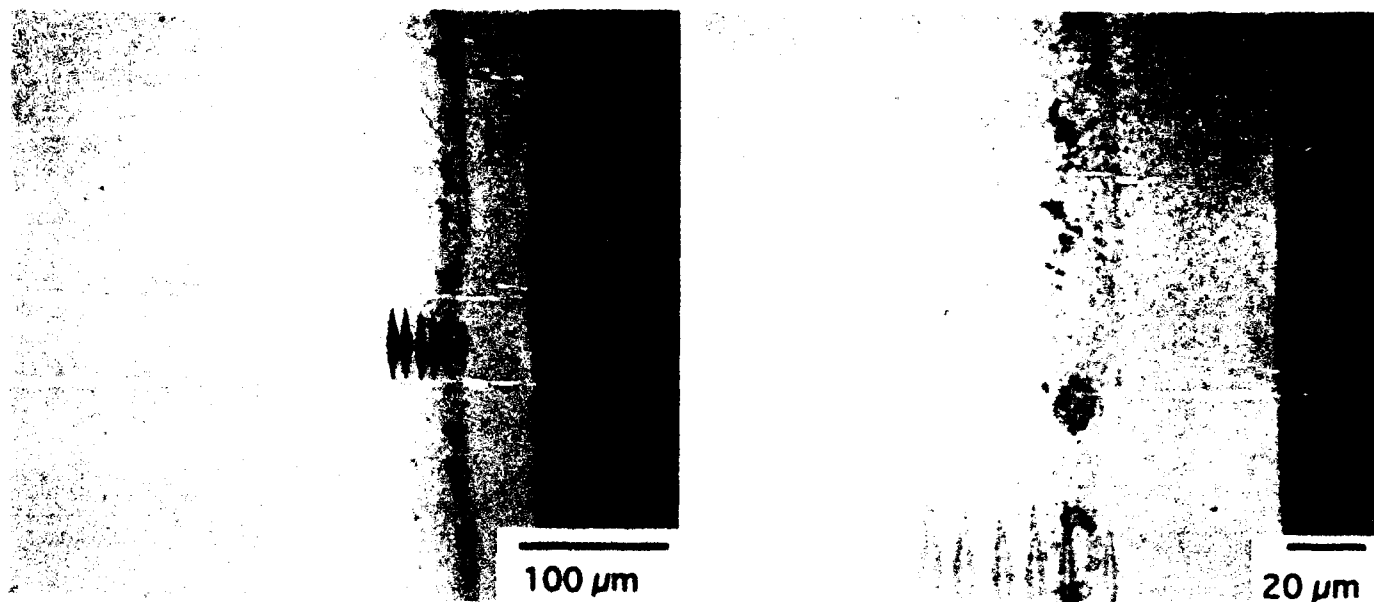


Figure 5.64 Optical cross sectional micrographs of etched 3899-3 after 760°C cyclic oxidation and hardness testing. A thick external scale and interstitial layer are observed.

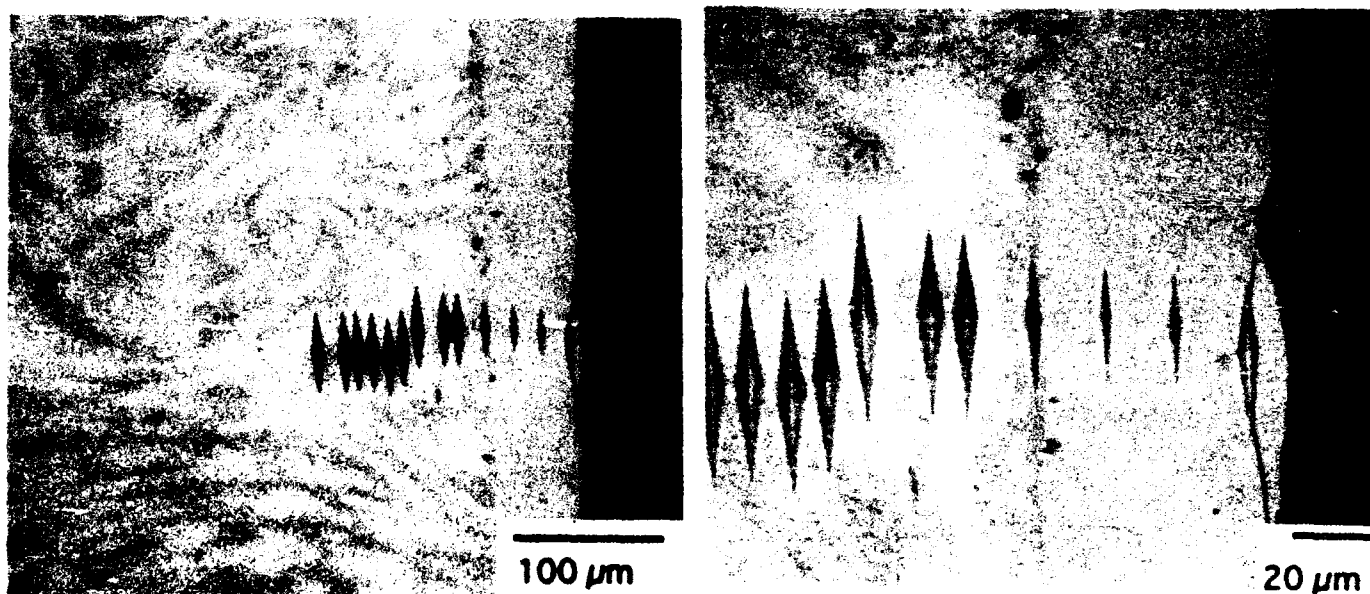


Figure 5.65 Optical cross sectional micrographs of etched Nb-32Ti-10Cr-6Al after 760°C cyclic oxidation and hardness testing. A thick external scale and interstitial layer are observed.

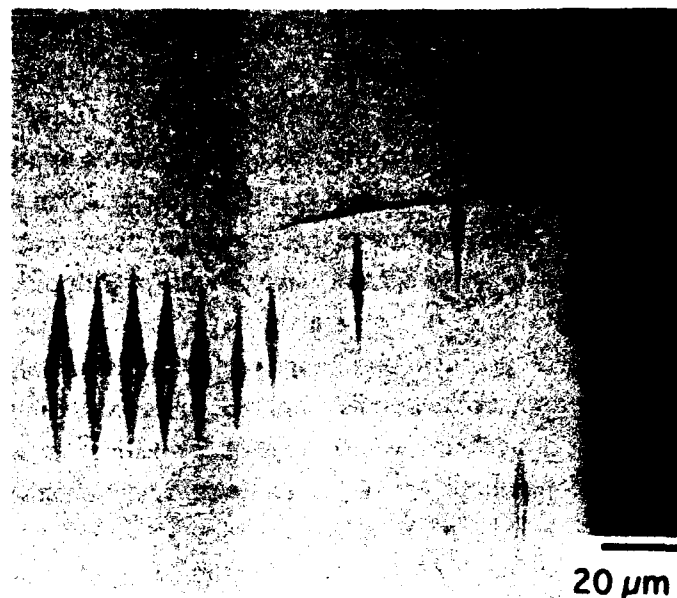
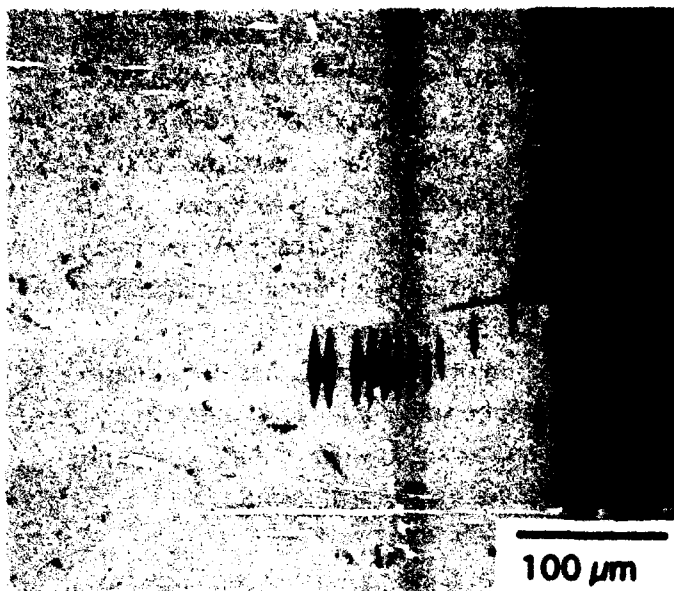


Figure 5.66 Optical cross sectional micrographs of etched Nb-28.5Ti-15Cr-1.5Si after 760°C cyclic oxidation and hardness testing. A thick external scale and interstitial layer are observed.

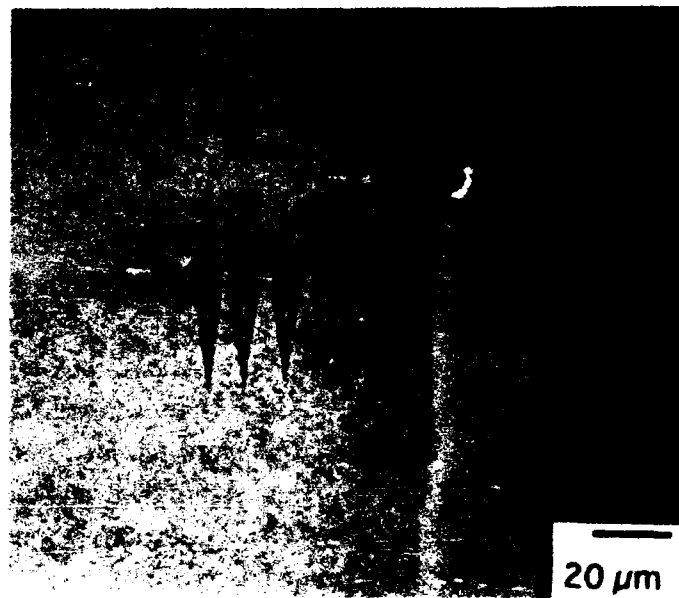
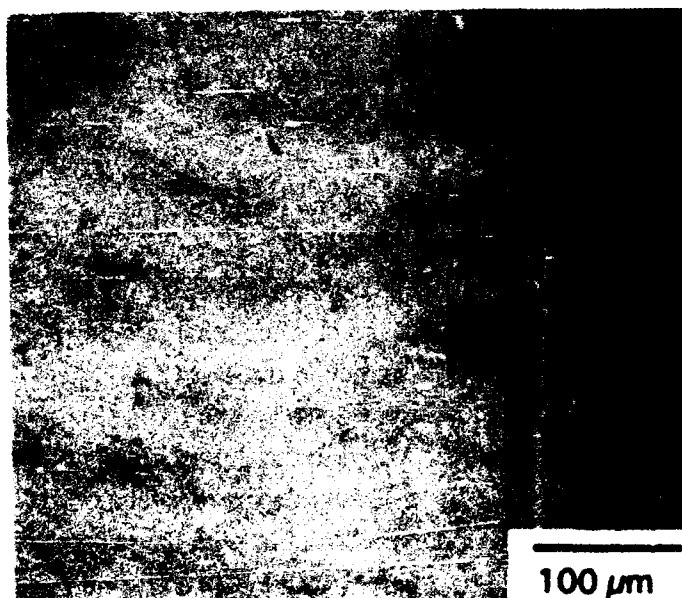


Figure 5.67 Optical cross sectional micrographs of etched Nb-41Ti-12.5Al-1.5Mo after 760°C cyclic oxidation and hardness testing. A thick external scale and interstitial layer are observed.

## 6.0 Summary

The use of Nb alloys in aircraft engines is limited by their extremely poor oxidation resistance, as evidenced by the oxidation test results for the conventional Nb alloys Cb752 and WC 3009 presented in this report in Sections 4.5 and 5.3.4. A significant screening effort aimed at improving the oxidation resistance of Nb base alloys was accomplished with several candidates being identified. In general, alloying to improve the oxidation resistance reduces the temperature capability of the Nb base alloys from the approximately 1350°C-1600°C range to below 1200°C. This strength reduction is due to the fact that the alloy additions which improve oxidation resistance are lower melting materials such as Ti or Al, while those which increase temperature capability such as W have poorer oxidation resistance than the Nb alloys. Promising candidates for a range of temperatures were identified in the screening studies performed and reported in Section 3 using both rapid solidification and Section 4 using ingot approaches. Several of the promising materials identified in the screening effort could not be studied due to program or technical constraints. One of the difficulties was problems producing powder of the high melting point alloys which prevented sufficient quantities being made for mechanical testing.

It should be pointed out that the improved oxidation resistance of these promising candidates is still not as good as a Ni base superalloy would be at temperature, but the oxidation resistance is significantly improved over the conventional Nb alloys. There are many beneficial properties of Nb alloys, such as low coefficient of expansion, and low modulus which could be used if the catastrophic oxidation problems could be overcome. Therefore, the improved oxidation resistance of the Nb-Ti alloys studied in this contract allow the other beneficial properties of Nb alloys to be considered in applications without the risk of catastrophic oxidation. However, the Nb-Ti alloys would require a stable environmental coating to achieve long life.

Three alloys were selected for scaleup based on the results of oxidation and screening mechanical property testing. The alloys were selected based on their level of maturity, demonstrated mechanical and oxidation properties and the expected opportunity to learn about possible future approaches to alloy improvements. Alloy 1 was selected early in the program since it had already undergone a screening study. Alloy 2 was selected based on its performance in the ingot screening studies and Alloy 3 was selected because of its good oxidation resistance and the opportunity to learn about approaches to future alloy improvements. Alloys 1 and 3 were finally produced as ingot and reduced to billet and were studied in this effort. The oxidation resistance of both of these alloys was significantly improved over conventional Nb alloys but with the expected reduction in high temperature mechanical properties.

Based on the useful properties of the relatively simple Nb-Ti alloys future studies should concentrate on further, higher level, alloy development to further improve the oxidation and mechanical properties of the base alloy. Environmental coatings for the alloys should be

surveyed and, if necessary, improved for both adhesion to increase life and protective capability. Also, methods of applying the coatings should be determined and demonstrated on the lower temperature capability Nb-Ti alloys. The choice of an improved coating application method would be required to reduce the need for a high temperature exposure, which is required in present coating methods, and can alter the microstructure in Nb-Ti alloys.

## 7.0 References

1. Behavior and Properties of Refractory Metals, T.E. Teitz, and J.W. Wilson, publ, 1965, Stanford University Press, Stanford, Ca.
2. J. H. Perepezko, et al., " High Temperature Phase Stability in the Ti-Al-Nb System," in High Temperature Aluminides and Intermetallics Symposium Proceedings, TMS-AIME, October 1989, Indianapolis IN
3. P. Kofstad, High Temperature Corrosion, Elsevier Applied Science, New York, 1988.
4. C.T. Sims, W. D. Klopp and R.I. Jaffee, "Studies of the Oxidation and Contamination Resistance of Binary Columbium Alloys," Trans. ASM, Vol. 51, 1959, pp. 282-297.
5. C.S. Wukusick, "Intermediate Temperature Behavior of Cb-Al Alloys," GE-ANPD, XDC 61-4-54, March 1961.
6. C.S. Wukusick, "Oxidation Behavior of Intermetallic Compounds in the Nb-Ti-Al System," US Atomic Energy Commission Contract AT(40-1)-2847, General Electric Report GEMP-218, July 1963.
7. G. Welsch and A. Kahveci, "Oxidation of Titanium Aluminide Alloys," in Oxidation of High Temperature Intermetallics, T. Grobstein and J. Doychak eds., TMS, 1989.
8. R.A. Perkins et al., "Effect of Alloying, Rapid Solidification, and Surface Kinetics on the High Temperature Environmental Resistance of Niobium," under AFOSR contract F49620-86-C-0018, January 1989.
9. J.R. Dobbs, D.G. Konitzer and J.C. Schaeffer, "Rapidly Solidified Oxidation Resistant Niobium Base Alloys," USAF Contract F33615-87-C-5298, Interim Report No. 8, May 1991.
10. Very High Temperature Titanium Base Materials, Contract F33615-86C-5073, Final Report WL-TR-91-4070, January 1993.